UNIVERSITÉ DE STRASBOURG

ÉCOLE DOCTORALE MSII (ED n°269)

INSA de Strasbourg

Laboratoire des sciences de l'ingénieur, de l'informatique et de l'imagerie (ICUBE)-UMR 7357

THÈSE présentée par :

Fu-Jiao TANG

soutenue le : **13 Décembre 2019**

pour obtenir le grade de : **Docteur de l'Université de Strasbourg**

Discipline/ Spécialité : **Mécanique, Génie Civil**

Investigation numérique sur l'échangeur de chaleur installé dans des sols peu profonds

THÈSE dirigée par :

M. NOWAMOOZ Hossein Maître de conférences (HDR), INSA de Strasbourg

RAPPORTEURS :

Mme. MASROURI Farimah Professeur, Université de Lorraine - ENSG

M. CUI Yu-Jun Professeur, École des Ponts ParisTech

AUTRE MEMBRE DU JURY :

M. MROUEH Hussein Professeur, Universitéde Lille

INVITE :

M. MIGAULT Bernard Maître de conférences (HDR), INSA de Strasbourg

UNIVERSITY OF STRASBOURG

Numerical investigation on the ground heat exchanger installed in shallow depth soils

by

Fu-Jiao TANG

A thesis submitted in partial fulfillment for

the degree of Doctor of Philosophy

in the

Doctoral School of MSII

December 2019

Acknowledgements

There are many people I would like to acknowledge during the Ph.D. study in Strasbourg, for the help, support and encouragement they have provided. Do not be surprised if you are not in the following list, you are in my heart.

I would like to show my sincere gratitude to my supervisor, Hossein NOWAMOOZ, for his motivation, patience, wisdom, efficiency, and immense knowledge. As the unique supervisor in my Ph.D. study, he has given me crucial guidance and precious suggestions.

I am grateful to Prof. Yu-Jun CUI and Prof. Farimah MASROURI, for being the rapporteurs of my dissertation and giving me insightful comments. Gratitude also goes to Prof. Hussein MROUEH, and Assoc. Prof. Bernard MIGAULT, for accepting to be part of the jury and providing valuable suggestions for this thesis.

I express my acknowledgements to the professors in the division of Civil Engineering and Energy at INSA de Strasbourg, Prof. Cyrille CHAZALLON, Assoc. Prof. Georg KOVAL, Assoc. Prof. Juan Carlos QUEZADA, and Assoc. Prof. Saida MOUHOUBI. They are kind and always ready to help.

My special thanks go to the previous and current Ph.D. students in our office: Peng JING, Xiao-Feng GAO, Gui-Xian LIU, Anicet DANSOU, Laura GAILLARD, Hossein ASSADOLLAHI, Lei MA, Léo COULON, Xiang ZHANG, Chong WANG and Hai-Tao GE, for their help, encouragement, and the memorable times we have spent together.

Besides, the financial support by China Scholarship Council (CSC) is quite appreciated.

Deep gratitude to my beloved parents and grandparents. We have hardly been together since 2009, but you have been giving me continuous support, comprehension and love that enable me to complete this thesis.

Publications

Journal Papers

Tang F, Nowamooz H. Factors influencing the performance of shallow Borehole Heat Exchanger. Energy Conversion and Management 2019; 181:571-583. https://doi.org/10.1016/j.enconman.2018.12.044.

Tang F, Nowamooz H. Long-term performance of a shallow borehole heat exchanger installed in a geothermal field of Alsace region. Renewable Energy 2018; 128: 210-222. https://doi.org/10.1016/j.renene.2018.05.073.

Tang F, Nowamooz H. Sensitive analysis on the effective soil thermal conductivity of the Thermal Response Test considering various testing times, field conditions and U-pipe lengths. Renewable Energy 2019; 143:1732-1743. https://doi.org/10.1016/j.renene.2019.05.120.

Tang F, Nowamooz H. Outlet temperatures of a slinky-type Horizontal Ground Heat Exchanger with the atmosphere-soil interaction. Renewable Energy 2020; 146:705-718. https://doi.org/10.1016/j.renene.2019.07.029.

Conference Papers

Tang F, Nowamooz H. Hydro-Thermal Properties of the Unsaturated Soil. Conference: Civil Infrastructures Confronting Severe Weathers and Climate Changes Conference. Hangzhou 2018. DOI: 10.1007/978-3-319-95744-9_2.

Tang F, Nowamooz H. The performance of Borehole Heat Exchanger installed in unsaturated soils. European Geothermal Congress 2019.

CONTENTS

LIST OF FIGURES

LIST OF TABLES

GENERAL INTRODUCTION

Renewable energy is continuing to gain importance since traditional energy sources are not unlimited in the long run, especially for an epoch with increasing energy demand. Moreover, environmental risks such as air pollution, regional acidification and climate change (Shortall et al., 2015) emerge gradually by consuming fossil fuels.

Shallow geothermal energy is among the many sources of renewable energy, and ground heat exchanger coupled heat pump system is often used to profit this energy, the system is conventionally called Ground Source Heat Pump (GSHP) system, composed mainly by ground heat exchanger and heat pump. The U.S. Environmental Protection Agency (EPA) has identified GSHP systems as the most energy-efficient and environmentally clean heating and cooling option (Atam and Helsen, 2016a). In our investigation, two typical closed-loop ground heat exchangers indicating Borehole Heat Exchanger (BHE) and Horizontal Ground Heat Exchanger (HGHE) are investigated.

Till now, there are various (semi-) analytical and numerical simulation approaches to evaluating the performance of ground heat exchangers. However, the hydrothermal transfer in surrounding soil has rarely been studied. Instead, the surrounding media is conventionally supposed to be homogeneous with effective soil thermal properties and average ground temperatures, especially in the analytical model. As shallow BHEs are often (partly) installed in soils, it is necessary to investigate the hydrothermal variation around the ground heat exchanger during its service period.

The installation of BHEs is increasing over the years, however, some drawbacks have also surfaced. For instance, Hein et al. (2016) report that some BHE applications are experiencing the gradual decrease of outflow temperatures and have to be shut down. Therefore, it is necessary to comprehensively study the aspects influencing the BHE performance. For

example, the geotechnical condition surrounding the BHE, the grout, the pipe and the carrying fluid. To ensure a stable operation of BHE, factors influencing its performance must be identified during the design stage.

In the perspective of BHE, Thermal Response Test (TRT) is often conducted to obtain the effective ground thermal conductivity surrounding the BHE. Nevertheless, the capital investment of TRT is not affordable for some small or medium projects. Therefore, it is necessary to provide guidance of the effective soil thermal conductivity surrounding the BHE for some small or medium projects.

Horizontal Ground Heat Exchanger (HGHE) is also one of those closed-loop heat exchangers. Unlike BHE, HGHE is installed shallowly beneath the ground surface, and the atmosphere-soil interaction can influence finally the HGHE performance. Therefore, the traditional boundary condition by setting time-varying ambient temperature on the ground surface might not be accurate. In order to reflect the ambient-soil interaction on the ground surface, Neumann boundary condition can be applied for the ground surface by having time varying heat fluxes considering ground surface energy and water balance.

There are mainly 4 objectives in this investigation:

1. Applying hydrothermal transfer physics in the numerical simulation model for both BHE and HGHE.

2. Exploring different factors influencing the performance of a shallow BHE installed in soils.

3. Providing an approach to estimating the effective soil thermal conductivity surrounding the BHE.

4. Estimating the performance difference of a HGHE by considering conventional Dirichlet boundary condition and the Neumann boundary condition on the ground surface.

The thesis consists of 6 chapters:

Chapter I presents the literature review over the ground heat exchanger systems, including its development and types, with major focuses on the different approaches to estimating the ground heat exchanger performance, the factors influencing the BHE in unsaturated soil, TRT conducted for shallow BHE and the general investigations for the HGHE. The research questions in this project have also been brought out in this chapter.

Chapter II presents a summary of basic physics included in investigating ground heat exchangers. These physics include mass and energy balance in soil, energy balance in grout, energy balance in pipe and energy balance in carrying fluid.

The following 4 chapters (III, IV, V and VI) are based on 4 published research papers in this project.

Chapter III conducts the numerical simulation of a BHE installed in Alsace region (France). The model contains hydrothermal transfer equations in porous media, which is also used for the subsequent chapters. In this chapter, the long-term (from 1 to 5 years) performance of a shallow BHE is evaluated for constant inlet temperature and seasonal heat load scenarios. In addition, the hydrothermal variation of the porous media surrounding the BHE has been analyzed during the working period of the ground heat exchanger. (*Based on* Tang F, Nowamooz H (2018). Long-term performance of a shallow borehole heat exchanger installed in a geothermal field of Alsace region. Renewable Energy 128, 210-222.)

Chapter IV investigates 15 design factors influencing the performance of a shallow BHE installed in two unsaturated soils (clay and sand) for 1 year. The main factors together with the tendency of BHE performance with different parameters are concluded in this chapter. The obtained results have practical values for BHE applications when choosing different BHE parameters. (*Based on* Tang F, Nowamooz H (2019). Factors influencing the performance of shallow Borehole Heat Exchanger. Energy Conversion and Management 181, 571–583.)

Chapter V provides an analytical approach to estimating the effective soil thermal conductivity for BHE installed in unsaturated soils by conducting sensitive analysis of the TRT considering various testing times, field conditions and U-pipe lengths. The approach can be used to roughly estimate the effective soil thermal conductivity for BHE installed in unsaturated soils. The approach is especially useful for small or medium projects with short BHEs which are not able to afford the TRTs. (*Based on* Tang F, Nowamooz H (2019). Sensitive analysis on the effective soil thermal conductivity of the Thermal Response Test considering various testing times, field conditions and U-pipe lengths. Renewable Energy 143, 1732-1743.)

Chapter VI identifies the HGHE performance with Dirichlet and Neumann boundaries on the ground surface. The Dirichlet boundary uses ambient temperature as ground surface boundary, while the Neumann boundary considers the ground surface energy/water balance. It should be

noted that Dirichlet boundary is traditionally used in computation models estimating the performance of a HGHE, however, the surface temperature can be influenced by the HGHE. This effect can further influence the HGHE performance since it is conventionally installed between 1 and 2 meters. The Neumann boundary on the ground surface is closer to real field condition, while it requires additional calculations, such as energy/water balance on the ground surface, which make it not popular to researchers. This chapter gives a general idea on how the two different boundaries influence the HGHE performance. (*Based on* Tang F, Nowamooz H (2020). Outlet temperatures of a slinky-type Horizontal Ground Heat Exchanger with the atmosphere-soil interaction. Renewable Energy 146, 705-718.)

Conclusions and perspectives are summarized in the additional chapter.

I. LITERATURE REVIEW

I.1. Introduction

In the 21st century, one of the major challenges is the global warming caused by burning fossil fuels: oil, coal, and natural gas. The major greenhouse gas leads to global warming is CO_2. Its emission in the last 18 years has been shown in Figure I.1 (International Energy Agency (IEA), 2018). The figure shows that the global energy-related CO_2 emissions grew 1.7% in 2018 to reach a historic level of 33.1 Gt, which was the highest growth rate since 2013.

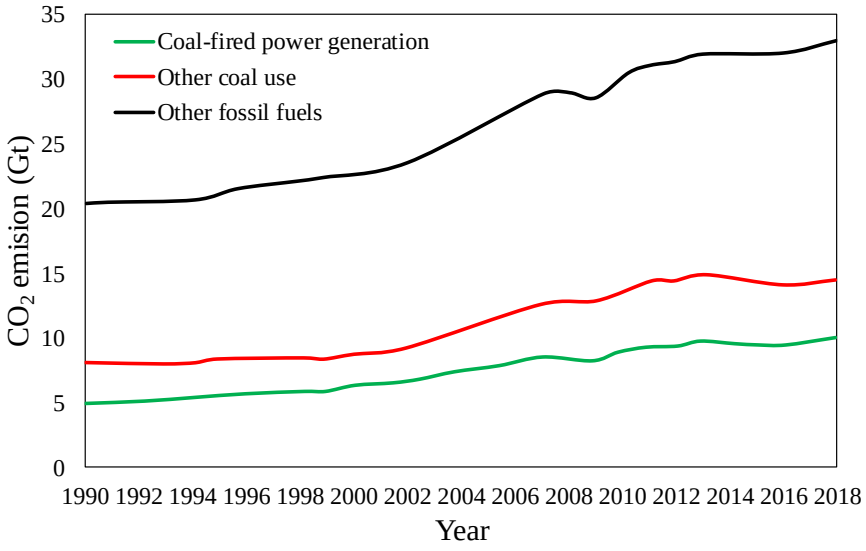

Figure I.1. Global energy-related carbon dioxide emissions by source, 1990-2018 (International Energy Agency (IEA), 2018)

To meet the ever-increasing energy need and ensure a clean environment, renewable and sustainable sources of energy such as geothermal, solar, wind, and wave energy should be adopted to substitute or lower the dependence on the use of fossil fuels, and there are a

number of policies encouraging the use of renewable energy (Singh et al., 2019). In the current work, geothermal energy was considered.

Generally speaking, the geothermal energy is identified by three categories: deep geothermal energy with high-temperature (higher than 150 ºC) for electricity production; intermediate geothermal resource (less than 150 ºC) for direct use; low-temperature reservoir (less than 32 ºC) for Ground Source Heat Pump (GSHP) applications (Omer, 2018). There are restrictions on the well depth and the local geological condition for the electricity production and direct use geothermal energy, while GSHP systems has less restrictions since ground temperature has negligible fluctuation as the depth reaches 10 m beneath the ground surface. The steady temperature beneath the ground surface has been profited since prehistoric times to store food or to live in (Sanner, 2017). Shallow geothermal energy can also be accessed both during the day and the night, without stop.

The GSHP applications include space heating and cooling, water heating, crop drying, agricultural greenhouses, government housing facilities, etc. (Bose et al., 2002). As one of the renewable energies, the GSHP applications are increasing over the last decades all over Europe as a result of their high energy efficiency and support from the renewable energy policies and European directives (Tsagarakis et al., 2018). Generally, the overall installation growth in Europe is continuing at a steady pace, and the installed capacity surpasses 23,000 MWth by 2018, distributed over more than 1.9 Million GSHP installations (EGEC, 2019). The main difference of GSHPs with a conventional Air Source Heat Pump (ASHP) is that they use the ground as a heat source or heat sink. The main advantage of GSHP systems over ASHPs is their stable and higher efficiency thanks to a relatively higher-lower (relatively higher for winter, relatively lower for summer) and stable ground temperature compared to the ambient air temperature (Atam and Helsen, 2016b). A detailed comparison between the ASHPs and GSHPs from different aspects is given in Table I.1.

Table I.1. Comparison of different characteristics between GSHPs and ASHPs (Atam and Helsen, 2016b) (0: weakest, 5: highest)

		ASHPs	*GSHPs*		
			Vertical	*Horizontal*	*Open-water*
Energy efficiency		1	5	3	3
Design criteria	Feasibility	3	1	1	1
	Construction difficulty	1	5	3	3

Capital cost		1	5	3	3
	Installation	1	5	3	3
Life cycle cost	Operation	3	1	1	1
	Maintenance	3	1	1	1
	Total	3	1	1	1
	CO_2 emissions	3	1	1	1
Environmental	Land disturbance	0	3	1	1
	Water contamination	0	0	0	1
Equipment life		1	3	3	3
	Operation restrictions	3	1	1	1
	Aesthetics	1	3	3	3
Practical issues	Quietness	1	5	5	5
	Vandalism	1	0	0	0
	Indoor comfortability	1	3	3	3
	Safety	3	3	3	3

According to Naldi and Zanchini (2018), Ground-Coupled Heat Pump (GCHP) is the most applied GSHP since it does not require groundwater extraction and can be installed almost everywhere. The most popular GCHP is the vertical-displaced ground heat exchanger system, called BHE system. The schematic diagram of a conventionally used GCHP system has been shown in Figure I.2. In the heating season, the ground heat exchanger will absorb heat from ground, and this energy will be transferred to heat pump, which is conventionally based on a vapor-compression refrigerant cycle. The heat pump is driven by electricity. After that, the energy will be used for distribution system (such as domestic heating).

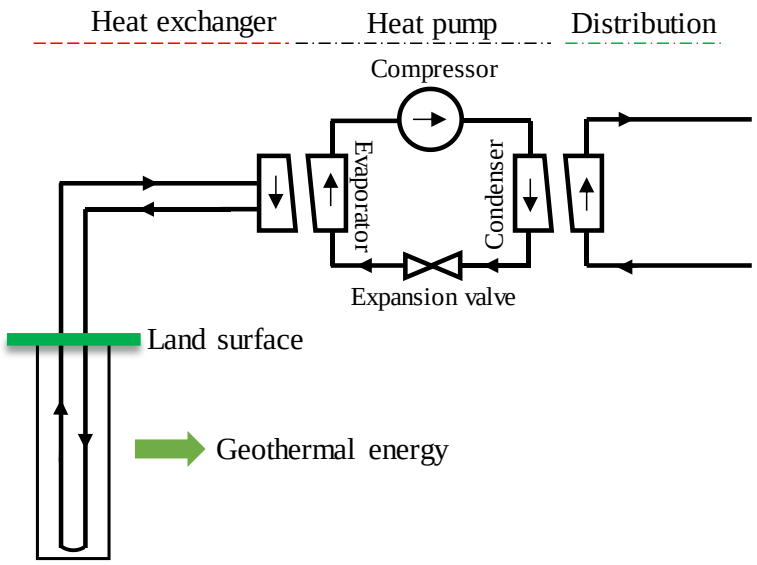

Figure I.2. Schematic diagram of a GCHP system

Blum et al. (2010) demonstrate that the CO_2 reductions for one installed GSHP unit with an average heating supply of 11 kW is at least 1800 kg per year in Germany. GSHP system is also reported as the most cost-effective heating and cooling systems (Serageldin et al., 2018). Due to its advantage, it has been estimated that about 1.3 million GSHP systems are installed worldwide in 2005, and this number has been increased at least twice in comparison to the year 2000. Bertani (2016) reports the installed capacity of geothermal energy all over the world increases 13.0% from 2005 to 2015, and there will be a 68.5% increase from 2015 to 2020. However, the high investment cost that involves in the GSHP systems in comparison with other more conventional systems, despite being more efficient, has led to a low implementation of these systems in zones like the South of Europe, especially in comparison with northern countries, where the use of GHSPs for heating applications is widespread (Cazorla-Marín, 2019). In 2008, Sweden represented more than one third of the total GSHPs in European countries, where GSHP systems supplied around 20% of the heating demand (reaching around 35% of savings in greenhouse gases emissions), followed by Norway (around 9%) and Finland (around 7%), while in southern countries they supplied less than 1% of the total heating demand (Bayer et al., 2012; Cazorla-Marín, 2019).

The shallow geothermal energy system has an approximate lifespan of 40-50 years and is regarded as a semi-permanent energy system (Lee et al., 2018). Generally, open and closed heat exchangers are available for the exploitation of shallow geothermal energy (Florides and Kalogirou, 2007), which are then served as low-potential sources of thermal energy for heat

pumps (Adamovsky et al., 2015a). Open-loop systems can provide a higher energy yield than closed-loop systems, however, they have a higher financial risk due to running costs and a higher environmental risk associated with possible groundwater pollution (Cui et al., 2016).

The thesis is mainly about investigating and improving the design techniques of closed-loop ground heat exchanger. In this chapter, some general ideas about ground heat exchangers and the related researches are going to be introduced.

The introduction about GSHP system is going to be presented in section I.2. The conventional open and closed-loop ground heat exchangers are shown in section I.3. Some existing models, investigations and solutions about the shallow Borehole Heat Exchangers (BHEs) are presented in section I.4. Further computational models, investigations and the problematic points about the Horizontal Ground Heat Exchangers (HGHEs) are shown in I.5.

I.2. The introduction about GSHP system

The first known record of the concept of GSHP is a patent issued in 1912 in Switzerland (Ball et al., 1983; Yang et al., 2010). The first wave of interest in the GSHP technology began in both North America and Europe after the 2nd World War and lasted until the early 1950s when gas and oil became widely used as the heating fuels. At that time, the basic analytical theory for the heat conduction of the GSHP system was proposed by Ingersoll and Plass (1948), which served as a basis for the development of some of the later design programs.

The next period of intense activity on the GSHPs started in North America and Europe in 1970s after the first oil crisis, with an emphasis on experimental investigation (Yang et al., 2010). Nonetheless, the lack of experience, quality, knowledge of the installers, etc. ruined the reputation of heat pumps in Germany around 1980, and the sales numbers of the GSHP dropped before the decrease of the oil price (Sanner, 2017). The systems used in the late 1980s are similar to modern systems which consists of a borehole drilled into the ground equipped with a heat exchanger. The heat exchanger commonly consists of a single U-shaped plastic tube in which a fluid is circulated to transfer heat from the bedrock surrounding the borehole (Johnsson and Adl-Zarrabi, 2019). In the ensuing decades, further efforts were made to establish the installation standards and to develop design methods (Yang et al., 2010).

The GSHP systems include the stand-alone GSHP systems and the hybrid GSHP systems. The major purpose of using hybrid GSHP systems is to reduce the high initial cost of GSHP

systems and to improve the system performance through maintaining the ground thermal balance. Auxiliary heat rejecters or absorbers are used in hybrid GSHP systems to supply a fraction of building cooling or heating demand. The cooling towers and solar thermal collectors are the most common auxiliary heat rejecters and heat absorbers in hybrid GSHP systems. In recent decades, some newly developed energy technologies such as Phase Change Materials (PCMs) and Photovoltaic Thermal (PVT) collectors have also been used to couple the GSHP systems (Xia, 2017).

The conventional GSHP systems are secondary loop geothermal systems, containing the loop installed in ground and the loop for heat pump. There are also explorations on direct expansion geothermal heat pump, which is a single loop configuration (Figure I.3). In this heat pump, the refrigerant is circulating directly through the pipe installed in the ground and there is no need of a loop to heat pump heat exchanger. Copper piping is commonly used in these systems due to its superior heat transfer characteristics (Self et al., 2013). The main advantages for this single loop configuration are reduced costs by eliminating the secondary loop ground side, low power consumption for operation, reduced maintenance costs and improved heat transfer conditions between the grout and the U-pipe thanks to copper used to manufacture the underground U-pipe compared to plastic used in secondary loop systems (Fannou et al., 2014). However, direct expansion systems are pressurized, necessitating good engineering since the probability of rupture is increased due to substantial above ground forces or abnormal operation. The entire system may need to be dug up for repairs if piping is damaged. Another disadvantage of this system is the requirement for increased refrigerant to accommodate the volume of the ground loop, which increases cost (Self et al., 2013).

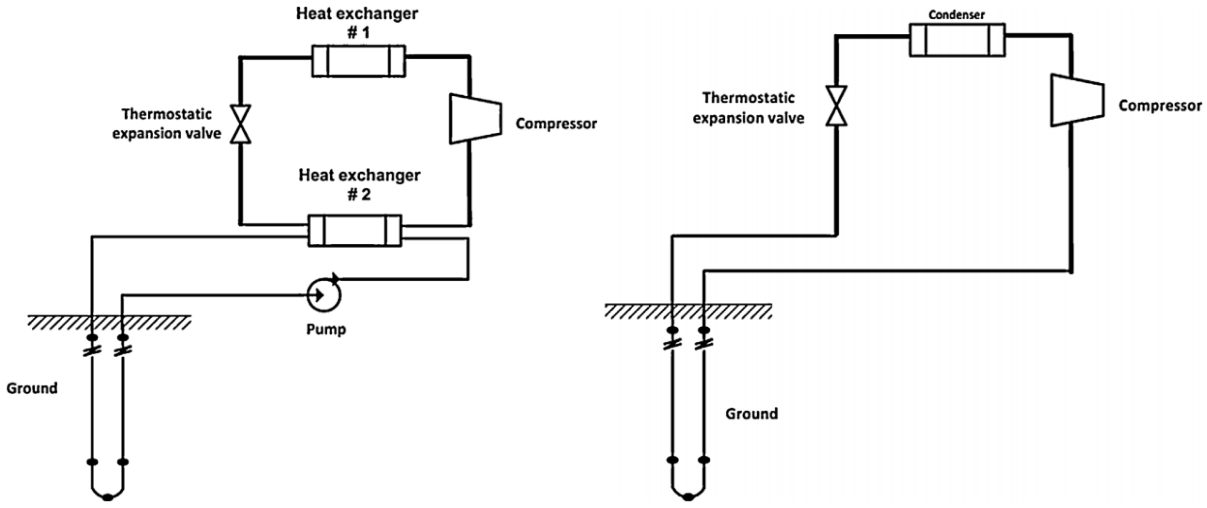

(a) (b)

Figure I.3. (a) Secondary loop geothermal systems and (b) single loop geothermal systems (Fannou et al., 2014)

In the recent years, numerous investigations have been also conducted on the stand-alone GSHP. There are also many (semi-) analytical and numerical approaches in estimating the performance of a ground heat exchanger. However, it is still necessary to estimate accurately the performance of a ground heat exchanger. The optimal design of a ground heat exchanger also enables the GSHP systems to have more economical and environmental benefits, as well maintain a positive reputation among customers. Our investigation aims to provide approaches to better design GSHP systems concerning the part of ground heat exchanger.

I.3. Different types of ground heat exchangers

The heat pump unit in a GSHP system can be connected with the ground heat exchanger in two general types, denoting open-loop and closed-loop ground heat exchangers (Suryatriyastuti et al., 2012). These two ground heat exchangers are introduced in the following sections. To select appropriate type of geothermal system, it is important to investigate the geology, heat flow, hydrogeological regime, fluid dynamics, fluid chemistry, faults and fractures, stress regime and the local lithological sequence (Eidesgaard et al., 2019; Moeck, 2014).

I.3.1. Open-loop ground heat exchangers

An open-loop ground heat exchanger system is a system that pumps water from a water source to provide heat for the heat pump, and the water that exits from the heat pump unit is discharged into drains, groundwater, or surface water bodies. The discharged water can be useful for other purposes including irrigation, consumption, etc. Most installations are based on a well-doublet scheme in a shallow aquifer including an extraction well, which pumps groundwater, and an injection well where the cooled or warmed water is injected back into the same aquifer at the same rate, but at a different temperature (Bayer et al., 2019). The depth of the wells is typically less than 50 m (Banks, 2012). The Open-loop heat exchanger systems can be connected via different configurations, depending on the type of water intake and discharge sources (Singh et al., 2019), a typical open-loop heat exchanger is shown in Figure I.4.

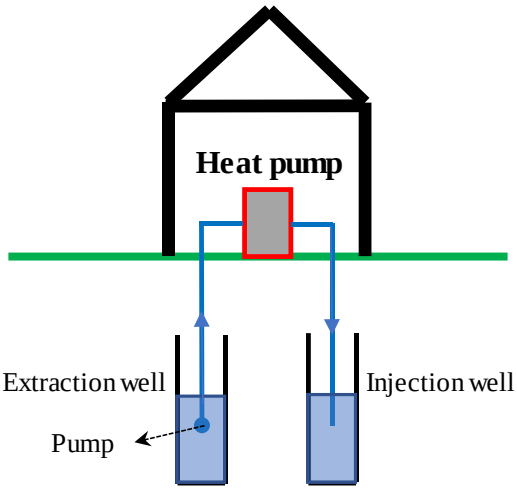

Figure I.4. A typical open-loop ground heat exchanger (Florides and Kalogirou, 2007)

Overall, the open loop systems are considered to have a better thermodynamic performance and a lower cost compared to the closed loop systems (Aresti et al., 2018). However, the system is not available in water shortage areas and its environmental risk is higher due to water pollution.

I.3.2. Closed-loop ground heat exchangers

The closed-loop ground heat exchangers are the most frequently applied ground heat exchangers (Bayer et al., 2019), they are either placed underground in horizontal, vertical or oblique position, and a heat carrier medium is circulated within the heat exchanger, transferring the heat from the ground to a heat pump or vice versa (Florides and Kalogirou, 2007). There are also closed-loop heat exchangers installed in rivers or seas to absorb or reject heat for buildings beside waters (Wu et al., 2019).

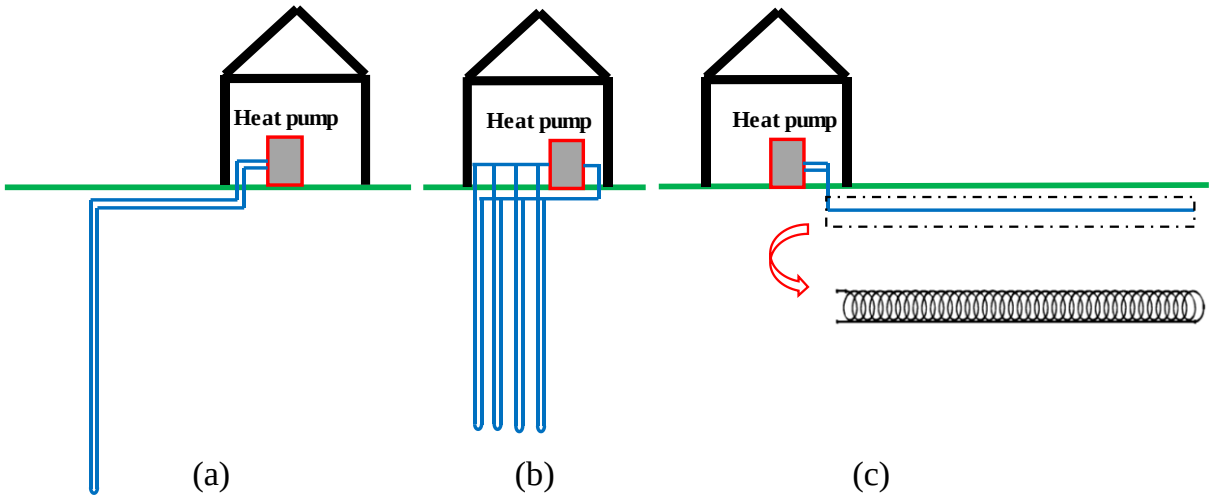

Figure I.5. Three typical closed-loop ground heat exchangers: (a) BHE; (b) energy pile and (c) HGHE

Three typical closed-loop ground heat exchangers are shown in Figure I.5. BHE (Figure I.5-a) is commonly installed vertically beneath the ground surface, commonly ranging between 20 and 200 m. The ground heat exchanger is traditionally surrounded by grout, and the diameter for the borehole ranges between 10 and 15 cm (Abuel-Naga and Al-Chalabi, 2016). To satisfy the energy demand of a building, multi-boreholes are conventionally drilled with at least 4.5 m of spacing between 2 boreholes (Singh et al., 2019). The most distributed BHE is the U-shaped one, which includes single U-pipe, double U-pipe, triple U-pipe, and multi-tube configurations. Figure I.6 shows the percentage of different pipe configurations. The statistics show that the U-pipe is the most widely used configuration of BHEs (72%), while the helix, coaxial, and W-tube configurations have percentages of 13%, 9%, and 6%, respectively (Javadi et al., 2019). Polyethylene (PE) pipe is the most comment pipe material (Javadi et al., 2019). Its main advantage is its space-saving capacity, and it is more efficient than HGHE since it is installed deeper beneath the ground surface. However, the initial cost of the BHE becomes higher compared to conventional heating/cooling systems, which is mainly due to its high drilling cost.

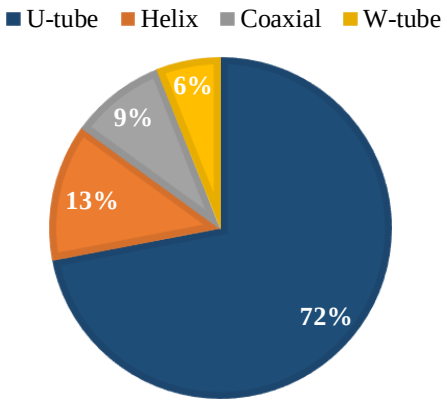

Figure I.6. The percentages of different BHE pipe configurations from 2010 to 2018 (Javadi et al., 2019)

Energy piles (Figure I.5-b) are vertical heat exchangers incorporated in foundation piles and thus limited to new buildings (Bayer et al., 2019). The energy pile can be used as heat exchanger and building structural element (Rammal et al., 2018). The initial drilling cost is eliminated since they are needed for structural support (Singh et al., 2019). Concrete is an

ideal heat transfer medium because of its high thermal energy storage capacity and thermal conductivity (Cui et al., 2018; You et al., 2015). Energy piles are conventionally shorter and wider than boreholes, and their aspect ratios (length to diameter ratio) typically fall below 50, while corresponding ratios for BHEs range between 200 and 1500, and it can accommodate a wide range of configurations (e.g., W shape, single-U, double-U, spiral) (Alberdi-Pagola et al., 2019). It should be noted that because energy piles are installed beneath buildings, the cooling and heating load should be evaluated carefully during the design stage since they are a potential risk of mechanical problems for the buildings. Energy piles are installed conventionally in the building foundations, which may thermally induce additional settlement or load, thus jeopardize the stability of the supported building. The fluid temperatures in energy piles must be kept above 0 (to 2) °C to ensure the structural integrity and to avoid the soil freezing and any deterioration of the bearing capacity (Ground Source Heat Pump Association, 2012).

Compared with BHE and energy piles, HGHE (Figure I.5-c) is less efficient and it requires larger installation areas, while it has the advantage of lower excavation cost, which makes it more suitable for suburban areas where sufficient area is available (Jeon et al., 2018a). HGHE is installed normally between 1 and 2 m beneath ground surface (Garcia Gonzalez et al., 2012), which causes it more tended to be influenced by meteorological conditions than BHE or energy piles. The HGHE is conventionally surrounded by backfill soil from the local site. Generally, a slinky-type pipe can be used as heat exchanger to improve the efficiency of the HGHE.

I.4. Shallow BHEs

The geothermal energy within a range of 0-400 m is categorized as shallow geothermal energy (Erol and François, 2014). Compared with the large initial capital investment required for deep BHE, shallow BHE is more economically feasible and appealing. Nowadays, shallow BHE is adopted in many office buildings due to its good efficiency, low maintenance cost, low noise, and no pollutions. Due to its sustainable characteristics, geothermal energy has been receiving attention over the years. Nowadays, GSHPs are reported as the most cost-effective heating and cooling systems (Serageldin et al., 2018). A schematic of the BHE and the surrounding temperature contour during service period is shown in Figure I.7.

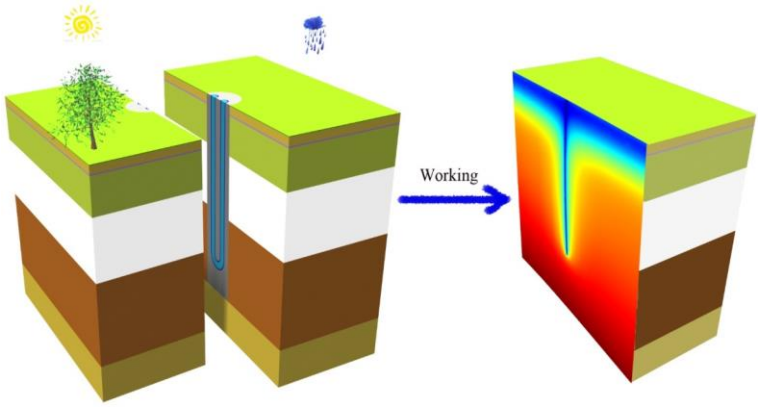

Figure I.7. An example of the BHE and the surrounding temperature during its working period

I.4.1. Computational models for shallow BHEs

There are different models used in the shallow BHE applications. The models based on thermal response factors and numerical simulation models are the most popular approaches in BHE applications. These models are presented in the following.

a) Thermal response factor models

At first, it is the models based on thermal response factors (Atam and Helsen, 2016b). The conventional way in which the thermal processes of a BHE are decomposed is in terms of the radius of the borehole: the process in the borehole is assumed to be in a steady state that is described by the effective thermal resistance of the borehole, R_b. The process outside the borehole depends on time and is represented by a G-function. Thermal response factor models represent techniques based on Infinite/Finite Line Source (I/FLS) theory, Cylindrical Source (CS) theory, etc. Several assumptions must be considered in the mathematic model (Li and Lai, 2015; Yuan et al., 2012):

- The ground is infinite or semi-infinite in extent, depending on whether or not the influence of the surface is considered;
- The ground is with the uniform temperature profile and its thermophysical properties are homogeneous and stable;
- The boundary condition for the wall of borehole or heat transfer pipe is either a constant flux or a constant temperature, and the heating exchange rate is constant;

- If the effect of the seepage of groundwater cannot be ignored, the flow is generally assumed to be homogeneous and parallel to the surface.

These approaches determine borehole wall temperatures in terms of net heat rate per borehole length from the ground and special functions, called G-functions introduced by Eskilson (1987):

$$T_b = T_0 - \frac{q}{k_s} \cdot G\left(\frac{t}{t_s}, \frac{r_b}{z_{U-pipe}}, \frac{B}{z_{U-pipe}}, \frac{D}{z_{U-pipe}}\right) \quad (1.1)$$

where T_b is the borehole wall temperature (°C), T_0 is the undisturbed ground temperature (°C), q is the average heat extraction rate per U-pipe length ($W.m^{-1}$), k_s is the ground thermal conductivity ($W.m^{-1}.K^{-1}$) and G is the G-function. The G-function varies according to the nondimensional time t/t_s, where $t_s = z_{U\text{-}pipe}^2/9\alpha_s$ is the characteristic time of the bore field, $z_{U\text{-}pipe}$ is the pipe length (m) and α_s is the ground thermal diffusivity ($m^2.s^{-1}$), $r_b/ z_{U\text{-}pipe}$ is the non-dimensional borehole radius, B the distance between two neighboring boreholes (m), $B/z_{U\text{-}pipe}$ is the non-dimensional borehole spacing, D the buried depth of the U-pipe (m), and $D/z_{U\text{-}pipe}$ is the non-dimensional buried depth (Cimmino, 2015).

Analytical, semi-analytic and numerical approaches can be used to derive G-functions. The most widely used approaches are based on FLS theory (Eskilson, 1987). Zeng et al. (2002) use the FLS method to obtain the average temperature variation along the U-pipe lengths. Lamarche and Beauchamp (2007) have simplified the solutions for the average temperature along U-pipe by using the FLS solution for the case $D = 0$ and Claesson and Javed (2011) for the case $D >= 0$. Cimmino and Bernier (2014) propose a semi-analytical method to derive the G-functions by dividing the pipe into series of FLS segments. A 2D axisymmetric finite element model to calculate G-functions has been developed by Zanchini and Lazzari (2013). The G-functions along the length of the boreholes are calculated for a uniform heat extraction rate. A 3D finite element model is developed by Monzó et al. (2015) to obtain the G-functions. In their investigation, boreholes are modeled as cylinders of highly conductive material connected above the ground surface. A constant heat is injected into the ground through the highly conductive material. Due to the high thermal conductivity, the temperature tends towards uniformity at the borehole walls and the model replicates Eskilson's G-functions accurately.

The commonly used analytical models to obtain G-functions in BHE applications are listed in the following:

1) ILS model

The ILS model is a direct utilization of the point and infinite line source solutions provided by Carslaw and Jaeger (1959). This model relies on the fact that the borehole heat exchanger is represented by an infinite line embedded along the vertical axis. Thus, it calculates the temperature change at specific location in an infinite homogeneous medium based on the formula of point heat source, then using integration to account for the effect of other point sources at that desired location. The model assumes that the contact between the soil and the BHE goes along the centerline of the borehole, not along its surface area.

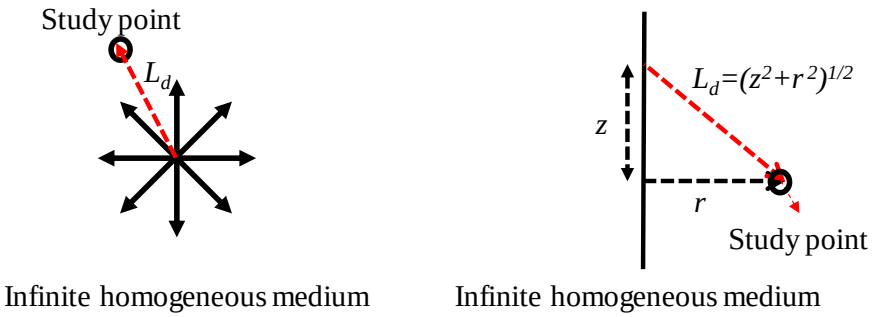

Figure I.8. Different heat sources (a) point source, and (b) infinite line source (Abdelaziz, 2013)

Ingersoll et al. (1948) propose that the temperature change at a distance r from a point heat source emitting instantaneously q' units of heat at a time t as shown in Figure I.8-a can be calculated as follows:

$$\Delta T = \left(\frac{q'\alpha_s}{k_s}\right)\left(\frac{1}{2\sqrt{\pi\alpha_s\tau}}\right)^3 e^{-(r^2+z^2)/(4\alpha_s\tau)} \quad (1.2)$$

where α_s is the soil thermal diffusivity ($m^2.s^{-1}$), k_s is the soil thermal conductivity ($W.m^{-1}.K^{-1}$), τ is time (s), $L_d = \sqrt{r^2 + z^2}$ is the distance between the point source and the study point (m).

Integration is then used to estimate the temperature change due to the ILS. Again, the source is represented by adjacent points which for each one of them the distance to the location of interest are L_d (Figure I.8-b), given as:

$$\Delta T = \int_{-\infty}^{+\infty} (\frac{q\alpha_s}{k_s})(\frac{1}{2\sqrt{\pi\alpha_s\tau}})^3 e^{-(r^2+z^2)/(4\alpha_s\tau)} dz \tag{1.3}$$

Therefore:

$$\Delta T = (\frac{q\alpha_s}{k_s})(\frac{1}{2\sqrt{\pi\alpha_s\tau}})^3 \int_{-\infty}^{+\infty} e^{-(r^2+z^2)/(4\alpha_s\tau)} dz = \frac{q\alpha_s}{4\pi k_s \tau} e^{-r^2/(4\alpha_s\tau)} \tag{1.4}$$

Suppose the heat source injects/extracts energy continuously from time 0 to t, the equation can be estimated as:

$$\Delta T = \frac{q\alpha_s}{4\pi k_s} \int_0^t \frac{e^{-r^2/(4\alpha_s\tau)}}{\tau} d\tau \tag{1.5}$$

By setting $\beta = r / (2\sqrt{\alpha_s \tau})$:

$$\frac{d\beta}{d\tau} = \frac{r}{2} \cdot \frac{1}{\alpha_s^{0.5}} \cdot \frac{1}{-2} \cdot \frac{1}{\tau^{1.5}} \tag{1.6}$$

$$\frac{d\tau}{\tau} = \frac{-4}{r} \cdot \alpha_s^{0.5} \cdot \tau^{0.5} \tag{1.7}$$

Therefore, the temperature variation with the integration of β can be deduced:

$$\Delta T = \frac{q}{2\pi k_s} \int_{\beta}^{+\infty} \frac{e^{-\beta^2}}{\beta} d\beta \tag{1.8}$$

The above equation is the final equation used for computing the temperature variation in the surrounding homogeneous medium by assuming the heat exchanger is an ILS.

2) FLS model

The FLS takes the BHE length into account and approximates it by a finite line constituting a series of point sources. The temperature in the soil is calculated by integrating the solution of the continuous point source case over the length of the borehole. For FLS model, an imaginary line source is considered, which has the same characteristic of the original line source, except that it has an opposite heat rate, indicating if the original line injects heat to the ground then the imaginary line extracts heat and vice versa, which enables the ground surface boundary to keep a constant temperature same as its initial one throughout the service period of the BHE.

The content below is the derivation of a general FLS model. The derivation starts from the point source model similar to ILS model as follows (Ingersoll et al., 1948):

$$\Delta T = (\frac{q'\alpha_s}{k_s})(\frac{1}{2\sqrt{\pi\alpha_s\tau}})^3 e^{-L_d^2/(4\alpha_s\tau)} = \frac{(\frac{q'\alpha_s}{k_s})}{8(\pi^{3/2})(\alpha^{3/2})(\tau^{3/2})} e^{-L_d^2/(4\alpha_s\tau)} \quad (1.9)$$

If a point source operates continuously from time 0 to t, the point source formula is integrated as:

$$\Delta T = \frac{(\frac{q'\alpha_s}{k_s})}{8(\pi^{3/2})(\alpha_s^{3/2})} \int_0^t e^{-L_d^2/(4\alpha_s\tau)} \tau^{-3/2} d\tau \quad (1.10)$$

The above formula integrating from time 0 to time t can be deduced as the following form by setting $\beta = L_d / (2\sqrt{\alpha_s\tau})$:

$$d\tau = \frac{-4}{L_d} \cdot \alpha_s^{0.5} \cdot \tau^{3/2} \cdot d\beta \quad (1.11)$$

$$\Delta T = \frac{(\frac{q'\alpha_s}{k_s})}{8(\pi^{3/2})(\alpha_s^{3/2})} \int_0^t e^{-\beta^2} \tau^{-3/2} \frac{-4}{L_d} \cdot \alpha_s^{0.5} \cdot \tau^{3/2} \cdot d\beta = \frac{(\frac{q'\alpha_s}{k_s})}{2(\pi^{3/2})\alpha_s L_d} \int_\beta^{+\infty} e^{-\beta^2} d\beta \quad (1.12)$$

$$\Delta T = \frac{(\frac{q'\alpha_s}{k_s})}{4\pi\alpha_s L_d} \cdot \frac{2}{\sqrt{\pi}} \int_\beta^{+\infty} e^{-\beta^2} d\beta \quad (1.13)$$

By introducing error function:

$$\frac{2}{\sqrt{\pi}} \int_\beta^{+\infty} e^{-\beta^2} d\beta = erfc(\beta) = erfc(\frac{L_d}{2\sqrt{\alpha_s t}}) \quad (1.14)$$

The temperature variation becomes:

$$\Delta T = \frac{q'}{4\pi k_s L_d} \cdot erfc(\frac{L_d}{2\sqrt{\alpha_s t}}) \quad (1.15)$$

For a U-pipe with the length of $z_{u\text{-}pipe}$, the temperature variation integration over its length can be given as:

$$\Delta T = \frac{q}{4\pi k_s}\int_0^{z_{U-pipe}} \frac{erfc(\frac{L_d}{2\sqrt{\alpha_s t}})}{L_d} dL_d \qquad (1.16)$$

Physically, the soil mass is semi-infinite, and the surface temperature variation has significant influence on the soil temperature. To model the soil mass as a semi-infinite region in the vertical direction and impose a prescribed temperature at the ground surface, the method of images can be utilized (Carslaw and Jaeger, 1959). This method was first introduced in the mathematical theory of electricity, and elegantly adopted to the solution of heat conduction in semi-infinite medium, where a constant temperature is imposed at the surface (Al-Khoury, 2012). The image has corresponding values as those in the original line but opposite in magnitude (Figure 2).

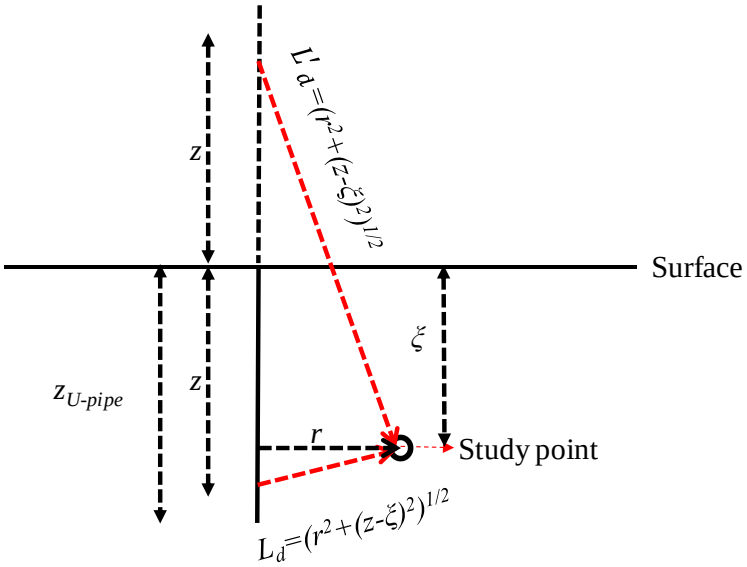

Figure I.9. Finite line source model (Al-Khoury, 2012)

Based on this technique, Eskilson (1987) introduced the FLS model, expressed as:

$$\Delta T = \frac{q}{4\pi k_s}\int_0^{z_{U-pipe}} \left(\frac{erfc(\frac{L_d}{2\sqrt{\alpha_s t}})}{L_d} - \frac{erfc(\frac{L_d'}{2\sqrt{\alpha_s t}})}{L_d'} \right) d\xi \qquad (1.17)$$

where

$$L_d = \sqrt{r^2 + (z-\xi)^2} \tag{1.18}$$

$$L_d' = \sqrt{r^2 + (z+\xi)^2} \tag{1.19}$$

Thus, the equation representing ground temperature variation for a FLS model can be given as:

$$\Delta T = \frac{q}{4\pi k_s}\int_0^{z_{U-pipe}} \left(\frac{erfc(\frac{\sqrt{r^2+(z-\xi)^2}}{2\sqrt{\alpha_s t}})}{\sqrt{r^2+(z-\xi)^2}} - \frac{erfc(\frac{\sqrt{r^2+(z+\xi)^2}}{2\sqrt{\alpha_s t}})}{\sqrt{r^2+(z+\xi)^2}} \right) d\xi \tag{1.20}$$

3) Solid Cylindrical Source (SCS) model

The CS solution for a constant heat transfer rate was first developed by Carslaw and Jaeger (1959), then refined by Ingersoll et al. (1948). The cylindrical heat source can be regarded as a collection of numerous line sources with a heating rate of $qd\varphi/(2\pi)$, disposed along a circle of the radius r_b. The temperature rise at any location with the radial coordinate r should be the sum, or integral, of all the individual temperature rises caused by the corresponding line sources. The solid cylindrical source model is provided as follows (Man et al., 2010):

$$\Delta T = \frac{qk_s}{\alpha_s}\int_0^t\int_0^{z_{U-pipe}} \frac{1}{8(\sqrt{\pi\alpha_s t})} I_0(\frac{rr_b}{2\alpha_s t}) \left(e^{-\left(\frac{r^2+r_b^2+(z'-z)^2}{4\alpha_s t}\right)} \right) dz'dt \tag{1.21}$$

where

$$I_0(x) = \frac{1}{\pi}\int_0^{\pi} e^{x\cdot\cos\varphi} d\varphi \tag{1.22}$$

4) Model improvements and some comments

Besides the basic conventional models described above, there are many developments on these models. Molina-Giraldo et al. (2011) provide an analytical approach from the FLS model that accounts for groundwater flow. It is a 3D model taking a constant surface temperature and vertical heat losses (axial effects) into account. Abdelaziz et al. (2014) introduce a finite line-source model for BHE embedded in a layered soil profile. They divide the heat exchanger into a number of segments to represent various soil layers along its length

and heat exchange induced temperature change at a certain location within the soil formation is subsequently evaluated by summing up the individual contributions of all these segments. Erol and François (2018) have extended the capability of the existing composite method of Abdelaziz et al. (2014) by taking into account the groundwater flow and the anisotropy in different layers. Bandos et al. (2009) present a solution to the three-dimensional FLS model for BHE that takes into account the geothermal gradient and allows arbitrary ground surface temperature changes. Analytical expressions for the average ground temperature are derived by integrating the exact solution over the line-source depth. This method has been further developed by Zhang et al. (2019), which can apply more complex boundary conditions. Based on CS model, Nian and Cheng (2018) propose a new analytical model of thermal response function that takes the effect of borehole heat capacity on ground thermal response into account. They find that their model shows higher precision for simulation of ground thermal response. Lamarche (2017) develop a modification of the classical finite line source solution in order to take into account the linear variation of a thermal load along the line source. The new mathematical solution allows a more precise representation of the thermal load along the borehole in the case of thermal simulation of ground heat exchangers.

The models based on thermal response factors are widely used in real applications, however, some aspects influencing the BHE performance have been neglected. For example, Fossa (2011) reports that FLS solution overestimates Eskilson's G-functions when thermal interaction between boreholes becomes significant due to the difference in the boundary condition at the borehole walls used to calculate the G-functions. Yang et al. (2010) note that both the ILS model and the CS model neglect the axial heat flow along the borehole depth, resulting that they are not adequate for analyzing the long-term BHE performance. Lamarche and Beauchamp (2007) compare the G-function obtained from the CS and the FLS model. They conclude that neither solution reaches a steady state value, which is due to the logarithmic behavior of the solution at infinity and they are not appropriate for a large time simulation. Li and Lai (2015) report that moisture transfer in porous medium can influence largely the thermal process in the ground, however, it seems that the analytical solutions are impossible to be used to investigate the moisture transfer in BHE applications. Hermanns and Ibáñez (2019) point out that G-function model is ill-posed when $D = 0$ m, indicating that a solution to the formulated problem with $D = 0$ m can be obtained for a given numerical discretization, but that solution will not converge to a unique solution as the numerical

discretization is refined. They have further adopted a method to solve this problem by assuming uniform heat injection rate per unit borehole length. Cimmino (2018) report that using series of FLS segments to model the boreholes significantly increases the computational time for the evaluation of the thermal response factors. The computational time is approximately proportional to the square of FLS in the bore field.

b) Numerical simulation approaches

Numerical modelling approaches in shallow BHE engineering are normally based on finite difference/volume/element methods and the models are large-scale models in general. The numerical simulation models are the most accurate models since they can consider dynamic ground surface boundary conditions, the effects of moisture in the soil and groundwater flow (Atam and Helsen, 2016a). However, the numerical simulation models require a large amount of calculation time compared with models based on thermal response factors. Nevertheless, the numerical simulation models are popular due to the increasing performance of computers, such as some packages in finite element software: COMSOL Multiphysics, FlexPDE, TOUGHREACT, FEFLOW, OpenGeoSys, GLD, etc. (Aresti et al., 2018).

The following equations show an example of the physics in the numerical simulation of heat transfer in a BHE regarding 2D cylindrical model by using equivalent method to simplify the geometry of the BHE (Yuan et al., 2012):

$$\rho_f C_{p-f}\left(\frac{\partial T_f}{\partial t}+u_f\frac{\partial T_f}{\partial z}\right)=Q_f \quad (x \le r_{e-i}) \tag{1.23}$$

$$\rho_p C_{p-p}\frac{\partial T_p}{\partial t}=\frac{1}{r}\frac{\partial}{\partial r}\left(k_p r\frac{\partial T_p}{\partial r}\right)+\frac{\partial}{\partial z}\left(k_p\frac{\partial T_p}{\partial z}\right)+Q_p \quad (r_{e-i} \le x \le r_{e-o}) \tag{1.24}$$

$$\rho_s C_{p-s}\frac{\partial T_p}{\partial t}=\frac{1}{r}\frac{\partial}{\partial r}\left(k_s r\frac{\partial T_s}{\partial r}\right)+\frac{\partial}{\partial z}\left(k_s\frac{\partial T_s}{\partial z}\right)+Q_s \quad (0 < z < z_{U-pipe}, r_{e-o} \le x \le r_\infty) \tag{1.25}$$

The equivalent radius for the U-pipe with unique radius (the conventional case) can be given as:

$$r_e=\sqrt{\frac{2\sum_{i=1}^{n} r_i^2}{n}} \tag{1.26}$$

With the initial condition:

$$T_s(r,z,0) = T_f(z,0) = T_p(r,z,0) = T_0 \quad (1.27)$$

Fluid inlet temperature is popular to be set as a boundary condition, the method by controlling temperature difference between inlet and fluid temperatures can also be used to set heat load as boundary condition. The boundary with fluid temperature can be given as:

$$T_f(z=0,\mathrm{t}) = T_{in} \quad (1.28)$$

The lateral boundary condition is normally considered to be adiabatic, defined as:

$$\left.\frac{\partial T_s}{\partial r}\right|_{r=\infty} = 0 \quad (1.29)$$

When there is no heat flux considered at the bottom, the boundary condition is given as:

$$\left.\frac{\partial T_s}{\partial z}\right|_{z=z_{U-pipe}} = 0 \quad (1.30)$$

For BHE, Dirichlet boundary condition is normally applied, and the ground surface temperature is conventionally assumed to be the same as the air temperature, therefore:

$$T_a = T_s(z=0) \quad (1.31)$$

where $r_{e\text{-}i}$ and $r_{e\text{-}o}$ indicate the inner and outer radius of the equivalent pipe (m), ρ_f, $C_{p\text{-}f}$, T_f, u_f, Q_f are the carrying fluid density (kg.m^{-3}), specific heat capacity (J.kg^{-1}.K^{-1}), temperature (°C), velocity (m.s^{-1}) and heat source (W.m^{-3}), ρ_p, $C_{p\text{-}p}$, T_p, k_p, Q_p are the pipe density (kg.m^{-3}), specific heat capacity (J.kg^{-1}.K^{-1}), temperature (°C), heat conductivity (W.m^{-1}.K^{-1}) and heat source (W.m^{-3}), ρ_s, $C_{p\text{-}s}$, T_s, k_s, Q_s are the soil density (kg.m^{-3}), specific heat capacity (J.kg^{-1}.K^{-1}), temperature (°C), heat conductivity (W.m^{-1}.K^{-1}) and heat source (W.m^{-3}), n refers to the U-pipe number.

In the numerical simulation, fully discretized models of BHE offer precise simulation results even if fast changing boundary conditions are applied (He et al., 2009). However, the application of fully discretized models leads to extensive computation times and a substantial effort. There are some optimizations of the numerical simulation model to reach a reasonable computation time, for example, heat conduction equation in pipe can be simplified as a thermal resistance equation since the energy variation in the pipe is negligible. Bauer et al. (2011) have introduced the thermal resistance models between the carrying fluids and the

grout zones, grout zones and the borehole wall, and the thermal resistance among the grout zones, which can be coupled with numerical simulation method, at the same time reach a reasonable computation speed. Further, heat transfer in the vertical direction is sometimes not considered to simplify the above equations. In this case, the axial effect is neglected. The above computations by simplifying BHE geometry and using thermal resistance models can influence the accuracy of the numerical simulation method, while increase the computational speed.

There are many numerical simulation models being used for the BHE applications. Al-Khoury et al. (2006) investigate transient heat transfer in a double U-shaped vertical heat exchanger by using a three-dimensional finite element method. Yang and Li (2014) develop a 2D numerical model and an analytical composite-medium model to investigate the short-time heat transfer processes in the BHE and their model has been compared with sand box experimental results. Yuan et al. (2016) have developed a mixed numerical/analytical method to investigate the thermal interference and the thermal performance restoration of multiple BHEs. Kerme and Fung (2020) present the analysis, implicit numerical simulation and performance study of heat transfer in a BHE to analyze the heat transfer process of both inside and outside the borehole by using unsteady heat transfer method. Biglarian et al. (2017) develop a transient numerical model for a single U-pipe to simulate the borehole in the short and long time. They have also investigated the effect of time step size on the accuracy of the results. Florides et al. (2013) present a 3D numerical model (finite element method) which accounts only for conductive media to evaluate the fluid temperature along the length of a GHE. Godefroy (2014) present a numerical model for single and double U-pipe boreholes based on the Thermal Resistance and Capacitance (TRC) approach where the borehole is divided into a number of vertical elements. The model is coupled to the infinite cylindrical source analytical solution to simulate ground heat transfer. Cui et al. (2008) use a finite element model to represent a single U-pipe borehole operating in alternative operation modes. Their model can satisfactorily reproduce experimental data with hourly inlet condition variations. Shirazi and Bernier (2013) develop a numerical model to take into account the transient behavior of a single U-pipe borehole. They use their 1D model in annual simulations to show that neglecting borehole thermal capacity (fluid and grout) can lead to a 4-5% overestimation of heat pump energy consumption. He et al. (2009, 2011) present a three-

dimensional numerical model of a borehole based on a finite volume solver to simulate fluid transport along the U-pipe as well as transient heat transfer in and around a GHE.

Some Artificial Neural Network (ANN) models have been recently used owing to the development of Machine Learning (ML) in the recent years, which can identify the complex relationships between inputs and outputs of a BHE (Atam et al., 2015; Esen et al., 2008; Gang and Wang, 2013; Gang et al., 2014). However, there are two obvious drawbacks for the ANN models according to Atam and Helsen (2016a): (a) an ANN based borefield model predicting both short and long term thermal effects in the ground requires training data over 10-20 years, which is not feasible, (b) ANN models may be very complex to be handled in mathematical optimization algorithms. Compared to the thermal response factor and the numerical simulation models, ANN is hardly used to evaluate the performance of a ground heat exchanger.

A qualitative comparison of the thermal response and numerical models is shown in Table I.2 (Atam and Helsen, 2016b). The comparison shows that there are different advantages using thermal response factor models and numerical models for the computation of shallow BHEs. Generally, thermal response models calculate faster, while it is less comprehensive than numerical simulation models.

Table I.2. A qualitative comparison of different modeling methods in terms of research challenges and model characteristics using a scale of 0-5 (0: lowest, 5: highest) (Atam and Helsen, 2016b)

Research challenges & model characteristics	*Modeling approaches*	
	Thermal response factor models	*Numerical models*
Accuracy	3	4
Complexity	4	5
Speed	3	1
Dynamic ground surface boundary condition inclusion capability	1	5
Moisture in the soil effect inclusion capability	1	5
Groundwater effect inclusion capability	1	5
Applicability to dense borefields	5	1
Easiness to obtain	3	1

I.4.2. Experimental methods on shallow BHEs

The experimental works conducted in the literature for BHEs are either performing tests in the field using full-size facilities or in the laboratory on a reduced scale (Salim Shirazi and Bernier, 2014).

For full-size monitoring, a suitable data set includes a high-quality independent measurement of the ground thermal properties at the site. The monitoring of the system also would include accurate measurements of the loop flow rate and the inlet/outlet temperatures, which should commence at the beginning of the system operation (Yavuzturk and Spitler, 2001). Javed and Fahlen (2010) reported on the development of a nine-borehole GSHP test facility, which can be used to develop and validate models for GSHP systems, conduct TRTs, and test operation/control strategies. Cauret and Bernier (2009) conducted experiments on short compact collectors linked to a fluid conditioning system replicating a residential heating load. Spitler et al. (2009) have used a 15-month period dataset collected on a 3-borehole facility from Oklahoma State University to compare various bore field simulation. An experimental facility for the study of hybrid GSHP systems was established at Oklahoma State University and has been reported by Hern (2004) and Gentry (2007). Minutely data have been collected from March 2005 to June 2006. The facility includes a ground heat exchanger array with three BHEs with a diameter of 114 mm, depth of 75 m and spaced 6 m apart. Ruiz-Calvo et al. (2016) provided operational details of a system at Valencia Polytechnic University and provided a long-term reference data set. Minutely data have been collected for a period of 6 years from 2005 to 2011 at the inlet and outlet of the BHE. The heat pump along with power consumption data have also been recorded. The system consists of 6 BHEs with 150 mm of diameter, 50 m of depth. They are spaced 3 m apart in a 2 by 3 rectangular formation. The boreholes are backfilled with soil. Spitler and Gehlin (2019) provided long-term measured system performance data from a GSHP system the new student center installed at Stockholm University for both heating and cooling demand. They used the measured performance data from the site to calculate the actual thermal performance of the GSHP system during one of its early years of operation. They showed additionally how the various system components affect the performance, presented an uncertainty analysis, and described how some unanticipated consequences of the design may be improved. Naicker and Rees (2020) collected a large ground heat exchanger array consisting of 56 boreholes during a period of 38 months since its start service time, which is associated with a mixed-use university building

that has both heating and cooling loads. They find that the ground heat exchange was found to be dominated by rejection of heat over the monitoring period.

There are also small-scale laboratory type facilities to investigate the performance of BHEs. Compared with full-scale measurements, small-scale tests are usually with shorter test time, while easier to control. In addition, it is more feasible to conduct a small-scale test than a full-scale in-situ test considering the time and financial investment. Gu (1995) provides a sandbox model with metal tank insulated on top, which is filled with local silty loam. The borehole has been molded at the center of the tank by pouring backfill soil. Thermocouples have been inserted in the tank to measure the inlet and outlet fluid temperature of the U-pipe. Two groups of five thermocouples have been additionally installed in the soil on each side of the borehole and evenly distributed radially at two vertical levels to examine the uniformity of the initial soil temperature. The duration for this test is up to 7 hours due to the restriction of the backfill soil. Beier et al. (2011) have constructed a large-scale laboratory sandbox with 18-m of length, which is positioned horizontally and filled with saturated sand for a single U-pipe BHE. The sandbox has been placed in a room with a controlled temperature. An aluminum tube has been used to represent the borehole wall, which has been centered horizontally along the length of the sandbox. A HDPE U-pipe is then inserted into the aluminum tube and grout is filled in. Sand temperatures were measured at several locations including at the borehole wall. Thermistors were installed in the sand on the horizontal plane that ran through the centerline of the U-pipe, all on the inlet side. A 52-hour TRT has been carried out with a steady heat input followed by an intentionally interrupted test to determine ground thermal conductivity as well as the borehole thermal resistance. The generated dataset can be useful to test borehole models and thermal response test analysis procedure. Erol and Francois (2014) have built a $1\times1\times1$ m^3 sand box to study the heat exchange rate and the borehole thermal resistance of a BHE made of various grouting material installed in dry and saturated soils. Fifty-hour TRTs have been conducted in their work. Further, they have compared the temperature distribution in the sand box over distance and over time with a prediction given by a line source solution. The authors have noticed discrepancies between the analytical solution and the experiments. They attribute these differences to the influence of the room temperature boundary condition that was not considered by the analytical solution. Salimshirazi (2012) has constructed a cylindrical tank with 1.35 of height and 1.40 m of diameter to study the transient heat transfer in the vicinity of boreholes. A 1.23 m long

borehole with a carefully positioned U-pipe and filled with well-characterized small glass beads which act as the grout has been installed in the tank. The borehole has been surrounded by the sand with known thermal properties. Sixty calibrated thermocouples have been installed for temperature measurement.

I.4.3. Some investigations on shallow BHEs

Till now, many investigations have been conducted on the shallow BHE. To ensure a stable operation of BHE, factors influencing its performance must be identified during the design stage. The factors influencing the BHE performance are categorized by 5 aspects in this investigation, indicating the environmental and geotechnical condition, grout thermal properties, U-pipe properties, carrying fluid properties and heat load conditions. The corresponding conducted investigations in literature are introduced in the following:

a) Environmental and geotechnical condition

The environmental and geotechnical conditions are generally the conditions that cannot be modified. For example, the initial surrounding temperature, the ground water flow, the geotechnical condition and the initial ground heat flux.

Liu et al. (2015) find that the meteorological parameters greatly impact the BHE performance and its feasibility in their energy simulations of a BHE installed in Qiqihaer, Shenyang and Beijing (China). By using analytical models, Samson et al. (2018) conclude that only groundwater flow with high velocities can apparently save the total cost of BHE, while groundwater flow angle is less significant. Raymond et al. (2011a) conclude that the existence of aquifer can improve the BHE performance, and thus a shorter borehole is needed to achieve the same performance compared to the case without groundwater. By using a Moving Finite Line Source (MFLS) model, Molina-Giraldo et al. (2011) declare that the influence of groundwater flow is negligible for Péclet numbers lower than 1.2. Choi et al. (2013) have studied how the magnitude and direction of groundwater flow affects borehole fields by using two-dimensional finite element method and find that it should be taken into account. By applying finite element model, Shrestha et al. (2015) assess the application of a GCHP in Tsugaru by considering the effective thermal conductivity of the ground and the subsurface temperature down to a 50 m depth. The results show that a higher effective thermal conductivity and subsurface temperatures increased the suitability of a GSHP. By conducting TRT, Luo et al. investigated surface water, groundwater and BHE systems in the city of

Wuhan (2018a). The results show that the site conditions are crucial to evaluate the installation feasibility of different types of GSHP systems. By using finite element code OpenGeoSys (OGS), Hein et al. (2016) build a model considering subsurface volumetric heat capacity varies from 1.6MJ.m^{-3}.K$_{-1}$ to 2.4MJ.m^{-3}.K^{-1}. Their result shows that the effect of volumetric heat capacity is insignificant on the recovery of the ground media, as well the heat pump performance. More specifically, the difference of the temperature with maximum and minimum thermal capacity is less than 0.4 °C in both cases.

b) Grout thermal properties

In general, the grout thermal properties include the grout thermal conductivity and grout volumetric heat capacity. Sand, soil from local site, concrete, etc. can be used as the grout material surrounding the U-pipe. Conventionally, grout is positive to the performance of a BHE, since it is with better thermal properties compared with the surrounding porous media. The influence of grout to the BHE performance includes mainly its material and diameter.

Luo et al. (2013) observe that the borehole diameters (0.121, 0.165 and 0.180 m) influences the BHE performance negligibly by conducting several in-situ investigations. By performing the TRT, Lee et al. (2011) find that cement provides a higher borehole thermal conductivity than bentonite grout. Kurevija et al. (2017) conclude that there is no real benefit of implementing thermal enhanced grout in an environment such as marly-clays with a mediocre thermal conductivity by performing a steady-state Thermal Response Step Tests (TRST) in a retrofit project containing 16 BHEs. By using finite difference method, Alberti et al. (2017) conclude that the effects of a significant groundwater flow can be enhanced by a high thermal conductivity grout. Lee et al. (2010) indicate that the thermal conductivity is improved with increasing content of silica-sand and graphite in an admixture, but the viscosity of the admixture also increases by conducting indoor experiments. They find that the thermal conductivity of bentonite-based admixture can reach 3.5 W.m^{-1}.K^{-1} by adding 30% graphite.

c) U-pipe properties

U-pipe is used for the carrying fluid circulating through the ground. The main properties influencing the BHE performance include its diameter, thickness, material (thermal conductivity), shank, spacing and configurations (double/triple parallel/cross U-pipe).

Cui et al. (2017) demonstrate that the heat transfer rate gradually increases with the shank spacing, and the influence of shank spacing becomes insignificant when it is greater than 0.06 m by using the Finite Volume Method (FVM). Cao et al. (2017) observe that the steel pipe with a thermal conductivity of 16.27 $W.m^{-1}.K^{-1}$ enhances 7% the BHE performance compared to the High-Density Polyethylene (HDPE) pipes with the thermal conductivity of 0.44 $W.m^{-1}.K^{-1}$ by numerical and experimental methods. By performing in-situ tests in Belgium, Desmedt et al. (2012) use the FLS model to analyze the thermal resistance of a BHE and conclude that 52% of thermal resistance can be reduced by adding additional U-pipe. Based on the numerical simulations, Bidarmaghz et al. (2012) report that the addition of a second U-pipe increases the thermal performance of a BHE between 5% and 37% when Reynolds number is higher than 2300. In the thermal resistance model, Bauer et al. (2011) demonstrate that the thermal resistance for double parallel U-pipe is smaller than the resistance of double cross U-pipe. Serageldin et al. (2018) find the oval shape pipe with space between the two legs decreases the borehole thermal resistance by 18.47% compared with the circular tube by using finite element code ANSYS FLUENT.

d) Carrying fluid properties

Carrying fluid is directly used for extracting/injecting heat from the ground, depending on the heating/cooling mode of a GSHP system. Anti-freezing solution is traditionally used as carrying fluid scenario if heating mode is necessary since the fluid temperature can be less than 0 °C. The main properties influencing the performance of a BHE for carrying fluid are its carrying fluid material and fluid velocity.

Casasso and Sethi (2014) conclude that calcium chloride (20%) solution performs better than other anti-freeze carrying fluids (propylene glycol at 25% and 33% volume concentration, ethanol at 24% volume concentration) by using FEFLOW 6.0 software. By conducting indoor experiments, Asadi (2018) finds that adding hybrid nanofluids within a microchannel can highly enhance the convective heat transfer coefficient.

e) Heat load

The heat load of a BHE is dependent on the building heat demand. One of the crucial elements for the BHE during the design stage is matching the heat load to the design factors, such as the length of a BHE. The main aspects of heat load influencing the performance of a BHE are the heat load level, heat load operation model (steady, intermittent, etc.).

Mensah et al. (2017) find through numerical and experimental investigations that a reduction of the peak load of building decreases the BHE length. Zhang et al. (2018) find through numerical simulations that the energy performance of a BHE highly depends on the building load. By conducting indoor experiment for ground heat exchanger installed in two different layers, Li et al. (2019) find the proportion of the temperature difference between sand and clay to the sand temperature increased from 12.9% to 32.7% by increasing four times the thermal load. By conducting a survey including 1105 installed GSHP in southwest Germany, Philipp Blum et al. (2010) find that the heating demand and the total length of BHE has an appropriate correlation. Hein et al. (2016) find that the soil can faster reach a quasi-steady-state and heat pump performs more efficiently with active cooling. Choi et al. (2011) find that the intermittent heat load operation of a shallow BHE performs better than a continuous heat load operation by using finite element code ABAQUS. They find that this effect is larger for shallow BHE installed in unsaturated soil. By combining the analytical solution and numerical solution, Cao et al. (2015) find that intermittence operation modes can improve the heat exchange performance of a BHE after inspecting 0.7, 1, 1.4, 2 and 3 of intermittent ratios.

I.4.4. TRTs for shallow BHEs

Shallow BHE is a traditional approach to exploiting geothermal energy, and TRT is popularly conducted during the design stage of a shallow BHE to mainly decide the effective ground thermal conductivity and the borehole thermal resistance, which are necessary to design a GCHP system. TRT can be also used to roughly estimate the heat extraction/injection capacity of a BHE. The TRT is however a main cost of a heat pump system (Marcotte and Pasquier, 2008).

A TRT unit typically consists of a pump, purge valves, an electric heating element, temperature sensors, a flow meter, and a data logger. TRT has firstly been proposed by Mogensen (1983). The first mobile measurement devices are introduced in Sweden (Eklöf and Gehlin, 1996) and then in the USA (Austin, 1998). Since then, the test approach has spread rapidly and is available in about 40 countries worldwide (Nordell, 2011; Spitler and Gehlin, 2015). The general procedure for assembling and conducting an in-situ TRT is shown in Figure I.10.

Figure I.10. General procedures to assemble and conduct in-situ TRT (Bae et al., 2019)

In a conventional TRT, a constant power input is applied to soil with a continuous water flow during 2 or 3 days (Bujok et al., 2014; Raymond et al., 2016), and the inlet/outlet fluid temperatures are continuously measured to determine bulk thermal properties over the borehole length (Angelotti et al., 2018; Raymond et al., 2011b). Longer TRTs are more expensive than shorter ones and practitioners are therefore tended to conduct shorter TRTs. However, the shorter test time can lead to the inaccuracy of the analytical results, for example, it can overestimate the effective ground thermal conductivity, therefore lead to a conservative design and increase the length of the BHE, thus increasing the final investment.

Generally, two methods are used to measure the undisturbed subsurface temperature. The first method consists in recording the vertical temperature profile in the ground heat exchanger. For the second method, water is circulated in the ground heat exchanger for 10 to 20 min without injecting heat and water temperatures are measured with the TRT unit, to allow the measured temperature to reach a constant value assumed representative of the average subsurface temperature (Raymond et al., 2011b). The first method appears more reliable than

the second method because, for the latter, heat produced by mechanical work of the pump while operating the TRT unit can be transferred to the water in the pipes and thus introduce a bias in the measured temperature (Gehlin and Nordell, 2003).

Before starting the test, air bubbles in the ground heat exchanger must be purged to ensure that air is not trapped in the system. The volumetric flow rate of water circulating in the pipe must be large enough for flow to remain transitional to turbulent to minimize thermal resistance due to fluid advection and to be representative of flow conditions prevailing when the heat pump system is in operation (Raymond et al., 2011b).

After measuring the background temperature purging the air trapped in the pipes, the test starts by injecting heat in the ground heat exchanger to disturb subsurface temperatures. It is a common practice to prevent external heat transfer by isolating any pipe lying at ground surface between the heat exchanger and the pump motor or the atmospheric air. However, the external heat transfer cannot be eliminated even with insulation, and it is therefore preferable to measure air temperature outside and inside the unit to quantify air temperature changes. During the test, a steady-power supply can help minimize fluctuations in heat injection, although these fluctuations are rarely eliminated.

Although the fiber-optic Distributed Temperature Sensing (DTS) (Beier et al., 2012; Fujii et al., 2009) is available now to characterize the vertical thermophysical properties, the traditional TRT has not lost its popularity and is often used in practice. The TRT provides an average depth of the ground, indicating that the ground heterogeneity and anisotropy can be ignored (Radioti et al., 2018). Figure I.11 shows a TRT performed in a multi-layered field and its corresponding effective thermal conductivity. By comparing two models with homogeneous and stratified subsurface layers, Luo et al. (2014) found that there was no significant difference between the fluid outlet temperatures in both models. After conducting the in-situ experiments for a heterogeneous rock, Radioti et al. (2018) employed the measured effective ground thermal conductivity in their numerical framework and concluded that the bedrock heterogeneity was not critical in the BHE simulations. Claesson and Eskilson (1988) found also that the temperatures in the heat extraction mode were not different in homogeneous and stratified grounds.

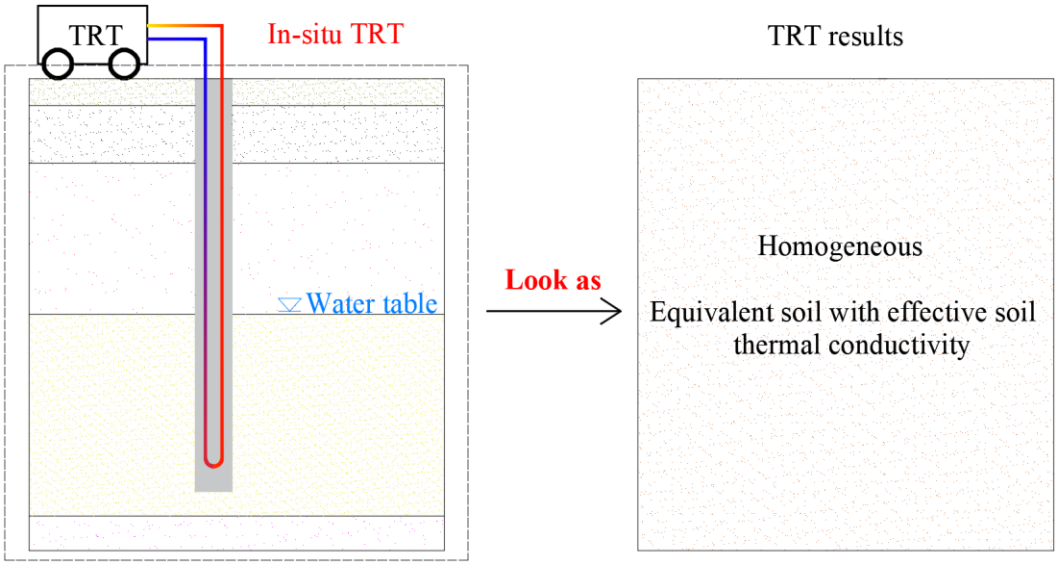

Figure I.11. Schematic diagram for TRT and test results

The traditional method to analyze the TRT results is the ILS model (Carslaw and Jaeger, 1959), and the ground temperature variation (ΔT) at a given time (t) and distance (r_s) can be expressed as:

$$\begin{aligned}\Delta T &= T(r_s,t) - T_0 = -\frac{q}{4\pi k_s} Ei\left(-\frac{C_{v-s} r_s^{\,2}}{4k_s t}\right) \\ &= -\frac{q}{4\pi k_s}\left(0.5772 + \ln\frac{C_{v-s} r_s^{\,2}}{4k_s t} - \sum_{m=1}^{\infty}\frac{(-1)^{m-1}\cdot C_{v-s} r_s^{\,2}/(4k_s t)}{m\cdot m!}\right)\end{aligned} \tag{1.32}$$

where, T_0 is initial ground temperature (°C), Ei is the integral exponential function, q is the heat per unit length of the line heat source (W.m^{-1}), k_s is the soil thermal conductivity (W.m^{-1}.K^{-1}), $C_{v\text{-}s}$ is the soil volumetric heat capacity (J.m^{-3}.K^{-1}), m is the index number, and 0.5772 is the Euler constant. When t is sufficiently large and $C_{v\text{-}s}r_s^2/(4k_s t)$ is sufficiently small (less than 0.05) (Brunetti et al., 2017), the above equation can be approximated as:

$$\Delta T = T(r_s,t) - T_0 = \frac{q}{4\pi k_s}\ln(t) - \frac{q}{4\pi k_s}\left(\ln\frac{C_{v-s} r_s^{\,2}}{4k_s} + 0.5772\right) \tag{1.33}$$

The borehole thermal resistance can be defined as:

$$R_b = \frac{\overline{T}_f - T(r_b,t)}{q} \tag{1.34}$$

where, r_b is the borehole radius (m).

Therefore, the average fluid temperature can be obtained:

$$\bar{T}_f = T(r_b,t) + qR_b = \frac{q}{4\pi k_s}\ln(t) - \frac{q}{4\pi k_s}\left(\ln\frac{C_{v-s}r_b^2}{4k_s} + 0.5772\right) + qR_b + T_0 \quad (1.35)$$

where, the average fluid temperature is conventionally defined as the mean value of the carrying fluid inlet and outlet temperature ($(T_{inlet}+T_{outlet})/2$). In the right part of the above equation, only the first term is variable with time and the other terms remain constant. Therefore, the effective soil thermal conductivity can be estimated after the stabilization of the fluid temperature with the natural logarithm of time:

$$k_s = \frac{q}{4\pi}\cdot\frac{\Delta\ln(t)}{\Delta\bar{T}_f} \quad (1.36)$$

Due to the simplicity and reliability of ILSM, it has been adopted into many investigations. Lee et al. (2018) used the method to analyze the TRT results of an in-situ Standing Column Well (SCW) geothermal heat exchanger. Luo et al. (2018a) applied the method to 17 in-situ TRTs with specific configurations and ground conditions in Wuhan (China). Radioti et al. (2018) used ILSM to get the effective ground thermal conductivity of 4 sites on the campus of the University of Liege (Belgium). Zhou et al. (2017) used ILSM to analyze in-situ TRTs conducted in Donghua University (China). Spitler et al. (2016) conducted 5 TRTs on the campus of Chalmers University of Technology (Sweden) and ILSM was used to estimate the thermal resistance of groundwater-filled boreholes in both heat extraction and injection modes.

Groundwater level affects the effective soil thermal conductivity obtained from the TRTs. The groundwater level divides the soil into saturated and unsaturated zones. The saturated zone has normally a higher soil thermal conductivity. In the unsaturated zone, the soil thermal conductivity is largely dependent on field geology and suction/water content profiles (Nowamooz et al., 2015). Luo et al. (2018b) conducted six TRTs at two sites in a loess deposit with different groundwater levels and they found that the effective ground thermal conductivity increased remarkably with the increase of groundwater level, indicating that the effective thermal conductivity of the ground increased from 1.64 $W.m^{-1}.K^{-1}$ to 2.07 $W.m^{-1}.K^{-1}$ when the groundwater level changed from 35 m to 10 m. By conducting TRTs for a BHE in a karstic aquifer field, Smith et al. (2018) identified the significant influence of the water table on the effectiveness of the system. They suggested that TRTs should be conducted multiple times to better characterize the saturated zone.

I.4.5 Necessary research investigations on shallow BHEs

Despite a large number of investigations on the factors influencing the BHE performance, there is a lack of considering thoroughly the field conditions for BHEs installed in different soils. This is due to the complex hydrothermal transfer in porous media and its fluctuation with time and space especially at shallow depths. Due to the computational costs and numerical convergence problems, few studies have considered the underground hydrothermal variation induced by the seasonal hydrothermal variations on the ground surface to investigate the performance of shallow BHEs. Rivera et al. (2015) report that the ground surface supplies up to 35% of the energy for a 100 m depth shallow BHE. Bidarmaghz et al. (2016) conclude that a depth reduction of 11% can be saved for a 30 m shallow BHE considering surface thermal recharge. Therefore, energy absorbed from ground surface plays a substantial role in the performance of shallow BHE.

Further, few studies have reported on the hydrothermal heat transfer between different soil layers in shallow BHE applications. Instead, underground domain was conventionally treated as a homogeneous medium. Choi et al. (2011) have implemented hydrothermal equations in finite element code ABAQUS to study the performance of a BHE, however, they assume that the initial temperature and the ground surface temperature to be constant, which is not the case in practice. Moreover, no hydraulic boundary condition was imposed on the ground surface, indicating the hydraulic profile was kept constant in their numerical simulation. In in-situ condition, water content and therefore the negative water pressure (suction) vary with time and space beneath the ground surface under seasonal fluctuations on the ground surface. Australian Standard on residential slabs and footing design (Standards Australia, 1996) reports that the depth of suction change around Victoria region is within the range of 1.5 - 2 m below surface. Rajeev et al. (2012) conduct an experiment at Altona North and Fawkner region in Australia to observe the variation of water content fluctuation with time and space. After a year, they find that the volumetric water content stays almost the same for Altona North at 1.0 m in depth and for Fawkner at 0.9 m in depth.

Since BHEs are conventionally installed beneath water level, the soil profile is separated into saturated and unsaturated zones. The existence of these saturated and unsaturated zones is another aspect of the problem, often neglected in numerical simulations. Therefore, a robust

model concerning a shallow BHE installed in different field conditions with the separation of the soil profile into saturated and unsaturated zones is still necessary.

In practice, the annual temperature fluctuation on the ground surface influences the ground temperature up to 10 m below ground surface. Thus, seasonal ground surface hydrothermal fluctuation also influences the TRT results (Choi and Ooka, 2016a). Few studies have considered the variations of water level and seasonal temperature on the TRT (Jensen-Page et al., 2018) and further studies are still necessary for the seasonal climate changes in shallow depths.

Further, it is necessary to find an alternative approach to estimating the local effective soil thermal conductivity since TRT is not conducted in some small or medium projects due to its considerable financial investment. For example, a TRT for a borehole with a depth between 100 and 120 m can cost between 3000 and 5000 £ in England (Synergy, 2018). In these cases, the ground thermal conductivity normally relies on the known results of TRTs conducted in nearby locations (Mikhaylova et al., 2016) or by empirical estimations.

I.5. HGHEs

Compared to BHE, HGHE is more cost effective although it requires more installation space (Self et al., 2013). The costs can be further reduced by using a slinky-type HGHE (Xiong et al., 2015), which enables it to be an appealing technology for residential and small non-residential applications (Al-Ameen et al., 2018). However, due to the shallow installation depth (conventionally between 1.0 and 2.0 m) (Garcia Gonzalez et al., 2012; Habibi and Hakkaki-Fard, 2018), it is more sensitive to the meteorological condition than VGHE. The investigation on HGHE is also more sparse compared with VGHE due to the smaller installation amount in Europe (Lund and Boyd, 2016), however, the HGHE continues to be largely used in North America (Raymond et al., 2015). The installation of a slinky-type HGHE has been shown in Figure I.12.

Figure I.12. The installation of a slinky-type HGHE (Pullen, 2019)

I.5.1. Computational models for HGHEs

Generally, analytical and numerical simulation models are often used in HGHE applications. Compared to BHEs, HGHEs are more complicated to be analyzed, even though they may be easier to install (Lamarche, 2019).

The analytic solutions to the HGHE are limited due to fewer applications and more complicated influencing factors on its performance. Li et al. (2012) have established a moving ring source model and solved it analytically to describe the temperature response of a spiral heat exchanger with the groundwater flow. Their model has further been validated by some experimental and simulation results. Kupiec et al. (2015) present a mathematical model of HGHE based on a one-dimensional equation of the transient heat conduction with an internal source of heat. They have validated the model capacity by experimental results. Xiong et al. (2015) have presented an analytical model relying on analytical ring source solutions to compute temperature response functions for slinky-type HGHEs. The model is based on thermal response function method of BHE, while there are some distinction differences. Their model has been validated by field test data. Wang et al. (2016a) propose an analytical solution for spiral-type HGHE based on Green's function. Their model has been validated by a field test and a 3D simulation model. Due to the shallow installation depth of HGHE, ground surface temperature fluctuation is considered in their model to increase accuracy. Jeon et al. (2018b) have also proposed a mathematical solution for spiral-type HGHE based on the mathematical model developed by Park et al. (2013). Green's equation has also been used in their model, compared to the model proposed by Wang et al. (2016a), it considers the real

geometry of spiral pipe instead of a series of rings. Based on thermal response factor models, Lamarche (2019) proposes a mathematical solution for a linear-type HGHE, which takes into account the effect of the air-soil boundary condition and the thermal interference between the different portions of pipes in the buried field.

Like numerical simulation models for BHEs, simulation models for HGHEs are with better accuracy since they can study more aspects related to the real in-situ situation. Despite using commercial software (FEFLOW, ANASYS, COMSOL Multiphysics, etc.), some in-house numerical simulation models were developed. For example, Mei (1986) develops a finite difference model for HGHE installed with the coil configuration. Gan (2018) proposes an in-house program to predict the performance of a HGHE by considering moisture transfer in soil.

I.5.2. Experimental methods on HGHEs

Similar to BHEs, experimental approaches for HGHEs can be also categorized to full-scale experiment and small-scale experiment. Due to the relatively cheaper cost of excavating HGHE ditches than digging deep boreholes, in-situ experiment for HGHE seems more feasible than that of shallow BHE.

Wu et al. (2010) have investigated the performance of a slinky-type HGHE installed at Talbot Cottage, Drayton St Leonard site, Oxfordshire, UK. Four parallel slinky-type HGHE loops have been installed in an 80 m long by 20 m wide paddock area at a depth of around 1.2 m beneath the ground surface. Water-ethylene glycol (30% by weight) mixture has been adopted for carrying fluid. The ground surface is overgrown with wildflowers. Soft sand was additionally used below and on top of the slinky heat exchanger in their experiment. Fujii et al. (2012) have conducted a series of tests for slinky-type HGHE located in a field with 18 m of groundwater level in the Kyushu University in 2008 and 2009. The diameter of the loop and the inner and outer diameters of the polyethylene pipe are 0.8 m, 0.034 m, and 0.024 m, respectively. In their investigation, the trench length and the depth are 72.0 and 1.5 m, respectively. Adamovsky et al. (2015b) have compared the thermal performance of a linear and slinky-type HGHEs used for heating the administration building and manufacturing halls of a company based in Prague. The linear HGHE has a total length of 330 m (41.473 m^2), and it is installed 1.8 m beneath ground surface with three loops with a 1 m span. The slinky-type HGHE has the total length of 200 m (20.107 m^2), which has been installed at a depth of 1.5 m in 53 circular loops with a span of 0.38 m. Anti-freeze solution with a mixture of 33% ethanol

and 67% water has been adopted in their experiment for both HGHEs. Thermal probes have also been installed underground to measure the temperature variation in their experiment. Ali et al. (2017) have conducted in-situ experiment in Saga University for slinky HGHEs with two orientations: reclined (parallel to ground surface) and standing (perpendicular to ground surface). The two type HGHE are installed 2.0 m apart from each other. For heat exchanger, they have chosen copper pipe with outer surface coated with Low Density Polyethylene (LDPE) to enhance the performance of the HGHE. The loop diameter, trench length and loop number for both HGHEs are 1.0 m, 7.0 m and 7, respectively. The pipe has a length of 39.5 m. The reclined GHE has been installed at 1.5 m beneath ground surface with 1.0 m of trench width, while the centers of standing GHE loops are installed at the depth of 1.5 m in a 0.5 m wide trench.

There are also some small-scale tests about HGHEs. Yoon et al. (2015a) have conducted two experiments in a sandy box for slinky-type HGHEs with pipe lengths of 24 and 66 m. A far-infrared radiation heater has been used to maintain constant the indoor temperature. In their experiment, a polybutylene pipe with inner and outer diameters of 16 and 20 mm has been installed at the depth of 0.5 m in a sand (dry sand) box, which has a length of 5 m, a width of 1 m and a depth of 1 m. Water has been used as carrying fluid and the test time is 30 hours. Al-Ameen et al. (2018) have designed and built at a small-scale test model in Nottingham Trent University to investigate and evaluate the thermal performance of a HGHE system in charging and discharging modes under different backfill soil and carrying fluid flow rate. The internal dimensions of the sank tank model are $1\times0.5\times0.125$ m^3. Copper has been adopted as the pipe, which has a total length of 5 m and water has been used as the carrying fluid.

I.5.3. Some investigations on HGHEs

In HGHE engineering, it is necessary to estimate accurately the performance of a given HGHE in the design stage (Kim et al., 2016). Numerical modeling is the most popular method since it is comprehensive and can reduce the initial capital investment. Till now, many investigations have been conducted to investigate the performance of a HGHE at different conditions.

By using an analytical solution (ring source model) for slinky-type HGHE, Larwa et al. (2019) have estimated the ground thermal properties by adjusting the model parameters to the measurement results. By using CFD code Fluent, Congedo et al. (2012) find that increasing

the installation depth of a HGHE from 1.5 to 2.5 m does not play an important role on the system performance. However, they conclude that the ground thermal conductivity is the most important parameter for the heat transfer performance of their system. By developing an in-house numerical simulation program, Gan (2013) finds that the soil freezing can generally increase the heat extraction rate of a HGHE. He observes especially that when the soil freezing happens in the vicinity of the pipe, the heat extraction rate increases 1.7% for the carrying fluid temperature of -1 °C. By using CFD model, Selemat et al. (2015, 2016) find out that the use of pipes made of materials that conduct heat well only slightly improves the heat transfer intensity. By using numerical simulator FEFLOW, Fujii et al. (2012) conducted a simulation of slinky-type HGHE by simplifying the spiral-type as plate-type. Thermal balance is considered in their numerical simulation and they find that the numerical simulation results match well the in-situ measurements. By using a transient three-dimensional finite volume model in ANSYS Fluent, Al-Ameen et al. (2018) find that adopting mill-scale copper slag instead of Leighton buzzard sand as a backfill material increases the HGHE performance. By using the finite volume method, Habibi and Hakkaki-Fard (2018) conclude that the slinky-type HGHE performs 75% and 9% better than the linear and spiral HGHEs, respectively. By using Midas NFX numerical program, Kim et al. (2016) find that the pipe diameter influences negligibly the heat exchange rate of the HGHE. By using COMSOL Multiphysics simulations for a spiral HGHE, Go et al. (2016) conclude that the increase of the flow rate generally has a positive influence on the HGHE performance. However, the total efficiency will decrease in inverse proportion to the flow rate if the coil pitch becomes too narrow. By conducting field test in Fukuoka City, Fujii et al. (2010) find that due to the less influence of atmospheric temperature changes, the horizontal installation of slinky coils (slinky-type HGHE) show better performance than vertical installation in terms of energy efficiency. They have further noticed that the horizontally installed slinky coils have comparable heat exchange capacity with vertical U-pipe GHEs drilled in a formation with favorable thermal conductivity.

Despite the popularity of the numerical simulations in HGHE engineering, there are some points often neglected or simplified in numerical investigations.

Due to the complex atmosphere-soil interaction, time-varying ground surface temperatures are often neglected in the numerical simulations. For example, the atmosphere temperature is conventionally applied as a surface boundary (Al-Ameen et al., 2018; Gao et al., 2016; Go et al., 2016; Habibi and Hakkaki-Fard, 2018; Han et al., 2017; Jeon et al., 2018a; Kim et al.,

2018; Li et al., 2017a; Pu et al., 2018; Selamat et al., 2016). Wu et al. (2010) have experimentally investigated a slinky-type HGHE in an 80 m long by 20 m wide paddock area at a depth of around 1.2 m below the ground surface at Talbot Cottage, Drayton St Leonard site, Oxfordshire, UK. They discover that the ground surface temperature is higher when no heat exchanger is installed, proving that the operation of the HGHE has influenced the ground surface temperature. This means that time-varying ground surface temperatures (such as atmosphere temperatures) might not be sufficient to estimate the HGHE performance. This point is often absent in the numerical simulations.

By measuring the soil thermal conductivity at five sites in Midwestern USA at the depth of 1.2 m, Naylor et al. (2015) find that the soil moisture fluctuations result in a very significant variation of the soil thermal conductivity. Gan (2018) concludes in his numerical simulations that the maximum differences of heat transfer through a HGHE between the models with and without moisture transfer are 24%, 17% and 18% in clay sand, loamy sand and sandy soils, respectively. Therefore, the consideration of the hydrothermal transfer in shallow zones is necessary for the design of HGHE, often neglected in the numerical simulations.

The first information about slinky-coil ground heat exchangers was reported by Bose and Smith in 1992 (Larwa et al., 2019). A slinky-type HGHE has a good performance and it is popular in real practice as they are easy to be assembled (Habibi and Hakkaki-Fard, 2018; Larwa et al., 2019; Lee et al., 2018). Linear-type and spiral-type HGHEs are often studied in the numerical simulations as their geometries are easier to be constructed (Selamat et al., 2016). However, numerical studies on the slinky-type HGHE are limited due to its complex geometry.

I.6. Summary

This chapter at first gives an introduction about the development of the GSHP. The conventional applied ground heat exchangers categorized by open and closed ground heat exchangers are then introduced. The approaches estimating the performance of different ground heat exchangers have been illustrated. Generally, analytical and numerical models are the most popular approaches used to evaluate the performance of ground heat exchangers. Some factors influencing the performance of a shallow BHE are also concluded in this chapter. Subsequently, the mechanism of TRT for shallow BHEs and some investigations on

it have been detailed. Finally, the investigations on HGHEs have been presented. The following conclusions can be drawn after reviewing the literature:

1) The increasing energy demand and the greenhouse gas emission are two urgent issues need to be solved urgently for a sustainable development. It promotes the research on sustainable and environmentally friendly energies, such as geothermal energy.
2) Compared to analytical models, the numerical simulation models are more comprehensive, while the computation time is larger than analytical approaches.
3) The numerical and analytical models assume conventionally the homogeneous ground temperature and thermal properties. A model considering heterogeneous ground temperature and ground thermal properties is necessary to evaluate the BHE performance in the design stage.
4) TRT is an expensive test to identify the ground thermal conductivity for some small or medium projects. Therefore, it is necessary to provide a cost-effective approach for these small or medium projects to identify the effective ground thermal conductivity.
5) Three primary aspects are often neglected in the simulations for HGHEs. They are ground surface water/energy balance, hydrothermal transfer in the surrounding media and slinky-type configuration HGHE.

The mentioned research needs provided in this chapter about BHEs and HGHEs are closely related to the research objectives of this project, and they are going to be investigated in the next chapters.

II. PHYSICS IN THE INVESTIGATION OF GROUND HEAT EXCHANGERS

II.1. Introduction

Energy follows the conservation law and cannot be created or destroyed. It can be transferred by kinetic, potential, thermal, gravitational, sound, light, elastic, and electromagnetic energy. Thermal energy is transferred by the ground energy systems. An isolated system of different components at different temperatures will reach a thermal equilibrium stage through thermal transfer.

In this chapter, the physics related to the heat transfer process in and between different components of a ground heat exchanger is going to be introduced. These components (Figure II.1) are porous medium (soil), grout, U-pipe and carrying fluid.

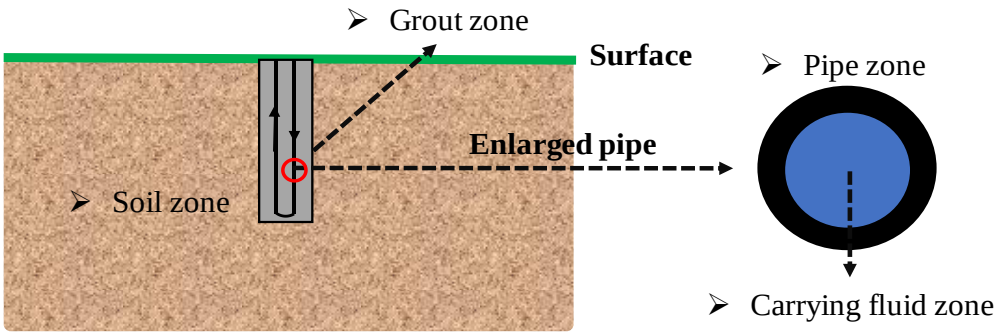

Figure II.1. Physics divided by component in this investigation

Heat transfer may occur via three principal mechanisms if phase change is not taken into account: conduction, convection, and radiation. This section introduces these three basic concepts included in ground heat exchanger designs.

II.1.1. Heat conduction

Heat conduction is the heat transfer by microscopic collisions of particles and movement of electrons, involving the transfer of kinetic energy at the molecular level. Conduction is the most significant ways of heat exchange within a solid or between solid objects in thermal contact. Fluids, especially gases, are less conductive. The heat conduction by Fourier's law is given by:

$$q_{flux} = k\nabla T \tag{2.1}$$

where k and T are thermal conductivity ($W.m^{-1}.K^{-1}$) and temperature (K), respectively.

II.1.2. Heat convection

Heat convection is an important form of heat transfer, basically associated with fluid flow, it refers to the heat transfer in heat-carrying mass like water or vapor. There are two types of convection: free and forced convection. Free convection is a mass transport caused in fluids by changes in density with temperature gradients. The density of the fluid is lower at higher temperature, giving rise to the upward displacement. On the other hand, the movement of liquids and gases forced to pass through the channel by pressure differences is defined as forced convection. Without considering diffusion, the heat flux by fluid advection in soil can be given as:

$$q_{flux} = \rho C_p u T \tag{2.2}$$

where ρ, C_p, u and T are fluid density ($Kg.m^{-3}$), specific heat capacity ($J.kg^{-1}.K^{-1}$), velocity and temperature (K), respectively.

Convection is sometimes identified by the heat transfer of a solid body in contact with a moving fluid. The energy in this scenario is transferred from or to the body by the fluid along its surface area. This kind of convection involves a wide class of heat transfer applications, particularly those dealing with heat exchangers including ground heat exchangers. Convective processes involving heat transfer from a boundary surface exposed to a relatively low velocity fluid of temperature is described by the Newton's law of cooling, as:

$$q_{flux} = h_{\text{int}}(T_{i-p} - T_f) \tag{2.3}$$

where h_{int} is the film heat transfer coefficient ($W.m^{-2}.K^{-1}$), $T_{i\text{-}p}$ is the inner pipe temperature (K), T_f is the outer pipe temperature (K).

II.1.3. Radiation

Radiation occurs through a vacuum or any transparent medium (solid or fluid or gas). All bodies with temperatures above absolute zero are capable to emit energy according to the Stefan-Boltzmann law. The temperature of the radiating body is the predominating factor in the estimation of heat radiation value. The Stefan-Boltzmann law relates the heat flux radiated from a "black body" (an ideal thermal radiator) to its absolute temperature:

$$q_{flux} = \sigma T^4 \tag{2.4}$$

where σ is the Stefan-Boltzmann constant ($W.m^{-2}.K^{-4}$), T is its absolute temperature in Kelvin. However, most bodies in reality are not purely black. Consequently, the rate of heat transfer is reduced compared to the idealized Stefan-Boltzmann law.

II.2. Moisture and heat transfers in soil

In soil, heat conduction occurs in all the constituents (particle, water liquid/vapor and pore air), which works as the predominating heat mechanism in ground heat transfer. For soils under natural condition, convection through air or water is usually negligible (Farouki, 1981). Soils can also provide radiation, emitting most of its radiation as long-wave radiation in a wavelength band between 0.5 and 30.0 μm at soil surface (An, 2017). Generally, it makes a negligible contribution to heat transfer in soil. For example, its effect in sand is less than 1% of the overall heat transfer at a normal unfrozen (i.e., within 0 - 40 °C) zone (Choi et al., 2011; Rees et al., 2000). Water and vapor in soil can vary with time and space, especially in different depths and seasons. Before bringing out the energy balance equation in soil, it is necessary to investigate the mass transfer in soil.

II.2.1. Moisture transfer in soil

The volumetric water content in soil can be measured by sensors installed at the targeted positions during the investigation period. However, this method is not able to measure the water content at other positions without installing the sensors, the approach is not feasible to measure long period of water content, either. Besides, unpredictable problems during the operation of the sensors in the long term period may happen, which might lead to uneconomic

expenses (An, 2017). Specifically, for the near soil surface region which is sensitive to atmosphere-soil interaction, direct monitoring of volumetric water content and especially suction meet some challenges (An, 2017; Cui and Zornberg, 2008). Compared with field measurements, numerical simualtion is less accurate, while it can be cost effective and feasible for long-term prediction of water content variation along the soil profile. The current investigation uses numerical simualtion methods to get the hydraulic variation in the soil profile.

Water in porous media is assumed to be incompressible and there is no mass transfer of soil particles. The hydraulic head (m) is used as a measure of water energy in soil, it can be expressed as:

$$h_{head} = D + \frac{P_w}{\rho_w g} \tag{2.5}$$

where D is the elevation (gravitational) head (m), P_w is the pore water pressure (Pa). The kinetic head (m) is negligible due to the low flow velocity of the groundwater. Therefore, pore water pressure can be deduced:

$$P_w = (h_{head} - D)\rho_w g \tag{2.6}$$

where ρ_w is the water density (kg.m^{-3}).

To describe water flow through unsaturated soil it is necessary to define the matric suction:

$$P_{suction} = P_a - P_w \tag{2.7}$$

where P_a is the pore air pressure (Pa) in the pores of the soil. The pore air pressure in the unsaturated zone will equal atmospheric pressure and it is positive (the value is conventionally referenced as zero (Tuller and Or, 2005)), while the pore water pressure remains negative. Suction is considered as a state variable which can describe the physical behavior of unsaturated soils (Chávez-Negrete et al., 2018; van Genuchten, 1980; Richards, 1931). There are also some soil properties based on the theory of suction, such as relative saturation (van Genuchten, 1980).

The classical description of flow rate for saturated soils is given by Darcy's law, which is valid for unsaturated soils (Chávez-Negrete et al., 2018). This law states that the water flow rate through a soil is directly proportional to the hydraulic head gradient, given as:

$$u_w = -K \cdot k_r(P_{suction}) \nabla h_{head} \quad (2.8)$$

where K is saturated hydraulic conductivity (m.s^{-1}), k_r is the relative hydraulic conductivity. If the soil volume change and chemical composition of the pore fluid are assumed to be insignificant, the hydraulic conductivity is almost constant for saturated soil; however, for unsaturated soil, the hydraulic conductivity is a function of the volumetric water content or the degree of saturation. Table II.1 shows the saturated hydraulic conductivity of difference soils according to Pachepsky and Park (2015), who divide the hydraulic conductivity of 1245 data sets into high and low bulk density groups using the splitting algorithm that create the most homogeneous groups.

Table II.1. Statistics of saturated hydraulic conductivity in low and high bulk density groups for each textural class (Pachepsky and Park, 2015)

Textural class	*Threshold bulk density*	*Low bulk density group*					*High bulk density group*				
		Data sets	*Quartiles*			*Geometric mean*	*Data sets*	*Quartiles*			*Geometric mean*
			25%	*50%*	*75%*			*25%*	*50%*	*75%*	
	g.m^{-3}	no.	cm h^{-1}				no.	cm h^{-1}			
Clay	1.26	14	0.98	4.19	197	4.26	101	0.26	1.17	7.48	0.52
Loam	1.36	24	1.15	6.28	12.8	4.29	57	0.26	0.67	2.52	0.79
Silt loam	1.35	58	1.31	3.37	10.0	3.68	157	0.34	1.12	5.09	0.88
Clay loam	1.35	17	1.5	2.86	5.8	2.69	92	0.1	0.72	5.71	0.77
Silty clay loam	1.30	18	0.44	3.35	5.7	2.42	65	0.23	0.53	1.79	0.51
Silty clay	1.33	-	-	-	-	-	22	0.5	1.11	3.92	0.19
Sandy clay	1.56	3	-	-	-	-	18	0.02	0.31	1.78	0.17
Sandy clay loam	1.62	124	0.25	1.71	5.5	1.98	015	0.13	0.42	0.5	0.52
Sandy loam	1.61	127	2.36	5.36	14.9	6.4	42	0.47	1.38	4.85	1.59
Loamy sand	1.66	62	8.46	13.9	90.2	14.79	14	1.59	4.04	6062	2.7
Sand	-	131	22.3	36.1	64.4	37.24	-	-	-	-	-

The volumetric water content or degree of saturation is a function of matric suction, as defined in the Soil-Water Characteristic Curve (SWCC), the unsaturated hydraulic

conductivity can also be considered a function of matric suction (Zhai and Rahardjo, 2015), which can be defined as hydraulic conductivity in the saturated soil multiplies a coefficient (relative hydraulic conductivity). According to Fredlund et al. (2012), four categories of models are used for estimating the relative hydraulic conductivity. They are empirical models, statistical models, correlation models, and regression models. Empirical models and statistical models appear to be most extensively used in geotechnical engineering (Zhang and Fredlund, 2015). Brooks and Corey (1964) equation is one example of an empirical model. Childs and Collis-George (1950), Burdine (1953), and Mualem (1976) are three commonly used integral formulas of relative hydraulic conductivity based on different physical models (Zhang and Fredlund, 2015), they differ in the manner the effective radius is estimated (Vereecken, 1995). Several models in estimating relative hydraulic conductivity are listed in Table II.2.

Table II.2. Different models in estimating relative hydraulic conductivity

Approach	*Function*		*Remark*
Gardner (1958a)	$k_r(h_p) = [(h_p)^c / a + 1]^{-1}$	(2.9)	Empirical approach, where h_p is the pressure head (m), a and c are the fitting parameters.
Averjanov (1950)	$k_r(S_e) = S_e^{3.5}$	(2.10)	Macroscopic approach, where S_e is the relative saturation.
Childs and Collis-George (1950)	$k_r(\theta) = S_e^x \dfrac{\int_0^{\theta} (\theta - \varepsilon) / {h_p}^{2+b} d\varepsilon}{\int_0^{\theta_{sat}} (\theta - \varepsilon) / {h_p}^{2+b} d\varepsilon}$	(2.11)	Statistical model, where θ is the volumetric water content, θ_{sat} is the saturated volumetric water content, b is the tortuosity, x is the pore interaction term.
Burdine (1953)	$k_r(\theta) = S_e^x \dfrac{\int_0^{\theta} 1 / h_p^{2+b} \, \mathrm{d}\theta}{\int_0^{\theta_{sat}} 1 / h_p^{2+b} \, \mathrm{d}\theta}$	(2.12)	Statistical model.
Mualem (1976)	$k_r(\theta) = S_e^x \left(\dfrac{\int_0^{\theta} 1 / h_p^{1+b} \, \mathrm{d}\theta}{\int_0^{\theta_{sat}} 1 / h_p^{1+b} \, \mathrm{d}\theta} \right)^2$	(2.13)	Statistical model.

Statistical models connect hydraulic conductivity function and the SWCC by the pore-size distribution of the soil. Consequently, the hydraulic conductivity function is developed based on the interpretation and application of the SWCC. To date, there have been many models proposed for SWCC (Brooks and Corey, 1964; Fredlund and Xing, 1994; Gardner, 1958b;

van Genuchten, 1980; McKee and Bumb, 1987). Among all the equations, those proposed by van Genuchten (1980) and Fredlund and Xing (1994) give more flexibility to the equation to best-fit the measured data (Leong and Rahardjo, 1997; Rahimi et al., 2015). These two models have been listed in Table II.3.

Table II.3. Two often used SWCC models

Approach	*Function*		*Remark*
Fredlund Xing (1994)	$\theta = C(P_{suction}) \frac{\theta_{sat}}{[\ln(e + (\frac{P_{suction}}{\alpha})^n)]^m}$	(2.14)	where α is a suction related the air-entry value of the soil (Pa), n is the fitting parameter related to the slope of the SWCC, m is the fitting parameter related to the residual water content of the soil, e is the natural number (2.71828), $P_{suction\_r}$ is the suction value corresponding to residual water content (Pa).
	where $C(P_{suction}) = 1 - \frac{\ln(1 + \frac{P_{suction}}{P_{suction\_r}})}{\ln(1 + (\frac{10^6}{P_{suction\_r}}))}$	(2.15)	
van Genuchten (1980)	$S_e = \frac{1}{\left[1 + \lvert \alpha H_p \rvert^n\right]^{1-1/n}}$	(2.16)	S_e equals to 1 in saturated zone, H_p is the suction head (m).

The fitted parameter α and n of 75 unsaturated soil samples for van Genuchten model (1980) are shown in Table II.4 (Ghanbarian-Alavijeh et al., 2010; Leij et al., 1996).

Table II.4. Soil properties of the 75 samples from the unsaturated soil hydraulic database (Leij et al., 1996) for the fitted van Genuchten model (1980) parameters n & α

Texture	*Number of samples*	*n*		*α (kPa^{-1})*	
		Min	*Max*	*Min*	*Max*
Sand	6	1.89	6.67	0.20	1.28
Loamy sand	8	1.19	3.13	0.30	1.30
Sandy loam	6	1.12	3.70	0.09	5.61
Sandy clay	5	1.08	1.64	0.20	1.60
Sandy clay	3	1.24	1.35	0.01	0.24
Loam	8	1.09	1.52	0.09	1.97
Silt loam	7	1.10	1.41	0.13	1.47
Silty clay	10	1.10	1.92	0.01	1.51
Clay loam	5	1.05	1.35	0.21	2.46
Silt	1	-	1.33	-	0.10
Silty clay	8	1.05	2.00	0.04	16.30
Clay	8	1.02	1.15	0.01	50.30

Water flow in unsaturated soils consists of liquid flow and vapor flow, it is driven by temperature and moisture gradient, the volumetric vapor flux coupled with temperature can be given as:

$$Q_v = -D_{Tv}\nabla T - D_{\theta v}\nabla\theta \tag{2.17}$$

where Q_v is the volumetric vapor flux ($m^3.m^{-2}.s^{-1}$), D_{Tv} is the thermal vapor moisture diffusivity ($m^2.s^{-1}.K^{-1}$), $D_{\theta v}$ is the isothermal vapor moisture diffusivity ($m^2.s^{-1}$).

The volumetric liquid flux ($m^3.m^{-2}.s^{-1}$) can be obtained if the temperature influence on the liquid transfer is considered:

$$Q_l = -D_{Tl}\nabla T - D_{\theta l}\nabla\theta - Kk_r\vec{i} \tag{2.18}$$

where D_{Tl} is the thermal liquid moisture diffusivity ($m^2.s^{-1}.K^{-1}$), $D_{\theta l}$ is the isothermal liquid moisture diffusivity ($m^2.s^{-1}$), i is the unit vector in the vertical direction.

The total moisture transfer flux can then be obtained:

$$Q_{total} = Q_v + Q_l \tag{2.19}$$

According to the mass balance theory, the moisture change rate in a control volume is equal to the sum of the net moisture rate flow into the volume and the rate of moisture injection into or extraction from the volume. Thus:

$$\frac{\partial\rho_w\theta}{\partial t} = -\nabla\cdot(\rho_w Q_{total}) + \rho_w\theta_{source} \tag{2.20}$$

where θ_{source} is the water source ($m^3.m^{-3}.s^{-1}$).

According to the above equations, the following mass balance equation can be obtained for liquid and vapor transfer in soil:

$$\frac{\partial\rho_w\theta}{\partial t} = \nabla\cdot(\rho_w(D_{Tl}+D_{Tv})\nabla T) + \nabla\cdot(\rho_w(D_{\theta l}+D_{\theta v})\nabla\theta) + \frac{\partial\rho_w Kk_r}{\partial z} + \rho_w\theta_{source} \tag{2.21}$$

II.2.2. Heat Transfer in soil

Heat transfer of the soil in a controlled volume results from sensible heat transfer by conduction due to the temperature gradient, latent heat transfer by vapor movement due to the

moisture gradient, convection by water transfer, therefore, the total heat flux in soil can be given as:

$$q_{flux\_total} = -(k + L\rho_w D_{Tv})\nabla T - L\rho_w D_{\theta v}\nabla\theta - \rho_w C_{p-w} u_w T_s \quad (2.22)$$

Energy balance requires that the heat exchange rate in a controlled volume should be equal to the sum of the net heat flow rate into the volume and the rate of heat generation/dissipation in the volume, therefore:

$$\frac{\partial(\rho_s C_{P-s} T_s)}{\partial t} = \nabla q_{flux\_total} + Q_s \quad (2.23)$$

where ρ_s, $C_{P\text{-}s}$, T_s and Q_s are the soil density (kg.m^{-3}), specific heat capacity (J.kg^{-1}.m^{-3}), temperature (°C) and heat source (W.m^{-3}).

The energy conservation equation in porous media containing heat conduction in soil, latent heat transfer by vapor movement and advection by water transfer is given as:

$$\frac{\partial(\rho_s C_{p-s} T_s)}{\partial t} = \nabla\cdot((k_s + \rho_w L D_{Tv})\nabla T_s) + \nabla\cdot(\rho_w L D_{\theta v}\nabla\theta) + \nabla\cdot\left(\rho_w C_{p-w} u_w T_s\right) + Q_s \quad (2.24)$$

Hartley and Black (1981) show that the latent heat has insignificant effect on the soil temperature response in the domain, although it may depend on many parameters including permeability of the soil (Olivella and Gens, 2000). And latent heat due to water evaporation and condensation is sometimes not considered (Cherati and Ghasemi-Fare, 2019). The magnitudes of the heat and mass change from some other field experiments caused by vapor flow are presented in Table II.5.

Table II.5. Heat and mass variation magnitudes due to vapor flux and the corresponding observed zones (Cahill and Parlange, 1998)

Author	*Maximum magnitude of heat flux caused by vapor flow (W.m^{-2})*	*Maximum magnitude of moisture flux caused by vapor flow (cm.s^{-1})*	*Depth of observation (cm)*
Cary (1965)	-	2×10^{-6}	Column
Rose (1968)	-	$(2\sim6)\times10^{-6}$	1~3
		$(2\sim4)\times10^{-6}$	3~12
Jackson et al. (1974)	-	$(2\sim7)\times10^{-6}$	0.5,1
Westcot and Wierenga (1974)	80	-	0.95
	70	-	1.5
	20	-	5

	10	-	11
Cahill and Parlange (1998)	40~60	7×10^{-6}	7~10

Moreover, due to the low hydraulic conductivity of water in soil, heat transfer by convection is often not taken into account. Therefore, the heat transfer in soil can be simplified as:

$$\frac{\partial(\rho_s C_{p-s} T_s)}{\partial t} = \nabla \cdot (k_s \nabla T_s) + Q_s \tag{2.25}$$

To solve heat transfer in soil, it is important to use a propriate model to obtain soil thermal properties. The influence of temperature on the soil thermal properties is not taken into account in this work since there is little influence of temperature on soil thermal properties when it is below 40 °C (Wang et al., 2016b).

Ten conventional approaches to obtaining the soil thermal conductivity are summarized in Table II.6.

Table II.6. Approaches to obtaining the thermal conductivity

Approach		*Equation*	*Parameter**
Kersten (1949)	$k_s = \left\{\left(\mathrm{a}_1 \log\omega - b_1\right)\times 10^{0.6242\rho_d - 3.4628}\right\}\times 418.6$	(2.26)	a_1, b_1, ω, ρ_d
de Vries (1963)	$x_{a-v} \le 0.5: k_s = \frac{x_{w-v}k_w + F_a x_{a-v}k_a + F_p x_{p-v}k_p}{x_{w-v} + F_a x_{a-v} + F_p x_{p-v}}$	(2.27)	$x_{a\text{-}v}$, $x_{w\text{-}v}$, $x_{p\text{-}v}$, k_a, k_w, k_p, $k_{p\text{-}w}$, F_a, F_p, F_{pw}
	$x_a > 0.5: k = \frac{x_a k_a + F_{pw}(x_w + x_p)\mathrm{k}_{pw}}{x_a + F_{pw}(x_w + x_p)}$	(2.28)	
	$k_p = k_q^{\,x_{q\text{-}v}} k_o^{\,1-x_{q-v}}$ (2.29) $\quad k_{sat} = k_p^{\,(1-n)} k_w^{\,n}$	(2.30)	
Johansen (1975)	$k_{dry} = \frac{0.135\rho_d + 64.7}{2700 - 0.947\rho_d} \pm 20\%\left(soils\right)$	(2.31)	k_p, k_q, $x_{q\text{-}v}$, m, k_o, k_w, n, S_r
	$k_{dry} = 0.039n^{-2.2} \pm 25\%\left(rocks\right)$	(2.32)	
	$k_s = (k_{sat} - k_{dry}) \times (m\log S_r + 1.0) + k_{dry}$	(2.33)	
Sakashita and Kumada (1998)	$k_{dry} = 0.0479 + 0.222(1-n) + 0.968(1-n)^3$	(2.34)	n, S_r
	$k_s = k_{dry}\left\{1 + \left[\left(9.750n - 0.706\right)S_r\right]^{0.285n+0.731}\right\}$	(2.35)	
Coté and Konrad (2005)	$k_s = (k_p^{\,(1-n)} k_w^{\,n} - \chi\times10^{-\eta n})k_e = \left[\frac{\mathrm{a}S_r}{1+(a-1)S_r}\right] + \chi\times10^{-\eta n}$	(2.36)	k_p, χ, η, n, k_w, k_p, a, S_r

Balland and Arp (2005)	$k_{sat} = k_p^{(1-n)} k_w^{n}$ (3.36)	$k_{dry} = \frac{(ak_p - k_a)\rho_b + k_a \rho_p}{\rho_p - (1-0.053)\rho_d}$ (2.37)	k_p, n, k_w, k_a, ρ_b, ρ_p, S_r, $x_{om\text{-}v}$, $x_{s\text{-}v}$, $x_{cf\text{-}v}$
	$k_e = S_r^{0.5(1+x_{om-v}-0.24x_{s-v}-x_{cf-v})} \left[\left(\frac{1}{1+\exp(-18.3S_r)} \right)^3 - \left(\frac{1-S_r}{2} \right)^3 \right]^{1-x_{om}}$ (2.38)		
	$k_s = (k_{sat} - k_{dry})\,\mathrm{k}_e + k_{dry}$ (2.39)		
Lu et al. (2007)	$k_p = k_q^{x_{q-v}} k_o^{1-x_{q-v}}$ (2.40)		k_q, k_o, $x_{q\text{-}v}$, n, α, S_r
	$k_s = \left[k_p^{1-n} k_w^{n} - (0.51 - 0.56n) \right] \exp\left[\alpha (1 - S_r^{\alpha - 1.33} \right] + 0.51 - 0.56n$ (2.41)		
Chen (2008)	$k_s = k_p^{1-n} k_w^{n} \left[(1-b)S_r + 0.0022 \right]^{0.78n}$ (2.42)		k_p, n, k_w, S_r
Haigh (2012)	$a_a = k_a / k_p \quad a_w = k_w / k_p \quad \xi = \frac{2n-1}{3}$ (2.43)		
	$\frac{k_s}{k_p} = 2(1+\xi)^2 \left\{ \begin{array}{l} \frac{a_w}{(1-a_w)^2} \ln\left[\frac{(1+\xi)+(a_w-1)x}{\xi + a_w} \right] + \\ \frac{a_a}{(1-a_a)^2} \ln\left[\frac{(1+\xi)}{(1+\xi)+(a_a-1)x} \right] \end{array} \right\}$ $+ \frac{2(1+\xi)}{(1-a_w)(1-a_a)} \left[(a_w - a_a)x - (1-a_a)\,a_w \right]$ (2.44)		k_a, k_w, k_p, n
Nowamooz et al. (2016; 2015)	$k_s = (0.443x_s + 0.081\gamma_d) \frac{(4.4x_s + 0.4)S_r}{1 + (4.4x_s - 0.6)S_r} + 0.087x_s + 0.019\gamma_d$ (2.45)		γ_d, x_s, S_r

* a_1, b_1, m, α, x, F_a, F_p, F_{pw} are the shape factors; ω is the gravimetric water content; ρ_d , ρ_p are the soil dry and particle densities (g.cm^{-3}); $x_{a\text{-}v}$, $x_{w\text{-}v}$, $x_{p\text{-}v}$, $x_{om\text{-}v}$, $x_{s\text{-}v}$, $x_{cf\text{-}v}$, $x_{j\text{-}v}$ are the volumetric content of air, water, porous particle, organic matter, sand, coarse fragment and different materials; k_{pw} is the weighing factor; k_w, k_a, k_p, k_q, k_o, k_{mj} are the thermal conductivity of water, air, soil particle, quartz, other minerals and different materials (W.m^{-1}.k^{-1}); k_{sat} and k_{dry} are the saturated and dry thermal conductivity (W.m^{-1}.k^{-1}); S_r is the soil saturation; n is the soil porosity; χ, η and a are the parameters related to soil mineral content; x_s is the gravimetric sand content; γ_d is the soil dry density multiplied by gravity (kN.m^{-3}).

The performance of 10 approaches was compared with experimental data from the literature for 7 different soils: sand (Abu-Hamdeh and Reeder, 2000; Alrtimi et al., 2016; Barry-Macaulay et al., 2013; Lu et al., 2007), loam (Lu et al., 2007), clay loam (Abu-Hamdeh, 2001; Barry-Macaulay et al., 2013; Lu et al., 2007), silt loam (Barry-Macaulay et al., 2013; Lu et al., 2007), bentonites (Tang et al., 2008), sandy clay loam (Barry-Macaulay et al., 2013), and silt clay loam (Barry-Macaulay et al., 2013). Four approaches with the highest coefficient of determination (R^2) are shown in Figure A.1. The R^2 is given as:

$$R^2 = 1 - \frac{SS_{res}}{SS_{tot}} = 1 - \frac{\sum_i (y_i - y_{i,prediction})^2}{\sum_i (y_i - \bar{y})^2} \quad (2.46)$$

where SS_{res} and SS_{tot} are the residual and total sum of squares, respectively, y, $y_{prediction}$ and $\bar{y}$ are the measured, predicted and the average values, repectively.

The R^2 of 10 models are reported in Table II.7. to facilitate the comparison. The results show the approach proposed by Nowamooz et al. (2015) has the highest R^2 among all the aforementioned models. Furthermore, it needs only three parameters.

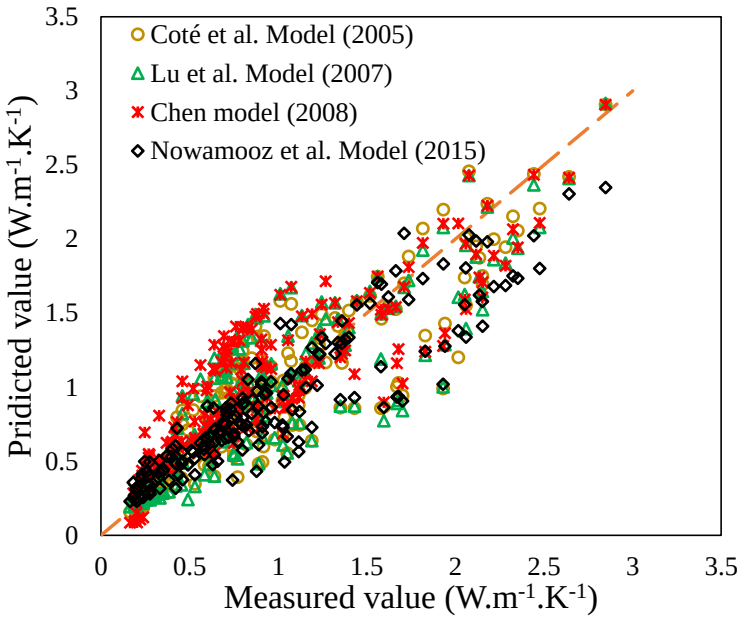

Figure II.2. Comparison of 4 approaches proposed for the thermal conductivity

Table II.7. R^2 of the 10 models

Model	R^2	*Model*	R^2
Kersten (1949)	0.640	Balland and Arp (2005)	0.366
de Vries (1963)	0.618	Lu et al. (2007)	0.669
Johansen (1975)	0.516	Chen (2008)	0.663
Sakashita and Kumada (1998)	0.074	Haigh (2012)	0.074
Coté and Konrad (2005)	0.744	Nowamooz et al. (2015)	0.762

Table II.8 summarizes the equations and parameters of two existing approaches as well as a newly proposed approach.

Table II.8. Approaches proposed for the soil volumetric heat capacity

Approach	*Equation*		*Parameter**
de Vries (1963)	$C_{v-s} = 0.46x_{p-v} + 0.60x_{om-v} + x_{w-v}\ (cal / cm^3 \cdot °C)$	(2.47)	$x_{p\text{-}v}$, $x_{om\text{-}v}$, $x_{w\text{-}v}$
Ghuman and Lal. (1985)	$C_{v-s} = \rho_b e^{-0.003X-1.071}\ (cal.g^{-1} \cdot K^{-1}))$	(2.48)	ρ_b, X

Novel approach	$C_{v\text{-}s} = (4.18 - 0.95\rho_d - 0.3x_s)S_r + 0.9\rho_d - 0.2x_s$	(2.49)	ρ_d, x_s, S_r

*$x_{p\text{-}v}$, $x_{om\text{-}v}$, $x_{w\text{-}v}$ are the volumetric water contents of particle, organic matter, and water; ρ_b and ρ_d are the soil bulk density and soil dry density (g.cm^{-3}); X is the sum of sand, silt and organic matter in percentages; x_s is the sand content by mass; S_r is the soil saturation.

Figure II.3. shows the estimations of 3 approaches compared with the experimental data reported by Abu-Hamdeh (2003) (sand and clay). Table II.9 shows the R^2 of the 3 models. The results show that the existing approaches are not the best choice due to the non-consideration of the mineral content or water content. This insufficiency can be solved by proposing a new approach for the volumetric heat capacity with a better correlation coefficient.

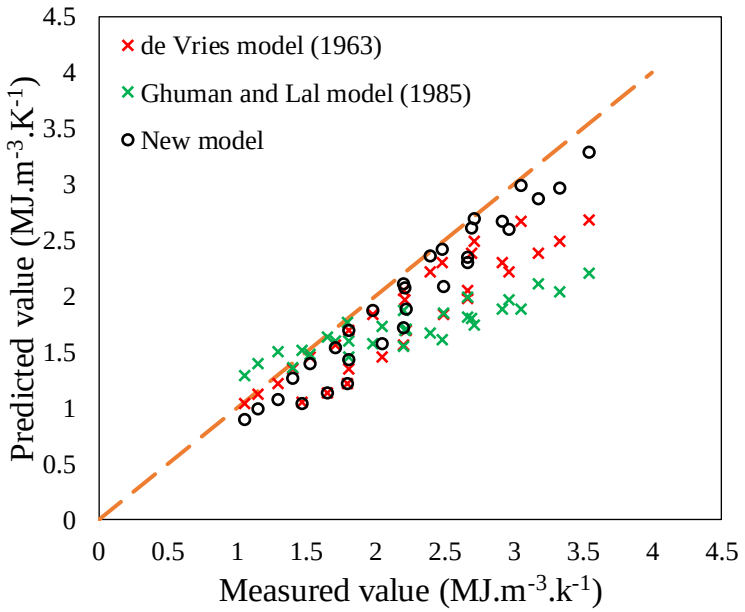

Figure II.3. Comparison of the 3 approaches proposed for the volumetric heat capacity

Table II.9. R^2 of the 3 models to predict soil volumetric heat capacity

Model	R^2
de Vries (1963)	0.4776
Ghuman and Lal. (1985)	-0.0979
Novel approach	0.8016

II.3. Heat transfer in grout

For BHE, concrete is often used as its grout material, which is normally supposed to be homogeneous. Heat transfer in the grout domain for a concrete material is dominated by conduction, given as:

$$\rho_g C_{p-g} \frac{\partial T_g}{\partial t} = k_g \nabla(\nabla T_g) + Q_g \tag{2.50}$$

where ρ_g is the grout density (kg.m^{-3}), $C_{p\text{-}g}$ is the grout specific heat capacity (J.kg^{-1}.K^{-1}), T_g is the grout temperature (°C), k_g is the grout thermal conductivity (W.m^{-1}.K^{-1}), Q_g is the grout heat source (W.m^{-3}).

II.4. Heat transfer in pipe

The outer pipe and the inner pipe exchange heat by conduction, the instant heat flux is therefore given as:

$$q_p = 2\pi \cdot r \cdot k_p \cdot \nabla T_p \tag{2.51}$$

where k_p is the thermal conductivity of pipe. The above equation can be further transferred to:

$$q_p \int_{r_{in}}^{r_{out}} \frac{1}{r} dr = 2\pi \cdot k_p \int_{T_{i-p}}^{T_{o-p}} dT_p \tag{2.52}$$

where r_{out} and r_{in} are the outside and inside radius of pipe, respectively, $T_{o\text{-}p}$ is the outer pipe temperature (°C). Therefore:

$$q_p = \frac{2\pi k_p}{\ln\left(r_{out} / r_{in}\right)} (\mathrm{T}_{o-p} - \mathrm{T}_{i-p}) \tag{2.53}$$

In quasi-static condition, the heat from grout to the pipe and the heat from pipe to the fluid is the same.

II.5. Heat transfer in carrying fluid

Carrying fluid flows in the pipe and exchanges heat with the surrounding medium, which is a crucial element in the ground heat exchanger applications. It is therefore necessary to be aware that how the carrying fluid exchanges heat with the surroundings.

The energy balance equation in carrying fluid can be given as:

$$A\rho_f C_{p-f}\frac{\partial T_f}{\partial t} + A\rho_f C_{p-f} u_f \cdot \nabla T_f = \nabla \cdot A k_f \nabla T_f + f_D \frac{\rho_f A}{2d_h}\left|u_f\right|u_f^{\,2} + Q_{wall} \quad (2.54)$$

where, A is the pipe inner cross-sectional area (m^2), ρ_f is the fluid density ($kg.m^{-3}$), C_{p-f} is the fluid specific heat capacity ($J.kg^{-1}.K^{-1}$), T_f is the fluid temperature (°C), u_f is the flowing velocity of fluid ($m.s^{-1}$), k_f is fluid conductivity ($W.m^{-1}.K^{-1}$), f_D is the Darcy friction factor for the description of friction losses, d_h is the hydraulic diameter (m) determined by the inner cross-sectional area and the wetted perimeter of the pipe, which is the diameter of the pipe in this investigation, Q_{wall} is the energy from the surrounding media ($W.m^{-1}$).

Heat exchange rate with the surrounding medium depends strongly on the flow conditions. Internal pipe flow is classified as either laminar or turbulent. In laminar flow, the fluid flow smoothly, largely linear and highly ordered. By contrast, the streamlines of turbulent flow are chaotic, and the velocity is subject to significant fluctuations. Turbulent flow has enhanced heat transfer characteristic compared with laminar flow, which is the reason that most ground heat exchangers adopt turbulent flow option to enhance the performance of a ground heat exchanger (Loveridge, 2012). Laminar and turbulent flow are determined by Reynolds number, which is the ratio between the inertial and the viscous forces in the fluid, defined by:

$$\mathrm{Re} = \frac{\rho_f d_h u_f}{\mu} \quad (2.55)$$

where μ is the dynamic viscosity of the fluid (Pa.s). Typically, the following classification is in use:

$\mathrm{Re} < 2300$	laminar	
$2300 < \mathrm{Re} < 4000$	transient	(2.56)
$\mathrm{Re} > 4000$	turbulent	

There are many methods to obtain the friction factor (Avci and Karagoz, 2009; Ćojbašić and Brkić, 2013; Eck, 1973; Haaland, 1983; Moody, 1944; Serghides, 1984; Swamee and Jain, 1976; Wood, 1968; Zigrang and Sylvester, 1982). Some of the equations to obtain the friction factor are listed in Table II.10.

Table II.10. Several models for friction factor

Model	*Equation **

Eck (1973)	$\frac{1}{\sqrt{f_D}} = -2\log(\frac{r_{ou}/d_{in}}{3.715} + \frac{15}{\mathrm{Re}})$	(2.57)
Swamee and Jain (1976)	$f_D = \frac{0.25}{[\log((\frac{r_{ou}/d_{in}}{3.7} + \frac{5.74}{\mathrm{Re}^{0.9}})]}$	(2.58)
	$f_D = \left[\left(\frac{8}{\mathrm{Re}}\right)^{12} + \frac{1}{(\alpha_- + \beta_-)^{3/2}}\right]^{1/12}$	(2.59)
	where	
Churchill (1977a)	$\alpha_- = \left[2.457\ln\frac{1}{(7/\mathrm{Re})^{0.9} + (0.27 r_{ou}/\mathrm{d}_{in})}\right]^{16}$	(2.60)
	$\beta_- = \left(\frac{37530}{\mathrm{Re}}\right)^{16}$	(2.61)
Zigrang and Sylvester (1982)	$\frac{1}{\sqrt{f_D}} = -2\log[\frac{r_{ou}/d_{in}}{3.7} - \frac{5.02}{\mathrm{Re}}\log(\frac{r_{ou}/d_{in}}{3.7} + \frac{13}{\mathrm{Re}})]$	(2.62)
Haaland (1983)	$\frac{1}{\sqrt{f_D}} = -1.8\log[(\frac{r_{ou}/d_{in}}{3.7})^{1.11} + \frac{6.9}{\mathrm{Re}}]$	(2.63)
Avci and Karagoz (2009)	$f_D = \frac{6.4}{(\ln(\mathrm{Re}) - \ln(1 + 0.01\,\mathrm{Re}\frac{r_{ou}}{d_{in}}(1 + 10\sqrt{\frac{r_{ou}}{d_{in}}})))^{2.4}}$	(2.64)

*r_{ou}: effective roughness, m; d_{in}: pipe inner diameter, m.

The energy transfer from the surrounding media to the fluid can be given as:

$$Q_{wall} = h_{\mathrm{int}} \cdot Z \cdot (T_{i-p} - T_f) \tag{2.65}$$

where Z is the pipe inner perimeter (m).

The film heat transfer coefficient is given as:

$$h_{\mathrm{int}} = Nu\frac{k_f}{d_h} \tag{2.66}$$

where Nu is the Nusselt number, which is the ratio of convective to conductive heat transfer.

For laminar flow, the heat transfer coefficient can be related directly to the Nusselt number. Nusselt number for the case of a constant heat flux pipe wall boundary condition can be given as:

$$Nu = 4.36 \tag{2.67}$$

For a constant pipe wall temperature boundary condition, Nusselt number can be given as:

$$Nu = 3.66 \tag{2.68}$$

For turbulent flow with fully developed thermal conditions (constant heat flux pipe wall or boundary constant pipe wall temperature conditions), the Nusselt number is not a constant but depends on the Reynolds number and the Prandtl number. *Nu* can be given as (Gnielinski, 1976):

$$Nu = \frac{0.125 f_D (-1000 + \mathrm{Re})\,\mathrm{Pr}}{1 + 12.7(f_D / 8)^{0.5}(\mathrm{Pr}^{2/3} - 1)} \tag{2.69}$$

Or by Dittus and Boelter (Bejan, 2013):

$$Nu = 0.023\,\mathrm{Re}^{4/5}\,\mathrm{Pr}^{n} \tag{2.70}$$

where Pr represents Prandtl number, which is determined at the mean temperature of the bulk fluid, n is a constant, taken as 0.4 for heating and 0.3 for cooling. However, this expression is only valid for Re>10,000 and may overestimate the Nusselt number and hence the heat transfer coefficient at smaller Reynolds numbers. The Dittus and Boelter equation also assumes a relatively small temperature difference and hence can result in errors when used with fluids which have highly temperature dependent properties, especially viscosity. Consequently, Incropera et al. (2007) suggest that up to 25% errors can result in some cases. These can be reduced to around 10% by Gnielinksi model (1976).

Prandtl number is given by:

$$\mathrm{Pr} = \frac{C_{p-f}\,\mu}{k_f} \tag{2.71}$$

II.6. Summary

The current chapter provides the fundamental physics in the computation of ground heat exchanger installed in soils.

Basic heat transfer means, including heat conduction, heat convection and radiation are introduced at first. Subsequently, heat transfer in different components (soil, grout, pipe, carrying fluid) of a ground heat exchanger system is brought out.

In the following chapters, the equations been introduced in this chapter would be selected and used in the numerical simulation framework.

III. LONG-TERM PERFORMANCE OF A SHALLOW BHE AT A GEOTHERMAL FIELD IN ALSACE

III.1. Introduction

Alsace region in France has a favorable condition for geothermal utilization with 0.1 $K.m^{-1}$ of the temperature gradient due to the local geological condition (Genter et al., 2003). Since 1986, Soultz-sous-Forêts project has been focused on studying deep geothermal storage in the Alsace region. In the September of 2016, the project starts providing electricity for industrial use with a capacity of 12,000 MWh per year, which could reduce 950 tons of CO_2 emission (ES, 2017a). Since the October of 2017, additional deep boreholes up to a depth of 3,000 m at Illkirch (Alsace region) have been conducted to provide 22,000 MWh of electricity per year and to reduce 11,000 tons of CO_2 emission once fully operated (ES, 2017b).

Compared to deep BHE, the economic and environmental risk of shallow BHE is smaller. Therefore, we studied the performance of a shallow BHE installed in a field situated at Illkirch (Alsace region). Then, a 3D numerical framework with the specified boundary conditions and the initial hydrothermal profiles was built by considering the local geological conditions. Next, the model was validated by the experimental measurements of thermal and humidity probes installed in the investigated zone, as well a TRT in Japan. Finally, the model was used to analyze and estimate the performance of the shallow BHE.

III.2. Governing Equations

Energy conservation is the principal concept of the model, introduced as:

$$E_{source} + \Delta E_{surrounding} = \Delta E_{fluid} \tag{3.1}$$

where E_{source} is the energy source (J) provided by ground surface, $\Delta E_{surrounding}$ denotes the energy variation of the surrounding media (grout, soil and sedimentary rock) (J), ΔE_{fluid} is the energy taken out by carrying fluid (J).

The model contains the following parts: the water transfer in unsaturated soils, the soil thermal properties, the heat transfer in the pipe, the heat transfer in the grout, and the heat transfer in porous media.

III.2.1. Water transfer equation in unsaturated soils

Water in porous media is assumed to be incompressible and there is no mass transfer of soil particles. The water vapor is not considered since it is not significant in our calculations.

The Richards equation is applied to estimate the variation of water potential with time and space, expressed as:

$$\rho_w \cdot \psi \cdot \frac{\partial h_{head}}{\partial t} + \cdot \rho_w \cdot \nabla \cdot \left[-K \cdot k_r \cdot \nabla \cdot h_{head} \right] = Q_{w\_source} \tag{3.2}$$

where, ρ_w is the water density (kg.m^{-3}), ψ is the specific moisture capacity (m^{-1}) derived from van Genuchten [10], h_{head} is the hydraulic head (m), t is the time (s), K is the hydraulic conductivity (m.s^{-1}) of porous media, k_r is the relative hydraulic conductivity, Q_{w_source} is the water source (kg.m^{-3}.s^{-1}).

van Genuchten [10] equation is used for the calculation of suction and relative saturation:

$$Se = \begin{cases} \dfrac{1}{\left[1 + \left| \alpha H_p \right|^n \right]^{1-1/n}} & H_p < 0 \\ 1 & H_p \geq 0 \end{cases} \tag{3.3}$$

where, α is related to the inverse of the air entry suction (m^{-1}), H_p is the suction heat (m). The volumetric water content can be obtained by:

The volumetric water content can be given by:

$$\theta = S_e \cdot (\theta_{sat} - \theta_{res}) + \theta_{res} \tag{3.4}$$

where θ_{sat} and θ_{res} are the saturated and the residual water content, respectively.

Therefore, the specific moisture capacity (m^{-1}) is given by:

$$\psi = \begin{cases} \dfrac{d\theta}{dh_{head}} = -\dfrac{\alpha m}{1-m}(\theta_{sat} - \theta_{res}) S_e^{1/m} (1 - S_e^{1/m})^m & h_{head} < 0 \\ 0 & h_{head} \geq 0 \end{cases} \quad (3.5)$$

where *l* is the pore connectivity parameter, *m* is defined as:

$$m = 1 - \frac{1}{n} \quad (3.6)$$

Mualem's equation (1976) is used for the calculation of relative hydraulic conductivity:

$$k_r = \begin{cases} S_e^{\,l} \left[1 - \left(1 - S_e^{\,n/(n-1)} \right)^m \right]^2 & H_p < 0 \\ 1 & H_p \geq 0 \end{cases} \quad (3.7)$$

Therefore, the soil saturation can be obtained by the following equation:

$$S_r = \frac{\theta}{\theta_{sat}} \quad (3.8)$$

III.2.2. Soil thermal properties

The approach proposed by Nowamooz et al. [12, 13] for the soil thermal conductivity is used in the numerical simulations:

$$k_s = (k_{sat} - k_{dry}) k_e + k_{dry} \quad (3.9)$$

where, k_{sat}, k_{dry} and k_e are the saturated soil thermal conductivity ($W.m^{-1}.K^{-1}$), the dry soil thermal conductivity ($W.m^{-1}.K^{-1}$), the shape and moisture factor, respectively.

As it has been derived from the experimental results reported by Ochsner et al. [14], Abu-Hamdeh [15] and Rajeev et al. [6], the soil heat capacity increases linearly with soil saturation. If dry and saturated soil volumetric heat capacity are obtained, a linear equation can be employed to calculate the volumetric capacity of the soil:

$$C_{v-s} = (C_{v-sat} - C_{v-dry}) \mathrm{S}_r + C_{v-dry} \quad (3.10)$$

with the dry and saturated volumetric heat capacity are given by:

$$C_{v-dry} = 0.09\gamma_d - 0.2x_s \quad (3.11)$$

$$C_{v-sat} = 4.18 - 0.005\gamma_d - 0.5x_s \quad (3.12)$$

where, S_r is the soil saturation, γ_d is the soil dry unit weight (kN.m^{-3}), x_s is the gravimetric sand content. The influence of temperature on the soil thermal properties is not taken into account in this work since the temperatures are below 40 °C [16].

III.2.3. Heat transfer in pipe carrying fluid

The pipe conveying fluid is regarded as 1D domain in the numerical simulation. The 1D heat transfer in the pipe includes its wall layer, its internal film, and the carrying incompressible fluid. Although the loss of kinetic head has a very small effect, we keep the term in the energy balance equation. By applying Churchill's relation to Darcy friction factor (Churchill, 1977b), the equation becomes as follows:

$$A\rho_f C_{p-f}\frac{\partial T_f}{\partial t} + A\rho_f C_{p-f} u_f \cdot \nabla T_f = \nabla \cdot Ak_f \nabla T_f + f_D \frac{\rho_f A}{2d_h}\left|u_f\right|u_f{}^2 + Q_{wall} \tag{3.13}$$

Churchill (1977a) relation was adopted in our investigation since it can be used for laminar, transitional and turbulent flow. Darcy friction factor from Churchill (1977a) relation is given by:

$$f_D = \left[\left(\frac{8}{\mathrm{Re}}\right)^{12} + \frac{1}{(\alpha+\beta)^{3/2}}\right]^{1/12} \tag{3.14}$$

where

$$\mathrm{Re} = \frac{\rho_f d_h u_f}{\mu} \tag{3.15}$$

$$\alpha = \left[2.457 \ln \frac{1}{(7/\mathrm{Re})^{0.9} + (0.27 r_{ou}/\mathrm{d}_{in})}\right]^{16} \tag{3.16}$$

$$\beta = \left(\frac{37530}{\mathrm{Re}}\right)^{16} \tag{3.17}$$

The energy transfer from the surrounding media to the fluid can be given as:

$$Q_{wall} = h_{\mathrm{int}} \cdot Z \cdot (T_{i-p} - T_f) \tag{3.18}$$

The film heat transfer coefficient is given as:

$$h_{\text{int}} = Nu\frac{k_f}{d_h} \tag{3.19}$$

In this investigation, a turbulent flow is anticipated in the pipe flow and therefore, *Nu* can be given as (Gnielinski, 1976):

$$Nu = \frac{0.125 f_D(-1000+\text{Re})\,\text{Pr}}{1+12.7(f_D/8)^{0.5}(\text{Pr}^{2/3}-1)} \tag{3.20}$$

where *Pr* is given by:

$$\text{Pr} = \frac{C_{p-f}\mu}{k_f} \tag{3.21}$$

The outer pipe and the inner pipe exchange heat by conduction, the instant heat flux is therefore given as:

$$q_p = 2\pi \cdot r \cdot k_p \cdot \nabla T_p \tag{3.22}$$

The above equation can be further transferred to:

$$q_p \int_{r_{in}}^{r_{out}} \frac{1}{r} dr = 2\pi \cdot k_p \int_{T_{i-p}}^{T_{o-p}} dT_p \tag{3.23}$$

Therefore:

$$q_p = \frac{2\pi k_p}{\ln\left(r_{out}/r_{in}\right)}(\text{T}_{o-p} - \text{T}_{i-p}) \tag{3.24}$$

III.2.4. Heat transfer in grout

Heat transfer in the grout is dominated by conduction, given as:

$$\rho_g C_{p-g}\frac{\partial T_g}{\partial t} = \nabla \cdot \left(k_g \nabla T_g\right) + Q_g \tag{3.25}$$

III.2.5. Heat transfer in soil

The energy conservation equation in porous media containing heat conduction is given as:

$$\frac{\partial(\rho_s C_{p-s} T_s)}{\partial t} = \nabla \cdot (k_s \nabla T_s) + Q_s \tag{3.26}$$

III.2.6. Approaches to investigating the heat pump performance

Coefficient of Performance (COP) is typically used to evaluate the performance of a heating or cooling system. This is the ratio of energy output (building heat load) to energy input (consumed by heat pump):

$$\mathrm{COP} = \frac{Q_{building}}{W_{hp}} \tag{3.27}$$

In the heating scenario, the building thermal load equals the sum of BHE thermal load and heat pump electricity consumption, therefore:

$$Q_{building} = \frac{\mathrm{COP}}{\mathrm{COP\text{-}1}} \cdot Q_{BHE} \tag{3.28}$$

Although there are many factors influencing the heat pump COP, it is widely accepted that heat pump COP can be expressed as a linear function of the outlet temperature of carrying fluid (Casasso and Sethi, 2014; Chen et al., 2019; Hein et al., 2016; Kahraman and Çelebi, 2009; Sanner et al., 2003; Shao et al., 2016). According to Glen Dimplex Deutschland GmbH (Glen Dimplex Deutschland GmbH, 2016), the relation between the outlet temperature and the heat pump COP for their apparatus SI 30TE can be shown in Figure III.1. To reach a heating fluid temperature up to 35°C (in the heating period), the heat pump COP is given as:

$$\mathrm{COP} = 0.1452 T_{out} + 4.0289 \tag{3.29}$$

where, T_{out} is the outlet temperature of carrying fluid from shallow BHE (°C).

Due to the positive inlet temperature of the carrying fluid, the heat pump COP is within the range of 4.29 and 5.70. The same range will be also investigated in this work.

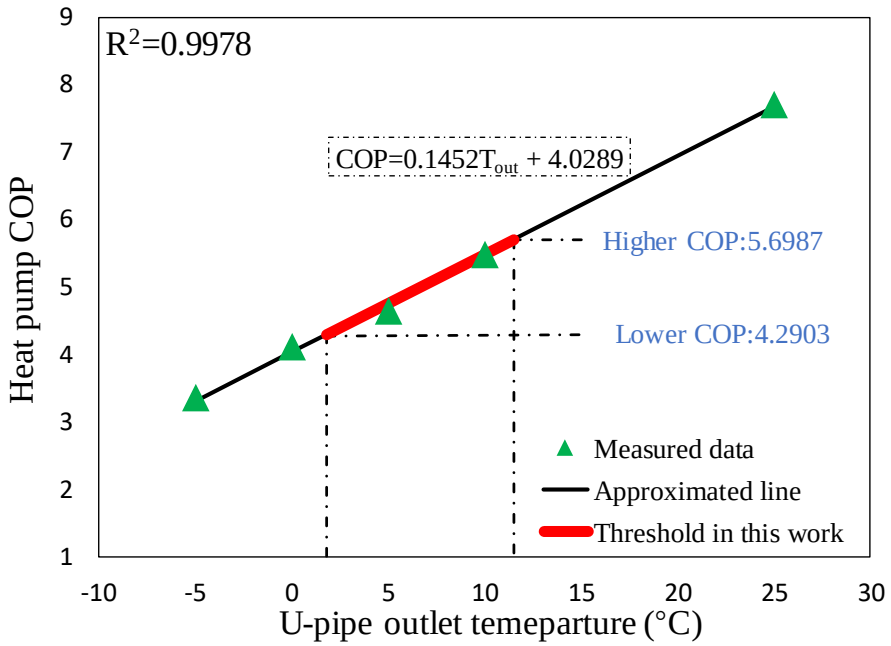

Figure III.1. Approximated COP and in-situ COP in literature (Glen Dimplex Deutschland GmbH, 2016)

The Total Extracted Energy (TEE) can be obtained by:

$$\frac{dQ_{ext}}{dt} = Au_f \rho_f C_{p-f} (T_{out} - T_{in}) \tag{3.30}$$

where, T_{in} is the inlet temperature of carrying fluid (°C).

III.3. Hydrothermal transfer numerical simulation model

A multi-layered field located in Illkirch (Alsace region, France) has been investigated for its capacity of shallow geothermal energy storage. For pursuing the different aspects influencing the performance of shallow BHE, COMSOL was used for the finite element numerical simulations. The pipe and the carrying fluid were considered as a 1D domain, while the grout and the surrounding soils were a 3D medium.

III.3.1. Model geometry and mesh

The numerical model is 3D with the side length of 30 m and the depth of 100 m (Figure III.2-a). The height is constituted of two parts: 30 m of soils on the top and 70 m of claystone (bedrock) on the bottom. The soil is composed of 7 soil layers including 4 different soils: clay loam, sandy loam 1, loam and sandy loam 2. The soil thickness of the investigated layers varies from 0.10 m to 11.0 m. The mesh used for the simulation is also presented in Figure

III.2-b. The appropriate mesh was selected by increasing the density of the mesh until the computation results became stable.

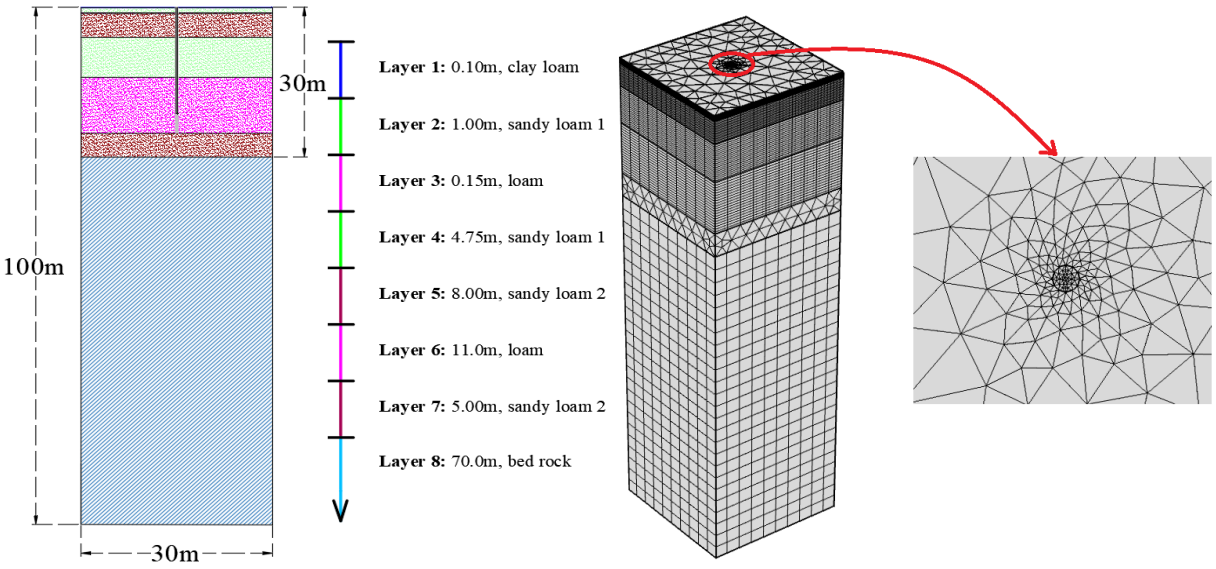

(a) (b)

Figure III.2. (a) Field description and (b) generated mesh used in the numerical modeling

The grout surrounding the single U-pipe is 25 m and the single U-pipe is with a depth of 20 m. The diameter of the borehole is 0.14 m. Inside the borehole, the U-pipe is symmetrically installed. The inner and outer diameter of U-pipe is 2.2 cm and 2.5 cm, and the shank spacing is 6.0 cm (Figure III.3).

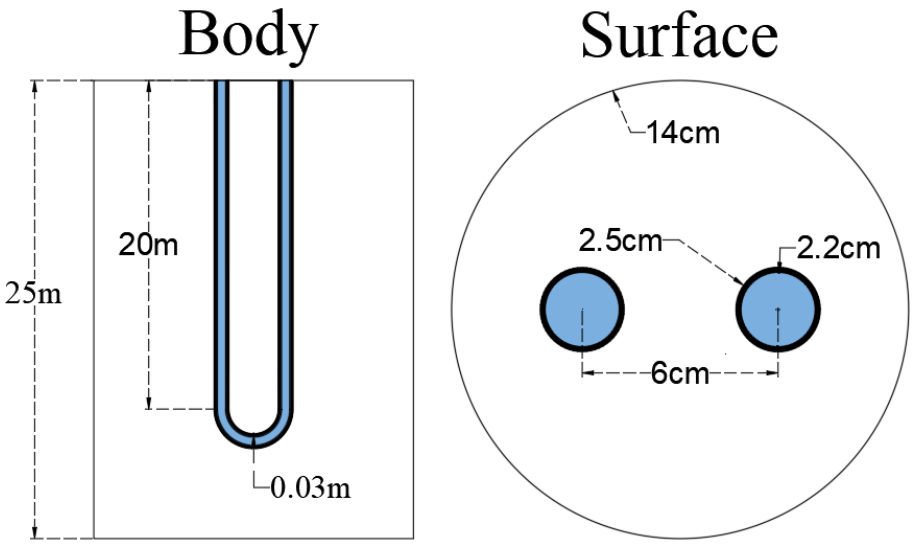

Figure III.3. Schematic of the grout and U-pipe

III.3.2. Parameters used in the numerical simulations

Table III.1 summarizes the main hydraulic properties of the multi-layered soil surrounding the shallow BHE (Ghanbarian-Alavijeh et al., 2010). For the studied soils, it was assumed that the volume change would be negligible during the wetting and drying cycles (Muñoz-Castelblanco et al., 2012) and therefore, van Genuchten (1980) parameters were set fixed during these hydraulic variations (Nguyen et al., 2017).

Table III.1. Hydrothermal properties of the studied soils

Material	$K\ (m.s^{-1})$	$L\ (-)$	$\alpha\ (m^{-1})$	$n\ (-)$	$\theta_s\ (-)$	$\theta_r\ (-)$	$x_s\ (-)$	$\gamma_s\ (kN.m^{-3})$	$\gamma_d\ (kN.m^{-3})$
Clay loam	1.53E-6	0.5	1.99	1.22	0.50	0.03	0.35	27.0	13.5
Sandy loam 1	1.78E-5	0.5	2.60	1.52	0.39	0.02	0.80	26.2	16.0
Loam	2.19E-6	0.5	2.35	1.38	0.47	0.02	0.50	26.8	14.2
Sandy loam 2	1.45E-5	0.5	2.48	1.50	0.40	0.02	0.60	26.7	16.0

Pure water was chosen as the carrying fluid since no negative temperature was considered in the simulations. Carrying fluid velocity was kept as 0.5 $m.s^{-1}$. The U-pipe is a High-Density Polyethylene (HDPE) pipe with high durability and strength (Florides and Kalogirou, 2007). The grout was used as the surrounding material for the U-pipe. Table III.2 has summarized the thermal parameters of the sedimentary rock (claystone), water, grout and pipe.

Table III.2. Thermal properties of the shallow BHE materials

Material	*Unit weight* $\gamma\ (kN.m^{-3})$	*Thermal conductivity* $k\ (W.m^{-1}.K^{-1})$	*Specific heat capacity* $C_p\ (KJ.kg^{-1}.K^{-1})$	*Dynamic viscosity* $\mu\ (mPa.s)$
Claystone	23	2.6	0.9	-
Water	10	0.6	4.2	1.3
Grout	25	2.5	0.8	-
Pipe	-	0.5	-	-

III.3.3. Initial hydrothermal boundary conditions

Seasonal suction and temperature conditions were imposed on the ground surface (Dirichlet boundary) for a period of 365 days (1 year). As presented in Figure III.4, an approximated

equation for the ground surface temperature was then derived from the measurements of the installed thermal probe on the ground surface over a year:

$$T_{surface}=10.5\cdot\sin(pi/182.5\cdot(t+91.25))+11.5 \quad (3.31)$$

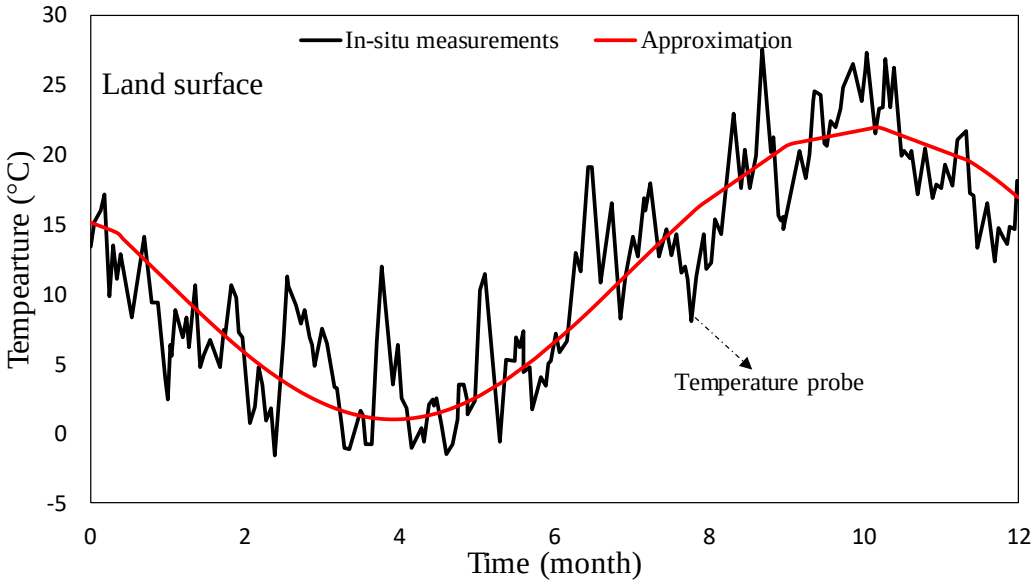

Figure III.4. Approximated ground surface temperature with in-situ probe measurement

The seasonal ground surface suction was assumed to vary between 0.01 MPa in winter corresponding to the saturated state, and 2 MPa in summer corresponding to the maximum suction value for a normally vegetated field (Rajeev et al., 2012). Therefore, the approximated seasonal ground surface suction is given as:

$$F_{surface}=0.995\cdot\sin(pi/182.5\cdot(t+91.25))+1.005 \quad (3.32)$$

The starting operation time of shallow BHE was considered in the middle of July. No water flow (out or in) was imposed on the side and bottom boundaries. Meanwhile, there was no heat flow on the side boundaries, and the temperature gradient on the bottom boundary was supposed to be 0.1 $K.m^{-1}$ as identified in Illkirch, Alsace region (Baillieux et al., 2013; Genter et al.; Gérard et al., 2006; Hooijkaas et al., 2006; Schill et al., 2017; Vidal et al., 2015).

III.3.4. Initial hydrothermal profiles

According to the aforementioned hydrothermal conditions, the initial local hydrothermal profiles were obtained after reaching an equilibrium stage. The suction and temperature

profile in this equilibrium stage are presented in Figure III.5. The initial suction profile (Figure III.5) indicates that the water table is at a depth of 7.63 m. For depth below 7.63 m, the soil was supposed to be saturated. It can be observed from Figure III.5-b that the temperature gradient below 30 m is 0.1 $K.m^{-1}$, which corresponds to the imposed bottom boundary condition. As expected, the temperature gradient varies at the shallow depth (less than 30 m) due to the heterogeneous soil/rock thermal properties. Furthermore, the temperature gradient in the soil is greater than that in the bedrock because of its lower thermal conductivity.

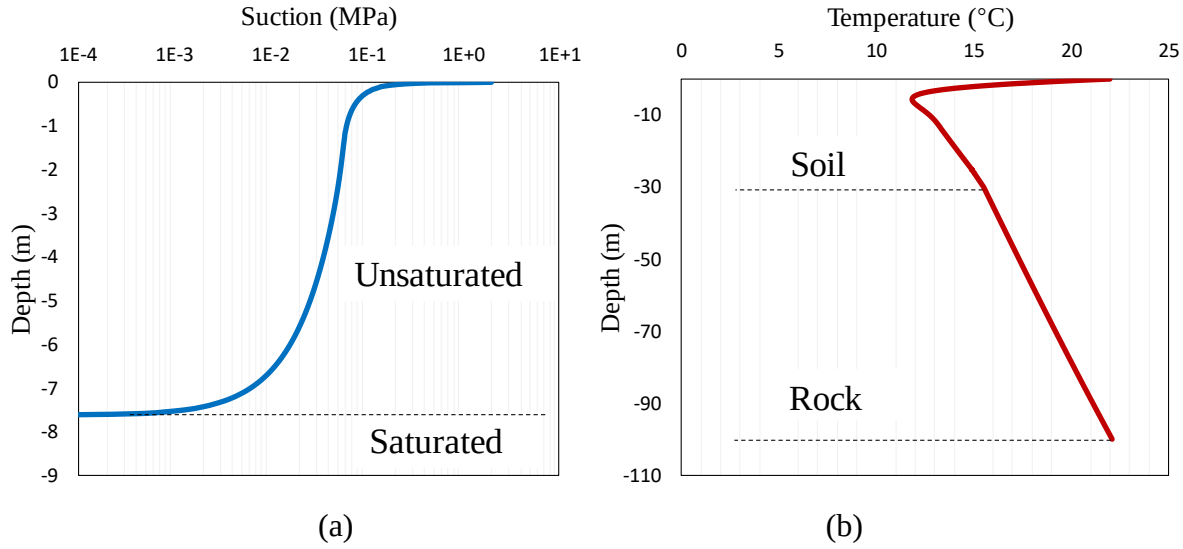

(a) (b)

Figure III.5. Initial hydrothermal profiles: (a) initial suction (MPa) and (b): initial temperature (°C)

III.3.5. Operation options

Alsace region has a mild climate in summer and a cold climate in winter. Therefore, a heating scenario was considered in our simulations. Through a year, the shutdown temperatures of the system (T = 10 °C) are controlled automatically by monitoring the ground surface temperatures. According to the Alsace meteorological condition (equation (3.31)), the studied shallow BHE operates 165 days per year when the ground surface temperature is lower than 10 °C.

Since there are various effects of thermal conditions of the U-pipe on the operation of a shallow BHE, two different scenarios were studied in this investigation: constant inlet temperature and variable seasonal heat load (Bidarmaghz et al., 2016; Shao et al., 2016). The

shallow BHE in both scenarios extracted the same amount of energy over a year. The constant inlet temperature (5 °C) and the seasonal heat load (varying between 8.82 and 26.45 $W.m^{-1}$) are shown in Figure III.6. The shallow BHE was supposed to be installed on 15th of July 2018. The appropriate time step for the numerical simulation model was selected by decreasing the time step until the computation results became stable. Finally, the time step was set as 0.5 d.

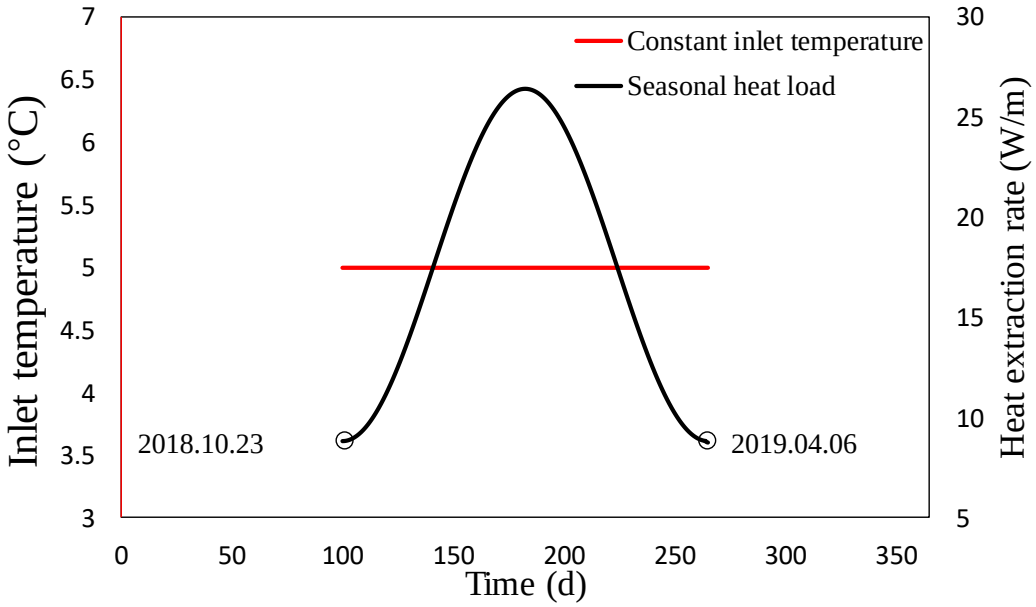

Figure III.6. Imposed inlet temperature (°C) and variable heat extraction rate (W.m-1) during the working period of a shallow BHE

III.4. Numerical simulation results

In this section, the capacity of the finite element model to simulate the field conditions is initially evaluated by the measured data from September 2012 to September 2013. Further, the hydrothermal variation is analyzed over this period.

Eventually, the performance of the shallow BHE is analyzed. To anticipate the performance of the system, the model was set to start working from 15th of July 2018 with the variations of ground surface temperature and suction presented in equations (3.31) and (3.32).

III.4.1. Validation of the numerical results

Figure III.7 shows the volumetric water content value of the numerical model compared with the in-situ measurements at the depth of 1.11 m between September 2012 and September 2013. The measured in-situ water content using humidity probe shows a greater fluctuation with time than the numerical simulation, which is due to the more variable natural hydraulic

conditions. Neglecting this daily climatic variability, the numerical simulations can be acceptable for the following calculations.

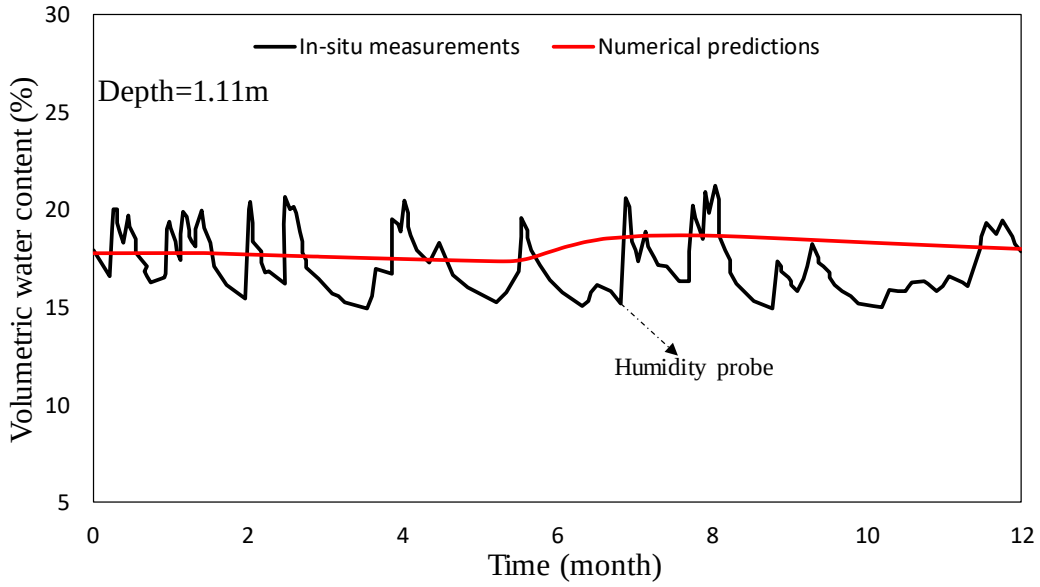

Figure III.7. Volumetric water content of the numerical model compared to the measurements

Further, energy conservation equation was used to obtain the underground temperatures between September 2012 and September 2013. Figure III.8 shows the comparison of the in-situ data for the four field-instrumented probes at three different depths (0.60, 1.10 and 1.25 m) with the prediction data over 1 year. Root-Mean-Square Error (RMSE) was used to evaluate the capacity of the numerical simulation framework. RMSE can be given as:

$$\mathrm{RMSE} = \left[\sum_{i=1}^{N} (T_{np,i} - T_{im,i})^2 / N \right]^{1/2} \tag{3.33}$$

where T_{np} is the temperature (°C) from the numerical prediction, T_{im} is the temperature (°C) from the in-situ measurement, N is the number of temperature data. As expected, the measured data are more variable than simulated data, nonetheless, the established numerical model is capable of simulating reasonably well the underground temperature fluctuation with RMSE values less than 1.9 °C.

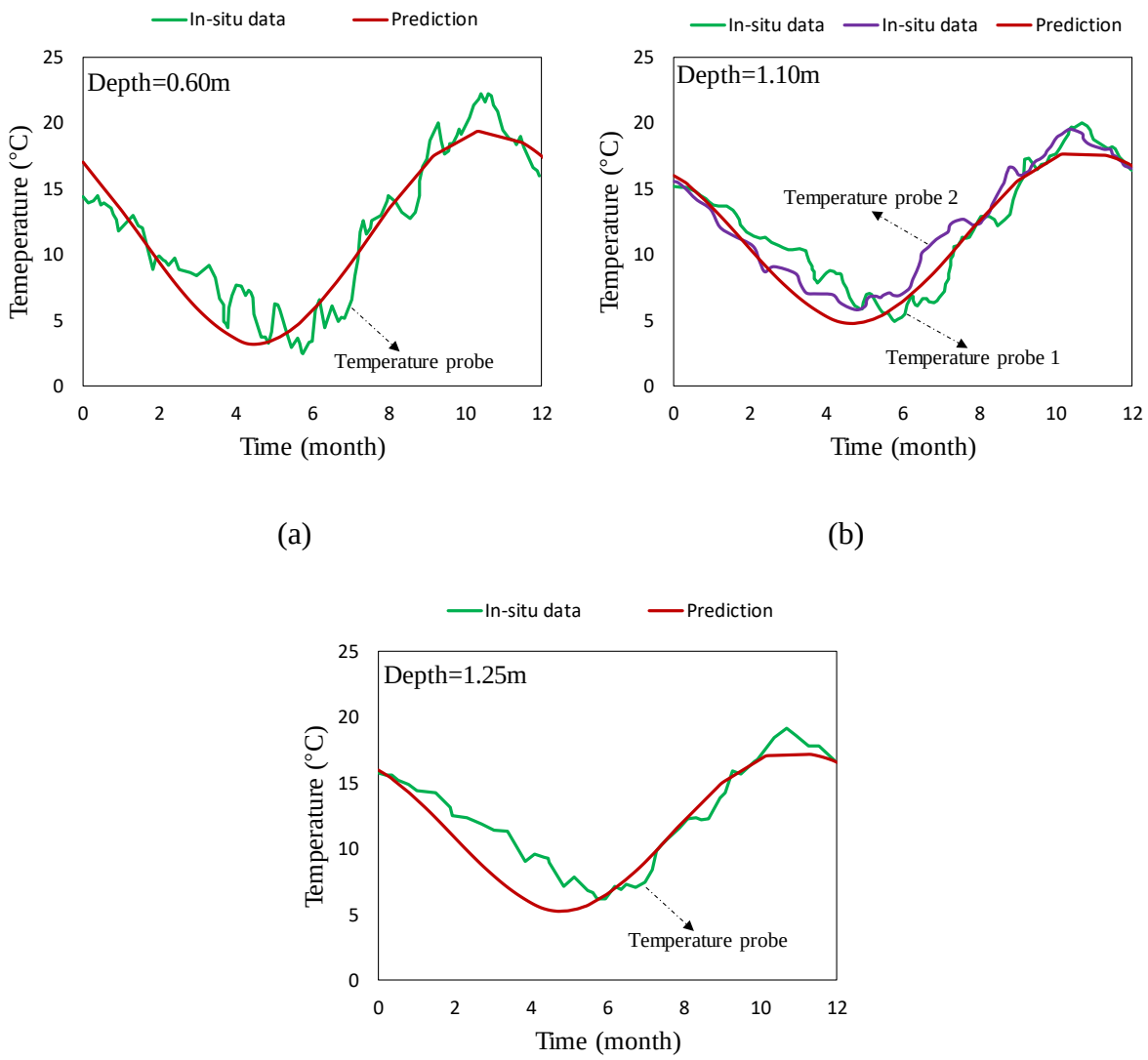

Figure III.8. Annual temperature of the numerical results compared to the in-situ measurements at different depths: (a) 0.6 m; (b) 1.1 m and (c) 1.25 m

Figure III.9-a shows also that the numerical simulations of the temperature profile close to the surface (less than 2 m) compared with the field data at the three aforementioned depths (0.6 m, 1.1 m and 1.25 m) considering three different times of a year. It could be seen the accuracy of the prediction model varies with time and space, which is largely dependent on ground surface temperature fluctuation. Nevertheless, the numerical results correspond well with the in-situ measurements.

Additionally, the temperature profile compared to the in-situ measurements (Baillieux et al., 2013; Genter et al., 2003; Vidal et al., 2015) are presented up to a depth of 65 m at different

times over 1 year (Figure III.9-b). The in-situ data are obtained more than 12 m below the ground surface, therefore, we presume they maintain constant temperatures all over the years due to the stable geological and meteorological condition in Alsace region (Gérard et al., 2006; Pouloupatis et al., 2011). Figure III.9-b shows the predicted subsurface temperatures match well the in-situ measurements. Besides, the temperature profile follows the ground surface temperatures at low depths, and the fluctuation of the temperature profile reduces with depth before being totally eliminated for depths greater than 12 m.

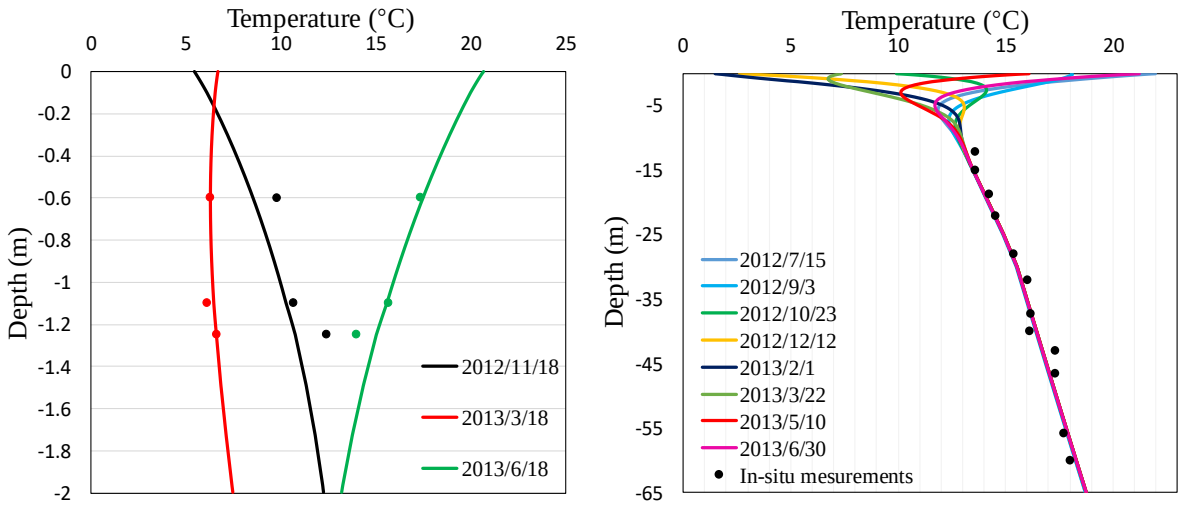

(a) (b)

Figure III.9. Simulated temperature profile compared to the in-situ measurements: (a) close to the surface and (b) larger depths between 0 and 65 m

To give more credit to the proposed numerical framework, the numerical simulation framework was also validated by using the TRT performed at the campus of Saitama University (SU) (Brunetti et al., 2017; Saito et al., 2014a). Tap water was circulated in both U-pipes for 48 h with a constant heating power. The average heat exchange rate was estimated 56.46 W m^{-1}. The parameters of the experimental apparatus were also listed in Table III.3.

Table III.3. Summary of the input parameters used in the simulations

Factor	*Parameter*	*Factor*	*Parameter*
Carrying fluid velocity	0.21 $m.s^{-1}$	Carrying fluid density	1000 $kg.m^{-3}$
Carrying fluid specific heat capacity	4182 $J.kg^{-1}.K^{-1}$	Carrying fluid thermal conductivity	0.6 $W.m^{-1}.K^{-1}$
U-pipe type	Double U-pipe	U-pipe thickness	0.003 m

U-pipe inner diameter	0.026 m	U-pipe thermal conductivity	0.51 $W.m^{-1}.K^{-1}$
U-pipe length	50 m	Borehole diameter	0.178 m
Grout thermal conductivity	2.2 $W.m^{-1}.K^{-1}$	Grout volumetric heat capacity	3.1 $MJ.m^{-3}.K^{-1}$
Shank spacing	0.058 m	Initial temperature	16.2 °C
Operation time	48 h	Inlet temperature minus outlet temperature	3 °C

Figure III.10 shows the profiles for the volumetric water content, the soil dry density and the sand content used in the numerical simulations. Below 50 m, all parameters were assumed constant. By knowing these profiles and using equations (3.9) and (3.10), the profiles for the thermal properties were followingly accessible.

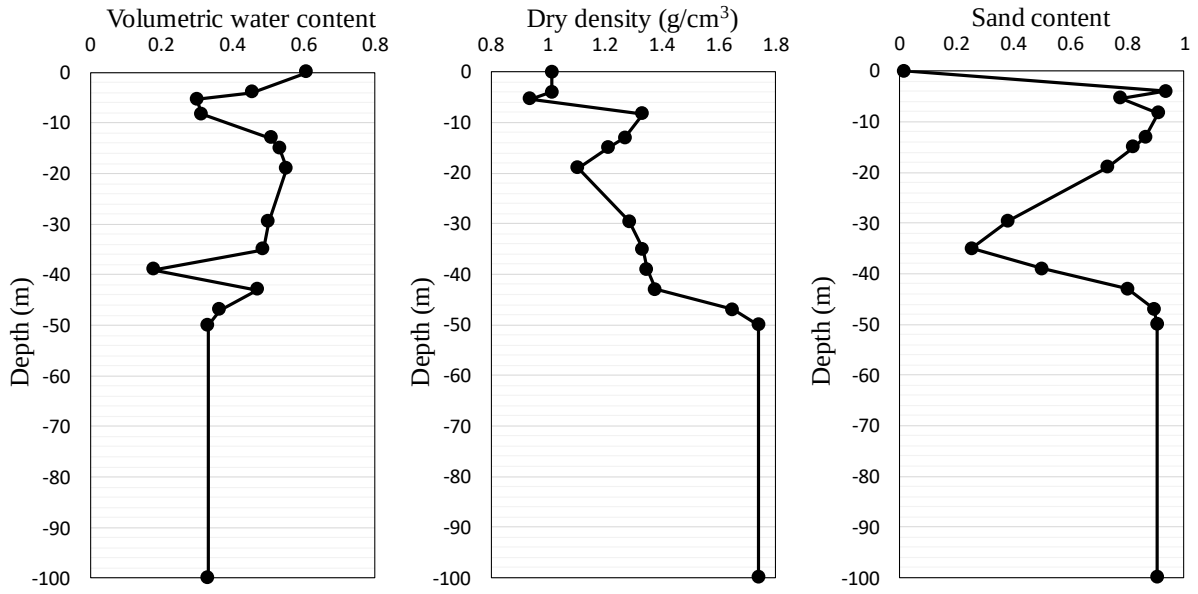

Figure III.10. Profiles for the volumetric water content, the soil dry density and the sand content used in the simulations (Brunetti et al., 2017)

The in-situ measurements (Saito et al., 2014a) and the simulation results were compared 20 h after the beginning of the TRT since it takes around 24 h for a TRT to eliminate initial disturbances (caused by voltage fluctuations and system adjusting) and reach a quasi-stable state (Zhou et al., 2017). Figure III.11 shows the comparison of the in-situ and predicted outlet temperatures by reporting the RMSE. A good correspondence between the predictions and the measurements authorized the utilization of the proposed numerical framework in the future simulations.

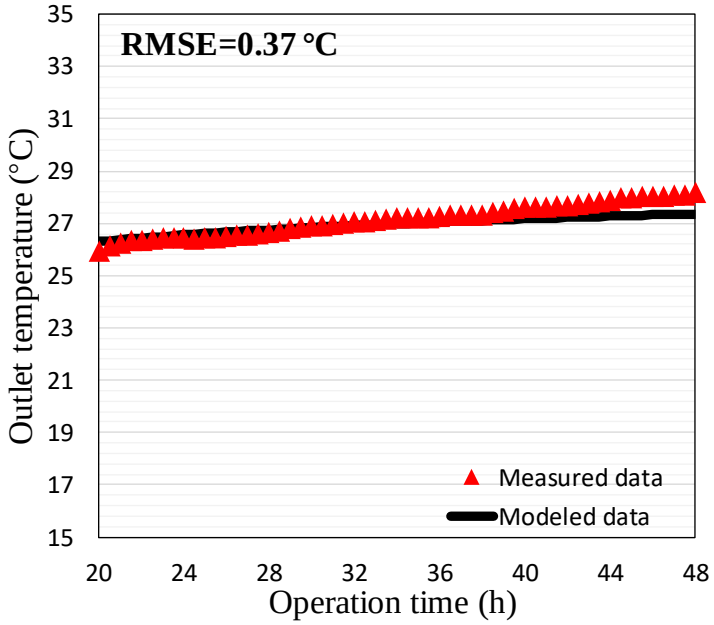

Figure III.11. Comparison between the measured and predicted outlet temperatures

III.4.2. Hydrothermal properties in the investigated field between September 2012 and September 2013

Figure III.12-a shows the fluctuation of suction profile over 1 year. The influenced depth is 1.5 m below surface. In the beginning, the ground surface has the greatest suction value (2.00 MPa), and after half a year, it has the lowest value (0.01 MPa). Figure III.12-b shows the fluctuation of volumetric water content with time, estimated by suction values and hydraulic parameters. The volumetric water content presents initially its smallest value (15.5%). After 6 months, it reaches its greatest value of 40.7%. Unlike the suction profile, the water content profile is not continuous along the depth, which is due to the different hydraulic characteristics of each layer. Figure III.12-c shows that the clay loam soil (layer 1) has a smaller thermal conductivity than the sandy loam (layer 2), revealing that soil thermal conductivity depends not only on water content but also on sand content and dry density. According to equations (3.10), soil volumetric heat capacity (Figure III.12-d) is largely dependent on water content and less dependent on dry density and sand content. Therefore, it increases proportionally with water content.

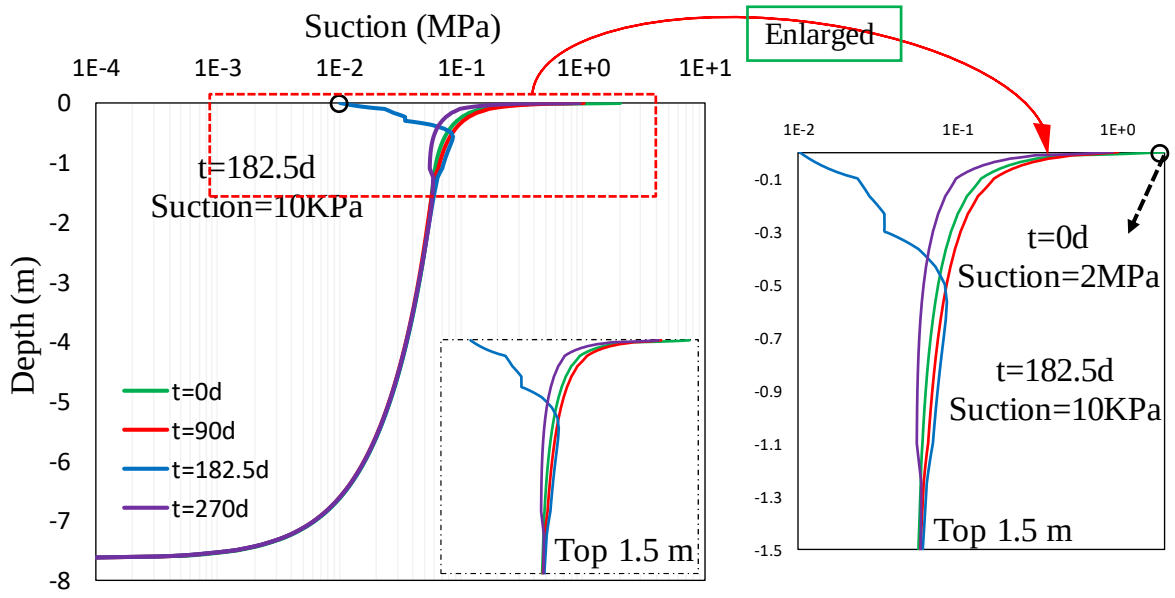
Suction (MPa)
1E-4
1E-3
1E-2
1E-1
1E+0
1E+1
Enlarged
Depth (m)
t=182.5d
Suction=10KPa
t=0d
t=90d
t=182.5d
t=270d
Top 1.5 m
t=0d
Suction=2MPa
t=182.5d
Suction=10KPa
Top 1.5 m

(a)

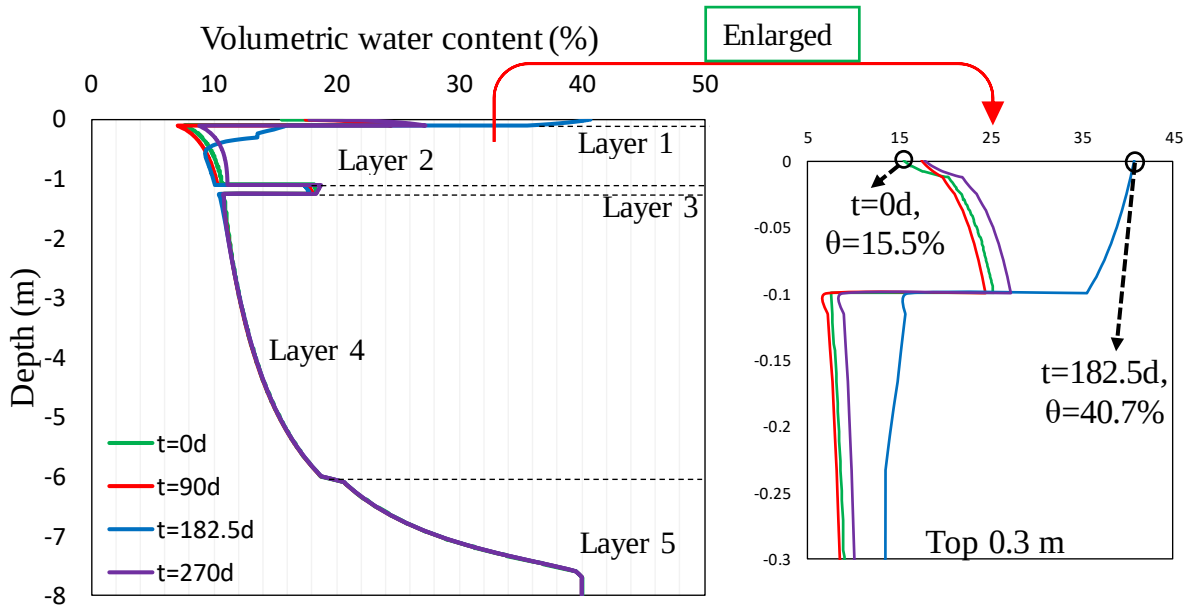
Volumetric water content (%)
Enlarged
Depth (m)
Layer 1
Layer 2
Layer 3
Layer 4
Layer 5
t=0d
t=90d
t=182.5d
t=270d
t=0d,
θ=15.5%
t=182.5d,
θ=40.7%
Top 0.3 m

(b)

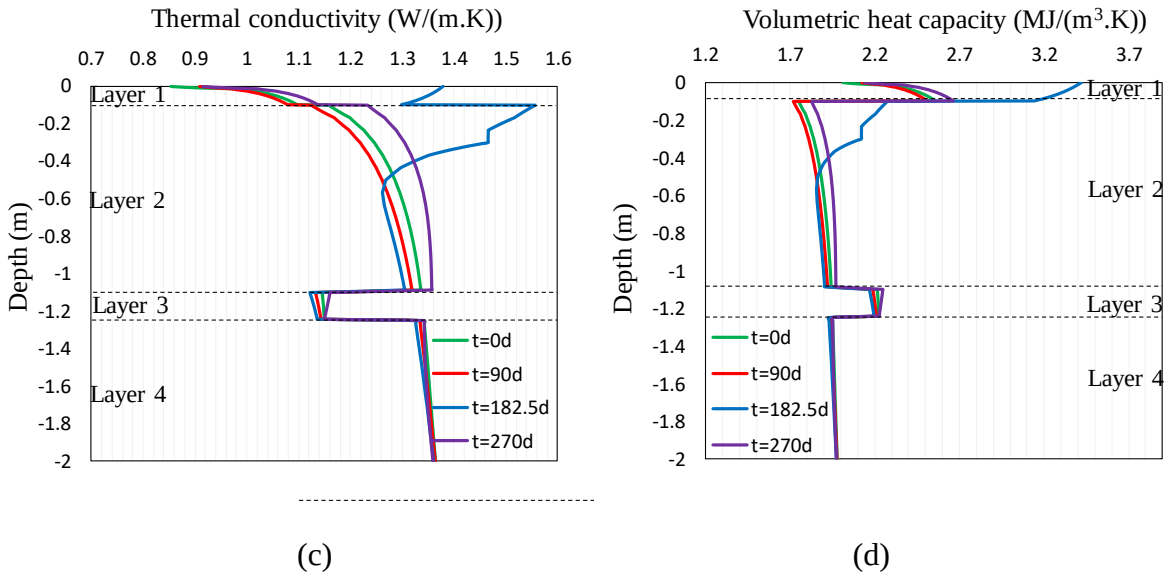

(c) (d)

Figure III.12. Hydrothermal properties of the investigated field with time and space: (a) suction; (b) volumetric water content; (c) soil thermal conductivity and (d) soil volumetric heat capacity

Figure III.13 shows the fluctuation of the volumetric water content at 7 different depths over 1 year. The first layer presents a larger range of variation, directly impacted by the suction variation on the ground surface. This variation of water content reduces with depth until it is eliminated at a depth of 1.5 m. Furthermore, the water content variation follows the same pattern for each layer and the time lag of the peak point increases with soil depth.

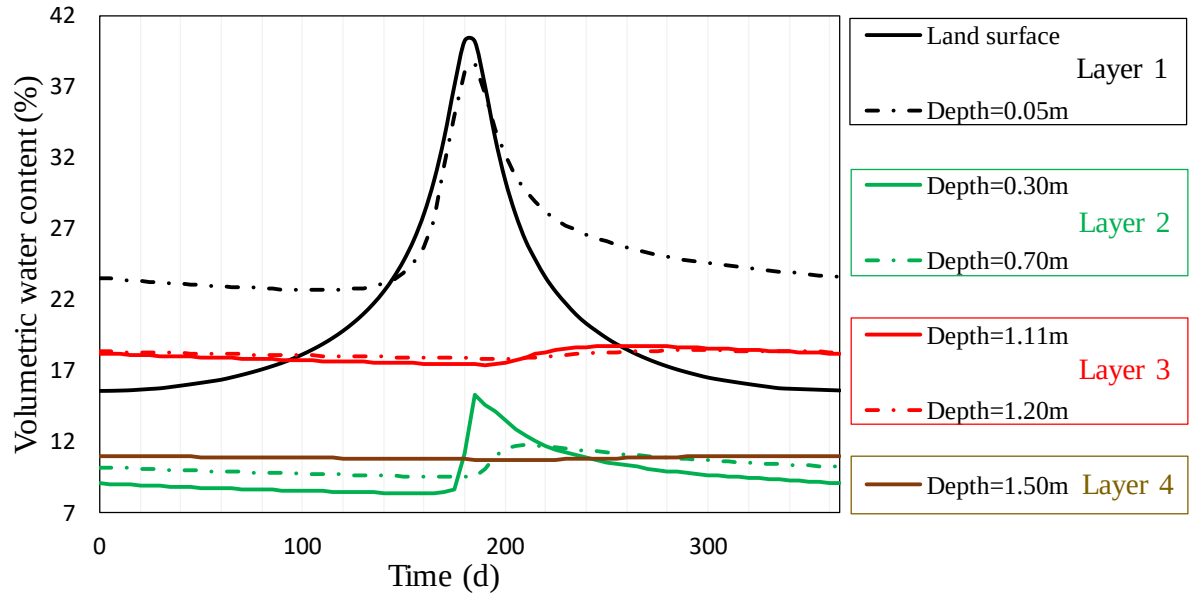

Figure III.13. Volumetric water content prediction for different depths over 1 year

III.4.3. Underground temperature with the impact of shallow BHE

As the developed numerical model predicted well the water content, the temperature profile at the local site, as well the in-situ TRT conducted in Japan, it was followingly used to predict the hydrothermal behavior of a shallow BHE installed in the same geotechnical, meteorological and hydraulic conditions. The starting operation time of shallow BHE was the 15th of July 2018.

Figure III.14 shows the underground temperature profile along the left wall of the shallow BHE at different times for two different scenarios. The first scenario is with constant inlet temperature and the second with variable seasonal heat load as illustrated in Figure III.6.

It can be observed in Figure III.14 that the installed shallow BHE influences the underground soil temperatures up to a depth of around 27 m in both scenarios, which is 7 m deeper than the depth of single U-pipe (20 m). After 100 days (the starting day of shallow BHE operation), an abrupt decrease of temperature occurs near the borehole. The temperature decreases particularly quick in the constant inlet temperature scenario (t = 101 d). When the shallow BHE is shut off, the subsurface temperatures near the left borehole wall increase in both scenarios. After 365 days, the underground temperature profile along the left borehole wall for both scenarios is almost the same (same energy deficit after 1 year), and the temperatures at shallow depths (< 1.5 m) have fully recovered after 365 days.

Despite the similarities, some differences exist. For the constant inlet temperature scenario, the temperatures in the vicinity of the shallow BHE decrease gradually until the shallow BHE is shut off (day 265). Further, subsurface soil in the vicinity of the borehole has almost the constant temperatures between 130 and 265 days. For the seasonal heat load scenario, there are more variations in the subsurface temperatures, which are due to the variable thermal load. The subsurface temperatures start to recover 9 days after the peak thermal load.

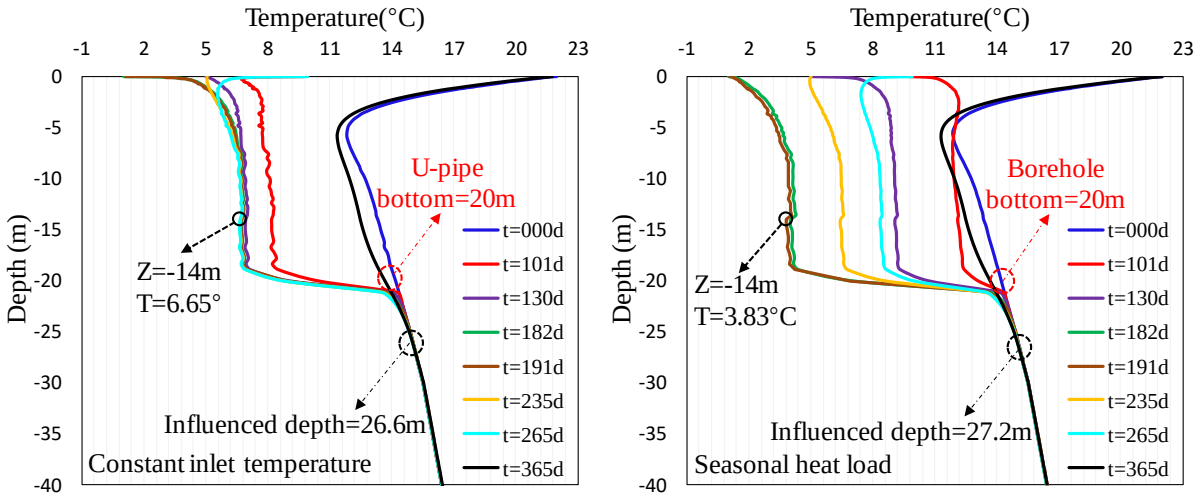

(a) (b)

Figure III.14. Temperature profile along the left borehole wall of shallow BHE at different times: (a) constant inlet temperature scenario and (b) seasonal heat load scenario

Figure III.15 illustrates the annual fluctuation of the underground temperatures at different depths. Figure III.15-a shows that the subsurface temperatures of the first scenario decrease drastically when the shallow BHE starts operating. Then, the subsurface temperatures remain almost stable (depth > 5 m). While Figure III.15-b shows that the subsurface temperatures of the second scenario decrease with time even 9 days after the peak heat load. After the appearance of the largest energy deficit (day 191), the subsurface temperature increases. The subsurface temperatures in both scenarios increase quickly as soon as the shallow BHE stops working. Further, while the subsurface temperatures increase after the shut-off of shallow BHE, the energy deficit is not able to be fully compensated especially for depths higher than 2.0 m.

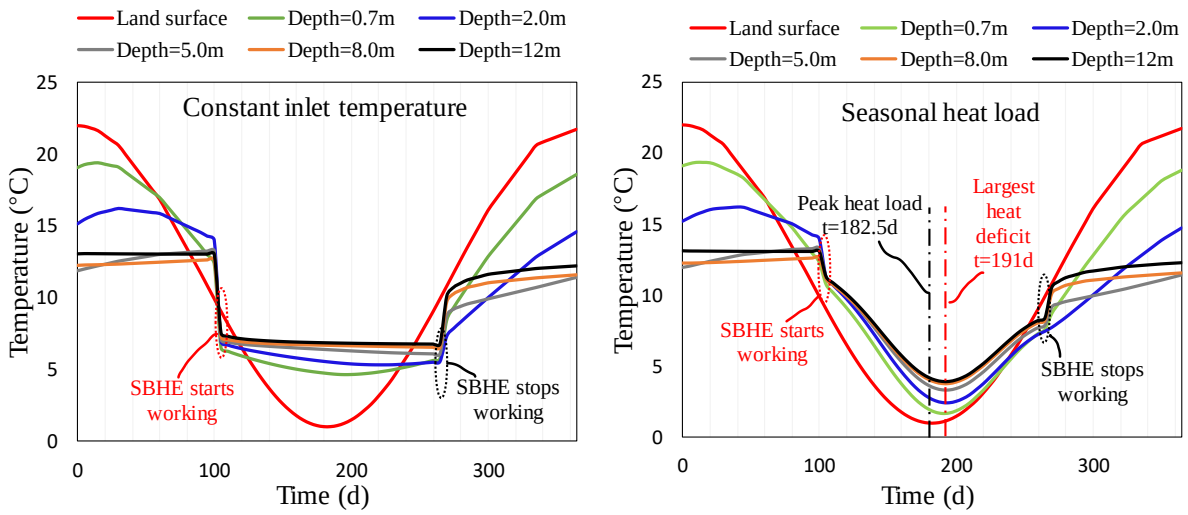

(a) (b)

Figure III.15. Temperature variations with time during one-year shallow BHE operation at different depths (in the vicinity of the left borehole): (a) constant inlet temperature and (b) seasonal heat load

III.4.4. Shallow BHE performance

Figure III.16 shows the carrying fluid temperatures along U-pipe up to a depth of 20 m at different time of a year for both scenarios. Figure III.16-a shows that the outlet temperatures decrease quickly for the period between 101 and 130 days. This decrease becomes less significant for the period between 130 and 235 days. Afterwards, the carrying fluid temperatures slightly increase with the increase of ground surface temperature for the period between 235 and 265 days. Figure III.16-b shows that the inlet temperatures for the seasonal heat load vary from 1.1 to 11.2 °C. The lowest inlet temperatures appear on day 191, 9 days after the peak heat load. Even though the heat load on days 101 and 265 is the same, the carrying fluid inlet and outlet temperatures of 101 days are larger than those of 265 days, which is due to the energy deficit generated during the heat extraction process. The same phenomenon happens for days 130 and 235.

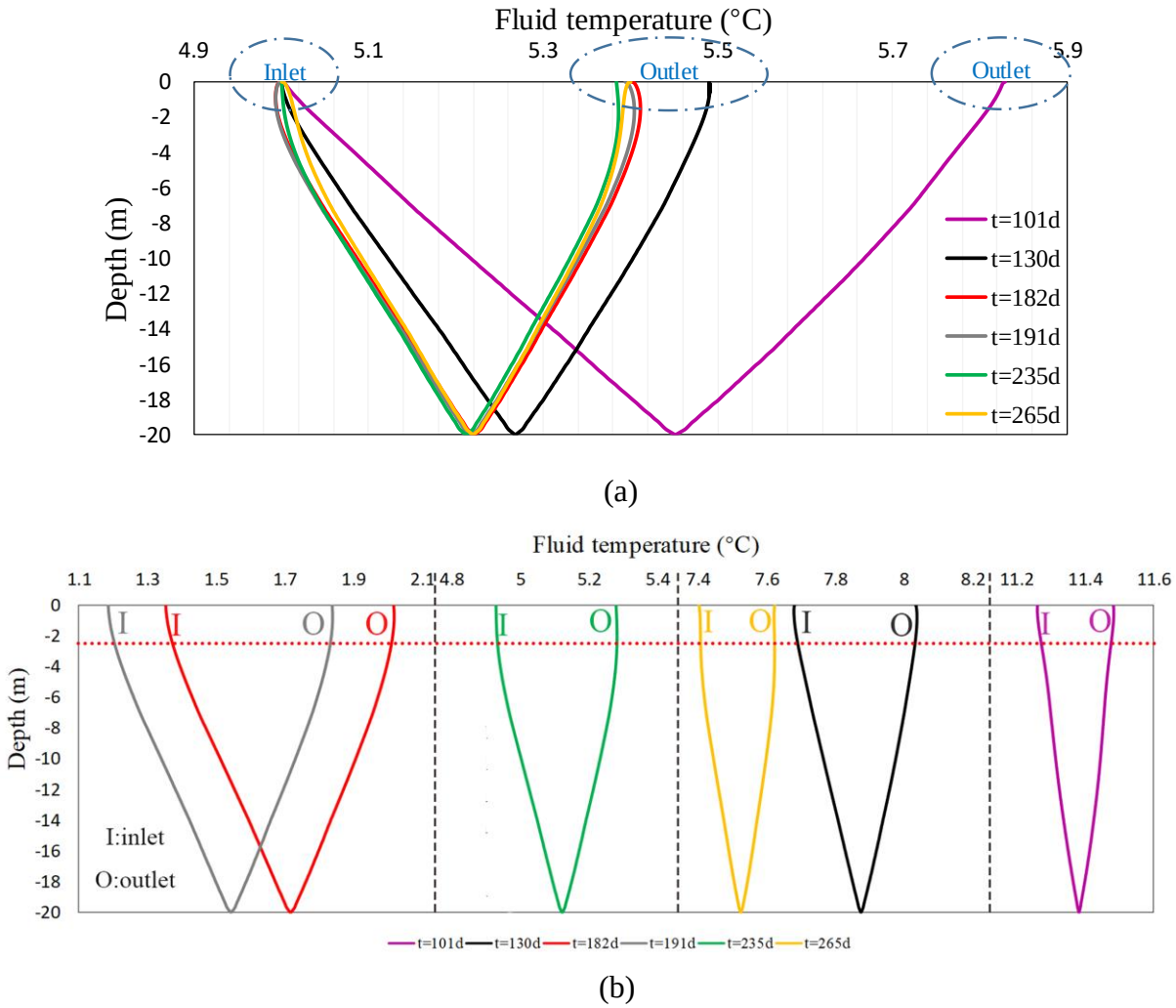

Figure III.16. Fluid inlet and outlet temperatures along U-pipe at different times: (a) constant inlet temperature and (b) seasonal heat load

Figure III.17 illustrates the variation of heat pump COP and TEE of the shallow BHE over 1 year for both scenarios. For TEE, both prescribed scenarios extract the same amount of energy over a year, indicating that the shallow BHE is able to exploit 17.63 W of energy per 1 meter. TEE for the constant inlet temperature scenario increases almost linearly during the working period of the shallow BHE, while it varies nonlinearly for the seasonal heat load scenario.

Heat pump COP for the constant inlet temperature scenario, remaining almost stable during the working days, ranges between 4.8 and 4.9. While COP for the seasonal heat load scenario, depending highly on its heat load, ranges between 4.3 and 5.7.

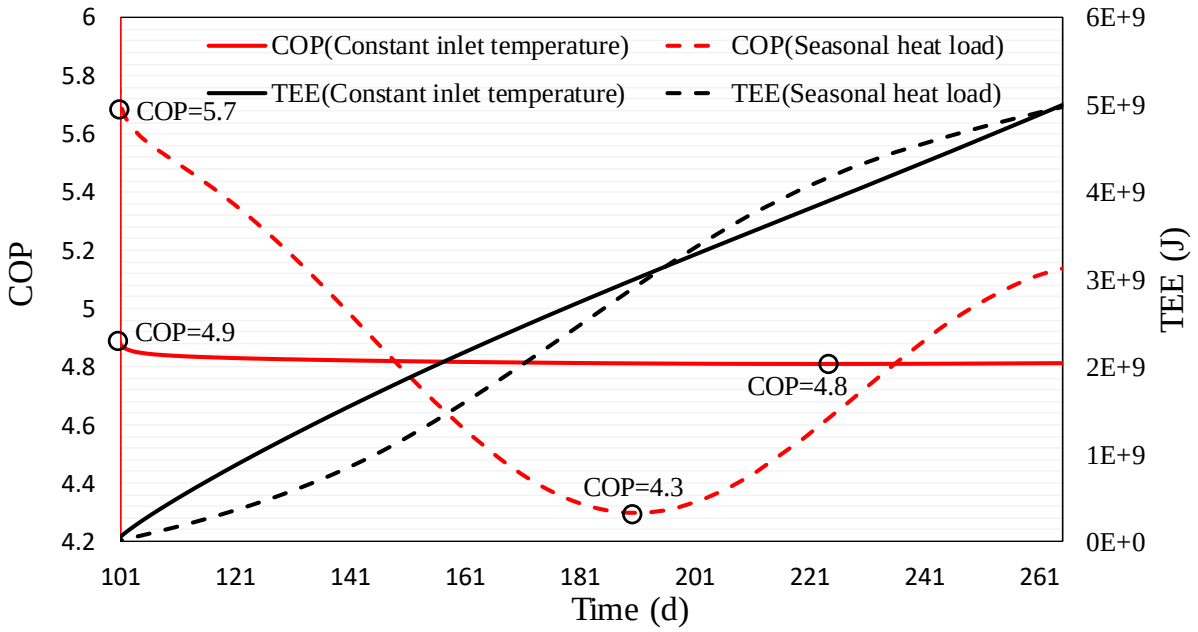

Figure III.17. Heat pump COP and TEE during the working period of shallow BHE for both prescribed scenarios

III.4.5. Estimation of the shallow BHE performance for a 5-year operation considering constant inlet temperature scenario

To assess the shallow BHE performance for a longer period, another numerical analysis considering a 5-year operation of the same shallow BHE was conducted for the constant inlet temperature scenario. In this numerical model, we maintained the meteorological and hydraulic conditions, as mentioned in equations (3.31) and (3.32). Hydrothermal conditions on the ground surface vary year by year and it is impossible to predict precisely the future ground surface hydrothermal conditions. Since the investigated zone has no sudden meteorological variations over the last years, therefore, 1-year meteorological data was used as a periodic data for our 5-year investigations. To eliminate the unexpected effect of boundary conditions for the five years, we enlarged the side length of the geometry from 30 m to 80 m.

Figure III.18 shows the extracted energy by year, while the largest energy deviation exists between the first and the second year (5.44%). From the third year, the difference becomes less significant. In our case, a period of 4 years is necessary to reach this equilibrium stage.

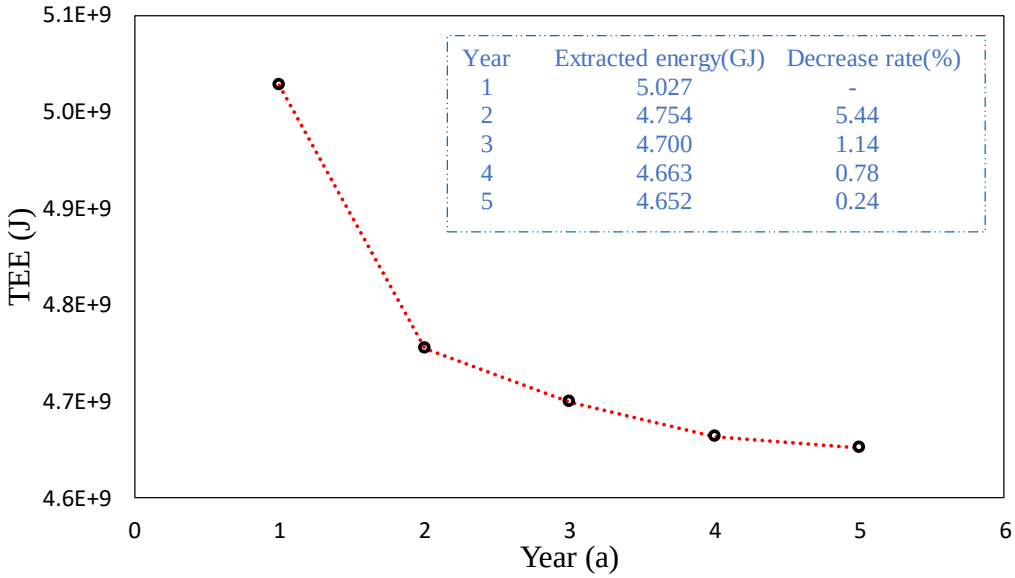

Figure III.18. Extracted energy by year for a 5-year period

As it has been stated, the high underground temperature gradient provides a favorable environment for the application of shallow BHE in the Alsace region. The heat extraction rate (17.63 $W.m^{-1}$) can be further improved by decreasing the inlet temperature, adding an additional pipe in the borehole, changing inlet velocity, using thermally enhanced grout, etc. For instance, a simple decrease of the inlet temperature from 5 °C (original value in this case) to 1 °C would increase 55.03% of the extraction rate from 17.63 $W.m^{-1}$ to 27.34 $W.m^{-1}$.

The stabilization of the TEE after several cooling and heating cycles is also an important element for the evaluation of shallow BHE performance. A period of 4 years is necessary to reach this equilibrium stage at the investigation site. After this period, the underground medium is able to output a stable energy for various uses.

III.5. Summary

This study presents the numerical modeling considering the seasonal hydrothermal fluctuation to investigate the shallow BHE performance installed in the Alsace region, France. The capacity of the model was first validated by using the in-situ measurements of the investigated field between September 2012 and September 2013 and a TRT in Japan. Then, the model was used to study the heat pump COP and the TEE over a year under two different scenarios: constant inlet temperature and seasonal heat load. It was fond that soil temperature in the vicinity of the shallow BHE is closely related to the imposed heat load. Heat pump COP for the constant inlet temperature scenario remains almost stable during the working period of the

shallow BHE, while for the seasonal heat load scenario, heat pump COP decreases gradually till the appearance of the largest energy deficit, which is 9 days after the peak heat load. Besides, TEE in the scenario of the constant inlet temperature increases almost linearly with time during the working period of the shallow BHE, while it varies nonlinearly for the seasonal heat load scenario.

Further, the performance of the shallow BHE considering constant inlet temperature over a 5-year period was analyzed. The results show that the largest difference of the extracted energy (5.44%) happens during the first two years, and the shallow BHE is capable of providing stable energy for various uses after the 4^{th} year.

The performance of the shallow BHE installed in the Alsace region has been estimated. However, some limitations still exist in the current numerical modeling to be applied to the other case studies. For example, seasonal hydrothermal conditions vary year by year, and meteorological data for several years might be necessary to judge the long-term shallow BHE performance in the other regions. Further, we use equilibrium method to get the initial temperature and suction profile of the investigated zone. Although the method is capable of predicting temperature variation, further experimental investigations are necessary to validate our proposed approach. In our studied zone, we encounter no underground water. Nevertheless, underground water can have a significant impact on the performance of a shallow BHE if Péclet number is large enough (Angelotti et al., 2014; Molina-Giraldo et al., 2011).

IV. FACTORS INFLUENCING THE PERFORMANCE OF SHALLOW BHE

IV.1. Introduction

The main contribution of the current investigation is to study the factors influencing the performance of BHE installed in different soils with their saturated and unsaturated profiles. The average annual heat pump COP is used to estimate the BHE performance due to its long-term evaluations. These findings provide a robust practical reference for the engineers working on the optimization of the BHE performance. This study can also offer some technical supports for the other shallow geothermal systems such as energy piles.

In this chapter, the factors affecting the performance of a BHE with a U-pipe length of 20 m are investigated, sensitive to seasonal hydrothermal variations due to its shallow depth. A 3D finite element numerical simulation model was used to estimate the yearly average heat pump COP of two typical reference models: the first one was installed in sand and the other in clay. Eventually, the variations of the yearly average heat pump COP were investigated for the shallow BHE installed in both soils under the influence of 15 factors, such as meteorological condition, hydraulic condition, multi-pipe solution, etc.

IV.2. Governing equations of the numerical framework

The same numerical framework has been used in the last chapter. The principal equations of this framework are summarized in Table IV.1.

Table IV.1. Principle equations of the numerical framework

Physics	Governing equation

$$\rho_w \cdot \psi \cdot \frac{\partial h_{head}}{\partial t} + \cdot \rho_w \cdot \nabla \cdot \left[-K \cdot k_r \cdot \nabla \cdot h_{head} \right] = Q_{w\_source} \tag{4.1}$$

$$S_e = \begin{cases} \dfrac{1}{\left[1 + \left|\alpha H_p\right|^n\right]^{1-1/n}} & H_p < 0 \\ 1 & H_p \geq 0 \end{cases} \tag{4.2}$$

Hydrothermal fluctuation in soil

$$\theta = S_e \cdot (\theta_{sat} - \theta_{res}) + \theta_{res} \tag{4.3}$$

$$S_r = \theta / \theta_{sat} \tag{4.4}$$

$$k_s = (0.443 x_s + 0.081 \gamma_d) \frac{(4.4 x_s + 0.4) S_r}{1 + (4.4 x_s - 0.6) S_r} + 0.087 x_s + 0.019 \gamma_d \tag{4.5}$$

$$C_{v-s} = (4.18 - 0.095 \gamma_d - 0.3 x_s) S_r + 0.09 \gamma_d - 0.2 x_s \tag{4.6}$$

Energy balance in soil

$$\frac{\partial (\rho_s C_{p-s} T_s)}{\partial t} = \nabla \cdot (k_s \nabla T_s) + Q_s \tag{4.7}$$

Energy balance in pipe

$$A \rho_f C_{p-f} \frac{\partial T_f}{\partial t} + A \rho_f C_{p-f} u_f \cdot \nabla T_f = \nabla \cdot A k_f \nabla T_f + f_D \frac{\rho_f A}{2 d_h} \left| u_f \right| u_f^2 + Q_{wall} \tag{4.8}$$

IV.3. Numerical simulation of the reference models

For distinguishing the influence of different factors on the performance of a shallow BHE installed in different geotechnical conditions, sand and clay were chosen for the reference models.

IV.3.1. Geometry and mesh

The numerical model was a 3D model with a side length of 30 m and a depth of 100 m (Figure IV.1). The height was constituted of two parts: 30 m of unsaturated soil on the top and 70 m of claystone (bedrock) on the bottom. The grout surrounding the single U-pipe was 25 m while the U-pipe depth was 20 m. The borehole diameter was 0.14 m. Inside the borehole, the U-pipe was symmetrically positioned and the shank spacing was 0.05 m. The inner and outer diameters of U-pipe were respectively 2.2 and 2.5 cm.

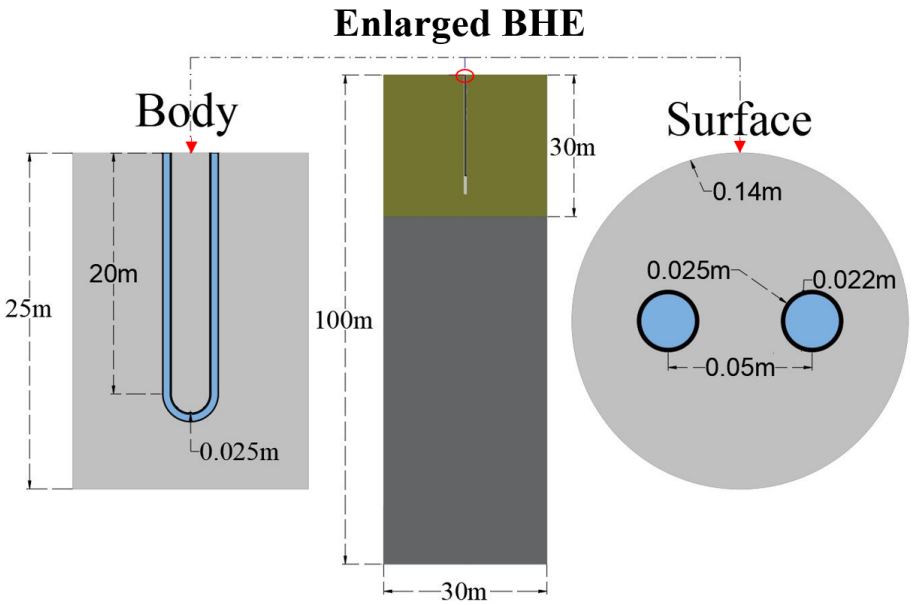

Figure IV.1. Schematic geometry of the BHE with its enlarged surface and body

The mesh used in the finite element simulations is presented in Figure IV.2. A swept mesh was selected to achieve a reasonable computation speed. Due to great hydrothermal fluctuations close to the surface, the mesh at shallow depths was denser than that of large depths.

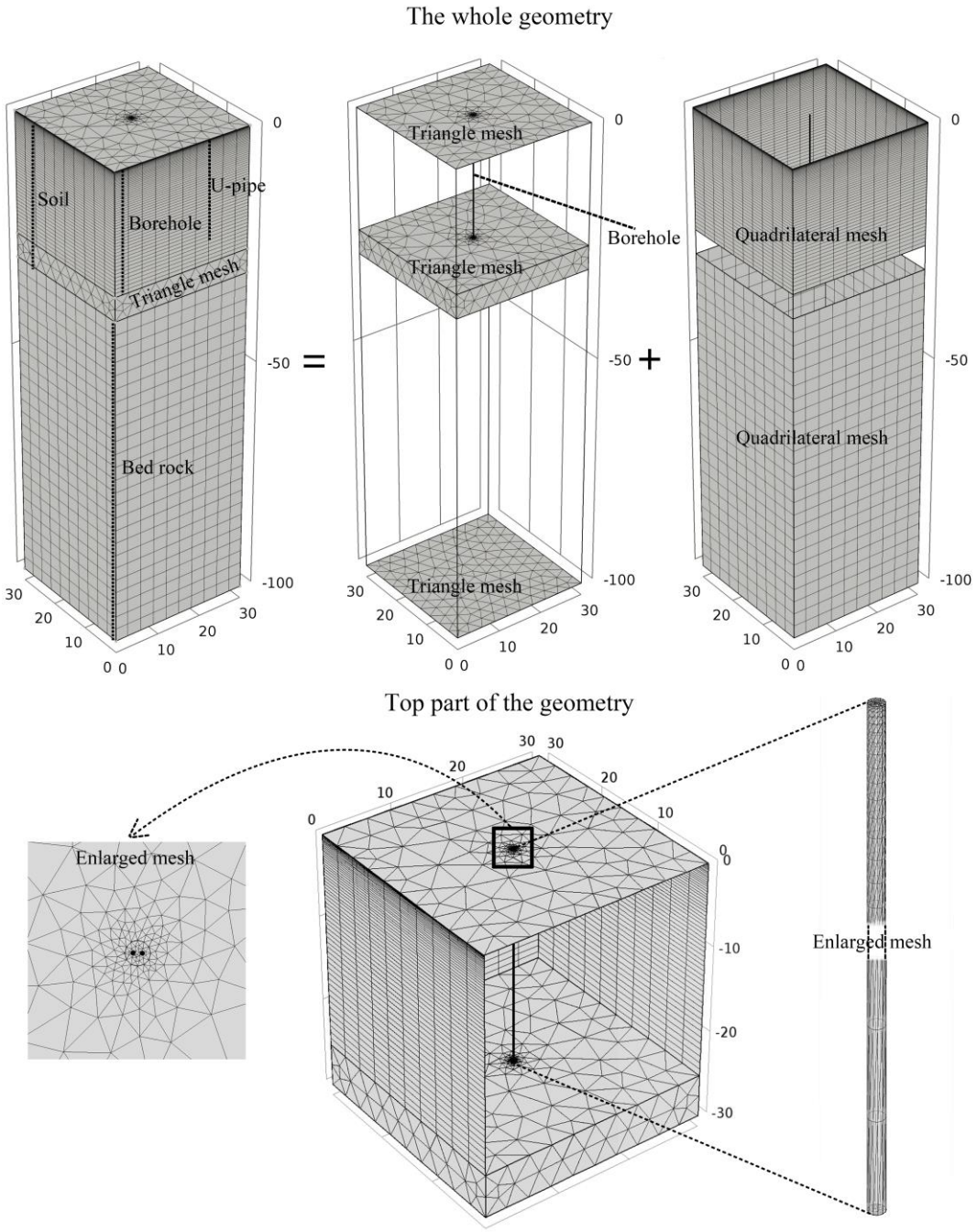

Figure IV.2. Generated mesh for the numerical simulations

IV.3.2. Two typical soils and sedimentary rock

Table IV.2 summarizes the main hydraulic properties (K (m.s^{-1}), l, α (m^{-1}), n, θ_s, θ_r), the sand content x_s, the soil specific unit weights γ_s (kN.m^{-3}) and the soil dry unit weights γ_d (kN.m^{-3}) of the soils surrounding the BHE (Guber and Pachepsky, 2010; Pachepsky and Park, 2015). For the sedimentary rock, the unit weight, the thermal conductivity and the specific heat capacity

were respectively 22.54 kN.m^{-3}, 2.6 W.m^{-1}.K^{-1} and 0.9 kJ.kg^{-1}.K^{-1}. The thermal conductivity of grout was 2.5 W.m^{-1}.K^{-1} and its volumetric heat capacity was 2 MJ.m^{-3}.K^{-1}.

Table IV.2. Hydrothermal properties of the studied soil

Material	γ_d *(kN.m^{-3})*	x_s *(-)*	*K (m.s^{-1})*	*L (-)*	α *(m^{-1})*	*n (-)*	θ_{sat} *(-)*	θ_{res} *(-)*	γ_s *(kN.m^{-3})*
Sand	16.1	0.9	1.03E-4	0.5	4.30	1.520	0.366	0.025	25.4
Clay	14.2	0.2	1.44E-6	0.5	1.98	1.086	0.481	0.010	27.4

IV.3.3. Initial hydrothermal conditions and operational mode

Seasonal suction and temperature conditions were imposed on the ground surface (Dirichlet boundary) for a period of 365 days (1 year). The ground surface hydrothermal conditions were applied by using the following equations respectively for the suction and temperature:

$$F_{surface} = -0.995 \cdot \cos\left(\frac{\pi}{182.5} \cdot t\right) - 1.005 \text{ (MPa)} \quad (4.9)$$

$$T_{surface} = 12.5 \cdot \cos\left(\frac{\pi}{182.5} \cdot t\right) + 12.5 \text{ (°C)} \quad (4.10)$$

where *t* represents time (d). The temperature reached its minimum value after 6 months in winter with a suction of 0.01 MPa, representing the saturated state of soil.

No water and heat flow (out or in) were imposed on the side boundaries. The temperature gradient on the bottom boundary was taken equal to 0 °C.m^{-1}. The water level was considered at the depth of 8.45 m. Instead of using the traditional analytical solutions (Baggs, 1983), an equilibrium approach was conducted to establish the initial hydrothermal profiles of the field. An equilibrium stage reached with a negligible difference in the suction or temperature profiles during the most recent years. Figure IV.3 shows the initial suction as well as the temperature profiles used in the reference models.

Heating scenario was considered in the simulations. Ethanol (24%) (Casasso and Sethi, 2014) was used as the carrying fluid, with a velocity of 0.5 m.s^{-1}. The pipe thermal conductivity was 0.5 W.m^{-1}.K^{-1}.

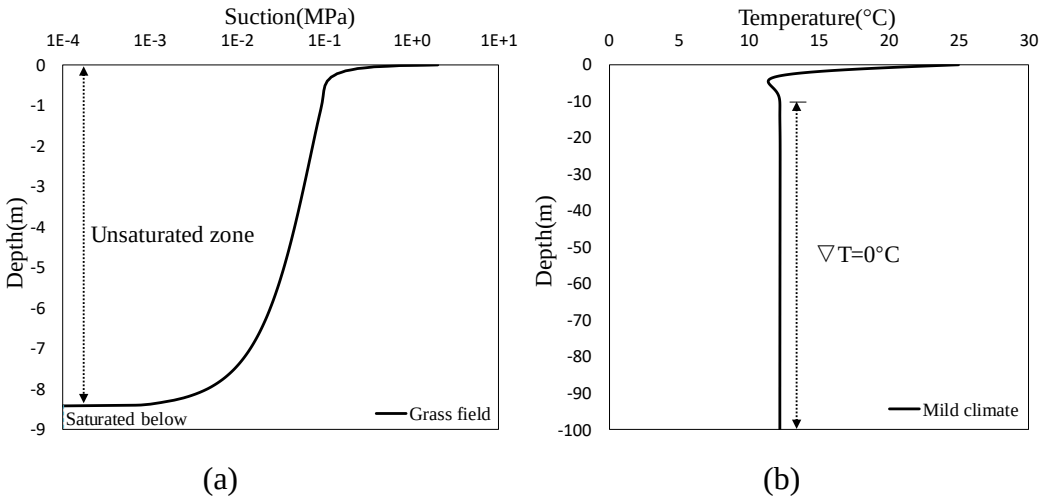

Figure IV.3. Initial hydrothermal profiles: (a) suction (MPa) and (b) temperature (°C)

When the ground surface temperatures were lower than 10 °C, the BHE would start working. On the contrary, it would stop working (Figure IV.4) for the temperatures higher than 10°C. During the operation period, a seasonal heat load varying between 10 and 46 W.m^{-1} was considered in the reference models (Figure IV.4). The seasonal heat extraction rate was kept constant in the different studied scenarios.

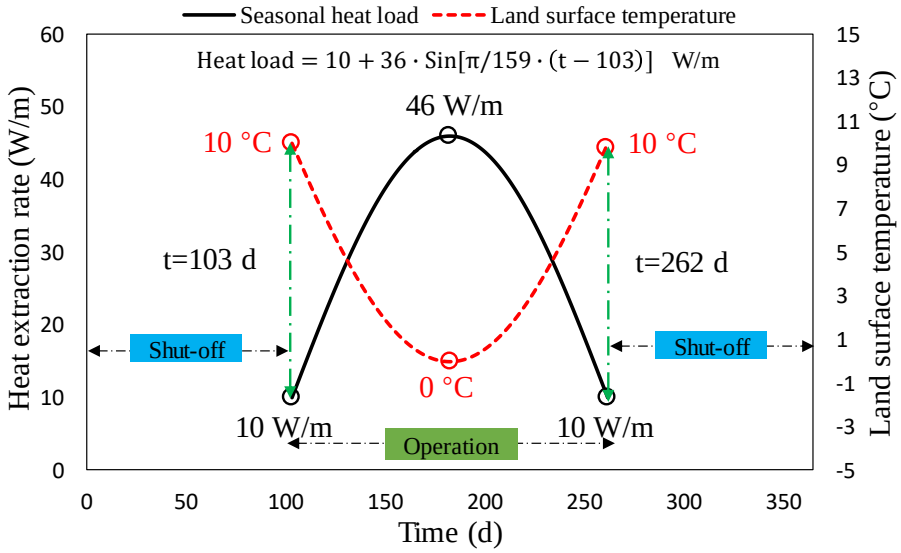

Figure IV.4. Seasonal heat load during the service period of the BHE

IV.3.4. Simulation results for the reference models

Figure IV.5 shows the variation of thermal conductivity with depth in sand and clay after 90 and 182.5 days. After 90 days, clay shows a higher thermal conductivity for depths less than 2

m while an opposite trend is observed for depths higher than 2 m. After 182.5 days, sand has a greater thermal conductivity than clay except for depths between 1 and 2 m.

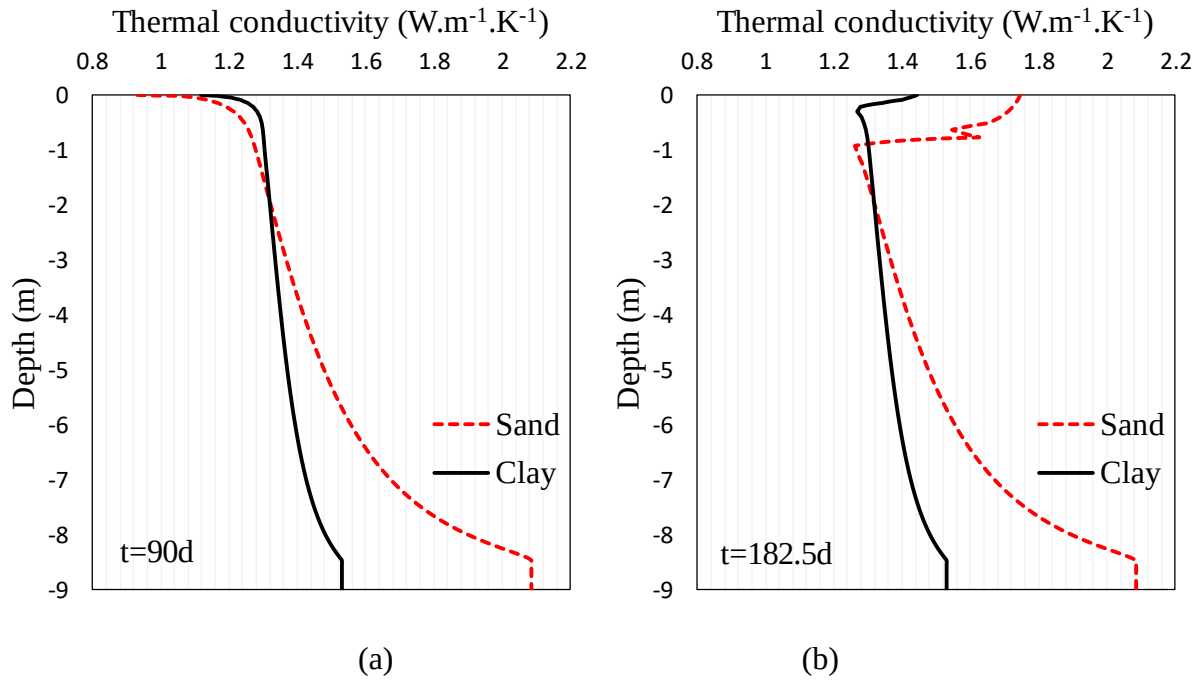

Figure IV.5. Thermal conductivity variation with depth for sand and clay after (a) 90 days and (b) 182.5 days

Figure IV.6 shows the variation of the subsurface temperature profiles with time along the left borehole wall of the BHE installed in sand and clay. After 104 days (Figure IV.6-a), clay has a higher left borehole wall temperature than sand (especially in its unsaturated zone) due to the lower thermal load in the shallow depths. When heat extraction process goes on (Figure IV.6-b & c), the left borehole wall temperature of the BHE installed in the sand is higher than in clay due to its higher thermal conductivity. The maximum temperature difference of left borehole wall between sand and clay reaches 2.5 °C after 6 months (182.5 days) for the depths ranging between 7.7 and 19 m.

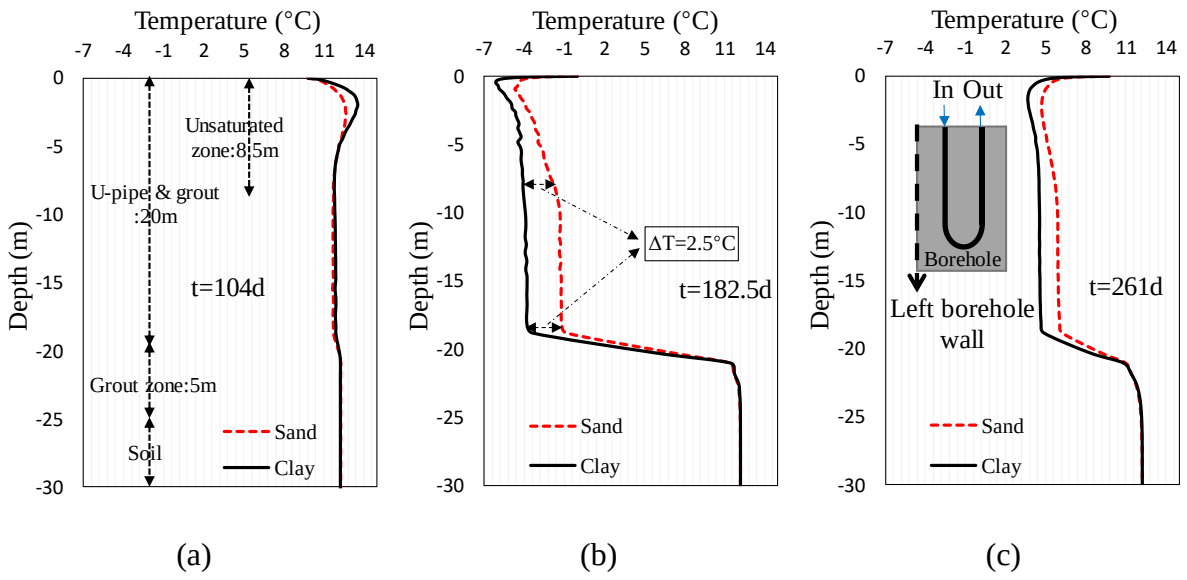

Figure IV.6. Subsurface temperature profiles along the left borehole wall of the BHE installed in sand and clay: (a) 104 days; (b) 182.5 days and (c) 261 days

Figure IV.7 shows the temperature of the carrying fluid at different times for the BHE installed in sand and clay, which follows consistently the subsurface temperature (Figure IV.6).

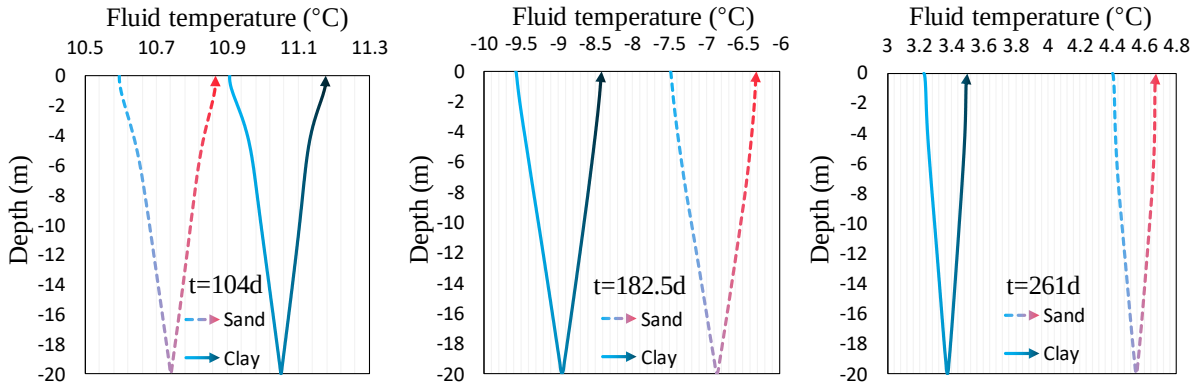

Figure IV.7. Carrying fluid temperature variations for the BHE installed in sand and clay: (a) 104 days; (b) 182.5 days and (c) 261 days

Figure IV.8 presents the heat extraction rate and the heat pump COP for the BHE installed in sand and clay. The heat pump COP decreases even 9 days after the peak heat load. Afterwards, the heat pump COP starts to increase until the BHE is shut off. Further, the yearly average heat pump COP installed in sand (3.55) is 8.6% higher than in clay (3.27) because of its higher thermal conductivity.

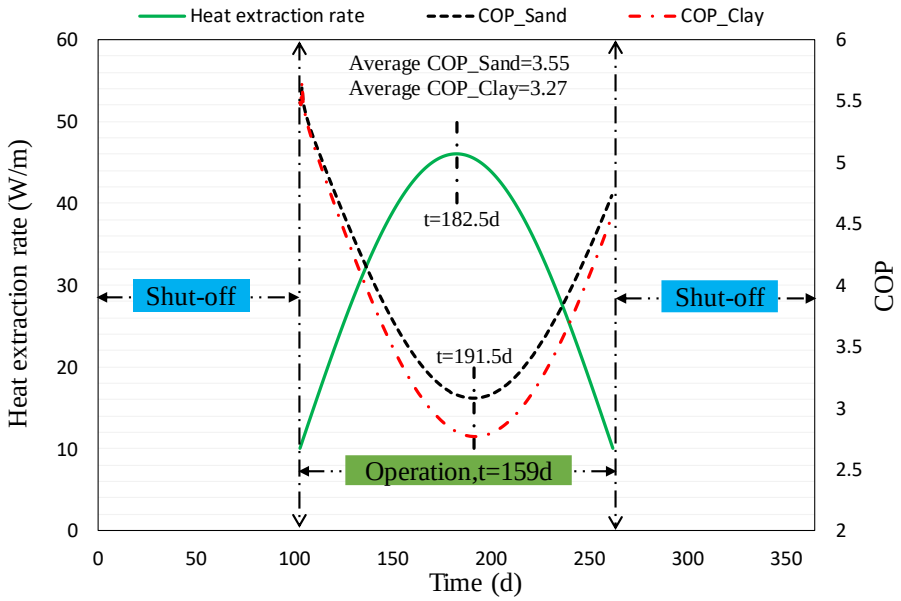

Figure IV.8. Heat extraction rate and COP for the BHE installed in sand and clay during its operation period over one year

IV.4. Factors influencing the shallow BHE performance

For the aforementioned soils, we studied 15 factors affecting the performance of the shallow BHE installed in sand and clay. The factors contained environmental aspects (meteorological condition, hydraulic condition, groundwater flow), grout properties (grout thermal conductivity, grout volumetric heat capacity, grout diameter), U-pipe properties (shank spacing, multi-pipe solution, pipe inner diameter, pipe thickness, pipe thermal conductivity), carrying fluid properties (carrying fluid material, carrying fluid velocity), and heat load scenarios (heat load mode, heat load level). A sensitive analysis of each parameter was carried out by maintaining constant the other parameters of the reference models.

IV.4.1. Investigated factors

Fifteen investigated factors were followingly detailed.

a) Meteorological condition

Three typical meteorological conditions concerning the fluctuation of ground surface temperature with time are presented in Table IV.3. Zero temperature gradient (∇T = 0 °C.m^{-1}) at high depths was employed for the three conditions. It should be noted that the temperature is has negligible fluctuation with time if the depth reaches 10 m beneath ground surface, and this temperature is close to the annual ground surface temperature if the temperature gradient

is kept 0 °C m^{-1}. It can be looked as that the meteorological condition reflects the average temperature surrounding the BHE.

Table IV.3. Three meteorological conditions used in the study

Meteorological condition	*Expression*
Cold climate	$T_{surface} = 12.5 \cdot \cos(\pi \cdot t / 182.5) + 7.5(°C)$ (4.11)
Mild climate	$T_{surface} = 12.5 \cdot \cos(\pi \cdot t / 182.5) + 12.5(°C)$ (4.12)
Warm climate	$T_{surface} = 12.5 \cdot \cos(\pi \cdot t / 182.5) + 17.5(°C)$ (4.13)

Figure IV.9-a shows the ground surface temperature of each meteorological condition. To compare the heating capacity of the BHE installed in these meteorological conditions, the same heat load was supposed. Therefore, the BHE started working automatically when the ground surface temperature decreased to 5, 10 and 15 °C respectively for the cold, mild and warm climates. The initial temperature profile of each meteorological condition was also obtained by using the same aforementioned equilibrium method (Figure IV.9-b).

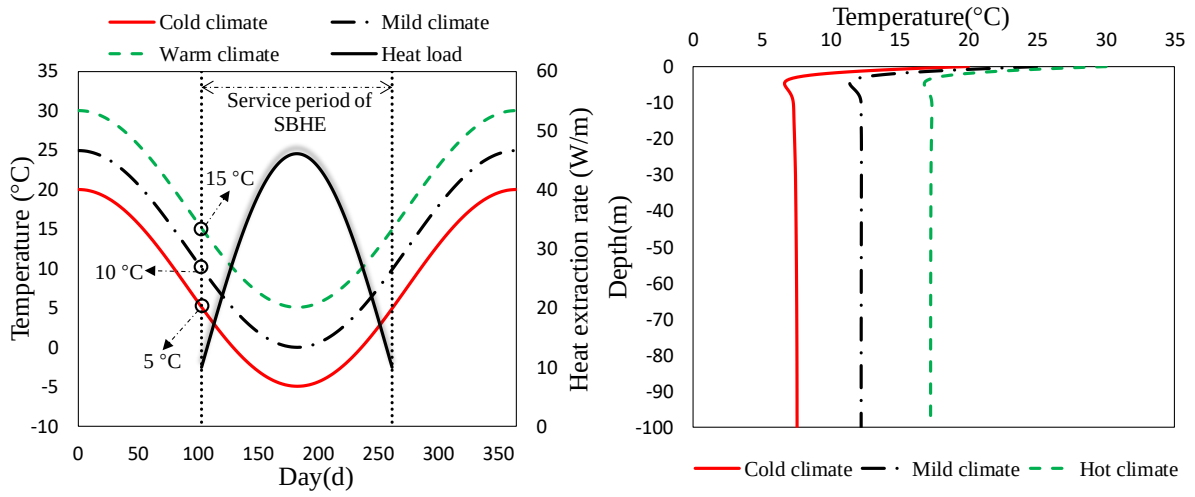

(a) (b)

Figure IV.9. (a) Boundary conditions on the soil surface (periodic temperature) and (b) initial temperature profiles

b) Hydraulic condition

Various vegetations of a field lead to different suction (negative water pressure), water content and soil thermal conductivity profiles. Three typical suction conditions (open, grass

and forest fields) were used in this study (Table IV.4). Figure IV.10-a shows the variation of seasonal hydraulic solicitations on the soil surface with time for these hydraulic conditions. By employing the same equilibrium method, the initial suction profiles of the different fields are also shown in Figure IV.10-b. The water levels were positioned at 4, 8.45 and 11.5 m respectively for the open, grass and forest fields.

Table IV.4. Three suction conditions imposed on the top boundary

Hydraulic condition	*Expression*
Open field	$F_{surface} = -0.245 \cdot \cos(\pi \cdot t/182.5) - 0.255$ (MPa) (4.14)
Grass field	$F_{surface} = -0.995 \cdot \cos(\pi \cdot t/182.5) - 1.005$ (MPa) (4.15)
Forest field	$F_{surface} = -4.995 \cdot \cos(\pi \cdot t/182.5) - 5.005$ (MPa) (4.16)

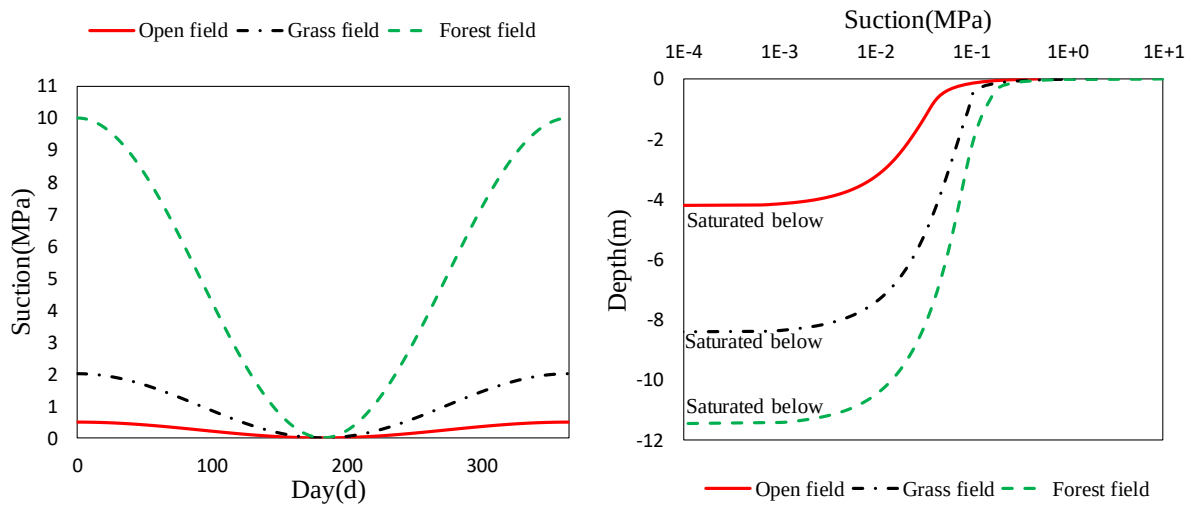

(a) (b)

Figure IV.10. (a) Boundary conditions on the ground surface and (b) initial suction profiles

c) Groundwater flow

To investigate the groundwater influence, a steady-state and uniform horizontal groundwater flow regime was then applied to a layer located between 15 and 20 m below the ground surface. Due to the restriction of the pressures in a shallow borehole (limited pressure/water head gradient) and the low hydraulic conductivity of clay, low groundwater velocities (0, 1E-7, 2E-7, 3E-7 $m.s^{-1}$) were mainly considered in the simulations.

d) Grout thermal conductivity

Grout can improve the heat transfer from the surrounding media to the pipe and protect the pipe from potential external forces. Different grout thermal conductivities of 0.8, 1.4, 2, 2.5 and 3.2 $W.m^{-1}.K^{-1}$ were investigated in this part.

e) Grout volumetric heat capacity

The grout volumetric heat capacity is another potential factor influencing the BHE performance. Grouts with the volumetric heat capacities of 1.2, 1.6, 2.0, 2.4 and 3.5 $MJ.m^{-3}.K^{-1}$ were explored in this study.

f) Grout diameter

In general, the grout diameter of a BHE ranges between 0.10 and 0.22 m (Luo et al., 2016) and it has some positive influences on the performance of BHE due to its high heat conduction capacity. Four grout diameters were tested in this study: 0.10, 0.14, 018 and 0.22 m.

g) Shank spacing

Shank spacing is the distance between the center of the pipes (Beier, 2014). The BHE performance decreases with the reduction of shank spacing and the phenomenon is conventionally called short-circuiting. In this part, the shank spacings of 0.03, 0.04, 0.05, 0.06, 0.09 and 0.11 m were tested.

h) Multi-pipe solution

For a better performance, some extra pipes are used in a borehole. Figure IV.11 shows the 4 layouts of multi-pipe solutions used in this part.

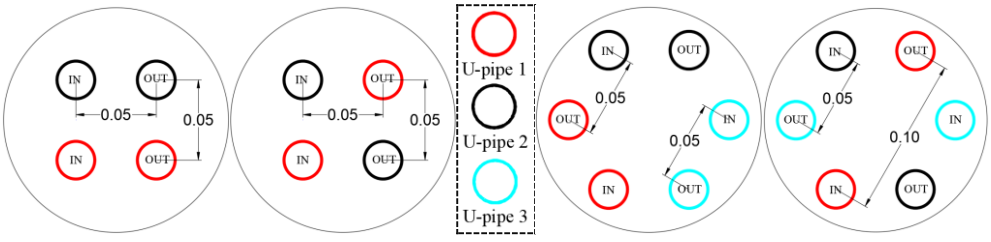

(a) (b) (c) (d)

Figure IV.11. Multi-pipe solutions in BHE (m): (a) double parallel; (b) double cross; (c) triple parallel and (d) triple cross

i) Pipe inner diameter

Four typical inner diameters of 0.018, 0.022, 0.026 and 0.030 m were investigated in the numerical simulations with a constant flow rate of 11.4 $L.min^{-1}$. Therefore, the corresponding flow velocities were respectively 0.747, 0.500, 0.358 and 0.269 $m.s^{-1}$ for these inner diameters.

j) Pipe thickness

The U-pipe thickness ensures a safe circulation of the carrying fluid. Different pipe thicknesses of 0.001, 0.0015, 0.0020 and 0.0025 m were studied in the numerical simulations.

k) Pipe thermal conductivity

The thermal conductivity of U-pipe depends highly on the U-pipe material such as Polyvinyl Chloride (PVC), HDPE and steel (Cao et al., 2017). Different U-pipe thermal conductivities of 0.25, 0.5, 2, 6, 11 and 16 ($W.m^{-1}.K^{-1}$) were tested in this part.

l) Carrying fluid material

Four anti-freeze carrying fluids (Casasso and Sethi, 2014) were used in the U-pipe, listed in Table IV.5. Water was not employed in this work due to negative carrying fluid temperatures in the U-pipe.

Table IV.5. Physical properties of the carrying fluids (Casasso and Sethi, 2014)

Carrying fluid	$T_{freezing}$ *(°C)*	*Cp* ($J.kg^{-1}.K^{-1}$)	*k* ($W.m^{-1}.K^{-1}$)	*ρ* ($kg.m^{-3}$)	*μ (mPa.s)*
Propylene Glycol (PG) 25%	-10	3974	0.450	1026	5.50
Propylene Glycol (PG) 33%	-15	3899	0.416	1015	8.17
Ethanol 24%	-15	4288	0.426	972	5.85
Calcium chloride ($CaCl_2$) 20%	-20	3030	0.540	1186	4.00

m) Carrying fluid velocity

The carrying fluid velocity influences the heat interaction rate between the pipe and the carrying fluid. Eight velocities were tested in this part: 0.1, 0.2, 0.3, 0.4, 0.5, 0.6, 0.7 and 0.8 $m.s^{-1}$. To reach the same heat extraction rate, the inlet and outlet temperatures were correspondingly altered in each case.

n) Heat load mode

In the reference models, the seasonal heat load was considered to evaluate the heat pump performance. Moreover, a steady heat load scenario was taken into account, indicating a constant heat extraction rate during the BHE service period while it provided the same TEE of the seasonal heat load scenario.

o) Heat load level

According to field and climate circumstances, the heat load varies in practice. Five heat load levels were investigated to consider this variability (Figure IV.12).

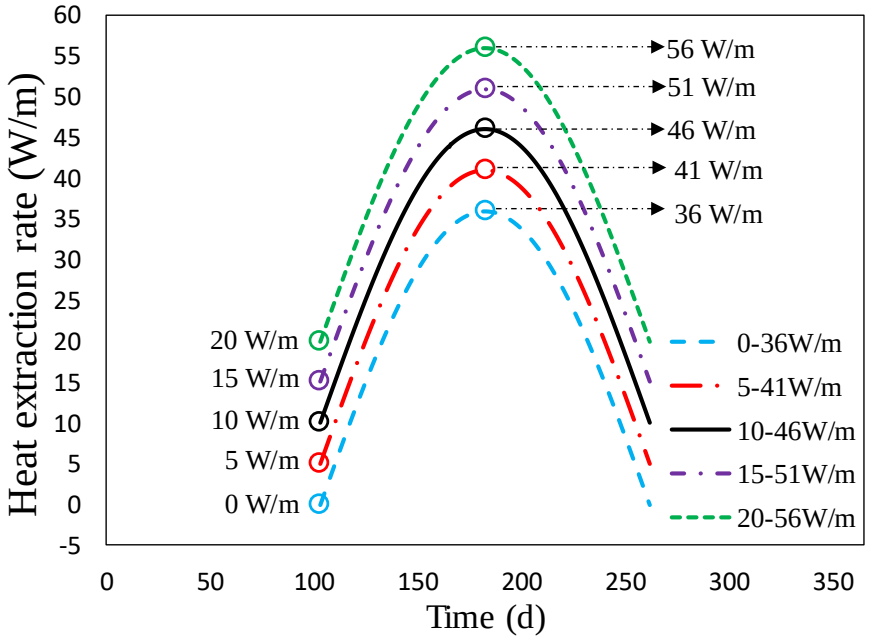

Figure IV.12. The 5 heat load levels

In general, 54 cases for each soil were investigated. Table IV.6 summarizes the 15 factors including their different investigated parameters. The reference parameters (used in the reference models of section 4) are also reported in Table IV.6.

Table IV.6. Summary of the studied factors with their corresponding values

No.	*Factor*	*Parameter (unit)*	*Reference parameter*
1	Meteorological condition	Cold, mild, warm climate (-)	Mild climate
2	Hydraulic condition	Open, grass, forest field (-)	Grass field
3	Groundwater flow	0, 1E-7, 2E-7, 3E-7 ($m.s^{-1}$)	0

4	Grout thermal conductivity	0.8, 1.4, 2.0, 2.5, 3.2 ($W.m^{-1}.K^{-1}$)	2.5
5	Grout volumetric heat capacity	1.2,1.6,2.0,2.4, 3.5 ($MJ.m^{-3}.K^{-1}$)	2.0
6	Grout diameter	0.10, 0.14, 018, 0.22 (m)	0.14
7	Shank spacing	0.03, 0.04, 0.05, 0.06, 0.09, 0.11 (m)	0.05
8	Multi-pipe solution	Single, double (parallel and cross), triple (parallel and cross) (-)	Single
9	Pipe inner diameter	0.018, 0.022, 0.026, 0.030 (m)	0.022
10	Pipe thickness	0.001, 0.0015, 0.0020, 0.0025 (m)	0.0015
11	Pipe thermal conductivity	0.25, 0.5, 2, 6, 11, 16 ($W.m^{-1}.K^{-1}$)	0.5
12	Carrying fluid material	Prop.glycol (25%), prop.glycol (33%), ethanol (24%), $CaCl_2$ (20%) (-)	Ethanol (24%)
13	Carrying fluid velocity	0.1, 0.2, 0.3, 0.4, 0.5, 0.6, 0.7, 0.8 ($m.s^{-1}$)	0.5
14	Heat load mode	Seasonal heat load, steady heat load (-)	Seasonal heat load
15	Heat load level	0-36, 5-41, 10-46, 15-51, 20-56 ($W.m^{-1}$)	10-46

IV.4.2. Effect of different factors on the yearly average heat pump COP

To study various factors affecting the performance of the BHE installed in 2 soils, the variation of yearly average heat pump COP in different conditions was explored in 108 scenarios (Figure IV.13.). The results of the reference models were also distinguished in this figure. The results will be presented in 5 principal aspects mentioned in the introduction.

Firstly, it is the influence of the environmental aspect on the BHE performance (Figure IV.13 a-c). Figure IV.13-a shows that the shallow BHE behaves better in the warmer climate. This conclusion is obtained for a field with a constant temperature gradient in its large depths, fixed for all the numerical simulations. Figure IV.13-b shows that the shallow BHE behaves better in a less vegetated field since it results in a higher water content profile and a higher soil thermal conductivity profile. Additionally, sand shows more variation of the COP value than clay when the field vegetation changes. Figure IV.13-c shows that the heat pump COP has a slight increase with the increase of groundwater velocity in both soils due to a better heat convection in a higher groundwater velocity. This increase becomes more apparent if the velocities higher than 3E-7 $m.s^{-1}$ will be tested in our simulations.

Secondly, the influence of the grout properties on the BHE performance is analyzed (Figure IV.13d to f). Figure IV.13-d shows the heat pump COP increases with the grout thermal

conductivity, while the increase rate reduces for high thermal conductivities. In other words, a grout with low thermal conductivity materials (such as some geopolymers pastes) can impair the BHE performance, while a grout with very high thermal conductivity materials (such as thermal enhanced grout) has a limited capacity to improve the BHE performance. Figure IV.13-e shows that the grout thermal volumetric heat capacity has a negligible influence on the BHE performance. Figure IV.13-f shows that the yearly average heat pump COP increases with the grout diameter since the grout has a greater thermal conductivity than the surrounding soils.

Thirdly, the influence of the U-pipe properties on the BHE performance is illustrated (Figure IV.13 g-k). Figure IV.13-g) shows that the short-circuit phenomenon decreases with the increase of shank spacing while its reduction rate stabilized for the shank spacing larger than 0.09 m. Figure IV.13-h shows that the heat pump COP increases with the number of U-pipes in the borehole. Moreover, the parallel layout of a double U-pipe behaves better than the double cross U-pipe and a negligible difference between the average COP of triple parallel and triple cross U-pipe is observed. Figure IV.13-i shows a slight increase of the average COP with the increase of the pipe inner diameter (and the decrease of the carrying fluid velocity) while the same flow rate of 11.4 $L.min^{-1}$ is applied in the current simulations to obtain the same TEE. Figure IV.13-j shows that the heat pump COP decreases linearly with the U-pipe thickness, mainly due to a lower thermal resistance of the U-pipe with a thinner wall. Figure IV.13-k shows that the heat pump COP increases with the pipe thermal conductivity. However, the increase becomes negligible when the pipe thermal conductivity reaches 2.0 $W.m^{-1}.K^{-1}$.

Fourthly, the influence of the carrying fluid properties on BHE performance is pointed out (Figure IV.13-l & m). Figure IV.13-l shows that the carrying fluids influence differently the heat pump COP due to their different thermal and physical properties. The carrying fluid $CaCl_2$ (20%) provides the highest heat pump COP compared to the other investigated fluids. Figure IV.13-m shows that the heat pump COP at first decreases with the carrying fluid velocity until the velocity reaches 0.3 $m.s^{-1}$, and then the average COP increases for the higher velocities.

Finally, the influence of the heat load is investigated (Figure IV.13 n-o). Figure IV.13-n shows that the yearly average heat pump COP of the steady heat load scenario is higher than

that of the seasonal heat load scenario. Figure IV.13-o shows that the heat pump COP decreases linearly with the heat load level and a higher heat load leads to an inferior heat pump performance.

Generally, the BHE installed in sand behaved better than that installed in clay. The studied factors had a similar effect (increase/decrease trend) on the heat pump COP in both soils. The highest difference between the estimated yearly average COP in two soils was found for the open field hydraulic condition and the heat load level ranging between 20 and 56 $W.m^{-1}$.

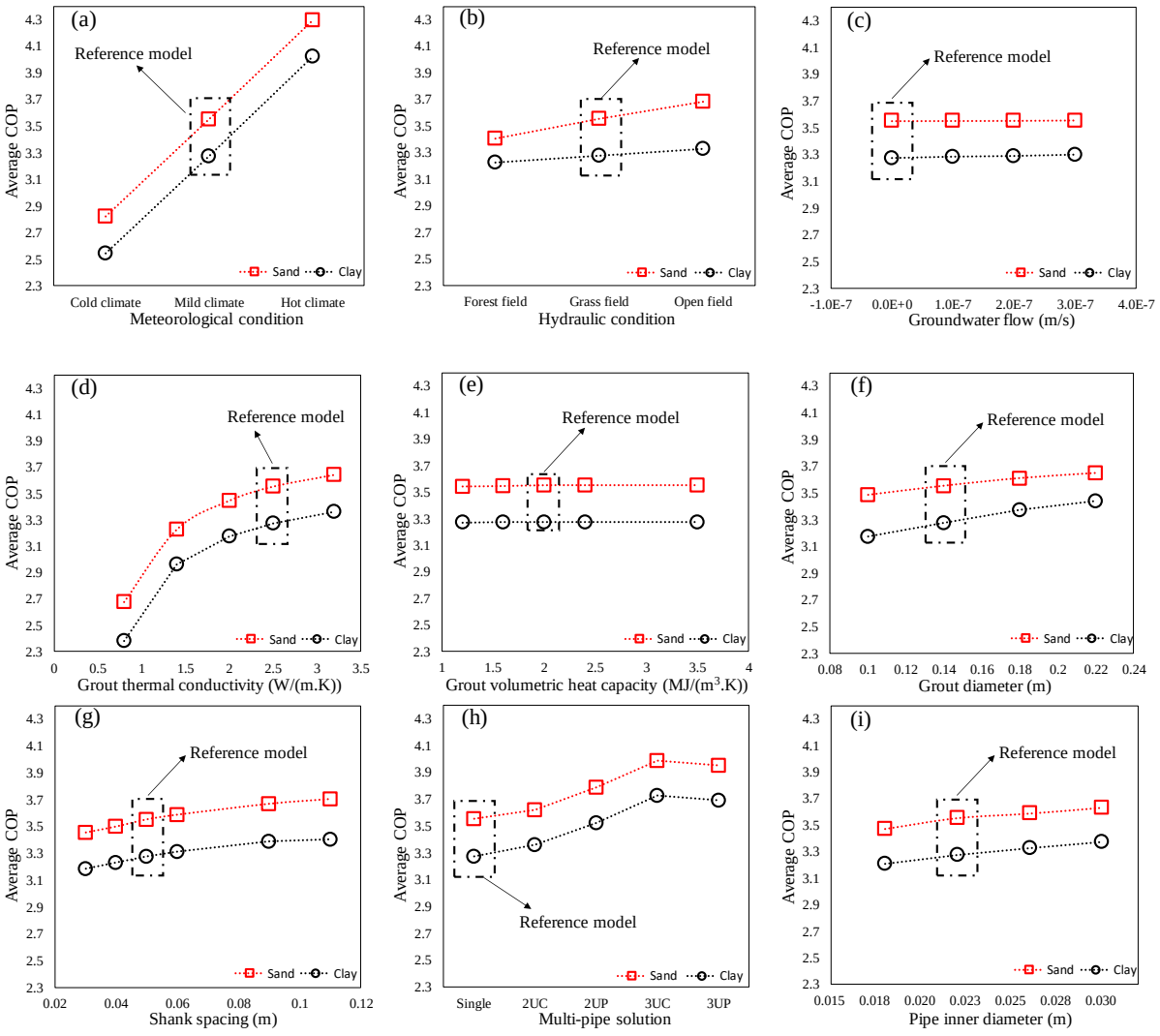

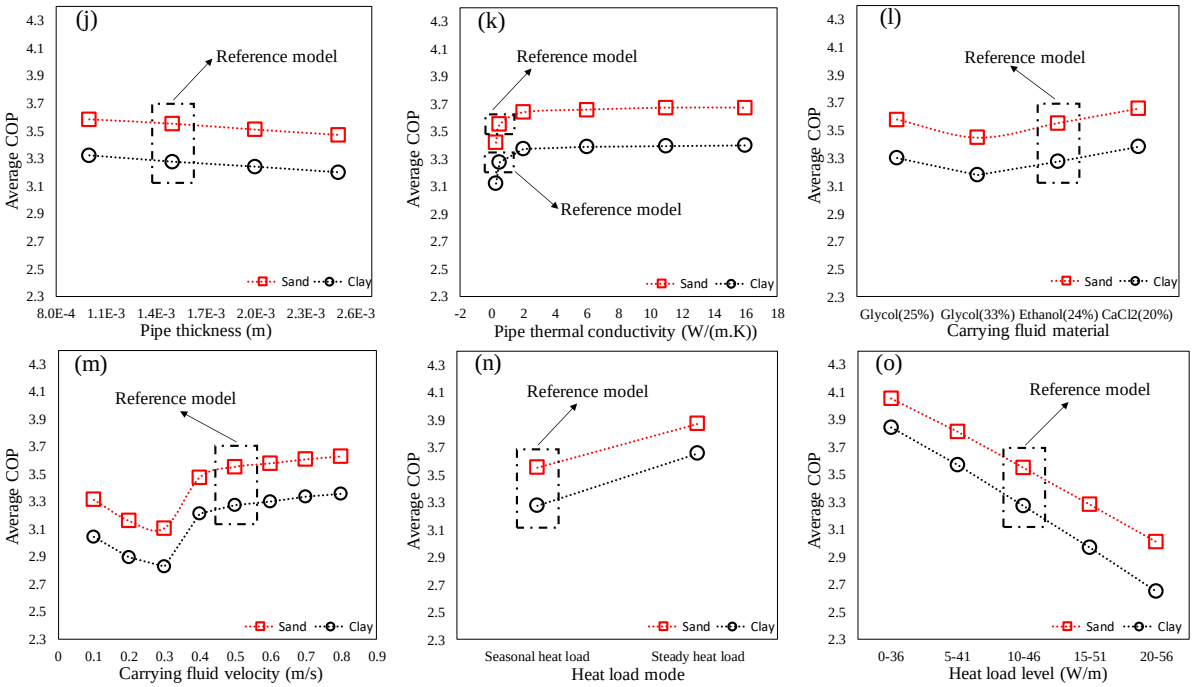

Figure IV.13. Fifteen factors influencing the yearly average heat pump COP of the shallow BHE installed in clay and sand: (a) meteorological condition; (b) hydraulic condition; (c) groundwater flow; (d) grout thermal conductivity; (e) grout volumetric heat capacity; (f) diameter; (g) shank spacing; (h) multi-pipe solution; (i) pipe inner diameter; (j) pipe thickness; (k) pipe thermal conductivity; (l) carrying fluid material; (m) carrying fluid velocity; (n) heat load mode and (o) heat load level

Figure IV.14 presents statistically the influence of the 15 factors on the yearly average heat pump COP for the shallow BHE installed in sand and clay compared to the reference models. The following points have been observed:

- the meteorological condition has the highest impact (41.6% in sand and 45.3% in clay) on the shallow BHE performance;
- the grout thermal conductivity (27.2% in sand, 30.1% in clay) and the heat load level (29.4% in sand, 36.4% in clay) have also a high impact on the shallow BHE performance;
- the multi-pipe solution, the carrying fluid velocity and the heat load level influence the yearly average COP in both soils between 12.2% and 16.2%;
- the hydraulic condition, the groundwater flow, the grout volumetric heat capacity, the grout diameter, the shank spacing, the pipe inner diameter, the pipe thickness, the pipe

thermal conductivity, the carrying fluid material, and the heat load mode have less impact on the yearly average heat pump COP (between 0.0% and 11.6%).

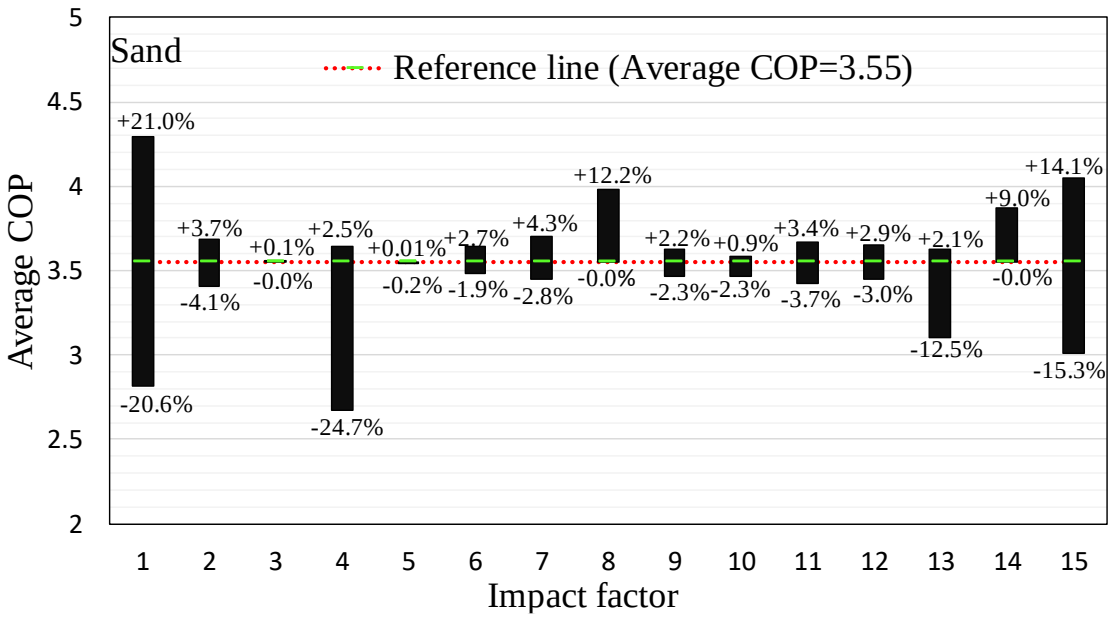

1-Meteorological condition 2-Hydraulic condition 3-Underground water 4-Grout thermal conductivity 5-Grout volumetric heat capacity 6-Grout diameter 7-Shank spacing 8-Multi-pipe solution 9-Pipe inner diameter 10-Pipe thickness 11-Pipe thermal conductivity 12-Carrying fluid material 13-Carrying fluid velocity 14-Heat load mode 15-Heat load level

(a)

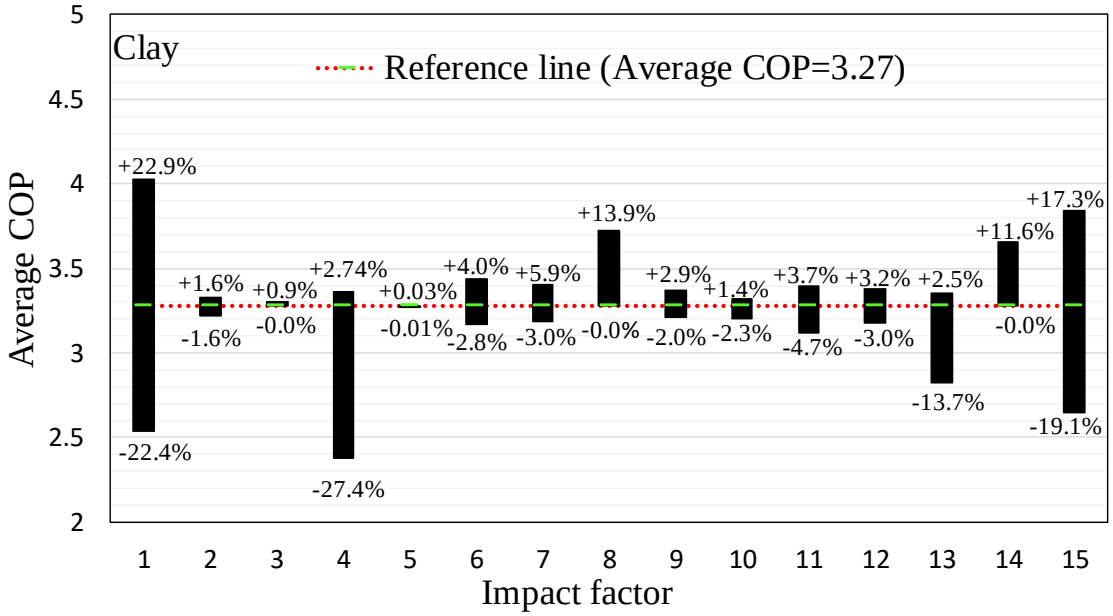

1-Meteorological condition 2-Hydraulic condition 3-Underground water 4-Grout thermal conductivity 5-Grout volumetric heat capacity 6-Grout diameter 7-Shank spacing 8-Multi-pipe solution 9-Pipe inner diameter 10-Pipe thickness 11-Pipe thermal conductivity 12-Carrying fluid material 13-Carrying fluid velocity 14-Heat load mode 15-Heat load level

(b)

Figure IV.14. Statistical influence of each factor on the yearly average heat pump COP compared to the reference models for the shallow BHE installed in two soils: (a) sand and (b) clay

Besides, the following points should be considered for the shallow BHE performance or the heat pump COP:

- Hydrothermal fluctuation on the ground surface influences the BHE performance when a short U-pipe is used. For our studied 20m-length U-pipe, a length of 8.45 m is unsaturated and significantly dependent to the ground surface hydrothermal fluctuation.
- The groundwater flow influences highly the terrain hydraulic conditions. A relatively high velocity of groundwater flow, especially in sand increases the temperature recovery rate and subsequently improve the BHE performance. The same fact has also been reported in the literature (Angelotti et al., 2014; Hein et al., 2016; Rivera et al., 2015; Zhang et al., 2015b).
- In extreme environmental conditions, the peak load shall be avoided to ensure a higher

yearly heat pump COP.

Selecting the appropriate properties for a BHE is crucial since more attention is put nowadays into the optimization of a BHE system. The main objective of the current investigation is to shed light on how the different factors influence the yearly heat pump COP. These findings can be used as a guideline in future investigation treating the BHE performance or the heat pump COP, especially for shallow BHE.

IV.5. Summary

Numerical simulations were performed to investigate the factors impacting the performance of a shallow BHE installed in unsaturated soils subjected to yearly hydrothermal fluctuation on their ground surface. It was first validated by the literature in-situ measurements.

After showing the good capacity of the proposed numerical framework, two reference models were constructed for the calculations of the shallow BHE installed in sand and clay. The BHE installed in sand behaved better than that installed in clay according to the simulation results.

Subsequently, the effect of 15 principal factors on the shallow BHE performance was investigated by covering 108 different cases. The yearly average heat pump COPs in different cases were compared with those of the reference models. The same impact of different factors was observed for the BHE installed in the two soils with an average difference of 8.6% between sand and clay (COP = 3.55 in sand and COP = 3.27 in clay). Globally, the BHE performance was better in warmer climate, less vegetated field, higher groundwater velocity, higher grout thermal conductivity, larger grout diameter, larger shank spacing, more additional U-pipes, larger U-pipe inner diameter, thinner U-pipe, higher U-pipe thermal conductivity, more stable heat load and lower heat load level. The grout volumetric heat capacity influenced negligibly the BHE performance. The usage of $CaCl_2$ (20%) as the carrying fluid improved the BHE performance and the BHE performance was the lowest when the carrying fluid velocity reached 0.3 $m.s^{-1}$.

The heating process was uniquely studied in this investigation to make the comparison in the similar cases. In hot climate regions, the cooling process or both cooling and heating processes are used, which can be also investigated by this numerical framework.

The current investigation was based on the numerical simulations and further experimental measurements are still necessary to complete this work. Moreover, some novel materials can

be used to optimize the BHE performance. For example, PCM can replace the grout and the carrying fluid (Zhao et al., 2016) to enhance the heat pump performance. A good characterization of PCM will be essential in the future optimization procedure. Hybrid Ground-Source Heat Pump (HGSH) can provide extra energy source to extract/inject heat (Emmi et al., 2015; Fine et al., 2018; Liu et al., 2017). Besides, the financial records of different scenarios will be helpful to determine the best optimized solution for the performance of a system.

V. SENSITIVE ANALYSIS ON THE TRT

V.1. Introduction

In this context, COMSOL was adopted to simulate the TRT during the hottest day(s) of a year in summer and during the coldest day(s) of a year in winter. The investigated soils are constituted of unsaturated and saturated zones, where the thermal properties in the saturated zone are constant and the soil thermal properties in the unsaturated zone are decided by the soil hydraulic profile. Due to the short test time of TRT, the ground surface temperature and the hydraulic profile of the surrounding soil were regarded constant during the simulation.

By analyzing the different cases in the numerical simulations, a new analytical approach was also proposed for the estimation of the effective soil thermal conductivity in BHE applications.

V.2. Governing equations

The same numerical framework has been used in the last chapter. Nevertheless, there are some differences of the governing equations between this chapter and the last chapter. Due to the short test time of the TRTs, the hydrothermal profiles were set constant in the simulation. However, the hydrothermal models were used to generate the initial suction and temperature profiles.

V.3. Validation of the numerical framework for the TRTs

In-situ TRTs conducted at the Chiba Experimental Station at the University of Tokyo (Japan) (Choi and Ooka, 2016b) were used to evaluate the capacity of the numerical framework. The water level is situated at a depth of 10 m and the U-pipe length is 50 m. The effective soil thermal conductivity of 1.96 $W.m^{-1}.K^{-1}$ was employed in the model [32]. All the site parameters are reported in Table V.1.

Table V.1. Input parameters of the simulated in-situ TRT in Tokyo (Japan) (Choi and Ooka, 2016a, 2016b)

Parameter, unit	Value
Carrying fluid density, $kg.m^{-3}$	1000
Carrying fluid specific heat capacity, $J.kg^{-1}.K^{-1}$	4200
Carrying fluid thermal conductivity, $W.m^{-1}.K^{-1}$	0.6
Carrying fluid velocity, $m.s^{-1}$	0.53
U-pipe type, -	Single
U-pipe thickness, m	0.0034
U-pipe inner diameter, m	0.0270
U-pipe heat conductivity, $W.m^{-1}.K^{-1}$	0.38
Borehole diameter, m	0.165
Grout heat conductivity, $W.m^{-1}.K^{-1}$	1.43 (Choi and Ooka, 2016a)
Grout volumetric heat capacity, $MJ.m^{-3}.K^{-1}$	1.9 (Choi and Ooka, 2016b)
Shank spacing, m	0.05
Effective soil thermal conductivity, $W.m^{-1}.K^{-1}$	1.96
Soil volumetric heat capacity, $MJ.m^{-3}.K^{-1}$	2.5
Initial temperature, °C	17
Operation time, h	72
Outlet temperature – inlet temperature, °C	1.673

Figure V.1 shows the comparison between the in-situ measurements and the model predictions of the inlet/outlet fluid temperatures. The difference between the measurements and the predictions is presented by χ, given as:

$$\chi = \frac{\left| T_{numerical} - T_{in-situ} \right|}{T_{numerical}} \times 100\% \tag{5.9}$$

The comparisons show that the numerical framework is capable to predict well the inlet and outlet temperatures, particularly after 20 h. The difference is relatively large in the first 20 h. After this time, the difference becomes less than 1%.

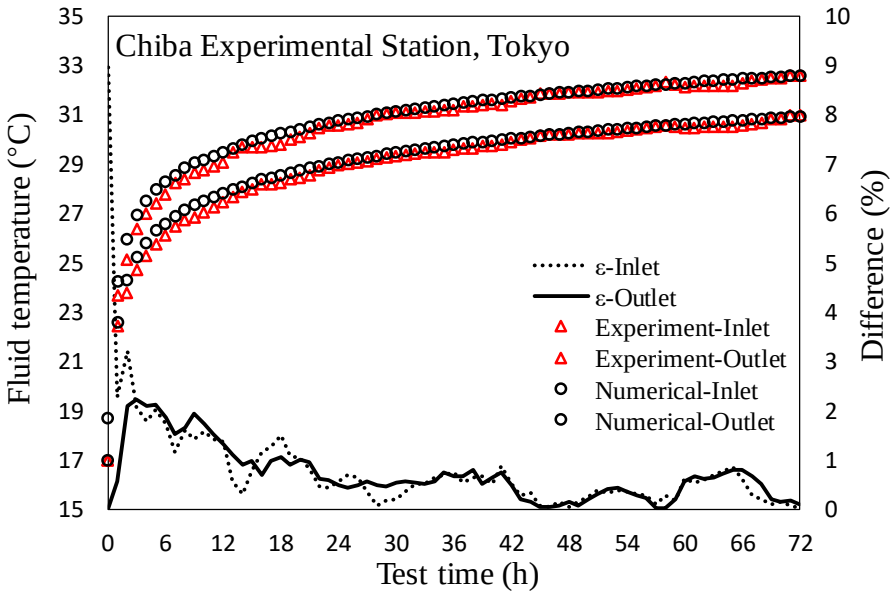

Figure V.1.Comparison between the in-situ measurements and the numerical simulations: the fluid inlet/outlet temperatures and their differences (ε)

However, the concept of TRTs is based on a homogenized one-layered soil but the ground is often stratified, and the thermal conductivity is then a function of depth: k = k (z). We use the following equation to obtain the equivalent thermal conductivity:

$$k = \frac{1}{L}\int_{z}^{z+L} k(z)dz \tag{5.10}$$

where, L is the length of the BHE (m), z is the starting depth where the BHE is installed (m).

To further evaluate the capacity of our proposed numerical framework, TRTs were simulated for a BHE installed in Alsace region (France) since we have access to an instrumented site in this region. Alsace has a semi-continental climate at low altitude and a continental climate at high altitude. At some parts of the region, the ground temperature gradient can reach 0.1 $K.m^{-1}$. The lowest daily average ambient temperature at the test site is around 1 °C in winter and the highest daily average ambient temperature in summer is around 22 °C. The annual average ambient temperature at the test site is around 11.5 °C. Table V.2 presents 6 different soil layers and their thicknesses. The U-pipe is surrounded by grout and water is the carrying fluid. Further details about the field, the weather condition, the grout thermal properties, the U-pipe description, the physical properties of the carrying fluid and the U-pipe layout are given in the 3rd chapter.

Table V.2. Six soil layers with their thicknesses at a site in Alsace region (France)

Soil layer	*Soil category*	*Thickness (m)*
1	Clay loam	0.1
2	Sandy loam 1	1.0
3	Loam	0.15
4	Sandy loam 1	4.75
5	Sandy loam 2	8.0
6	Loam	11.0

By using equation (5.10), the equivalent soil thermal conductivities are then obtained 1.659 and 1.662 $W.m^{-1}.K^{-1}$ respectively in summer and winter. The heat injection rate was set as 60 $W.m^{-1}$. Figure V.2 shows the comparison of the average fluid temperatures of the TRTs conducted in summer and winter for the stratified and its equivalent soil. It shows that the effect of the heterogeneity is not significant in the numerical approach and the equivalent thermal conductivity can represent the effective thermal conductivity in the TRT.

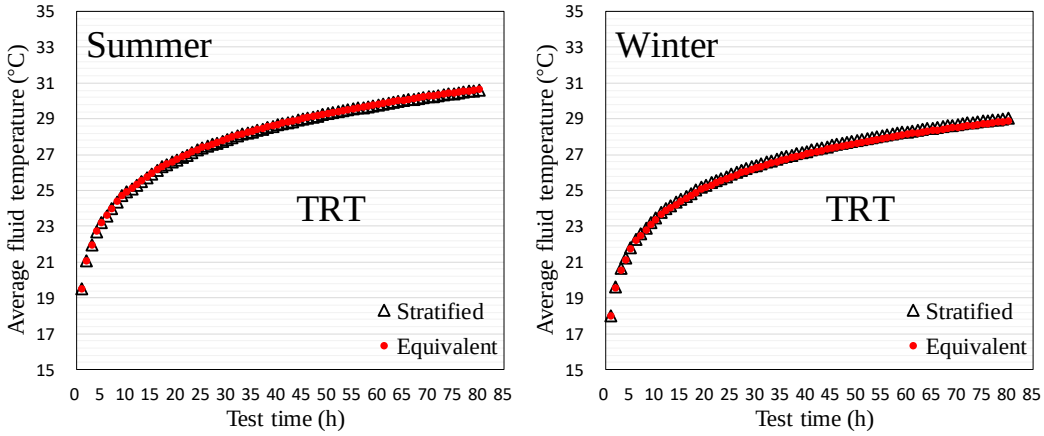

(a) (b)

Figure V.2. Comparison of the average carrying fluid temperatures for the stratified field and its equivalent soil in two seasons conducting TRTs: (a) summer and (b) winter

V.4. TRT simulation results

In this section, the simulation results of the TRTs conducted in different scenarios are presented.

V.4.1. Model description

A 3D geometry with a length of 30 m, a width of 30 m and a depth of 100 m was used in the numerical simulations. The borehole diameter was 0.14 m. Inside the borehole, the single U-pipe was symmetrically positioned with a shank spacing of 0.05 m. The inner and outer diameters of U-pipe were respectively 2.2 and 2.7 cm.

In practice, a BHE is conventionally surrounded by unsaturated and saturated soils, and the depth of the unsaturated zone varies with the water level. The soil thermal properties vary with time and space, particularly in the unsaturated zone. To better investigate the influence of this unsaturated zone on the effective soil thermal conductivity, a λ ratio is introduced:

$$\lambda = \frac{z_u}{z_{U-pipe}} \tag{5.11}$$

where, z_u is the depth of unsaturated zone/water level (m), $z_{U\text{-}pipe}$ denotes the U-pipe length (m). In the investigation, the λ ratio ranges between 0 to 1, indicating that the unsaturated zone does not exceed the U-pipe length.

To have a more comprehensive investigation, 10 scenarios were considered by modifying either the U-pipe length or the water level. In this work, the U-pipe length is between 11.5 and 34.03 m, the water level is between 8.45 and 15 m and the λ ratio is between 0.34 and 1. Table V.3 summarizes these scenarios with their corresponding λ ratios.

Table V.3. Summary of the 10 scenarios for 6 U-pipe lengths and 3 water levels

Scenario	*U-pipe length $z_{U\text{-}pipe}$ (m)*	*Water level z_u (m)*	$\lambda=z_u/z_{U\text{-}pipe}$
S1	15	8.45	0.56
S2		11.5	0.77
S3		15.0	1
S4	20.42	11.5	0.56
S5	11.5		1
S6	25	8.45	0.34
S7		11.5	0.46
S8		15.0	0.6
S9	34.03	11.5	0.34
S10	19.17		0.6

It is expected that the effective ground thermal conductivity ranges between a value obtained during the hottest day(s) of a year and a value obtained during the coldest day(s) of a year. Hot days of a year are supposed to be in summer and cold days of a year are in winter. Thus, summer and winter express these extreme conditions in our simulations. The daily average ground surface temperatures for the hottest day(s) in summer and the coldest day(s) in winter are respectively considered 25 and 0 °C. The temperature profiles on the hottest and the coldest days are also presented in Figure V.3-a.

To explore the influence of the water level on the TRT, three water levels of 8.45 m, 11.5 m and 15.0 m were considered for the different scenarios as mentioned in Table V.3. The suction profiles of these 3 water levels in summer and winter are then presented in Figure V.3 b-d.

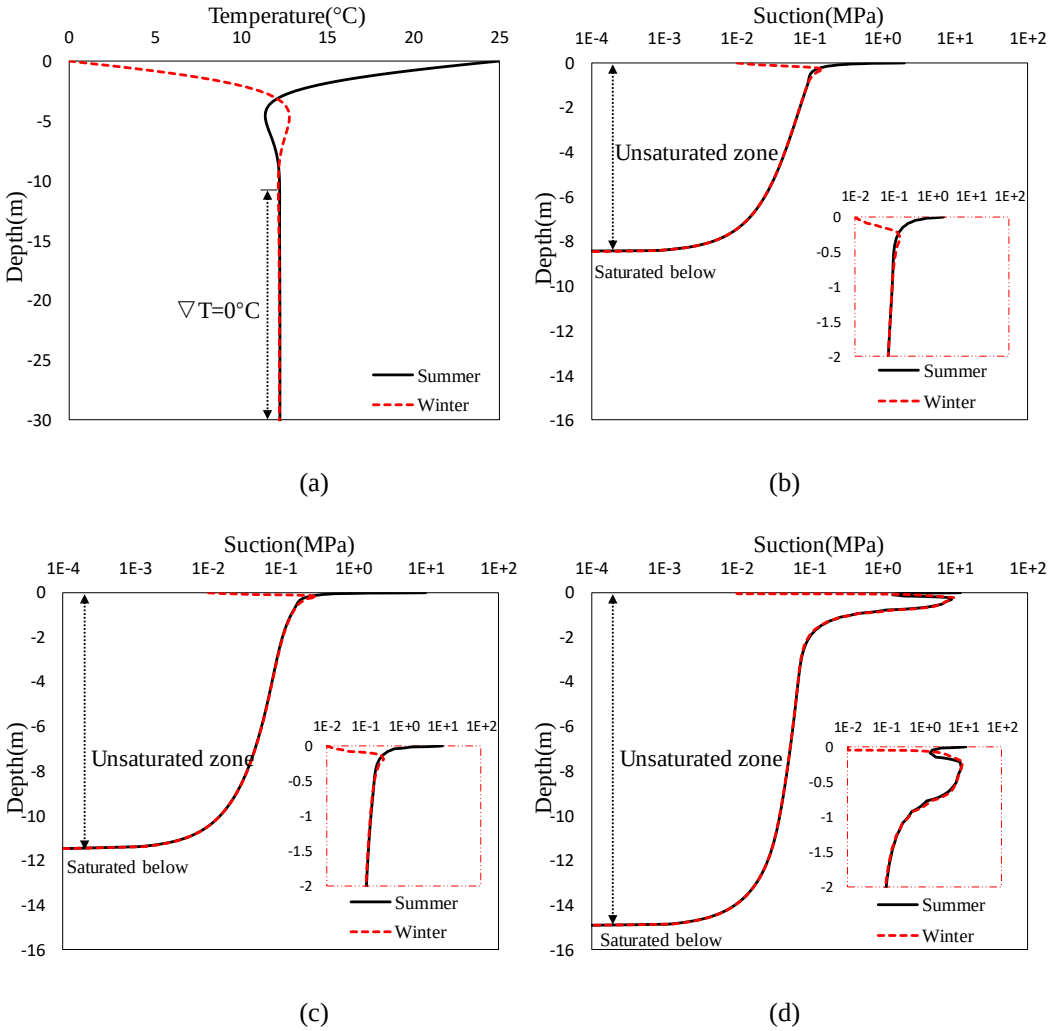

Figure V.3. Initial hydrothermal profiles of the model for 2 seasons (winter & summer): (a) ground temperature; (b) suction profiles in scenarios S1 and S6; (c) suction profiles in scenarios S2, S4, S5, S7, S9 and S10; and (d) suction profiles in scenarios S3 and S8

The sand content is used in this work to represent the different field conditions since it affects directly the soil thermal properties in the numerical framework (equations (5.5) and (5.6)). Three typical soils with 20%, 60% and 90% of sand content, representing clay, sandy loam and sand were adopted to investigate the TRTs in the different geotechnical (field) conditions. Table V.4 summaries the necessary hydrothermal parameters and their corresponding values for the 3 soils. The soil specific unit weights (γ_s) are also presented.

Table V.4. Hydrothermal properties of the studied soils

Soil	γ_d *(kN.m^{-3})*	x_s *(-)*	*K (m.s^{-1})*	*l (-)*	α *(m^{-1})*	*n (-)*	θ_{sat} *(-)*	θ_{res} *(-)*	γ_s *(kN.m^{-3})*
Clay	14.2	0.2	1.44E-6	0.5	1.98	1.086	0.481	0.010	27.4
Sandy loam	16.1	0.6	4.42E-6	0.5	2.49	1.170	0.392	0.010	26.4
Sand	16.1	0.9	1.03E-4	0.5	4.30	1.520	0.366	0.025	25.4

The SWCCs and their corresponding soil thermal properties obtained from equations (5.5) and (5.6) for the studied soils are presented in Figure V.4. The variation of these thermal properties is presented with the degree of saturation (Figure V.4-b & c). As it is known, soil is conventionally made up of mineral particles (represented by sand content in this study), water and air. Water (with a thermal conductivity of 0.6 W.m^{-1}.K^{-1}) has a higher thermal conductivity than air (with a thermal conductivity of 0.026 W.m^{-1}.K^{-1}) and it acts as bridges to connect mineral particles together. The higher the water content, the higher the soil thermal conductivity (Figure V.4-b). A higher sand content results in a higher thermal conductivity (Figure V.4-b). The volumetric heat capacity decreases inversely with the increase of the sand content (Figure V.4-c).

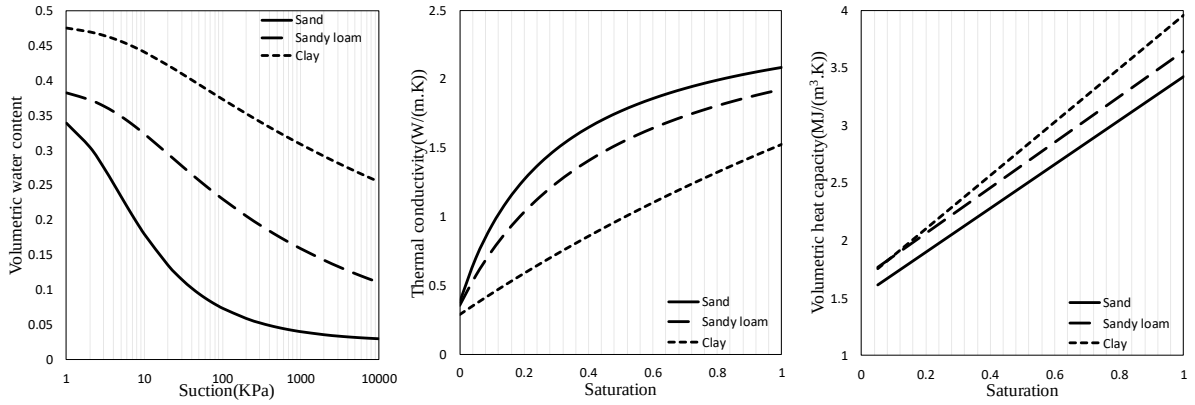

(a) (b) (c)

Figure V.4. Hydrothermal properties of the 3 soils: (a) SWCCs; (b) thermal conductivity and (c) volumetric heat capacity

By using equations (5.5) and (5.6), and the initial suction profiles (presented in Figure V.3), the initial soil thermal properties can be obtained. Figure V.5 shows the initial thermal properties of the 3 soils at the water level of 8.45 m (scenarios S1 and S6) in summer and winter. In general, clay has the lowest thermal conductivity. Sand has the highest thermal conductivity in the saturated zone while sandy loam has the highest thermal conductivity in the unsaturated zone. Furthermore, clay has the highest volumetric heat capacity.

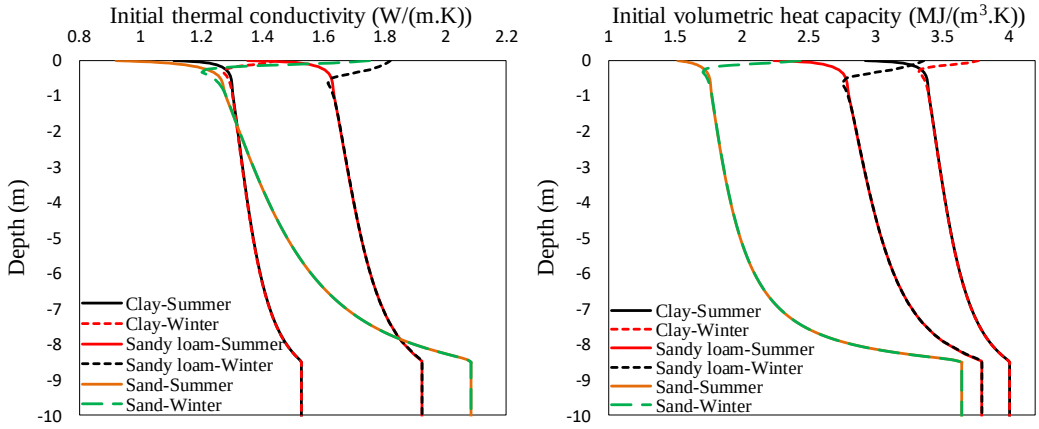

(a) (b)

Figure V.5. Initial thermal properties of the studied soils for a water level of 8.45 m (scenarios S1 and S6) in summer and winter: (a) thermal conductivity and (b) volumetric heat capacity

Water was selected as the circulating fluid in the U-pipe with the velocity of 0.5 $m.s^{-1}$. The thermal conductivity of pipe was 0.5 $W.m^{-1}.K^{-1}$. The grout has a thermal conductivity of 2.5 $W.m^{-1}.K^{-1}$, a density of 2500 $kg.m^{-3}$ and a specific heat capacity of 800 $J.kg^{-1}.K^{-1}$.

Due to a limited hydraulic velocity in clay and the water head difference in shallow BHEs, no groundwater flow was imposed in the numerical simulations.

Conventional TRTs usually need a time between 48 and 72 hours (Bujok et al., 2014; Raymond et al., 2016). Consequently, a period of 120 h was considered in our simulations to cover sufficiently this period.

The heat injection process was considered in our investigation, which is common in the TRT practice. ASHRAE standards recommend a thermal load between 50 and 80 $W.m^{-1}$ for a TRT (Ashrae, 2011; Zhang et al., 2015a). Cai et al. (2016) have experimentally conducted TRTs subjected to 3 heat loads and found that the heating power influenced less than 5% the ground thermal conductivity. Accordingly, a heat injection rate of 60 $W.m^{-1}$ was chosen for the following TRT simulations.

V.4.2. Numerical simulation results for carrying fluid temperature

The carrying fluid temperatures were obtained for the 10 scenarios in clay, sandy loam and sand in summer and winter. Figure V.6 shows the variation of the mean carrying fluid temperature with the natural logarithm of time for clay and sand in summer and winter where Su, Wi, Cl and Sa stand respectively for summer, winter, clay and sand. The figure shows that the fluid temperature increases with time due to the heat accumulation in soil. Moreover, the fluid temperature is higher in summer than in winter, mainly due to a higher ground surface temperature in summer. The fluid temperature of BHE installed in sand has a larger range of variation. The fluid temperature increases with the λ ratio in summer for all the studied soils. However, it decreases with the increase of λ ratio for some cases in clay and in winter: S4-Wi-Cl, S5-Wi-Cl, S9-Wi-Cl and S10-Wi-Cl. The carrying fluid temperature in sand also increases with the λ ratio in all the scenarios. Since the TRT results in sandy loam show the same tendency observed in clay, these results are not presented in Figure V.6. In the next section, these results will be considered.

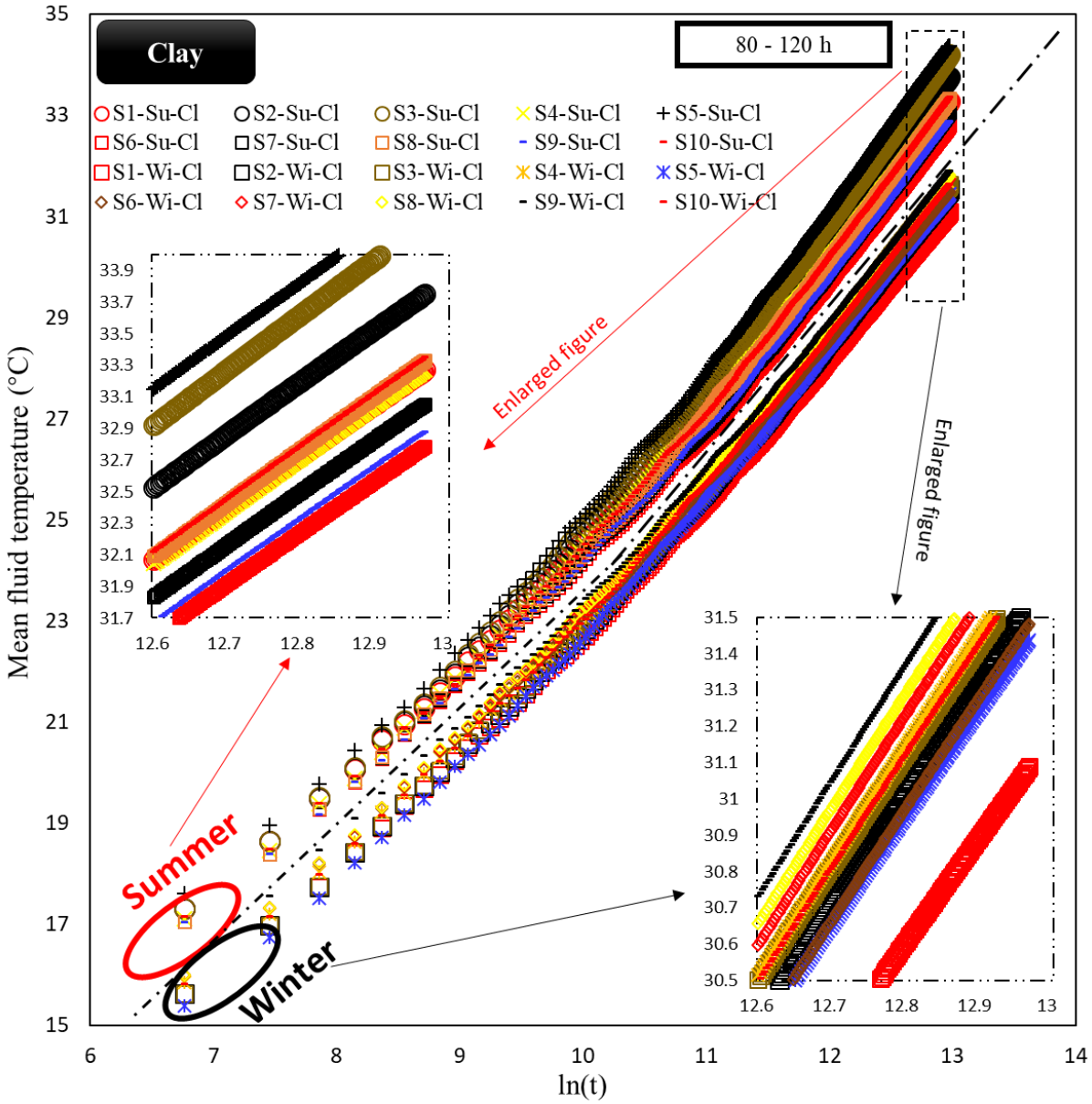
Clay
80 - 120 h
S1-Su-Cl
S2-Su-Cl
S3-Su-Cl
S4-Su-Cl
S5-Su-Cl
S6-Su-Cl
S7-Su-Cl
S8-Su-Cl
S9-Su-Cl
S10-Su-Cl
S1-Wi-Cl
S2-Wi-Cl
S3-Wi-Cl
S4-Wi-Cl
S5-Wi-Cl
S6-Wi-Cl
S7-Wi-Cl
S8-Wi-Cl
S9-Wi-Cl
S10-Wi-Cl
Enlarged figure
Enlarged figure
Summer
Winter
Mean fluid temperature (°C)
ln(t)

(a)

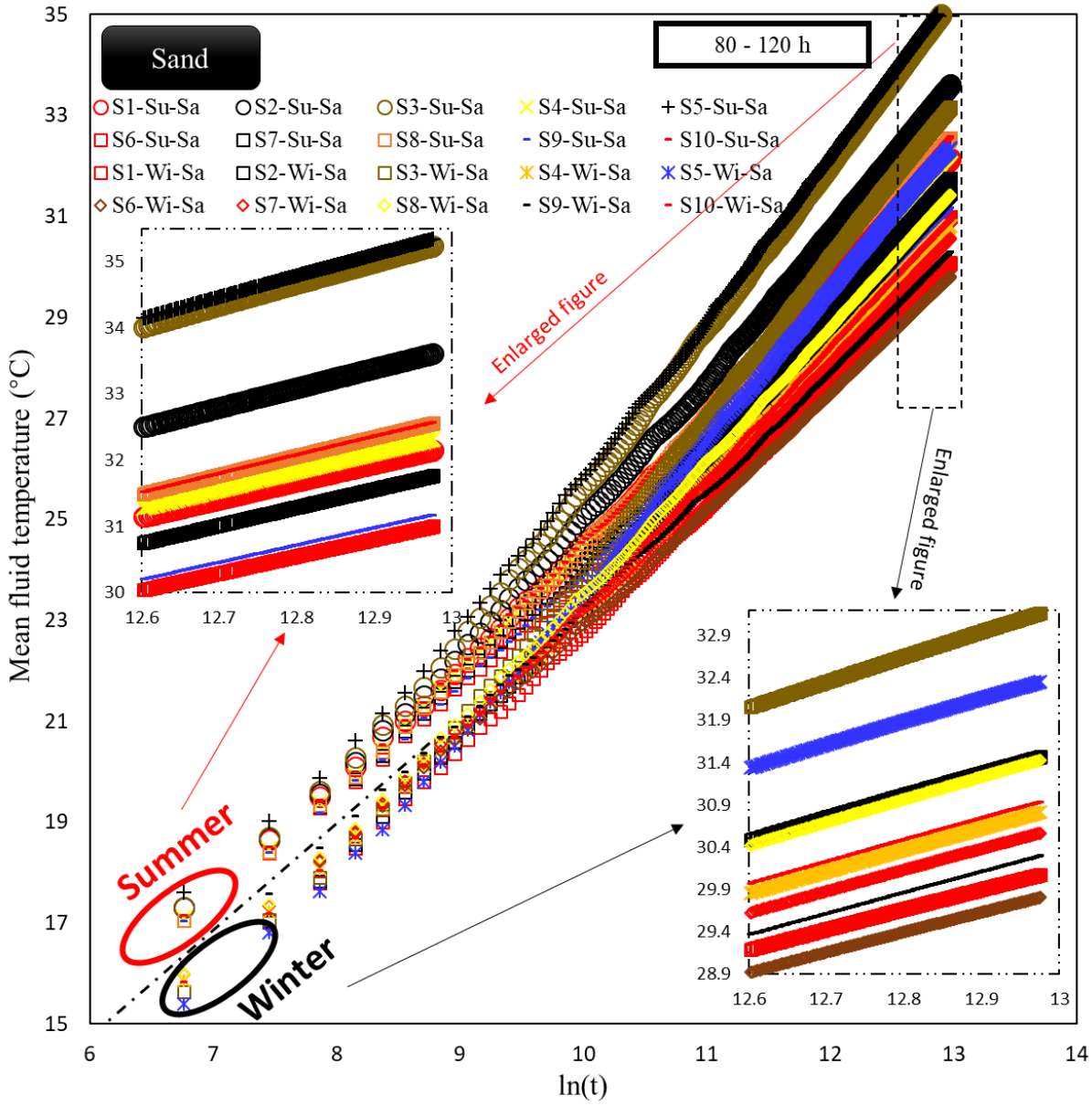

(b)

Figure V.6. Mean carrying fluid temperature from TRTs in summer and winter for different soils: (a) clay and (b) sand

V.4.3. Numerical simulation results for the effective soil thermal conductivity

The testing time, the soil, the λ ratio and the U-pipe length influence the fluid temperature, and consequently the effective soil thermal conductivity. The fluid temperature between 80 and 120 h were eventually chosen to acquire the effective soil thermal conductivity, since the TRT reaches a steady state in this stage. From ILS model, the effective soil thermal conductivity is given as:

$$k_s = \frac{q}{4\pi} \cdot \frac{\Delta \ln(t)}{\Delta \overline{T}_f} \tag{5.12}$$

To better analyze the TRT results and explore the effect of λ ratio and U-pipe length on the results, the tests were divided into 2 groups as presented in Table V.5.

Table V.5. Two proposed groups for a more comprehensive analysis of the TRTs

Group	*Scenario*	*Water table (m)*	*U-pipe length (m)*
1	S1, S2, S3, S6, S7, S8	Variable	15 & 25 (Constant)
2	S2, S4, S5, S7, S9, S10	11.5 (Constant)	Variable

Figure V.7 shows the variation of the effective thermal conductivity of clay, sandy loam and sand with the λ ratio and the U-pipe length in summer and winter for the two groups. The results of the second group are presented with both λ ratio and U-pipe length.

The figure shows that the effective soil thermal conductivities obtained in winter are higher than those in summer (3.8% to 14.0% for clay, 5.8% to 24.3% for sandy loam, and 5.2% to 17.9% for sand), and the largest difference exists for the shortest U-pipe. The phenomenon is due to a favorable heat transfer during the heat injection period in winter.

The figure also shows that the effective soil thermal conductivity varies linearly with the λ ratio (Figure V.7 a-f) and it additionally varies in a (2^{nd} degree) polynomial form with the U-pipe length (Figure V.7 g-i).

Generally, clay has the smallest effective thermal conductivity among the 3 soils. Sand and sandy loam have a larger variation of the effective thermal conductivities than clay. Further, sandy loam has a greater effective thermal conductivity than sand in shallow U-pipes. The phenomenon can be explained by Figure V.5-a, where sandy loam has a higher thermal conductivity in its unsaturated zone. However, the advantage would diminish with the increase of the U-pipe length, since sand has a higher thermal conductivity in the saturated zone.

In Group 1 with a variable water level, the decrease of the effective soil thermal conductivity with the λ ratio is observed for all the soils (Figure V.7 a-c). In Group 2 with a variable U-pipe length, the same trend is observed for clay and sandy loam in summer while an increase

of their effective thermal conductivity occurs during winter (Figure V.7-d & e). Figure V.7-f illustrates that the effective soil thermal conductivity of sand decreases with the λ ratio in summer and winter.

Moreover, the difference between the effective thermal conductivity in summer and winter decreases with the increase of U-pipe length, and the decrease rate is stabilized for the lengths longer than 30 m (Figure V.7 g-i). It means that the testing time affects less the TRT results in long U-pipes.

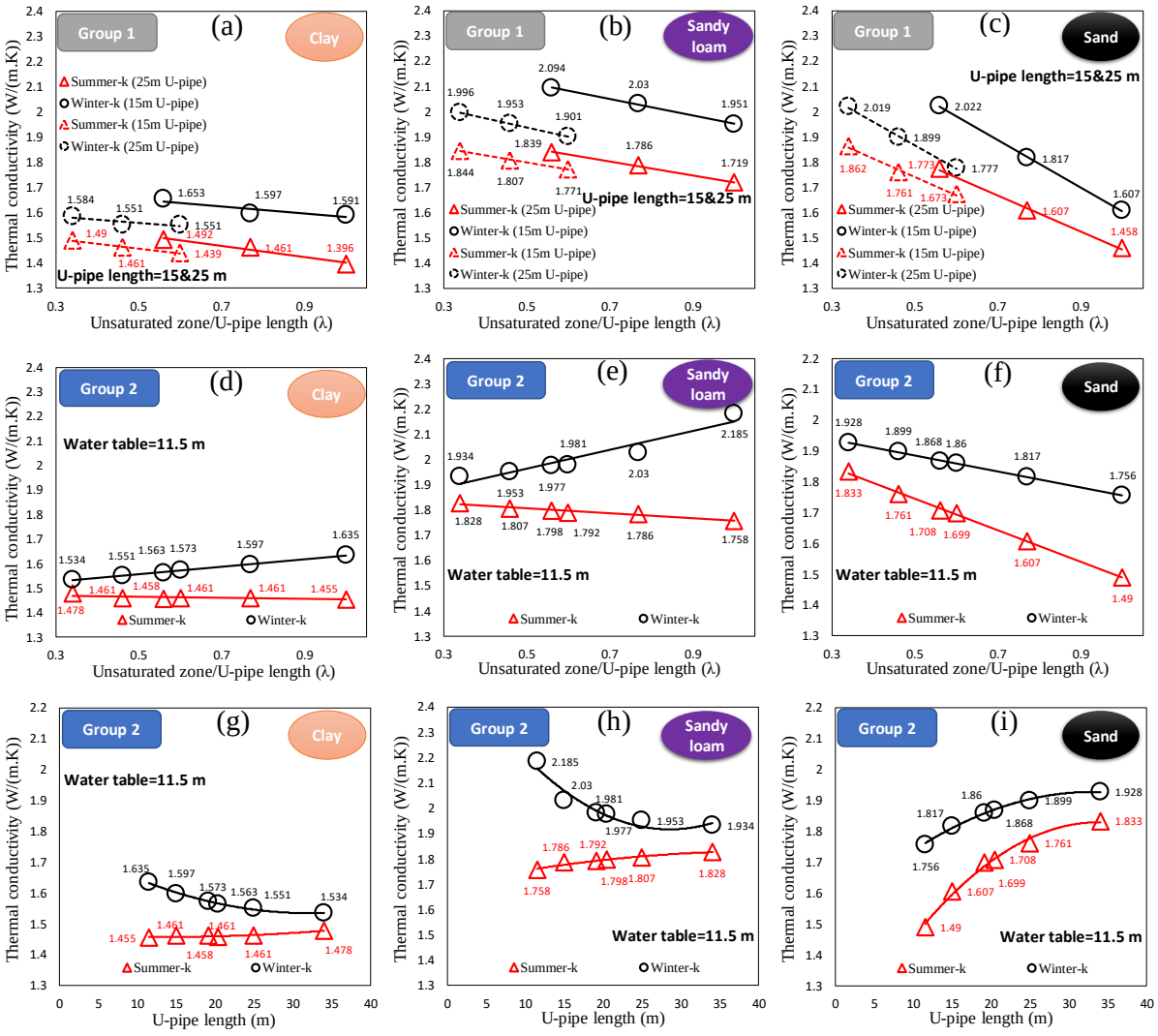

Figure V.7. Effective soil thermal conductivity variation of the 3 soils in summer and winter for group 1 with the λ ratio (a to c) and for group 2 with the λ ratio (d to f) and the U-pipe length (g to i)

V.5. An analytical approach for the effective soil thermal conductivity

In this section, an analytical approach is first proposed and then applied to 6 in-situ measurements and a geothermal multi-layered field in Alsace region (France).

V.5.1. The proposed analytical approach

It has been obtained in the last section that the soil effective thermal conductivity varies linearly with the λ ratio (Figure V.7 a-f) and it varies with the U-pipe length in a polynomial form (Figure V.7 g-i). Figure V.7 g-i also show that the effective soil thermal conductivity is stabilized for the long U-pipes. This maximum U-pipe length in which the stabilization occurs is noted as L_{max} (m).

According to the results in the last section, the following solution is proposed to predict the effective soil thermal conductivity:

$$k_{eff} = \begin{cases} a + b \cdot \lambda + c \cdot \chi^2 + d \cdot \chi & (\chi < 1) \\ e + b \cdot \lambda & (\chi \geq 1) \end{cases} \quad (5.13)$$

where a (W.m^{-1}.K^{-1}), b (W.m^{-1}.K^{-1}), c (W.m^{-1}.K^{-1}), d (W.m^{-1}.K^{-1}) and e (W.m^{-1}.K^{-1}) are constant parameters. The λ ratio varies between 0 and 1. χ is another dimensionless factor, defined as:

$$\chi = \frac{z_{U-pipe}}{L_{max}} \quad (5.14)$$

By fitting the results, all the parameters estimated in the two seasons for the 3 soils are summarized in Table V.6. The table indicates that the proposed equation (5.13) considers indirectly the soil saturation, its dry density, and its sand content since the coefficients vary with the soil type and the season. It also confirms that the λ ratio define reasonably the effect of the unsaturated zone on the effective thermal conductivity.

Table V.6. Fitted parameters of the proposed analytical solution (equation (5.13)) for the 3 soils in summer and winter

Soil	*Season*	*a* (*W.m^{-1}.K^{-1}*)	*b* (*W.m^{-1}.K^{-1}*)	*c* (*W.m^{-1}.K^{-1}*)	*d* (*W.m^{-1}.K^{-1}*)	*e* (*W.m^{-1}.K^{-1}*)	L_{max} *(m)*
Clay	Summer	1.810	-0.2092	0.26134	-0.52295	1.549	30.6
	Winter	2.060	-0.1936	0.45347	-0.90740	1.606	34.9

Sandy loam	Summer	2.178	-0.273	0.25685	-0.51449	1.920	31.7
	Winter	3.028	-0.312	0.98515	-1.96840	2.045	30.4
Sand	Summer	2.354	-0.7261	0.29137	-0.58208	2.07	41.4
	Winter	3.154	-0.9278	0.90042	-1.80194	2.252	34.5

As the sand content is the unique instinctive parameter distinguishing the three studied soils in this work, the relation between the fitted parameters with the sand content are also presented in Figure V.8. The figure shows that 3 parameters (*a*, *b* and *e*) increase/decrease constantly with the sand content. However, the other parameters (*c*, *d* and L_{max}) do not follow a continuous trend (decrease or increase) with the sand content, which is due to the climate changes in shallow depths. When the U-pipe length is beyond L_{max}, the corresponding parameters (*b* and *e*) increase/decrease constantly with the sand content.

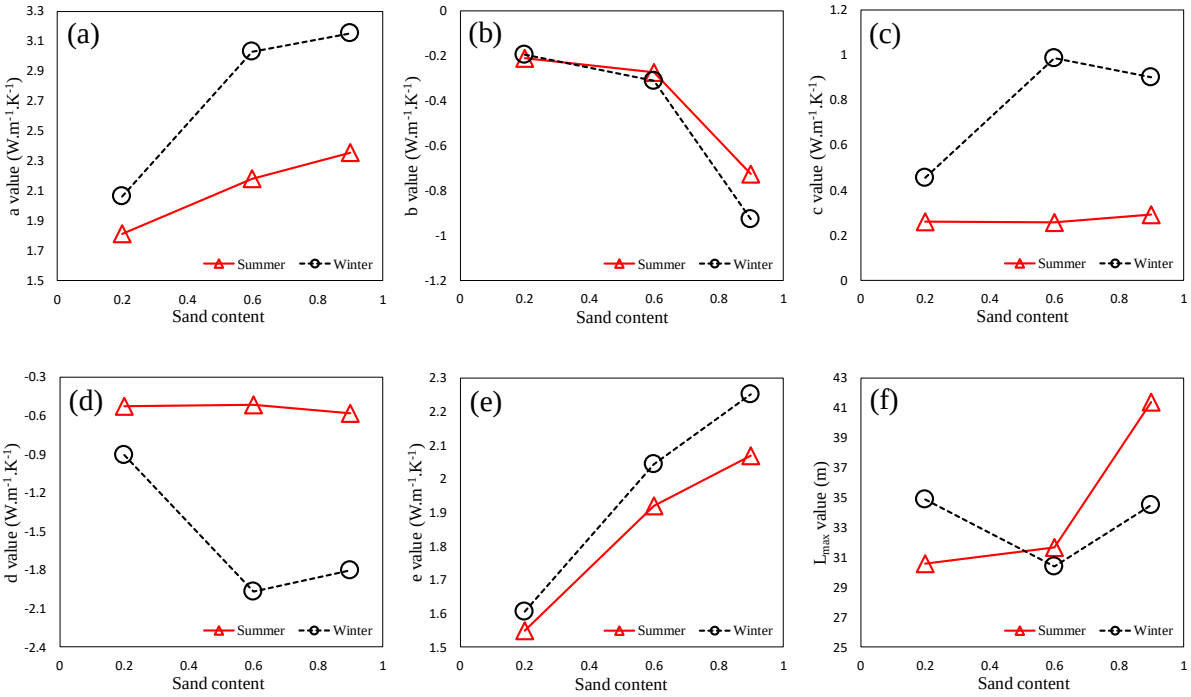

Figure V.8.Variation of the fitted parameters for the proposed approach with the sand content in summer and winter: (a) parameter *a*; (b) parameter *b*; (c) parameter *c*; (d) parameter *d*; (e) parameter *e* and (f) parameter L_{max}

The fitted curves of the proposed approach and the TRT simulation results are additionally shown in the 3D (effective thermal conductivity - λ ratio - U-pipe length) plane, presented in Figure V.9. The results show that the proposed approach predicts well the effective soil thermal conductivities with RMSE values less than 0.035 $W.m^{-1}.K^{-1}$.

The L_{max} values varying between 30 and 42 m confirm also the necessity of the proposed analytical solutions since the traditional TRTs are normally conducted for BHEs beyond 50 m and these TRTs are independent of the U-pipe length based on our calculations.

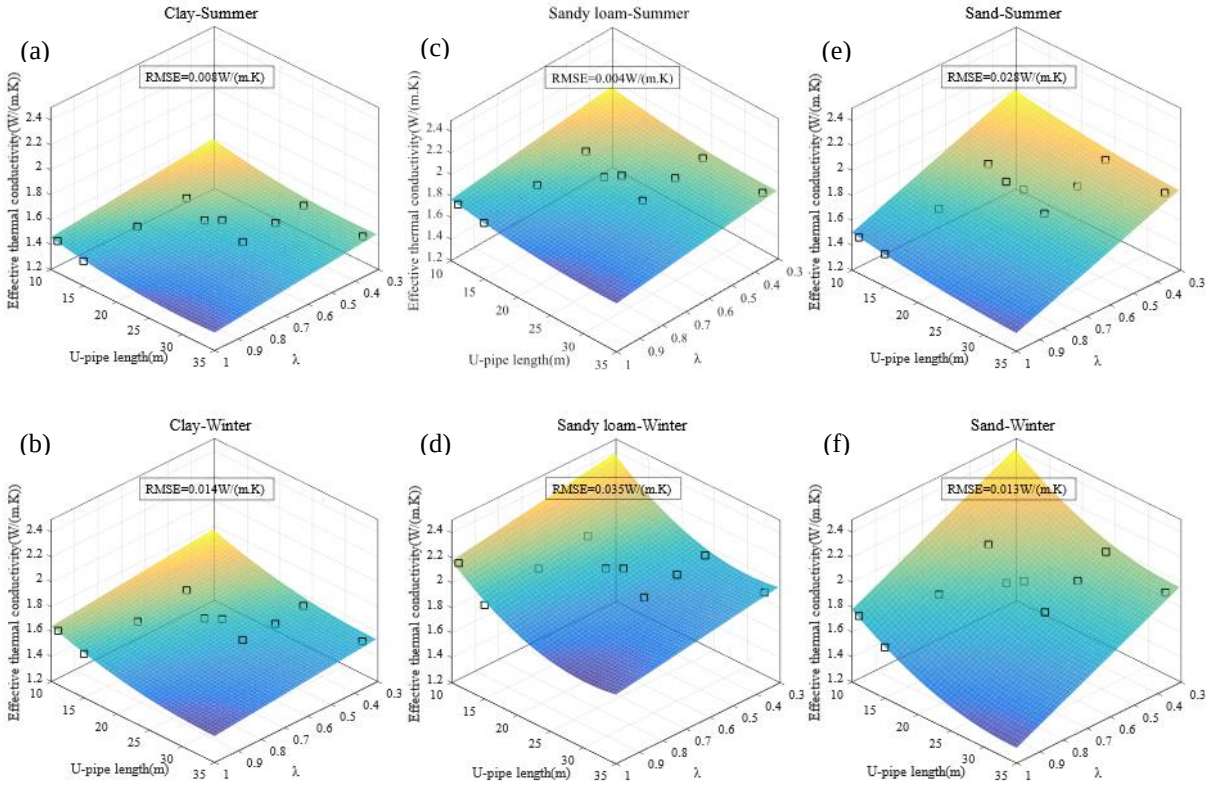

Figure V.9. Fitted curves and the simulation results in the (effective thermal conductivity - λ ratio - U-pipe length) plane: (a) clay in summer; (b) clay in winter; (c) sandy loam in summer; (d) sandy loam in winter; (e) sand in summer and (f) sand in winter

V.5.2. The application of the proposed approach to the in-situ measurements

The approach has been used to predict the effective soil thermal conductivity of 6 sites all around the world. As observed in Figure V.7 g-i, the effective soil thermal conductivity is less influenced by the testing time (winter or summer) when the U-pipe length exceeds L_{max}. Since all these studies have a U-pipe length longer than 50 m, it is not necessary to estimate two different thermal conductivities in summer and winter as the difference will be less than 5.5%. Therefore, an average value of the effective soil thermal conductivity in summer and winter is estimated for the three soils (Table V.7). The measured in-situ effective soil thermal conductivities are also reported in Table V.7. The results show that the in-situ soil thermal

conductivities for the 6 sites are between the smallest (clay k_{eff}) and the largest (sand k_{eff}) values, proving the capacity of the proposed approach.

The proposed approach can be also used to approximate the geotechnical field condition by comparing the in-situ thermal conductivity with the predicted values for the different soils. For example, it can be declared that the Japanese soil in Choi and Ooka's work (Choi and Ooka, 2016b) has a geotechnical texture between sand and sandy loam and the Cyprian soil in Florides and Kalogirou's work (Florides and Kalogirou, 2008) has more or less a clayey texture.

Table V.7. Comparison of the measured and predicted effective soil thermal conductivities (k_{eff}) for the 6 sites

Source	*Country*	z_u *(m)*	$z_{U\text{-}pipe}$ *(m)*	*Predicted* k_{eff} *(W.m^{-1}.K^{-1})*			*In-situ* k_{eff} *(W.m^{-1}.K^{-1})*
				Clay	*Sandy*	*Sand*	
Choi and Ooka (2016b)	Japan	10	50	1.54	1.92	2.00	1.96
Saito et al. (2014b, 2016)	Japan	11	50	1.53	1.92	1.98	1.71
Luo et al. (2018b)	China	35	120	1.52	1.90	1.92	1.64
Luo et al. (2018b)	China	10	120	1.56	1.96	2.09	2.07
Florides and Kalogirou	Cyprus	15	50	1.52	1.89	1.91	1.61
Soldo et al. (2016)	Croatia	15	100	1.55	1.94	2.04	1.92

V.5.3. The application of the approach to a multi-layered field in Alsace

To further verify the capacity of the proposed approach, TRTs were also simulated in Alsace region (France) for a BHE with a U-pipe length of 20 m and a water level of 7.63 m (presented in section 3). The U-pipe has also penetrated through 6 soil layers (Table V.2).

The validity of an equivalent one-layered soil in the TRT numerical simulations was confirmed in section 3 in this chapter. Figure V.2 compared the average carrying fluid temperatures of a one-layered equivalent soil with a multi-layered soil for TRTs conducted in summer and winter and for a period of 80 hours.

Figure V.10 shows additionally the average carrying fluid temperatures of the one-layered equivalent soil with the natural logarithm of time to deduce the effective soil thermal

conductivity. The derived effective soil thermal conductivities range between 1.71 $W.m^{-1}.K^{-1}$ in summer and 1.79 $W.m^{-1}.K^{-1}$ in winter. The effective thermal conductivity is rationally higher in winter than in summer. The effective soil thermal conductivities of the different studied soils in summer and winter are also reported in Figure V.10 as the reference values. The obtained effective soil thermal conductivities are close to the equivalent thermal conductivity derived from equation (5.10): 1.659 $W.m^{-1}.K^{-1}$ in summer and 1.662 $W.m^{-1}.K^{-1}$ in winter (presented in section 3). These facts give more credits to the proposed approach for the estimation of the effective soil thermal conductivity in a shallow BHE.

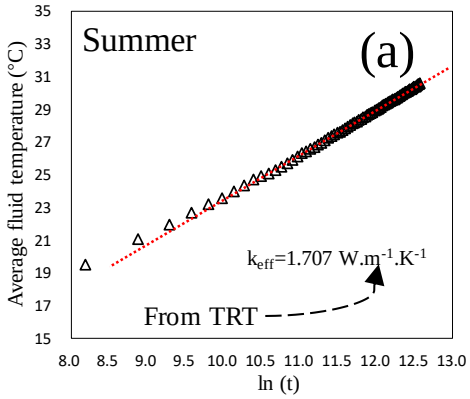

Summer

Prediction model	k_{eff} ($W.m^{-1}.K^{-1}$)
Clay	1.50
Sandy loam	1.85
Sand	1.82

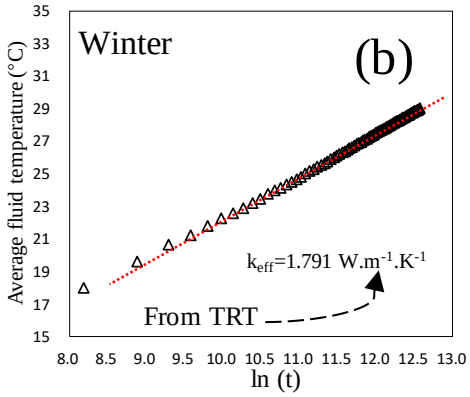

Winter

Prediction model	k_{eff} ($W.m^{-1}.K^{-1}$)
Clay	1.59
Sandy loam	2.04
Sand	2.01

Figure V.10. Comparison of the effective soil thermal conductivity from the numerical simulation and the analytical approach for a multi-layered soil in Alsace region (France), in (a) summer and (b) winter

V.6. Summary

In this investigation, the impacts of testing time, field condition and U-pipe length on TRTs have been studied. Eventually, an analytical approach was proposed to estimate the effective soil thermal conductivity in BHE applications.

Generally, the TRT numerical simulations were conducted in 3 soils, 2 seasons, 3 water levels and 6 U-pipe lengths. In total, 60 cases were simulated, and their corresponding effective soil thermal properties were obtained. The results show that the TRTs in winter have higher effective soil thermal conductivities, due to the heat injection process. The influence of the testing time becomes less significant as the U-pipe length increases. The effective soil thermal conductivity varies linearly with the λ ratio (= water level/ U-pipe length) and it decreases generally with the increase of the λ ratio in summer. On the contrary, it increases with the λ ratio for the tests in clay and sandy loam with a constant water level during winter. Moreover, the effective thermal conductivity varies with the U-pipe length in a (2^{nd} degree) polynomial form, and the influence of U-pipe length on effective soil thermal conductivity generally gets stabilized when the U-pipe is beyond 30 m.

By analyzing the TRT results, an analytical solution was proposed to estimate the effective soil thermal conductivity, with a RMSE less than 0.035 $W.m^{-1}.K^{-1}$. The approach has been used to estimate the effective soil thermal conductivities of 6 sites in Japan, China, Cyprus and Croatia, along with a shallow BHE installed in a multi-layered field in Alsace region (France). The comparisons proved the good capacity of the proposed approach to estimate the field effective thermal conductivities in the BHE projects with various field conditions and U-pipe lengths. The proposed approach is particularly interesting for short BHEs with limited capital investments.

VI. PERFORMANCE OF A HGHE WITH THE ATMOSPHERE-SOIL INTERACTION

VI.1. Introduction

The main objective of this investigation is to construct a numerical simulation framework to evaluate the HGHE performance in field conditions by considering energy and water balance on the ground surface. This investigation also aims to visualize how the HGHE influences the ground surface temperature and the heat flux through the ground surface, rarely studied so far. Moreover, the investigation has compared the numerical simulation results under two different surface boundary conditions (with/without considering atmosphere-soil interaction), which helps identify the reliability of the traditional method by setting time-varying temperature as ground surface boundary.

In this chapter, a validated finite element model established in COMSOL is used to estimate the performance of a HGHE installed in a multi-layered soil field. The often-neglected points such as ground surface energy/water balance, hydrothermal fluctuations and a slinky-type HGHE are addressed in this numerical framework.

It should be noted that the site studied in this chapter is the same as the site investigated in Chapter IV. However, the ground surface boundary conditions are different from the previous chapter. In this chapter, Neumann instead of Dirichlet boundary condition was applied for the hydrothermal boundary condition on the ground surface due to the shallow installation of the HGHE. Compared with Chapter IV, the boundary condition in this chapter is relatively complicated, however, closer to reality, and more accurate to estimate the performance of a shallow installed HGHE.

VI.2. Governing equations

HGHE is conventionally installed shallowly beneath the ground surface. The working of HGHE could influence the ground surface heat flux, thus influencing the ground surface temperature distribution, especially for estimating the long-term performance of a HGHE. The ground surface energy and water balance equations are therefore used for the numerical simulation work of HGHE. However, the equations in this section are not used for the numerical simulation framework of BHE, since it is installed deep beneath the ground surface, and its performance is less influenced by the two different boundary conditions (Dirichelet and Neumann boundary conditions).

Figure VI.1 shows a schematic diagram of the concerning phenomenon in HGHE engineering. The necessary governing equations considering the atmosphere-soil-HGHE interaction are constituted of 4 parts: a) the soil surface energy balance; b) the soil surface water balance; c) the hydrothermal transfer in subsurface soil and d) the heat transfer in pipe.

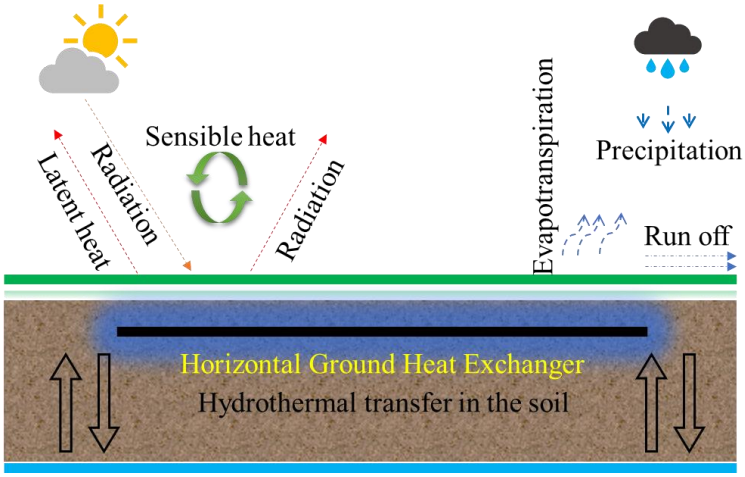

Figure VI.1. Schematic diagram for the considered mechanism of the energy and water transfer in this study

VI.2.1. Ground surface energy balance

Soil surface heat flux is a crucial variable and also a field of interest for a number of engineering and technical applications to deploy intermediate storage of heat or various uses of GCHP which entail a significant generation of heat. The soils thermal dynamics is important for a number of environmental processes. These processes include solar radiation heat flux into the ground, longwave radiation, latent heat flux resulting from evaporating

water, sensible heat flux from the convection of air, all of these influences depend strongly on the soil temperature as well as on soil water content (Bryś et al., 2020).

Different approaches to measure soil surface heat flux in terms of heat transfer during atmosphere-soil interaction were examined by Kustas and Daughtry (1990), Heusinkveld et al. (2004) at different sites. Compared with local-scale micrometeorological, climatological, and hydrological methods, remote sensing technology has more advantage in estimating large spatial coverage provided by satellite observations of ground surfaces (Liu et al., 2007). In this investigation, a series of models have been accumulated in getting the radiation heat flux, the sensible heat flux, the latent heat flux, and finally the ground heat flux flow into/off the ground surface. The detailed information about the models are introduced in this section.

Energy balance on the ground surface is given as (Chalhoub et al., 2017):

$$R_n + H - LE - G = 0 \tag{6.1}$$

where R_n is the net radiation heat flux ($W.m^{-2}$), H is the sensible heat flux ($W.m^{-2}$), LE is the latent heat flux ($W.m^{-2}$), G is the ground heat flux ($W.m^{-2}$). It should be noted that the net radiation and the sensitive heat flux have both positive and negative values while the latent heat flux has only positive values. The ground heat flux indicates the total heat flux flow through the ground surface. A positive value represents the heat flux into the ground. On the contrary, a negative value represents the heat flux out from the ground. To calculate the ground heat flux, it is necessary to obtain the net radiation heat flux, the sensitive heat flux and the latent heat flux.

At first, net radiation is the sum of short-wave radiation and long-wave radiation. The short-wave radiation is made of by direct and diffuse radiations. The long-wave radiation is emitted from the ground surface. The net radiation is the difference between the total incoming and outgoing radiations. It can be obtained by direct measurement or by calculation. Net radiometer is usually used after calibration for the direct measurement. The radiometer is with high sensitivity, usually ranges between 6% and 20% (Halldin and Lindroth, 1992). Moreover, only total solar radiation is monitored in a standard weather station, and the measurement of net radiation is conducted only in some specific circumstances. These facts limit the use of standard meteorological data for investigating atmosphere-soil interactions, and this also explains the high interest of researchers for the development of calculation methods for the

purpose of net radiation determination from standard meteorological data (An et al., 2017). The net radiation can be given by:

$$R_n = (1 - a_l)R_s + (R_a - \varepsilon\sigma T_s^4) \quad (6.2)$$

where a_l is the surface albedo, R_s is the shortwave radiation (W.m^{-2}), R_a is the incoming longwave radiation (W.m^{-2}), $\varepsilon\delta T_s^4$ is the outcoming longwave radiation (W.m^{-2}), ε is the soil surface emissivity, σ is Stephan-Boltzman constant (W.m^{-2}.K^{-4}), T_s is the soil temperature (K). The suggested values of α_l and ε for different soil surfaces are listed in Table VI.1.

Table VI.1. Values of soil albedo and surface emissivity at various soil surface (Most are daily averages) (Evett et al., 2011)

Surface	*Albedo*	*Emissivity*	*Source*
Soils, dark, wet to light, dry	0.05–0.50	0.90–0.98	Oke (1987)
Sand, wet	0.09	0.98	van Wijk (1963)
Sand, dry	0.18	0.95	van Wijk (1963)
Dark clay, wet	0.02–0.08	0.97	van Wijk (1963)
Dark clay, dry	0.16	0.95	van Wijk (1963)
Snow, fresh	0.95	0.99	Oke (1987)
Snow, old	0.40	0.82	Oke (1987)
Grass, long (1 m)	0.16	0.90	Oke (1987)
Grass, short (0.02 m)	0.26	0.95	Oke (1987)
Grass, green	0.16–0.27	0.96–0.98	van Wijk (1963)

There are many formulae proposed for net radiation, most of them are based on Stefan-Boltzmann law. An et al. (2017) have summarized the models into 2 methods: method relies merely on air temperature (Brutsaert, 1975; Jensen et al., 1990; Weiss, 1982; Wright and Jensen, 1972); method involves both air and soil surface temperatures (Bisht et al., 2005; Brutsaert, 1982; Cui et al., 2010; Hemmati et al., 2012; Ortega-Farias et al., 2000; Saito et al., 2006).

Some typical models calculating the net radiation are summarized in Table VI.2, including the methods consider merely the air temperature and the method considering both air and soil temperatures.

Table VI.2. Methods to calculate the net radiation

Method	*Equation* *	
Consider merely the air temperature	$R_n = (1-a_l)R_s - [1.35(\frac{R_s}{R_{so}}) - 0.35](0.35 - 0.14e_d^{0.5})\sigma(\frac{T_m^4 + T_n^4}{2})$ (Allen et al., 1994a, 1994b; Irmak et al., 2010)	(6.3)
Consider both the air and soil temperature	$R_n = (1-a_l)R_s - \sigma\varepsilon(T_s^4 - T_{sky}^4)$ (Gan, 2014)	(6.4)
	$R_n = (1-a_l)R_s - \varepsilon[\sigma(T_s)]^4 + \varepsilon_a[\sigma(T_a)]^4$ (Cui et al., 2010)	(6.5)

* R_{so}: solar radiation in case of clear sky (W.m^{-2}); T_m: the maximum air temperatures (K) in one day; T_n: the minimum air temperatures (K) in one day; T_{sky}: sky temperature (K); T_a: air temperature (K).

In order to capture the effect of soil surface temperature on the longwave radiation, the model considering both air and soil temperatures is used. Equation (6.4) is used for calculating net radiation in this investigation.

The sky temperature T_{sky} (K) is a fictitious temperature, introduced to model the long wave radiation exchanges with the sky (Adelard et al., 1998). There are different models for sky temperature. Some models are based on air temperature (Daguenet, 1985; Swinbank, 1963), some formulae take into account the water vapor tension of the air and the air temperature, which is considered to be more accurate (Adelard et al., 1998; Centeno, 1982; Daguenet, 1985). There are also formulae considering cloud cover, air temperature and water vapor tension of the air (Adelard et al., 1998). In this investigation, a formulae of sky temperature decided by cloud cover c_c and air temperature T_a (K) is used (Cole, 1976):

$$T_{sky}^4 = 9.365574\times10^{-6}(1-c_c)T_a^6 + c_c[(1-0.84\cdot c_c)(0.527+0.161\cdot \mathrm{e}^{8.45(1-\frac{273.15}{T_a})}) + 0.84\cdot c_c]T_a^4 \quad (6.6)$$

Secondly, it is the sensible heat flux, which is the convective heat transfer between the ground surface and the ambient air (Choi et al., 2018). In a remote sensing method, the sensible heat flux density is usually estimated by following the Ohm's Law, i.e. using a ratio of the surface-air temperature difference $(T_a - T_s)$ and an aerodynamic resistance to heat transfer (r_a) (Liu et al., 2007). The sensible heat flux can be given as:

$$H = \rho_a C_{p-a}(T_a - T_s)/r_a \quad (6.7)$$

where ρ_a is the air density (kg.m^{-3}), C_{p-a} is the air specific heat capacity (J.kg^{-1}.K^{-1}), r_a is the aerodynamic resistance to heat transfer (s.m^{-1}).

Eight parameterizations for aerodynamic resistance based on the Monin-Obukhov Similarity (MOS) theory are introduced and compared in the work of Liu et al. (2007). According to the MOS theory, the integral gradient of the wind and temperature profiles in a horizontally homogeneous surface layer can be formulated as:

$$u_{wind} = \frac{u_*}{\kappa}[\mathrm{In}(\frac{z_m - d}{z_{om}}) - \psi_m(\varsigma, \varsigma_{0m})] \tag{6.8}$$

$$T_a - T_{aero} = P_{r0}\frac{T_*}{\kappa}[In(\frac{z_m - d}{z_{oh}}) - \psi_h(\varsigma, \varsigma_{oh})] \tag{6.9}$$

where u_{wind} is the wind speed ($m.s^{-1}$), u_* is the friction velocity ($m.s^{-1}$), κ is the von Karman constant, z_m is the height where the meteorological parameters are measured (m), d is the displacement height (m), z_{om} is the roughness length for momentum (m), ς, ς_{0m} and ς_{0h} are stability parameters defined as $\varsigma = z_{m\_d}/L$, $\varsigma_{0m} = z_{om}/L$ and $\varsigma_{0h} = z_{oh}/L$, respectively ($z_{m-d} = z_m - d$), L_{M-O} is the Monin-Obukhov length (m), T_{aero} is the aerodynamic surface temperature (K), P_{r0} is the turbulent Prandt number describing the difference between the eddy diffusivities of momentum and of heat, z_{oh} is the roughness length for water vapor (m). The aerodynamic resistance to heat transfer can be given as:

$$r_a = \frac{1}{\kappa^2 u_{wind}}[\mathrm{In}(\frac{z_m - d}{z_{om}}) - \psi_m(\varsigma, \varsigma_{0m})] \cdot [\mathrm{In}(\frac{z_m - d}{z_{oh}}) - \psi_h(\varsigma, \varsigma_{0h})] \tag{6.10}$$

In neutral conditions, $\psi_m(\varsigma, \varsigma_{0m}) = \psi_h(\varsigma, \varsigma_{0h}) = 0$, the aerodynamic resistance to heat transfer can be simplified to the following equation, which has also been used in this investigation (Allen, 1986; Liu et al., 2007):

$$r_a = \frac{\ln(\frac{z_m - d}{z_{om}}) \cdot \ln(\frac{z_m - d}{z_{oh}})}{\kappa^2 u_{wind}} \tag{6.11}$$

The displacement height is linear to the vegetation height h_c (m) (Chalhoub et al., 2017):

$$d = 2h_c / 3 \tag{6.12}$$

The roughness length for momentum transfer is calculated by the following equation (Chalhoub et al., 2017):

$$z_{om} = 0.123h_c \tag{6.13}$$

The roughness length for vapor transfer is given as (Chalhoub et al., 2017):

$$z_{oh} = 0.1 z_{om} \tag{6.14}$$

Finally, the latent heat flux is represented by *LE*, constituted by the latent heat vaporization of water L ($J.kg^{-1}$) and the actual evaporation E ($mm.s^{-1}$). Evaporation is a collective term covering all processes in which liquid water is transferred as water vapor to the atmosphere. Transpiration is the evaporation from within the leaves of a plant via water vapor flux through leaf stomata. Evapotranspiration is defined as the sum of transpiration and evaporation from the soil surface (McMahon et al., 2013). In arid and semiarid regions, evapotranspiration is often nearly equal to precipitation, while in humid areas, it is limited by available energy (Zhang et al., 2001). Under very dry conditions, potential evapotranspiration exceeds precipitation, and actual evapotranspiration equals precipitation. Under very wet conditions, water availability exceeds potential evapotranspiration, and actual evapotranspiration will asymptotically approach the potential evapotranspiration (Zhang et al., 2001).

Actual evaporation of soil sample can be measured directly by sensitive weighing scales (Kondo et al., 1990) or weighing lysimeters (Benson et al., 2001). Specifically, sensitive weighing scales are applied for soil sample in small size in the laboratory. The weighing lysimeters are used for measuring soil water evaporation of soil sample in a large scale in the field or in the laboratory. However, in these two approaches, the bottom of soil sample is isolated with the surrounding environment, limiting the accuracy of measurement results (Benson et al., 2001). In addition, different kinds of prediction models were also reported in literature allowing the estimation of potential evaporation and actual evaporation. For the potential evaporation, the mass transfer models are frequently applied because of their simplicity and reasonable accuracy. In the mass transfer models, there are three governing factors: vapor pressure gradient, temperature and wind speed. In general, the mass transfer model is in a simple form with several measurable variables, allowing the estimation of potential evaporation. Besides, different models for the estimation of soil evaporation (actual evaporation) can be classified into three types: the resistance models, the vapor pressure models and the models considering energy exchanges.

Potential evaporation is defined as the amount of evaporation that would occur if a sufficient water source were available, it has been used to provide a reference level for actual evaporation in many studies of ground surface heat and water balance (Choudhury, 1997).

Obviously, the actual evaporation is not bigger than the potential evaporation. There are also different approaches in evaluating potential evaporation (Monteith, 1965; Penman, 1948; Priestley, 1972). Jensen et al. (1990) identify that the Penman-Monteith equation (Monteith, 1965; Penman, 1948) provides the most accurate estimate of monthly evaporation from well-watered grass under varied climatic conditions after comparing 20 different methods of estimating potential evaporation. The Penman-Monteith model (Monteith, 1965) is usually adopted to estimate potential evaporation from a vegetated surface (McMahon et al., 2013). It should be noted that the evaporation potential calculated by Penman-Monteith model assume that the grass cover is well-watered or the water supply for the soil is unrestricted (Chalhoub et al., 2017; Choudhury, 1997), this is not the case at the field condition in our investigation. Therefore, an actual evaporation model based on catchment area was introduced in this work to simulate the real field condition. Besides introducing the model used in this investigation, some other methods have been adopted to get the actual evaporation. For example, Chalhoub et al. (2017) assume that actual evaporation equals potential evaporation when the soil surface is wet (rainy days), otherwise it is less than potential evaporation and depends on soil water content. The Penman-Monteith model is given as:

$$E_p = \frac{1}{L}\left[\frac{\Delta \cdot R_n + \rho_a C_{p-a}(e_s - e_a)/r_a}{\Delta + \gamma(1 + r_c / r_a)}\right] \tag{6.15}$$

where Δ is the slope of the saturation vapor pressure curve (kPa.K^{-1}), e_s is the saturation vapor pressure (kPa), e_a is the actual vapor pressure (kPa), γ is the psychrometric constant (kPa.K^{-1}), r_c is the crop canopy resistance (s.m^{-1}).

Budyko curve (Budyko, 1974) is a curve based on the water balance and the energy balance, which is often used to describe the relationship between the long-term water partitioning, represented by the ratio of actual evaporation over precipitation, and long-term climate, represented by the ratio of potential evaporation over precipitation, namely the aridity index (Budyko, 1958, 1974). There have been many investigations conducted to find this relation (Budyko, 1974; Fu, 1981; Ol'dekop, 1911; Pike, 1964; Potter and Zhang, 2009; Schreiber, 1904; Turc, 1954; Zhang et al., 2001, 2004). The following equation (Chen and Buchberger, 2018; Gerrits et al., 2009; Pike, 1964; Turc, 1954) for catchment area has been used to estimate the field actual evaporation in this investigation:

$$E = P \cdot \left[1 + (E_p / P)^{-v}\right]^{-\frac{1}{v}} \tag{6.16}$$

where P is the rainfall rate (mm.s^{-1}), E_p is the evaporation potential (kg.m^{-2}.s^{-1} or mm.s^{-1}), v is a parameter referring landscape properties such as vegetation coverage and soil properties. The parameter v needs to be a positive number, and its typical value is 2 (Chen and Buchberger, 2018). The ratio of actual evaporation over precipitation to the ratio of potential evaporation over precipitation for the above equation has been shown in Figure VI.2. The figure indicates that the actual evaporation is close to precipitation when the ratio of potential evaporation over precipitation is large enough. However, the actual evaporation is much smaller than precipitation when the potential evaporation is small.

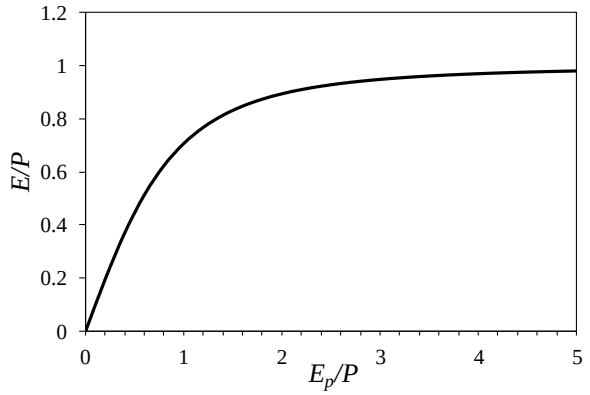

Figure VI.2. The ratio of actual evaporation over precipitation to the ratio of potential evaporation over precipitation for equation (6.16)

The slope of the saturation vapor pressure is given by:

$$\Delta = 4098 e_s / (T_a - 35.85)^2 \tag{6.17}$$

The saturation vapor pressure is related to air temperature T_a (K):

$$e_s = 0.6108 \cdot \exp\left(17.27(T_a - 273.15) / (T_a - 35.85)\right) \tag{6.18}$$

The actual vapor pressure is positive to air humidity RH (%):

$$e_a = RH \cdot e_s / 100 \tag{6.19}$$

The psychrometric constant is calculated by:

$$\gamma = C_{p-a} \cdot P_{at} / (L \cdot r_{mw}) \tag{6.20}$$

where P_{at} is the atmospheric pressure (Pa), r_{mw} is the molecular weight of water vapor to dry air.

The crop canopy resistance is:

$$r_c = r_1 / (0.5 \cdot LAI) \tag{6.21}$$

where r_1 is the stomatal resistance of a single leaf (s.m^{-1}), LAI is the leaf area index [26,35] (Allen et al., 1989; Chalhoub et al., 2017):

(a) For clipped grass (h_c = 0.05 - 0.15 m):

$$LAI = 24 \cdot h_c \tag{6.22}$$

(b) For other crops:

$$LAI = 5.5 + 1.5 \ln(h_c) \tag{6.23}$$

VI.2.2. Ground surface water balance

It is assumed that the precipitation (P) is the only water source at the field condition, which is kept balanced with water run off (W_r), actual evaporation (E), and infiltration (W_i) through the ground surface (Dietrich et al., 2016). Therefore:

$$P = W_r + E + W_i \tag{6.24}$$

The water flux can therefore be calculated if the precipitation, actual evaporation and water runoff are obtained. As the precipitation can be obtained conveniently from the local weather station and the actual evaporation has been illustrated in the previous part, it is necessary to determine water runoff amount. Runoff is a complex interaction between precipitation and landscape factors. Water runoff can be predicted by different models for different catchments and different rainfall conditions. The lumped-parameter model and the spatially distributed model are two main models for rainfall runoff prediction according to Knapp et al. (1991) and Tedela (2009). The lumped-parameter model ignores the spatial heterogeneity of the catchment response to achieve an important advantage of simplicity (Ponce and Hawkins, 1996), while the spatially distributed model attempts to simulate most of the heterogeneous responses at a local scale (Beven, 1989; Garbrecht et al., 2001). As a rule of thumb, a lump model is applicable to a small watershed characterized by its quick response to rainfall while a distributed model is recommended for large watersheds. Rational method is one of the

lumped-parameter model, and it has been employed for over 150 years to determine maximum runoff flow rates for designing urban drainage structures such as storm sewers and culverts, and it is found in the majority of urban drainage manuals and textbooks because it is easy to use and condenses essential components of runoff estimation and drainage system principles, which are good for teaching the fundamentals of storm water management. The strength of rational method lies in its simplicity and the ease of implementation (Asare-Kyei et al., 2015). Compared with the alternative methods, rational method has theoretical advantages of estimating maximum flow rate at a certain probability (Wang and Wang, 2018). The rational model operates on a number of assumptions including (Asare-Kyei et al., 2015): the entire unit of analysis is considered as a single unit; rainfall is uniformly distributed over the drainage area; predicted peak runoff has the same probability of occurrence (return period) as the used rainfall intensity; the runoff coefficient is constant during the rainstorm.

The rational method in determining surface runoff can be given as:

$$W_{r\_f} = CP \tag{6.25}$$

where W_{r_f} is the peak runoff flux ($m.s^{-1}$), C is the runoff coefficient. A reference for surface runoff coefficients by the Ministry of Education, Culture, Sports, Science and Technology, Japan is listed in Table VI.3 (Tsutsumi et al., 2004). It is supposed in this investigation that water runoff includes the water intercepted by canopy during the rainfall.

Table VI.3. Surface runoff coefficients by the Ministry of Education, Culture, Sports, Science and Technology, Japan (Tsutsumi et al., 2004)

Type of ground surface	*Coefficient of surface runoff*
Road:	
Pavement	0.70–0.90
Permeable pavement	0.30–0.40
Gravel road	0.30–0.70
Shoulder or top of slope:	
Fine soil	0.40–0.65
Coarse soil	0.10–0.30
Hard rock	0.70–0.85
Soft rock	0.50–0.75
Grass plot of sand:	
Slope 0–2%	0.05–0.10

Slope 2–7%	0.10–0.15
Slope 7%	0.15–0.20
Grass plot of clay:	
Slope 0–2%	0.13–0.17
Slope 2–7%	0.18–0.22
Slope 7%	0.25–0.35
Roof	1.00
Unused bare land	0.20–0.40
Athletic field	0.40–0.80
Park with vegetation	0.10–0.25
Mountain with a gentle slope	0.30
Mountain with a steep slope	0.50
A paddy field or water	0.70–0.80
Farmland	0.10–0.30

VI.2.3. The other physic equations

The principal equations of the other equations related to ground heat exchangers considering hydrothermal fluctuation in soil, energy balance in soil and energy balance in pipe have been introduced in the previous chapters.

VI.3. Validation of the proposed numerical framework

The atmosphere-soil-HGHE interaction is considered in our numerical simulation framework. To evaluate the capacity of the proposed model, the atmosphere-soil interaction was firstly evaluated by using a local instrumented temperature probe (Lin et al., 2018). Subsequently, the soil-HGHE interaction was evaluated by an indoor experiment conducted by Yoon et al. (2015b).

VI.3.1. Validation for the atmosphere-soil interaction

A local site in Alsace region (France) was chosen for this validation since we have access to the geological, metrological and hydraulic conditions of this field (Lin et al., 2018; Nowamooz et al., 2015). The soil at the top 20 m is constituted of 4 soils and 6 soil layers (Figure VI.3): layer 1 with 0.1 m of clay loam; layer 2 with 1 m of sandy loam; layer 3 with 0.15 m of loam; layer 4 with 4.75 m of sandy loam; layer 5 with 8 m of a second sandy loam

and layer 6 with 6 m of loam. The same geological condition has also been presented in Chapter III.

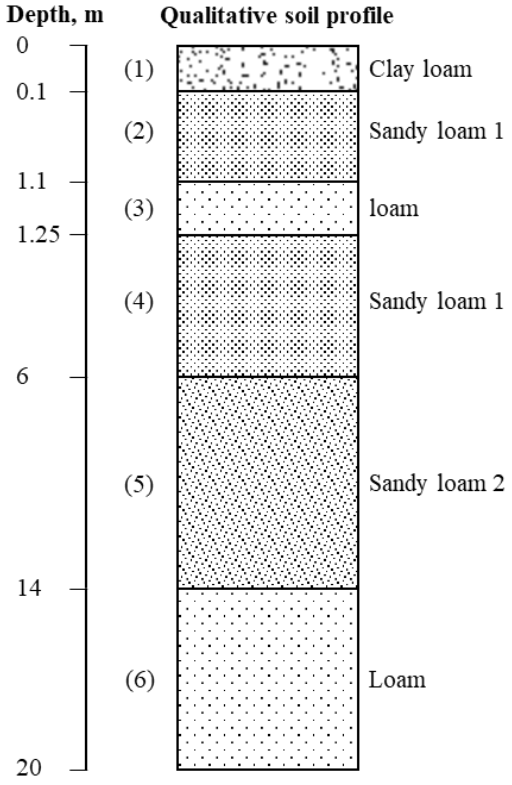

Figure VI.3. Six soil layers at the investigated site

A temperature probe was installed at a depth of 1.03 m on this site. To validate the capacity of the model for the atmosphere-soil interaction, the model was run for three years without the installation of the HGHE.

Table VI.4 and Table VI.5 present the parameters for the atmosphere-soil interaction. Table VI.4 presents the parameters for the soil surface energy balance and Table VI.5 summarizes the hydrothermal properties of the subsurface soils.

Table VI.4. Parameters for the soil surface energy balance

Parameter	*Description*	*Value*	*Unit*
a_l	Albedo	0.25	-
ε	Soil emissivity	0.97	-
σ	Stephan-Boltzman constant	5.67×10^{-8}	$W.m^{-2}.K^{-4}$
ρ_a	Air density	1.25	$Kg.m^{-3}$
$C_{p\text{-}a}$	Air specific heat capacity	1.003×10^{3}	$J.kg^{-1}.K^{-1}$

z_m	Height to collect the meteorological data	2	m
h_c	Grass height	0.06	m
κ	von Karman constant	0.41	-
L	Latent heat of vaporization	2.260	$J.kg^{-1}$
P_{at}	Atmospheric pressure	102000	Pa
r_{mw}	Molecular weight of water vapor to dry air	0.622	-
r_1	Stomatal resistance of a single leaf	100	$s.m^{-1}$

Table VI.5. Hydrothermal properties of the subsurface soils

Material	$K\ (m.s^{-1})$	$l\ (-)$	$\alpha\ (m^{-1})$	$n\ (-)$	$\theta_s\ (-)$	$\theta_r\ (-)$	$x_s\ (-)$	$\gamma_s\ (kN.m^{-3})$	$\gamma_d\ (kN.m^{-3})$
Clay loam	1.53E-6	0.5	1.99	1.22	0.50	0.03	0.35	27.0	13.5
Sandy loam 1	1.78E-5	0.5	2.60	1.52	0.39	0.02	0.80	26.2	16.0
Loam	2.19E-6	0.5	2.35	1.38	0.47	0.02	0.50	26.8	14.2
Sandy loam 2	1.45E-5	0.5	2.48	1.50	0.40	0.02	0.60	26.7	16.0

The ambient temperatures of the investigated site have been monitored during several years (Cuny et al., 2015; Lin et al., 2018). Based on the in-situ measurements, the following equation is used for approximating ambient temperature (Cuny et al., 2015; Lin et al., 2018):

$$T_a = 13.4\text{-}9.43\cdot\sin(2\cdot\pi/(365\times24\times3600)\cdot t+4.63)+ (\text{-}3.52+2.1\times\sin(2\cdot\pi/(365\times24\times3600)\cdot \text{t-}1.25))\cdot\sin(2\cdot\pi/(24\times3600)\cdot \text{t+}1) \quad (6.34)$$

where t is time (s). The comparison between the approximated and measured ambient temperatures from July 2014 to July 2017 is shown in Figure VI.4:

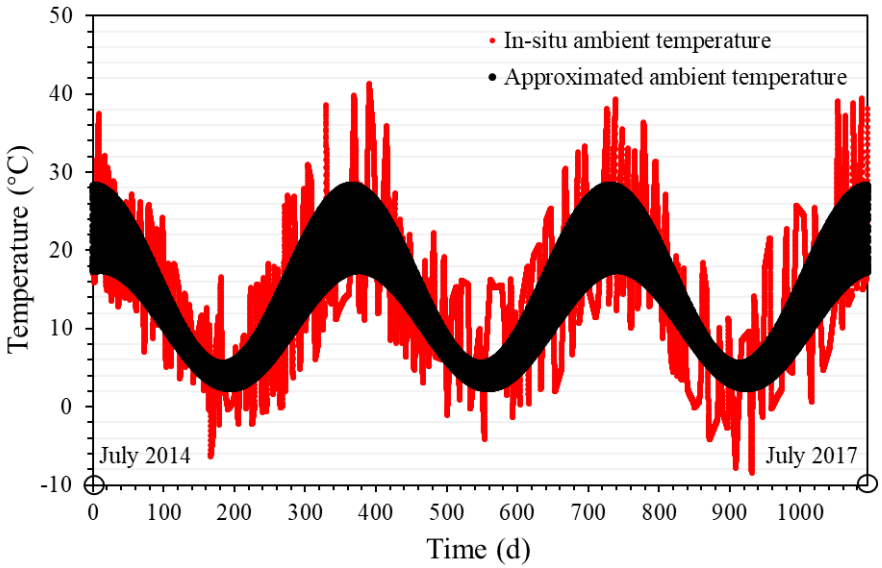

Figure VI.4. Comparison between the approximated and measured ambient temperatures for a duration of 3 years from July 2014 to July 2017 (Cuny et al., 2015; Lin et al., 2018)

Moreover, the local shortwave radiation is given as:

$$R_s = 130 + 80 \cdot \cos(2 \cdot \pi / (365 \times 3600 \times 24) \cdot t) \quad (6.35)$$

At the site, there is no obvious seasonal fluctuation of cloud cover, wind speed, precipitation and air humidity with time. Therefore, an average cloud cover of 0.41, an average wind speed of 2 $m.s^{-1}$, an average monthly precipitation of 55.7 mm, and an average air humidity of 83% are applied in the numerical simulation model to capture the main meteorological condition of the local site.

Estimating water runoff on the ground surface depends not only on soil characteristics (type, initial water content, slope catchment size and surface vegetation), but also on rainfall rate and duration (Chiew and McMahon, 1994). Water runoff coefficient is a dimensionless coefficient relating the amount of runoff to the amount of precipitation received. Li et al. (2017b) find through indoor experiment that water runoff coefficient decreases with the increase of the grass coverage ratio, and the influence of grass coverage on the reduction of runoff shows a high degree of spatial variation. The annual water runoff coefficient ranges between 0.1 and 0.25 for a park with vegetation inside (Tsutsumi et al., 2004). For the investigation site in this work, it was assumed that the annual water runoff coefficient was 0.2. Therefore, 20% of the precipitation runoff, and the other 80% participates into evapotranspiration or infiltration.

Table VI.6 summarizes all the imposed hydrothermal boundary conditions in this part. The temperature gradient at the bottom boundary is set 0.142 $K.m^{-1}$ (Baillieux et al., 2013), and the extra water from the precipitation is drained at the bottom boundary. The groundwater level is set constant at the depth of 7.5 m in the whole year. No hydrothermal flow is imposed on the lateral boundaries.

Table VI.6. Hydrothermal boundary conditions for the scenario with the atmosphere-soil interaction

Surface	*Hydraulic condition, value (unit)*	*Thermal condition, value (unit)*
Top	Neumann, equation (6.24) ($m.s^{-1}$)	Neumann, equation (6.1) ($W.m^{-2}$)

Lateral	Adiabatic, -	Adiabatic, -
Bottom	Dirichlet, model height – groundwater level (m)	Neumann, bottom temperature gradient × bottom soil thermal conductivity ($W.m^{-2}$)

An equilibrium method is used to obtain the initial hydrothermal profiles. Figure VI.5 shows the suction and temperature profiles derived from this approach.

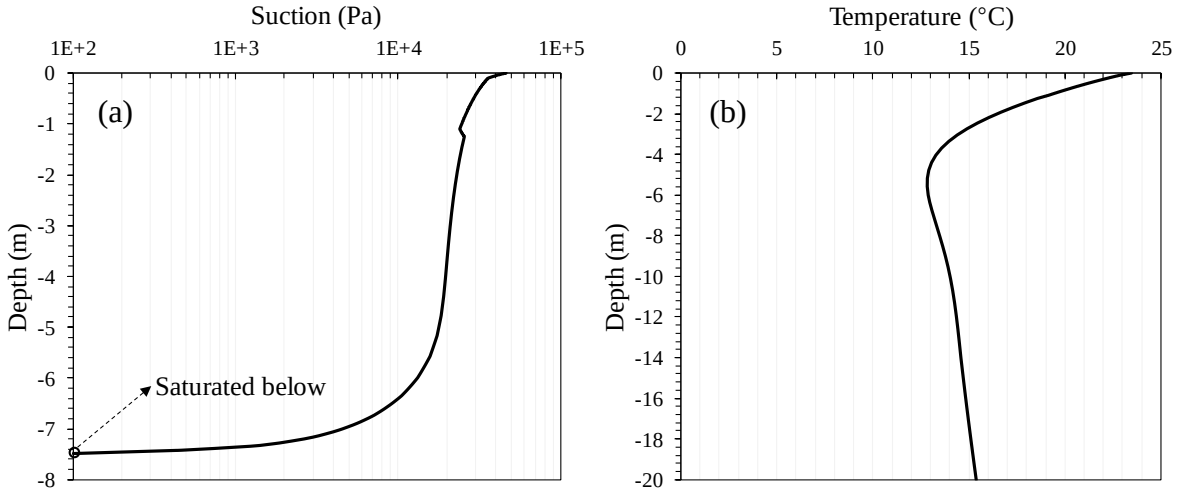

Figure VI.5. Initial hydrothermal profiles: (a) suction profile and (b) temperature profile

After the obtention of the initial suction profile, the corresponding initial profiles for the volumetric water content (Figure VI.6-a), the soil thermal conductivity (Figure VI.6-b) and the soil volumetric heat capacity (Figure VI.6-c) are deduced by using the equations (6.30), (6.31), and their parameters reported in Table VI.5.

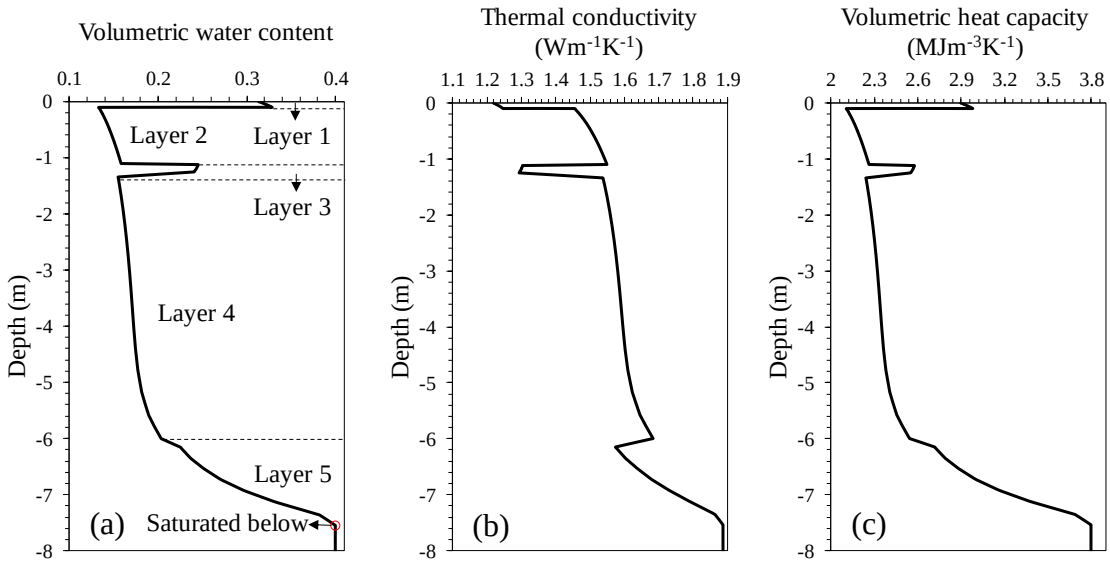

Figure VI.6. Initial hydrothermal profiles deduced from the initial suction profile: (a) volumetric water content profile; (b) thermal conductivity profile and (c) volumetric heat capacity profile

Figure VI.7 shows the comparison of the numerical prediction for a duration of 3 years from July 2014 to July 2017. The comparison shows that the numerical framework is capable to predict the soil temperature with the RMSE value of 1.6 °C.

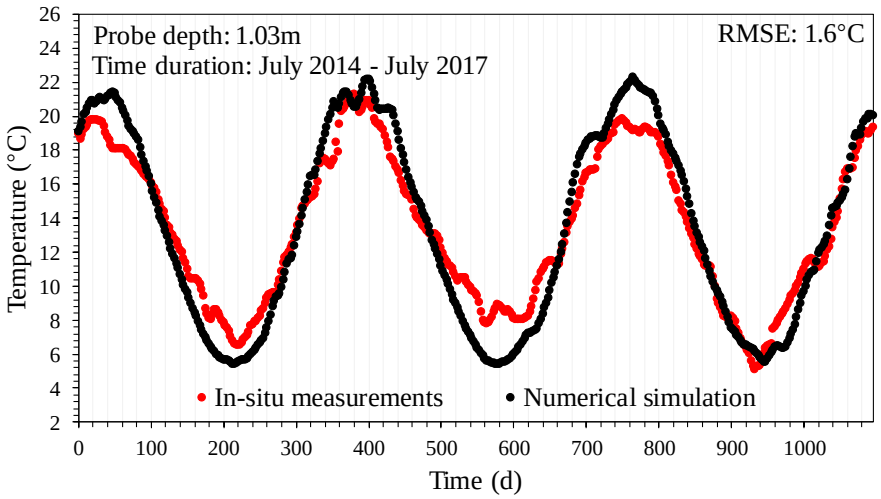

Figure VI.7. Comparison between the numerical predictions and the in-situ measurements (Lin et al., 2018) for 3 years (from July 2014 to July 2017)

VI.3.2. Validation for the soil-HGHE interaction

The soil-HGHE interaction of the proposed numerical framework was evaluated by an indoor experiment reported by Yoon et al. (2015b). In their work, two experiments were conducted in a sandy box for slinky-type HGHEs with pipe lengths of 24 and 66 m. They have further used a far-infrared radiation heater to maintain constant the indoor temperature. In their experiment, a polybutylene pipe with inner and outer diameters of 16 and 20 mm was installed at the depth of 0.5 m in a sand box. The sand box has a length of 5 m, a width of 1 m and a depth of 1 m. The surrounding dry sand has a thermal conductivity of 0.26 $W.m^{-1}.K^{-1}$, specific heat capacity of 785 $J.kg^{-1}.K^{-1}$ and a density of 1.397 $g.cm^{-3}$. The carrying fluid was water with a velocity of 0.3921 $m.s^{-1}$. The initial box temperature was between 17 and 18 °C. The time duration is 30 h for the two experiments. Table VI.7 summarizes the imposed thermal boundary conditions for this indoor experiment. Water transfer in soil is not considered in this experiment.

Table VI.7. Thermal boundary condition for the indoor experiment reported by Yoon et al. (2015b)

Surface or element	*Thermal condition, value (unit)*
Top	Dirichlet, 17.5 (°C)
Lateral	Adiabatic, -
Bottom	Adiabatic, -
HGHE inlet	Dirichlet, time-varying values (Yoon et al., 2015b) (K)

Figure VI.8 shows the comparison of the carrying fluid outlet temperatures between the in-situ measurements and the numerical predictions. A good correspondence between the experiment and prediction proves that the established numerical model considers appropriately the soil-HGHE interaction in its framework.

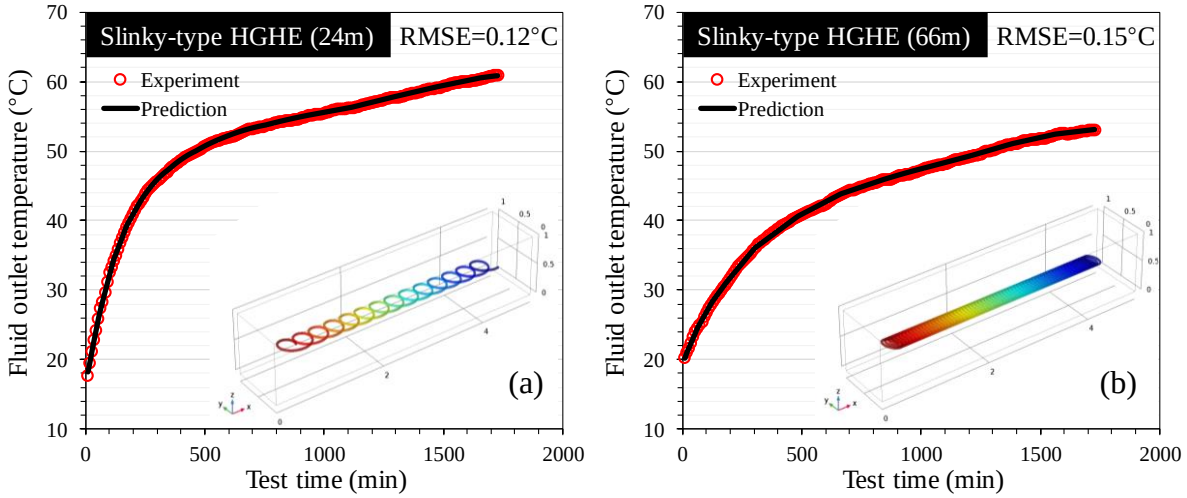

Figure VI.8. The comparison between the experiment and the numerical prediction for the carrying fluid outlet temperatures: (a) slinky-type HGHE with a total pipe length of 24 m and (b) slinky-type HGHE with a total pipe length of 66 m

VI.4. Numerical simulation results with the atmosphere-soil-HGHE interaction

After validating the numerical framework, the simulation results are subsequently presented in this section considering the atmosphere-soil-HGHE interaction. The same site presented in section 3.1 is investigated in this section. To identify the effect of the atmosphere-soil interaction, another scenario is also tested without considering the atmosphere-soil interaction.

VI.4.1. Geometry, mesh and operation options

The studied geometry has a length of 30 m, a width of 12 m and a height of 20 m. This deep geometry was selected to have no hydrothermal impact of the seasonal metrological condition on the bottom boundary. The hydrothermal conditions on the lateral boundaries were also not influenced during the simulation. A slinky-type HGHE with 0.03 m of inner diameter and 0.036 m of outer diameter is installed 1 m below the surface, covered with the backfill soil (sandy loam 1). The geometry strictly followed the geological profile illustrated in the site description. A swept mesh was deployed to obtain reasonable computation time. It should be noted that the generated meshes are denser in the shallow depths since the shallow ground is more sensitive to hydrothermal fluctuation on the ground surface. In addition, the meshes around the HGHE are also denser due to the steep temperature and suction gradients (Choi

and Ooka, 2016a). In total, 75894 meshes were generated for this numerical simulation model. The geometry and its mesh are shown in Figure VI.9.

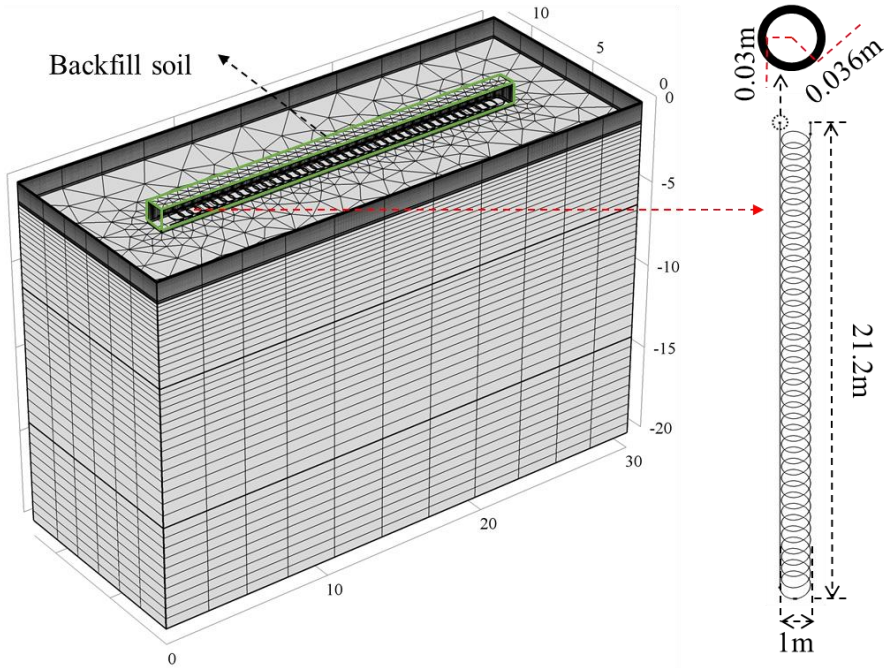

Figure VI.9. Geometry and its mesh for the numerical simulations

The meteorological condition corresponds completely to the local condition presented. The same parameters reported in Tables VI.5 & VI.6 are used for the atmosphere-soil interaction. The same aforementioned cloud cover, wind speed, precipitation and air humidity are also applied. The ambient temperatures for three successive years presented in Figure 7.3 are approximated for one year in Figure VI.10-a. Figure VI.10-b presents the shortwave radiation with time for one year derived from equation (6.35).

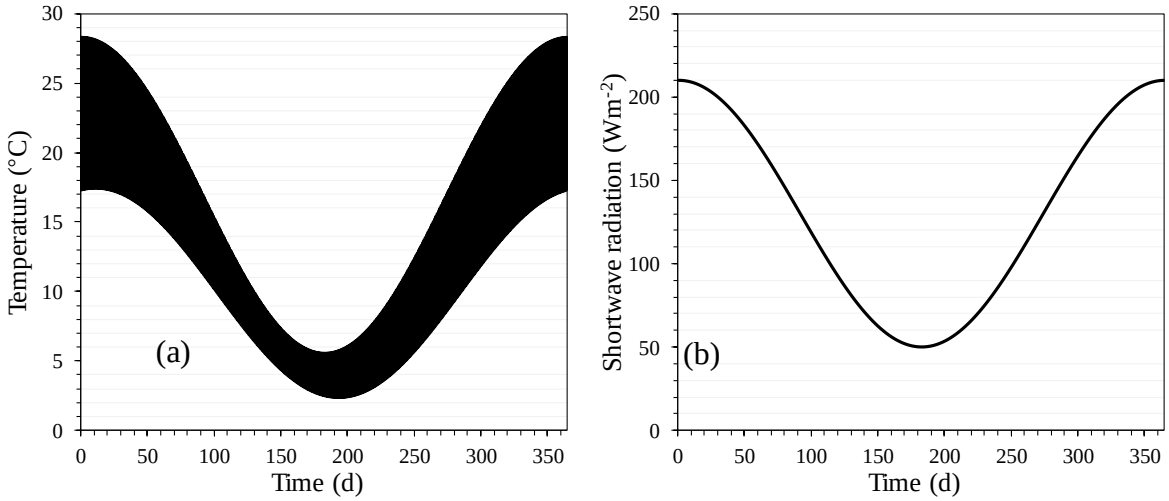

Figure VI.10. (a) Ambient temperature fluctuation for one year and (b) shortwave radiation fluctuation for one year

The pipe was a HDPE pipe with the thermal conductivity of 0.4 $W.m^{-1}.K^{-1}$. PG with a volume concentration of 25% was selected as the carrying fluid. It has a dynamic viscosity of 0.0055 Pa.s, a density of 1026 $kg.m^{-3}$, a thermal conductivity of 0.45 $W.m^{-1}.K^{-1}$ and a specific heat capacity of 3974 $J.kg^{-1}.K^{-1}$ (Casasso and Sethi, 2014). The carrying fluid velocity was 0.5 $m.s^{-1}$ during the operation period.

A heating scenario was considered in our simulations according to the local climate condition. The HGHE works from the 100^{th} day to the 265^{th} day in a year. A seasonal heat extraction rate varying from 10 to 40 $W.m^{-1}$ was applied to the HGHE during its operation period (Figure VI.11). The time step for the numerical simulation model is 0.5 day.

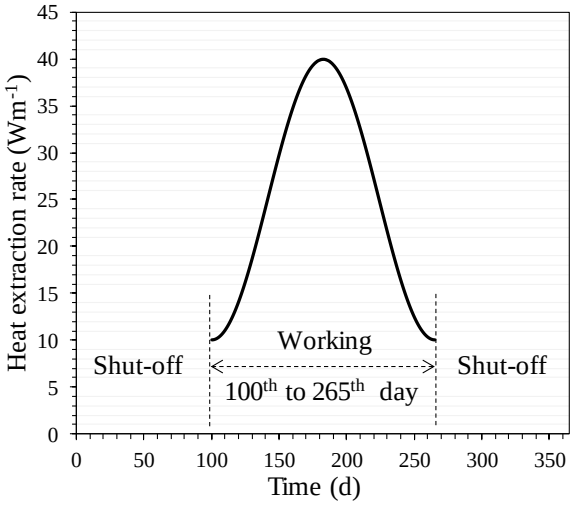

Figure VI.11. Heat extraction rate ($W.m^{-1}$) during the operation period of the HGHE

VI.4.2. The fluctuation of the hydrothermal properties and the HGHE performance

To visualize the spatial and temporal hydrothermal fluctuation in soil, five horizontal line probes were positioned at five different depths: surface (or zero), 1, 2.5, 5 and 10 m (Figure VI.12). All the probes were installed in the same vertical plane through the center of the HGHE.

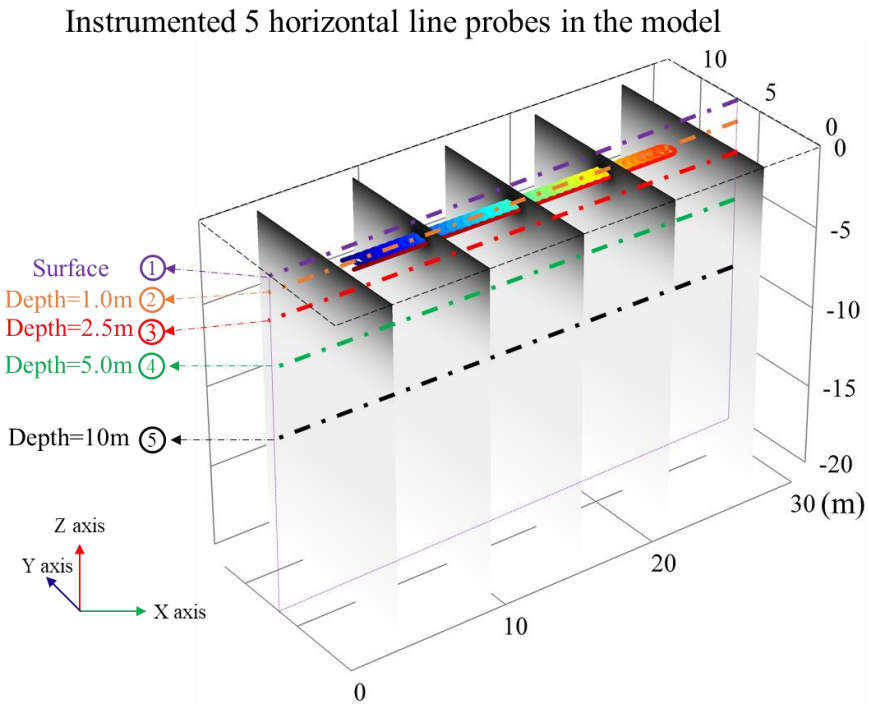

Figure VI.12. Five horizontal line probes positioned at different depths: 0, 1, 2.5, 5 and 10 m

Figure VI.13 shows the variation of the volumetric water content (Figure VI.13-a) and the temperature (Figure VI.13-b) in the 5 probes at different times (99, 130, 182.5, 200 and 260 days). Figure VI.13-a shows that the volumetric water content has less fluctuation with time as the depth increases. The fluctuation of volumetric water content becomes negligible as the depth is higher than 5 m. Due to the existence of the backfill soil, the volumetric water content differs spatially along the HGHE, especially on the ground surface. The same effect can be observed at the depth of 1.0 m, while it disappears at a depth higher than 2.5 m. Figure VI.13-b shows that the seasonal temperature fluctuation is obvious in the shallow depths, while it almost vanishes when the depth reaches 10 m. During the service period, the temperature around the HGHE decreases. The line probe 2 is the most influenced probe because it is positioned at the same depth of the HGHE. The effect is also evident at the depth of 2.5 m. The surface temperature has also been influenced during the service period of the HGHE, and a difference of 0.6 °C is observed after 200 days. The HGHE operation influences less the subsurface temperature when the distance from the HGHE becomes larger. The soil temperature is negligibly influenced by the HGHE at the depth of 5 m, and this effect can be considered absent at the depth of 10 m.

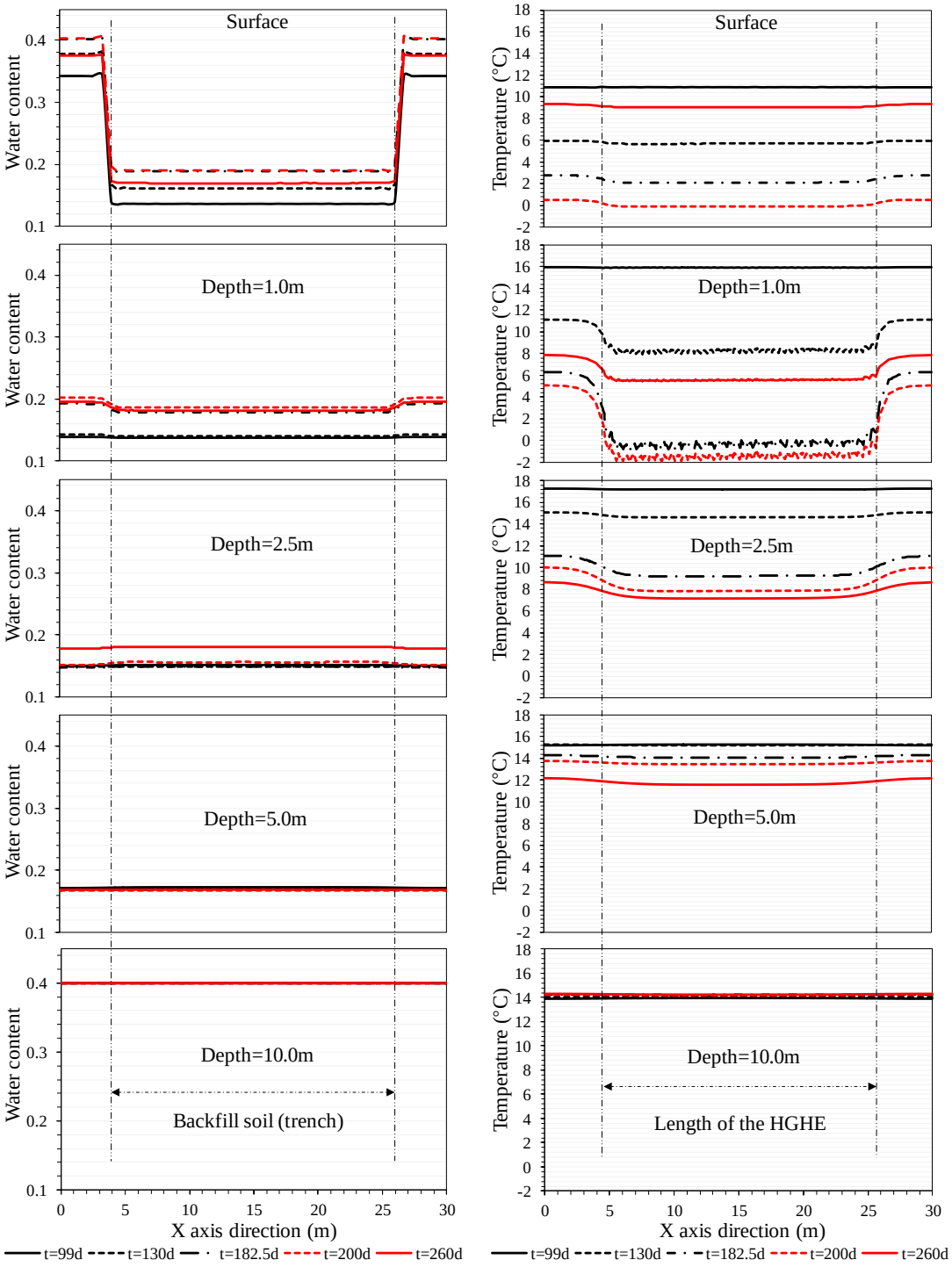

Figure VI.13. Volumetric water content and temperature fluctuation at 5 times of a year for the five horizontal probes: (a) volumetric water content fluctuation and (b) temperature fluctuation

The HGHE operation affects the ground surface temperature and consequently its ground heat flux. To visualize this effect, the heat flux fluctuation is presented along the surface line probe (probe 1) in Figure VI.14. The ground heat flux remains unchanged during the first 99 days. When the HGHE starts working, the ground heat flux at the zone affected by the HGHE is higher than the non-affected zone due to the heat extraction during the heating season. Specifically, the ground heat fluxes at the zone affected by the HGHE are 2.7, 9.2, 8.5 and 2.7 $W.m^{-2}$ higher than the unaffected zone on the days 130, 182.5, 200 and 260, respectively.

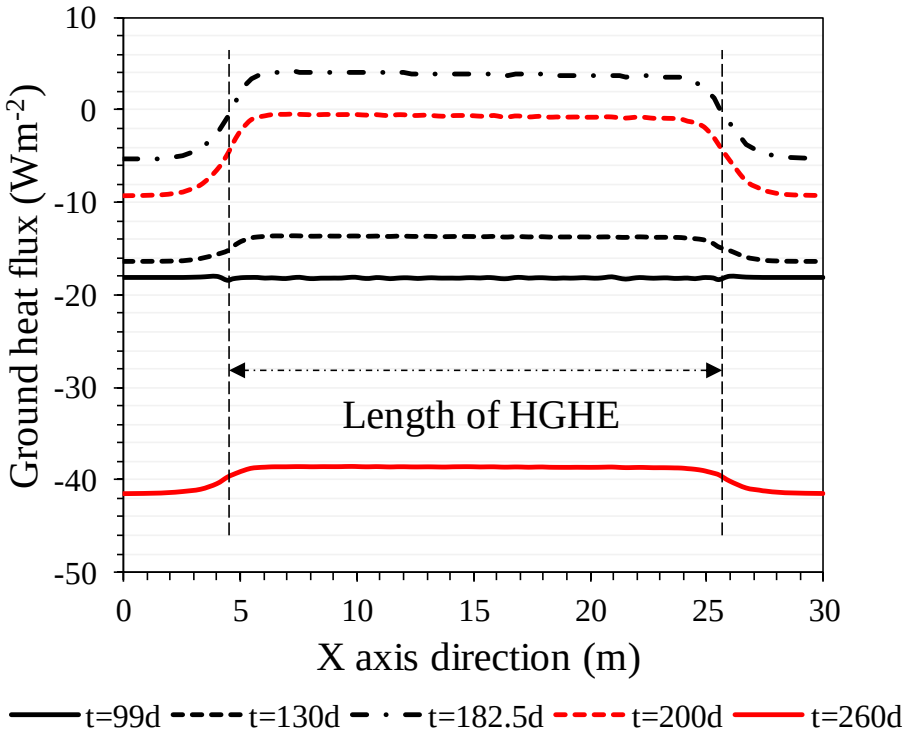

Figure VI.14. Ground heat flux fluctuation detected by the horizontal line probe 1 on the ground surface

During the service time of the HGHE, the TEE can be obtained by the following equation:

$$TEE = \int A\rho_f u_f C_{p-f}(T_{out} - T_{in})dt \tag{6.36}$$

where T_{in} is the fluid inlet temperature (°C).

Figure VI.15 shows the TEE and the fluid outlet temperature of the HGHE during its annual working period. The figure shows that the installed HGHE can extract 7.52 GJ of energy after 1 year. The annual average fluid outlet temperature can be obtained as 3.41 °C in the operation period. Generally, the fluid outlet temperature decreases continuously until the day

201, and then it increases until it stops working. The phenomenon illustrates that a time lag of 18.5 days exists between the peak heat load (t = 182.5 d, Figure VI.11) and the lowest ground temperature (t = 201 d) surrounding the HGHE.

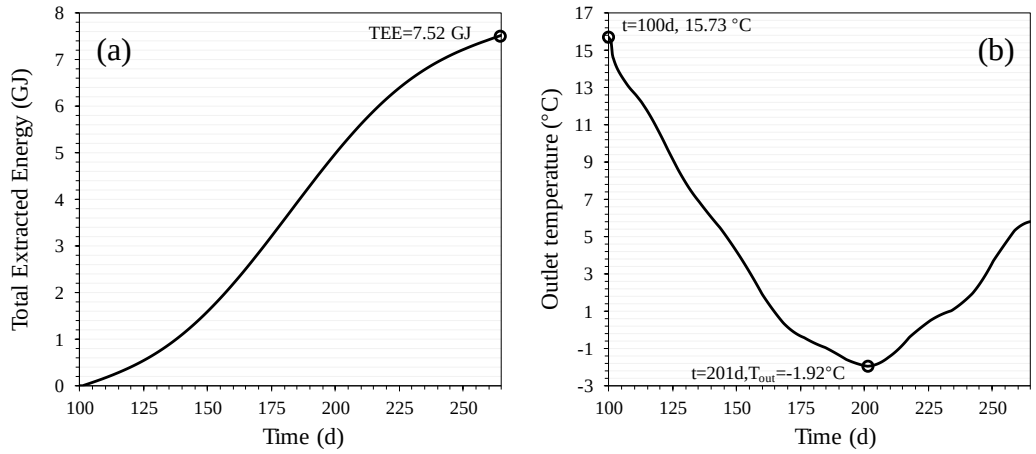

Figure VI.15. The extracted energy and the fluid outlet temperature with time during the service period of the HGHE: (a) extracted energy with time and (b) fluid outlet temperature with time

VI.4.3. The comparison of the HGHE performance at different depths with and without considering the atmosphere-soil interaction

As shown in Figure VI.13-b and Figure VI.14, the HGHE operation influences simultaneously the ground surface temperature and the ground heat flux. To identify this influence on the outlet temperature of the HGHE, another scenario is tested in this part without considering the atmosphere-soil interaction. Compared to the boundary conditions with the atmosphere-soil interaction (Table VI.6), the popular Dirichlet boundary condition on the ground surface is considered in this new scenario (Table VI.8), where the atmosphere temperature (equation (6.34)) is imposed to the ground surface and the operation of the HGHE has no effect on the ground surface temperature and heat flux. In both scenarios, the energy extraction rate (Figure VI.11) and the TEE (Figure VI.15-b) are kept the same.

Table VI.8. Hydrothermal boundary conditions for the scenario without the atmosphere-soil interaction

Surface	*Hydraulic condition, value (unit)*	*Thermal condition, value (unit)*
Top	Neumann, equation (6.24) ($m.s^{-1}$)	Dirichlet, equation (6.34) (°C)
Lateral	Adiabatic, -	Adiabatic, -

Bottom	Dirichlet, model height – groundwater level (m)	Neumann, bottom temperature gradient × bottom soil thermal conductivity ($W.m^{-2}$)

Figure VI.16 shows the fluid outlet temperatures obtained in both scenarios for the HGHE installed at the depths of 0.5, 1.0, 1.5 and 2 m. The figure shows that the non-consideration of the atmosphere-soil interaction overestimates the fluid outlet temperatures, and this overestimation declines with the increase of the installation depth. When the HGHE is installed at a larger depth, the fluctuation of its outlet temperatures is less significant in both scenarios.

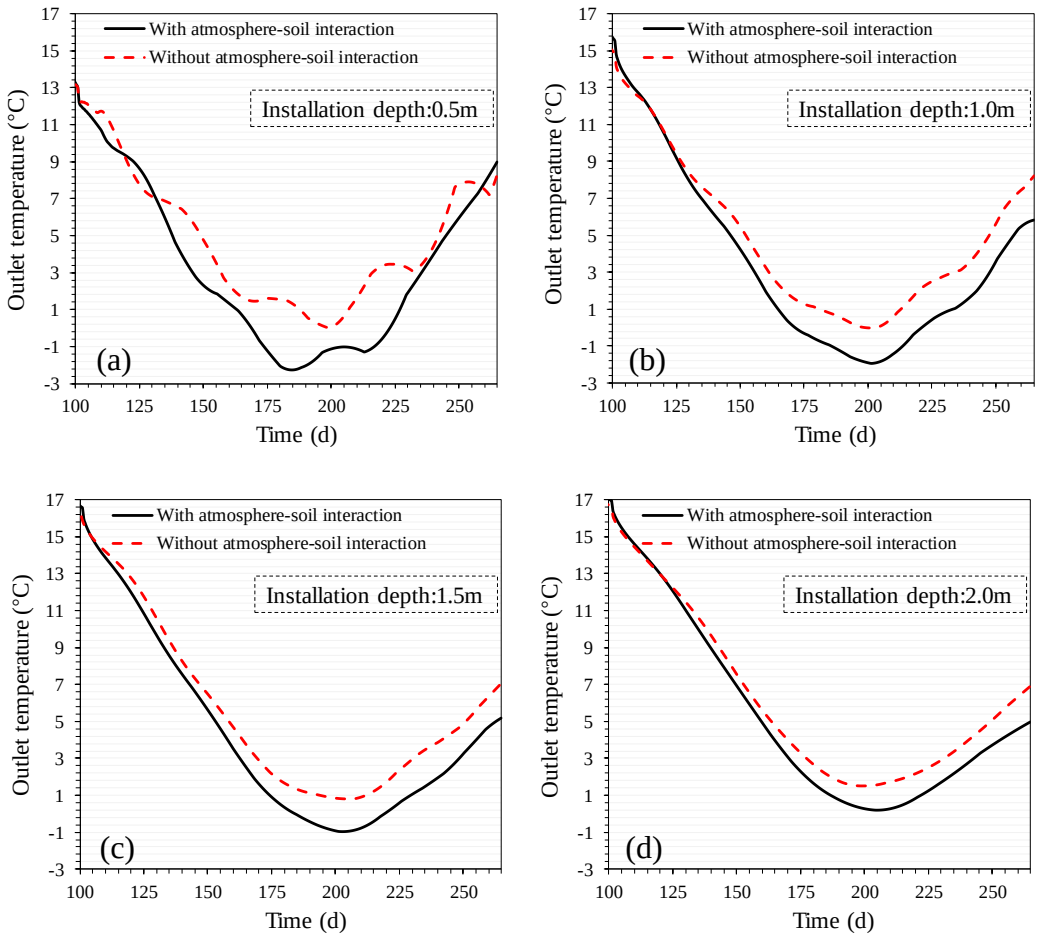

Figure VI.16. Carrying fluid outlet temperatures with time regarding with and without the atmosphere-soil interaction for the HGHE installed at 4 different depths: (a) 0.5 m; (b) 1 m; (c) 1.5 m and (d) 2 m

Figure VI.17 compares the annual average fluid outlet temperatures of these 2 scenarios. Generally, a deep installation improves the fluid outlet temperature. When the installation

depth increases from 0.5 to 2 m, the annual average fluid outlet temperatures increase 61.11% and 27.56% correspondingly for the scenarios with and without considering the atmosphere-soil interaction. The increase of the installation depth from 0.5 to 1 m has an insignificant effect on the annual average fluid outlet temperatures in both scenarios.

Furthermore, the results confirm the significant influence of the atmosphere-soil interaction in the HGHE simulations. The annual average fluid outlet temperatures are highly overestimated when the interaction is absent in the calculations especially if the HGHE is installed close to the ground surface. The overestimation caused by the non-consideration of the atmosphere-soil interaction decreases with the increase of the installation depth. In general, the overestimation decreases from 47.99% to 17.16% as the installation depth increases from 0.5 to 2 m.

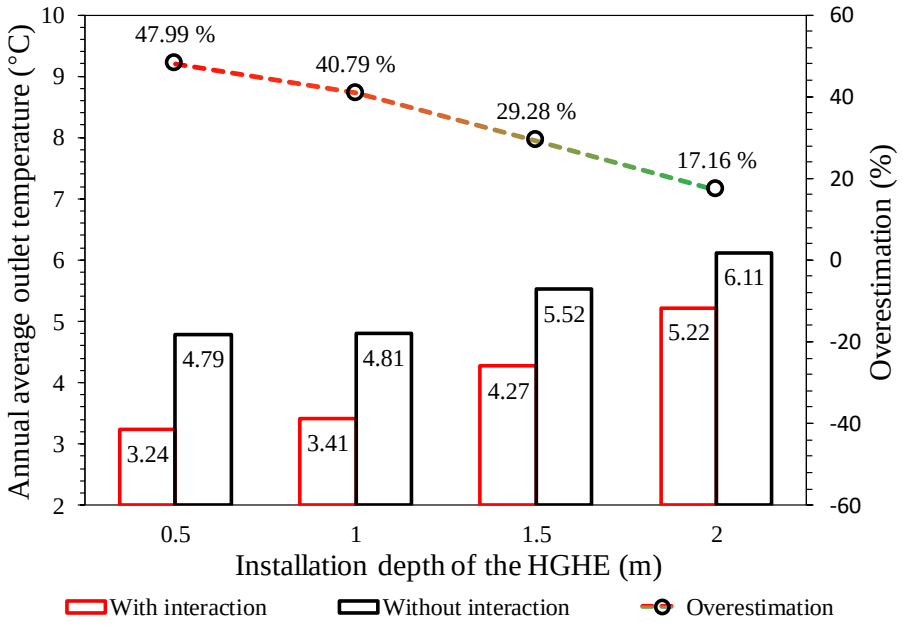

Figure VI.17. Comparison between the annual average fluid outlet temperatures with and without the atmosphere-soil interaction

As it has been reported regularly in the literature (Casasso and Sethi, 2014; Hein et al., 2016; Shao et al., 2016), the fluid outlet temperature from the HGHE is linear to the heat pump performance, and consequently the HGHE performance. The higher the fluid outlet temperature in the heating scenario, the higher the HGHE performance. Therefore, the same conclusions observed for the fluid outlet temperature can be generalized for the HGHE performance.

VI.5. Summary

This paper has evaluated the outlet temperatures of a slinky-type HGHE installed in a multi-layered soil field by considering the local metrological and geological conditions.

The numerical simulations were firstly validated by the measured data from literature. The results showed the good capacity of the proposed framework to consider the atmosphere-soil-HGHE interaction.

The yearly variations of the in-situ hydrothermal properties were investigated on the horizontal line probes positioned at 5 different depths. The results showed that the soil surface temperature and the ground heat flux were obviously affected during the service period of the HGHE. The affected surface zone had lower temperatures than the unaffected zone while a higher ground heat flux was observed in this zone. Subsequently, the annual average fluid outlet temperature for the in-situ site was estimated at 3.41 °C under the seasonal heat load.

Moreover, the fluid outlet temperatures were further compared for the HGHE installed at 4 different depths with and without considering the atmosphere-soil interaction. Generally, a deep installation increased the fluid outlet temperatures; however, this increase was insignificant when the installation depth increased from 0.5 to 1 m. The results also showed the importance of considering atmosphere-soil interaction in the numerical calculations. The annual average fluid outlet temperature was overestimated when the atmosphere-soil interaction was not considered. This overestimation decreased from 47.99% to 17.16% as the installation depth of the HGHE increased from 0.5 to 2 m.

These findings are important in the design stage of the HGHE engineering. The effect of the atmosphere-soil interaction on the HGHE performance is a crucial factor. This effect is more /less intensified when the installation depth decreased/increased. A deep installation of the HGHE improves the system performance, but it increases the trench digging cost. An appropriate cost/performance ratio may be the best practical solution in HGHE engineering.

CONCLUSIONS AND PERSPECTIVES

General conclusions

This thesis introduces hydrothermal transfer model in soil surrounding the ground heat exchangers, investigates factors influencing the performance of a shallow BHE, conducts sensitive analysis of TRTs and estimates the performance difference of a HGHE with two ground surface boundaries. At first, a validated numerical simulation framework considering hydrothermal transfer was built to estimate the shallow BHE performance installed in a geothermal field in Alsace region (France). Secondly, 15 factors influencing the performance of a shallow BHE was investigated by considering hydrothermal transfer in the soil. The parameters of each factor were chosen with a rational range. Thirdly, an analytical approach was proposed after conducting sensitive analysis on TRTs considering various testing times, field conditions and U-pipe lengths. The analytical solution can help estimate effective soil thermal conductivity for projects with limited capital investments. Next, the influences of Dirichlet and Neumann boundary conditions on the ground surface of HGHE were investigated. The investigation aims to identify the performance difference of HGHE when using the popular ground surface temperature variation for ground surface boundary and the less often used heat flux boundary on the ground surface.

1) Shallow BHE performance in Alsace region

In this investigation, an equilibrium method was proposed to get the initial hydrothermal profiles for the numerical simulation model by considering seasonal ground surface hydrothermal transfer. It is observed in the numerical simulation results that the seasonal hydrothermal fluctuation on the ground surface influences the water content till 1.5 m beneath ground surface and the temperature until 12 m beneath the ground surface. The soil temperature in the vicinity of the shallow BHE is closely related to the heat load of the heat

exchanger. The heat pump COP remains almost stable during the working period of the shallow BHE in the constant inlet temperature scenario. While for the seasonal heat load scenario, heat pump COP decreases gradually till the largest energy deficit, which is 9 days after the peak heat load. Besides, TEE in the scenario of the constant inlet temperature increases almost linearly with time during the working period of the BHE, while it varies nonlinearly for the seasonal heat load scenario. Further, the performance of the shallow BHE considering constant inlet temperature over a 5-year period has been analyzed. The results show that the largest difference of the extracted energy (5.44%) happens during the first two years, and the shallow BHE is capable of providing stable energy for various uses after the 4^{th} year.

2) Factors influencing the performance of a shallow BHE

The effect of 15 principal factors on the shallow BHE performance was investigated numerically by covering 108 different cases in this investigation. Yearly average heat pump COPs in different cases were compared with two reference models representing BHE installed in clay and sand. It has been found that BHE installed in sand behaved better than BHE installed in clay (around 8.6%) in all the scenarios conducted in this investigation. Generally, the BHE behaved better in warmer climate, less vegetated field, higher groundwater velocity, higher grout thermal conductivity, larger grout diameter, larger shank spacing, more additional U-pipes, larger U-pipe inner diameter, thinner U-pipe, higher U-pipe thermal conductivity, more stable heat load and lower heat load level scenarios. The grout volumetric heat capacity influenced negligibly the BHE performance. The usage of $CaCl_2$ (20%) as the carrying fluid improved the BHE performance and the BHE performance was the lowest when the carrying fluid velocity reached 0.3 $m.s^{-1}$. This investigation can provide guidance for BHE applications to choose the proper parameters in the design stage.

3) Sensitive analysis on TRTs

The investigation shows that in the heat injection process, the TRTs in winter result to higher effective soil thermal conductivities. This effect is less obvious for longer BHEs. The effective soil thermal conductivity varies linearly with a newly proposed λ ratio (= water level/ U-pipe length). Moreover, the effective thermal conductivity varies with the U-pipe length in a (2^{nd} degree) polynomial form, and the influence of U-pipe length on effective soil thermal conductivity generally gets stabilized when the U-pipe is beyond 30 m.

An analytical solution is finally proposed to estimate the effective soil thermal conductivity from the numerical simulated TRTs, with a RMSE less than 0.035 $W.m^{-1}.K^{-1}$. The proposed approach has been used to estimate the effective soil thermal conductivities of 6 sites in Japan, China, Cyprus and Croatia, along with a shallow BHE installed in a multi-layered field in Alsace region (France). The comparisons prove the good capacity of the proposed approach to estimate the field effective thermal conductivities in the BHE projects with various field conditions and U-pipe lengths. The investigation is interesting for small or medium projects with BHE installed in unsaturated soils since TRT is comparably expensive for these projects. It should be noted that the investigation is especially useful for shallow BHEs, since the climate condition and water table are counted in the analytical approach.

4) Outlet temperature of a HGHE considering two ground surface boundaries

The investigation was mainly conducted to identify the effects of Neumann and Dirichlet boundary conditions on the performance of the HGHE. The results showed that the soil surface temperature and the ground heat flux were obviously affected during the service period of the HGHE. The affected surface zone had lower temperatures than the unaffected zone while a higher ground heat flux was observed in this zone. Subsequently, the annual average fluid outlet temperature for the in-situ site was estimated 3.41 °C under the seasonal heat load.

The fluid outlet temperatures were compared for the HGHE installed at 4 different depths with (Neumann boundary condition) and without (Dirichlet boundary condition) considering the atmosphere-soil interaction. Generally, a deep installation increased the fluid outlet temperatures; however, this increase was insignificant when the installation depth increased from 0.5 to 1 m. The results also showed that the annual average fluid outlet temperature was overestimated when using Dirichlet instead of Neumann boundary condition on the ground surface. This overestimation decreased from 47.99% to 17.16% as the installation depth of the HGHE increased from 0.5 to 2 m.

Perspectives

The project has studied the behavior of ground heat exchangers installed in soils. Some novel insights have been brought in to BHE and HGHE. However, there are further questions to be addressed by additional researches.

The first is the accurate field meteorological conditions and soil thermal properties in the numerical modeling. Although the numerical simulation can predict generally well the local hydrothermal variations by using approximated parameters or parameters from the literature, more accurate meteorological and field conditions can help to achieve a better accuracy to predict the ground heat exchanger performance. These necessary parameters at the local site are ambient temperature, solar radiation, wind speed, cloud cover, precipitation, infiltration, parameters related to SWCCs, sand content, dry density, hydraulic conductivity, vegetation height, etc.

The second question is comparing the in-situ and numerical simulated long-term ground heat exchanger performance. Till now, many short-term tests of ground heat exchanger performance have been conducted, including TRTs and Thermal Performance Tests (TPTs). These tests are traditionally having a test time between 24 and 120 h, which is not enough to predict the yearly performance of a ground heat exchanger. However, in-situ long-term tests are both time and money consuming, which is not feasible for many projects. Particularly, the thermal load and meteorological conditions should be monitored constantly during the working period of a ground heat exchanger. A long-term in-situ monitoring of ground heat exchanger performance can better adjust a numerical simulation model and one of main perspectives of the investigation.

The third is the investigations on mechanical behavior of the soil surrounding the ground heat exchangers. In our work, the mechanical effect of a ground heat exchanger on the surrounding soil was not investigated. The ground heat exchanger working in the extreme conditions can result the freeze and thaw effect in soil, which can influence both the stability of soil and the ground heat exchanger performance, especially for energy piles installed beneath the buildings. Further investigation can be carried out considering hydro-thermo-mechanical effect of surrounding soils around the ground heat exchangers.

The fourth is the economic aspects of GSHP systems. The installation cost of GSHP system is higher compared with conventional systems like ASHP systems. Although GSHP is energy efficient, the capital investment is a major concern in applications. To estimate the economy behavior of a GSHP system, it is important to know the heating load of a building, the local electricity prize, the subvention from the local government, the electricity consumed by water

pump, the electricity consumed by heat pump, the installation and maintenance fees for the system. Conventionally, the payback period is often used to evaluate the economy aspect of a GSHP.

The fifth is the hybrid GSHP systems. There are some GSHP systems working together with other systems, such as solar panels and cooling towers. These systems can reduce the temperature imbalance in the subsurface and provide extra energy in applications. Further, the hybrid GSHP systems can help to improve the COP of a system and reduce the CO_2 emissions. Proper inspecting of hybrid GSHP systems can help the system to achieve better energy efficiency and realize better economic benefits.

NOMENCLATURE

Symbol	*Definition*
A	U-pipe cross-sectional area, m^2
a_l	surface albedo
b	tortuosity
c_c	cloud cover
C_p	specific heat capacity, $J.kg^{-1}.K^{-1}$
C_v	volumetric heat capacity, $J.m^{-3}.K^{-1}$
d	displacement height, m
d_h	hydraulic diameter, m
d_{in}	inner diameter of the U-pipe, m
D	elevation head, m
D_h	inner diameter of the U-pipe, m
D_T	thermal moisture diffusivity, $m^2.s^{-1}.K^{-1}$
D_{Tl}	thermal liquid moisture diffusivity, $m^2.s^{-1}K^{-1}$
D_θ	isothermal moisture diffusivity, $m^2.s^{-1}$
$D_{\theta l}$	isothermal vapor moisture diffusivity, $m^2.s^{-1}$
e_a	actual vapor pressure, kPa
e_s	saturation vapor pressure, kPa
E	actual evaporation on the soil surface, $mm.s^{-1}$
E_p	evaporation potential, $kg.m^{-2}.s^{-1}$ or $mm.s^{-1}$
f_D	Darcy friction factor

$F_{surface}$	surface suction, MPa
G	total heat flux through ground surface, $W.m^{-2}$
h	heat transfer coefficient, $W.m^{-2}\cdot K^{-1}$
h_c	vegetation height, m
h_{head}	hydraulic head, m
h_{int}	heat transfer coefficient, $W.m^{-2}.K^{-1}$
h_p	pressure head, m
H	sensible heat flux, $W.m^{-2}$
H_p	suction head, m
k	thermal conductivity, $W.m^{-1}.K^{-1}$
k_e	shape and moisture factor
k_r	relative hydraulic conductivity
K	hydraulic conductivity, $m.s^{-1}$
l	pore connectivity parameter
L	latent heat of vaporization for water, $J.kg^{-1}$
L_d	distance between the point source and the study point, m
$L_{M\text{-}O}$	Monin-Obukhov length, m
LAI	leaf area index
m	index
n	independent parameter
Nu	Nusselt number
P	rainfall rate, $mm.s^{-1}$
P_a	pore air pressure, Pa
P_{at}	atmospheric pressure, Pa
P_{r0}	turbulent Prandt number
$P_{suction}$	matric suction, Pa
$P_{suction\_r}$	suction value corresponding to residual water content, Pa
P_w	pore water pressure, Pa
q	heat extraction rate, $W.\ m^{-1}$

q_p	heat flux in pipe wall, $W.m^{-1}$
Q_f	fluid heat source, $W.m^{-3}$
Q_l	volumetric liquid flux, $m^3.m^{-2}s^{-1}$
Q_s	soil heat source, $W.m^{-3}$
Q_v	volumetric vapor flux, $m^3.m^{-2}.s^{-1}$
Q_{w_source}	water source or sink, $kg.m^{-3}.s^{-1}$
Q_{wall}	heat from the surrounding, $W.m^{-1}$
r	pipe radius, m
r_1	stomatal resistance of a single leaf, $s.m^{-1}$
r_a	aerodynamic resistance to heat transfer, $s.m^{-1}$
r_c	crop canopy resistance, $s.m^{-1}$
r_{e-i}	inner radius of the equivalent pipe, m
r_{e-o}	inner and outer radius of the equivalent pip, (m
r_{mw}	molecular weight of water vapor to dry air
r_{ou}	effective roughness, m;
r_s	distance between borehole center and surrounding medium, m
R_a	income longwave radiation, $W.m^{-2}$
R_b	borehole thermal resistance, $K.m.W^{-1}$
R_n	net radiation, $W.m^{-2}$
R_s	shortwave radiation, $W.m^{-2}$
R_{so}	solar radiation in case of clear sky, $W.m^{-2}$
R_{st}	steady part of the thermal resistance, $K.m.W^{-1}$
RH	air humidity, %
S_e	relative saturation of soil
S_r	saturation of soil
t	time, s
T	temperature, °C or K
$\overline{T}_f$	average carrying fluid temperature (°C)
T_0	initial temperature, °C

T_{in}	inlet temperature, °C
T_m	maximum air temperatures in one day, K
T_n	minimum air temperatures in one day, K
T_{out}	outlet temperature, °C
T_s	ground surface temperature, K
T_{sky}	sky temperature, K
u	velocity, $m.s^{-1}$
u_{wind}	wind speed, $m.s^{-1}$
u_*	friction velocity, $m.s^{-1}$
W_i	infiltration, $mm.s^{-1}$
W_r	water run off, $mm.s^{-1}$
x	pore interaction term
x_s	gravimetric sand content
Z	U-pipe inner perimeter, m
z	depth beneath ground surface, m
z_m	height for measuring meteorological conditions, m
z_{oh}	water vapor roughness length, m
z_{om}	momentum roughness length, m
z_u	depth of unsaturated zone, m
$z_{U\text{-}pipe}$	U-pipe length, m

Greek

Δ	slope of the saturation vapor pressure curve, $kPa.K^{-1}$
α	independent parameter, m^{-1}
α_s	soil thermal diffusivity, $m^2.s^{-1}$
γ	psychrometric constant, $kPa.K^{-1}$
γ_d	soil dry unit weights, $kN.m^{-3}$
γ_s	soil specific unit weights, $kN.m^{-3}$
ε	soil surface emissivity

θ	volumetric water content
κ	von Karman constant
μ	dynamic viscosity, Pa.s
ρ	density, kgm^{-3}
σ	Stephan-Boltzman constant, $W.m^{-2}.K^{-4}$
χ	difference, %
ψ	specific moisture capacity, m^{-1}

Subscript

a	air
b	borehole
eff	effective
f	carrying fluid
g	grout
i-p	inner pipe wall
inlet	inlet node of U-pipe
outlet	outlet node of U-pipe
p	pipe
r	residual
s	soil
sat	saturated
w	water

Acronym

ANN	Artificial Neural Network
ASHP	Air Source Heat Pump
BHE	Borehole Heat Exchanger
CS	Cylindrical Source
COP	Coefficient of Performance

EPA	Environmental Protection Agency
FLS	Finite Line Source
FVM	Finite Volume Methods
GCHP	Ground-Coupled Heat Pump
GSHP	Ground Source Heat Pump
HDPE	High-Density Polyethylene
HGHE	Horizontal Ground Heat Exchanger
HGSH	Hybrid Ground-Source Heat Pump
IEA	International Energy Agency
ILS	Infinite Line Source
LDPE	Low Density Polyethylene
ML	Machine Learning
MFLS	Moving Finite Line Source
PCM	Phase Change Material
PG	Propylene Glycol
PVT	Photovoltaic Thermal
RMSE	Root-Mean-Square Error
SCW	Standing Column Well
SCS	Solid Cylindrical Source
SWCC	Soil-Water Characteristic Curve
TEE	Total Extracted Energy
TRC	Thermal Resistance and Capacitance
TPT	Thermal Performance Test
TRT	Thermal Response Test
VGHE	Vertical Ground Heat Exchanger

REFERENCES

Abdelaziz, S.L.A.M. (2013). Deep Energy Foundations: Geotechnical Challenges and Design Considerations. Virginia Polytechnic Institute and State University.

Abdelaziz, S.L., Ozudogru, T.Y., Olgun, C.G., and Martin, J.R. (2014). Multilayer finite line source model for vertical heat exchangers. Geothermics *51*, 406–416.

Abuel-Naga, H.M., and Al-Chalabi, R.R. (2016). Borehole thermal resistance of U-tube borehole heat exchanger. Géotechnique Letters *6*, 250–255.

Abu-Hamdeh, N.H. (2001). Measurement of the Thermal Conductivity of Sandy Loam and Clay Loam Soils using Single and Dual Probes. Journal of Agricultural Engineering Research *80*, 209–216.

Abu-Hamdeh, N.H. (2003). Thermal Properties of Soils as affected by Density and Water Content. Biosystems Engineering *86*, 97–102.

Abu-Hamdeh, N.H., and Reeder, R.C. (2000). Soil Thermal Conductivity: Effects of Density, Moisture, Salt Concentration, and Organic Matter. SOIL SCI. SOC. AM. J. *64*, 6.

Adamovsky, D., Neuberger, P., and Adamovsky, R. (2015a). Changes in energy and temperature in the ground mass with horizontal heat exchangers—The energy source for heat pumps. Energy and Buildings *92*, 107–115.

Adamovsky, D., Neuberger, P., and Adamovsky, R. (2015b). Changes in energy and temperature in the ground mass with horizontal heat exchangers—The energy source for heat pumps. Energy and Buildings *92*, 107–115.

Adelard, L., Pignolet-Tardan, F., Mara, T., Lauret, P., Garde, F., and Boyer, H. (1998). Sky temperature modelisation and applications in building simulation. Renewable Energy *15*, 418–430.

Al-Ameen, Y., Ianakiev, A., and Evans, R. (2018). Recycling construction and industrial landfill waste material for backfill in horizontal ground heat exchanger systems. Energy *151*, 556–568.

Alberdi-Pagola, M., Poulsen, S.E., Jensen, R.L., and Madsen, S. (2019). Thermal design method for multiple precast energy piles. Geothermics *78*, 201–210.

Alberti, L., Angelotti, A., Antelmi, M., and La Licata, I. (2017). A Numerical Study on the Impact of Grouting Material on Borehole Heat Exchangers Performance in Aquifers. Energies *10*, 703.

Ali, Md., Kariya, K., and Miyara, A. (2017). Performance Analysis of Slinky Horizontal Ground Heat Exchangers for a Ground Source Heat Pump System. Resources *6*, 56.

Al-Khoury, R. (2012). Computational Modeling of Shallow Geothermal Systems (CRC Press).

Al-Khoury, R., and Bonnier, P.G. (2006). Efficient finite element formulation for geothermal heating systems. Part II: transient. Int. J. Numer. Meth. Engng *67*, 725–745.

Allen, R.G. (1986). A Penman for All Seasons. Journal of Irrigation and Drainage Engineering *112*, 348–368.

Allen, R., Smith, M., Perrier, A., and Pereira, L. (1994a). An update for the definition of reference evapotranspiration. ICID Bulletin *43*, 1–34.

Allen, R., Smith, M., Pereira, L., and Perrier, A. (1994b). An update for the definition of reference evapotranspiration. ICID Bulletin *43*, 35–92.

Allen, R.G., Jensen, M.E., Wright, J.L., and Burman, R.D. (1989). Operational Estimates of Reference Evapotranspiration. Agronomy Journal *81*, 650.

Alrtimi, A., Rouainia, M., and Haigh, S. (2016). Thermal conductivity of a sandy soil. Applied Thermal Engineering *106*, 551–560.

An, N. (2017). Numerical investigation of soil-atmosphere interaction: application to embankments of treated soils. Université Paris-Est.

An, N., Hemmati, S., and Cui, Y.-J. (2017). Assessment of the methods for determining net radiation at different time-scales of meteorological variables. Journal of Rock Mechanics and Geotechnical Engineering *9*, 239–246.

Angelotti, A., Alberti, L., La Licata, I., and Antelmi, M. (2014). Energy performance and thermal impact of a Borehole Heat Exchanger in a sandy aquifer: Influence of the groundwater velocity. Energy Conversion and Management *77*, 700–708.

Angelotti, A., Ly, F., and Zille, A. (2018). On the applicability of the moving line source theory to thermal response test under groundwater flow: considerations from real case studies. Geothermal Energy *6*.

Aresti, L., Christodoulides, P., and Florides, G. (2018). A review of the design aspects of ground heat exchangers. Renewable and Sustainable Energy Reviews *92*, 757–773.

Asadi, A. (2018). A guideline towards easing the decision-making process in selecting an effective nanofluid as a heat transfer fluid. Energy Conversion and Management *175*, 1–10.

Asare-Kyei, D., Forkuor, G., and Venus, V. (2015). Modeling Flood Hazard Zones at the Sub-District Level with the Rational Model Integrated with GIS and Remote Sensing Approaches. Water *7*, 3531–3564.

Ashrae (2011). ASHRAE Handbook - HVAC Applications.

Atam, E., and Helsen, L. (2016a). Ground-coupled heat pumps: Part 2—Literature review and research challenges in optimal design. Renewable and Sustainable Energy Reviews *54*, 1668–1684.

Atam, E., and Helsen, L. (2016b). Ground-coupled heat pumps: Part 1 – Literature review and research challenges in modeling and optimal control. Renewable and Sustainable Energy Reviews *54*, 1653–1667.

Atam, E., Patteeuw, D., Antonov, S.P., and Helsen, L. (2015). Optimal Control Approaches for Analysis of Energy Use Minimization of Hybrid Ground-Coupled Heat Pump Systems. IEEE Trans. Contr. Syst. Technol. 1–1.

Austin, W.A. (1998). Development of an in Situ System for Measuring Ground Thermal Properties. M.S. Thesis. Oklahoma State University.

Avci, A., and Karagoz, I. (2009). A Novel Explicit Equation for Friction Factor in Smooth and Rough Pipes. Journal of Fluids Engineering *131*, 061203.

Averjanov, S.F. (1950). About permeability of subsurface soils in case of incomplete saturation. In English Collection *7*, 19–21.

Bae, S., Nam, Y., Choi, J., Lee, K., and Choi, J. (2019). Analysis on Thermal Performance of Ground Heat Exchanger According to Design Type Based on Thermal Response Test. Energies *12*, 651.

Baggs, S.A. (1983). Remote prediction of ground temperature in Australian soils and mapping its distribution. Solar Energy *30*, 351–366.

Baillieux, P., Schill, E., Edel, J.-B., and Mauri, G. (2013). Localization of temperature anomalies in the Upper Rhine Graben: insights from geophysics and neotectonic activity. International Geology Review *55*, 1744–1762.

Ball, D.A., Fischer, R.D., and Hodgett, D.L. (1983). Design methods for ground-source heat pumps. ASHRAE Trans. *89*, 416–440.

Balland, V., and Arp, P.A. (2005). Modeling soil thermal conductivities over a wide range of conditions. Journal of Environmental Engineering and Science *4*, 549–558.

Bandos, T.V., Montero, Á., Fernández, E., Santander, J.L.G., Isidro, J.M., Pérez, J., Córdoba, P.J.F. de, and Urchueguía, J.F. (2009). Finite line-source model for borehole heat exchangers: effect of vertical temperature variations. Geothermics *38*, 263–270.

Banks, D. (2012). An introduction to thermogeology: ground source heating and cooling (Hoboken, NJ: John Wiley & Sons, Ltd).

Barry-Macaulay, D., Bouazza, A., Singh, R.M., Wang, B., and Ranjith, P.G. (2013). Thermal conductivity of soils and rocks from the Melbourne (Australia) region. Engineering Geology *164*, 131–138.

Bauer, D., Heidemann, W., Müller-Steinhagen, H., and Diersch, H.-J.G. (2011). Thermal resistance and capacity models for borehole heat exchangers. Int. J. Energy Res. *35*, 312–320.

Bayer, P., Saner, D., Bolay, S., Rybach, L., and Blum, P. (2012). Greenhouse gas emission savings of ground source heat pump systems in Europe: A review. Renewable and Sustainable Energy Reviews *16*, 1256–1267.

Bayer, P., Attard, G., Blum, P., and Menberg, K. (2019). The geothermal potential of cities. Renewable and Sustainable Energy Reviews *106*, 17–30.

Beier, R.A. (2014). Transient heat transfer in a U-tube borehole heat exchanger. Applied Thermal Engineering *62*, 256–266.

Beier, R.A., Smith, M.D., and Spitler, J.D. (2011). Reference data sets for vertical borehole ground heat exchanger models and thermal response test analysis. Geothermics *40*, 79–85.

Beier, R.A., Acuña, J., Mogensen, P., and Palm, B. (2012). Vertical temperature profiles and borehole resistance in a U-tube borehole heat exchanger. Geothermics *44*, 23–32.

Bejan (2013). Convection heat transfer (Hoboken: John Wiley & Sons, Inc).

Benson, C., Abichou, T., Albright, W., Gee, G., and Roesler, A. (2001). Field Evaluation of Alternative Earthen Final Covers. International Journal of Phytoremediation *3*, 105–127.

Bertani, R. (2016). Geothermal power generation in the world 2010–2014 update report. Geothermics *60*, 31–43.

Beven, K. (1989). Changing ideas in hydrology — The case of physically-based models. Journal of Hydrology *105*, 157–172.

Bidarmaghz, A., Narsilio, G., and Johnston, I. (2012). NUMERICAL MODELLING OF GROUND LOOP CONFIGURATIONS FOR DIRECT GEOTHERMAL APPLICATIONS. *47*, 6.

Bidarmaghz, A., Narsilio, G.A., Johnston, I.W., and Colls, S. (2016). The importance of surface air temperature fluctuations on long-term performance of vertical ground heat exchangers. Geomechanics for Energy and the Environment *6*, 35–44.

Biglarian, H., Abbaspour, M., and Saidi, M.H. (2017). A numerical model for transient simulation of borehole heat exchangers. Renewable Energy *104*, 224–237.

Bisht, G., Venturini, V., Islam, S., and Jiang, L. (2005). Estimation of the net radiation using MODIS (Moderate Resolution Imaging Spectroradiometer) data for clear sky days. Remote Sensing of Environment *97*, 52–67.

Blum, P., Campillo, G., Münch, W., and Kölbel, T. (2010). CO2 savings of ground source heat pump systems – A regional analysis. Renewable Energy *35*, 122–127.

Bose, J.E., Smith, M.D., and Spitler, J.D. (2002). ADVANCES IN GROUND SOURCE HEAT PUMP SYSTEMS AN INTERNATIONAL OVERVIEW. (Beijing), pp. 313–324.

Brooks, R.H., and Corey, A.T. (1964). HYDRAULIC PROPERTIES OF POROUS MEDIA (Colorado State University).

Brunetti, G., Saito, H., Saito, T., and Šimůnek, J. (2017). A computationally efficient pseudo-3D model for the numerical analysis of borehole heat exchangers. Applied Energy *208*, 1113–1127.

Brutsaert, W. (1975). The roughness length for water vapor, sensible heat, and other scalars. Journal of the Atmospheric Sciences *32*, 2028–2031.

Brutsaert, W. (1982). Evaporation into the atmosphere: theory, history, and applications (Springer).

Bryś, K., Bryś, T., Sayegh, M.A., and Ojrzyńska, H. (2020). Characteristics of heat fluxes in subsurface shallow depth soil layer as a renewable thermal source for ground coupled heat pumps. Renewable Energy *146*, 1846–1866.

Budyko, M.I. (1958). The Heat Balance of the Earth's Surface (Washington, D. C: U.S. Dep. of Commer.).

Budyko, M.I. (1974). Climate and life (New York: Academic Press).

Bujok, P., Grycz, D., Klempa, M., Kunz, A., Porzer, M., Pytlik, A., Rozehnal, Z., and Vojčinák, P. (2014). Assessment of the influence of shortening the duration of TRT (thermal response test) on the precision of measured values. Energy *64*, 120–129.

Burdine, N.T. (1953). Relative Permeability Calculations From Pore Size Distribution Data. Journal of Petroleum Technology *5*, 71–78.

Cahill, A.T., and Parlange, M.B. (1998). On water vapor transport in field soils. Water Resour. Res. *34*, 731–739.

Cai, Y., Xu, H., and Chen, S. (2016). Testing and analysis of the influence factors for the ground thermal parameters. Applied Thermal Engineering *107*, 662–671.

Cao, S.-J., Kong, X.-R., Deng, Y., Zhang, W., Yang, L., and Ye, Z.-P. (2017). Investigation on thermal performance of steel heat exchanger for ground source heat pump systems using full-scale experiments and numerical simulations. Applied Thermal Engineering *115*, 91–98.

Cao, X., Yuan, Y., Sun, L., Lei, B., Yu, N., and Yang, X. (2015). Restoration performance of vertical ground heat exchanger with various intermittent ratios. Geothermics *54*, 115–121.

Carslaw, H.S., and Jaeger, J.C. (1959). Conduction of Heat in Solids (Oxford (UK): Oxford University Press).

Cary, J.W. (1965). Water flux in moist soil: thermal versus suction gradients. Soil Science *100*, 168–175.

Casasso, A., and Sethi, R. (2014). Efficiency of closed loop geothermal heat pumps: A sensitivity analysis. Renewable Energy *62*, 737–746.

Cazorla-Marín, A. (2019). Modelling and experimental validation of an innovative coaxial helical borehole heat exchanger for a dual source heat pump system. Universitat Politècnica de València.

Centeno, M. (1982). New formulae for the equivalent night sky emissivity. Solar Energy *28*, 489–498.

Chalhoub, M., Bernier, M., Coquet, Y., and Philippe, M. (2017). A simple heat and moisture transfer model to predict ground temperature for shallow ground heat exchangers. Renewable Energy *103*, 295–307.

Chávez-Negrete, C., Domínguez-Mota, F.J., and Santana-Quinteros, D. (2018). Numerical solution of Richards' equation of water flow by generalized finite differences. Computers and Geotechnics *101*, 168–175.

Chen, S.X. (2008). Thermal conductivity of sands. Heat Mass Transfer *44*, 1241–1246.

Chen, X., and Buchberger, S.G. (2018). Exploring the relationships between warm-season precipitation, potential evaporation, and "apparent" potential evaporation at site scale. Hydrology and Earth System Sciences *22*, 4535–4545.

Chen, C., Shao, H., Naumov, D., Kong, Y., Tu, K., and Kolditz, O. (2019). Numerical investigation on the performance, sustainability, and efficiency of the deep borehole heat exchanger system for building heating. Geotherm Energy *7*, 18.

Cherati, D.Y., and Ghasemi-Fare, O. (2019). Analyzing transient heat and moisture transport surrounding a heat source in unsaturated porous media using the Green's function. Geothermics *81*, 224–234.

Chiew, F., and McMahon, T. (1994). Application of the daily rainfall-runoff model MODHYDROLOG to 28 Australian catchments. Journal of Hydrology *153*, 383–416.

Childs, E.C., and Collis-George, N. (1950). The permeability of porous materials. Proceedings of the Royal Society of London, Series A: Mathematical and Physical Sciences *201*, 392–405.

Choi, W., and Ooka, R. (2016a). Effect of disturbance on thermal response test, part 2: Numerical study of applicability and limitation of infinite line source model for interpretation under disturbance from outdoor environment. Renewable Energy *85*, 1090–1105.

Choi, W., and Ooka, R. (2016b). Effect of natural convection on thermal response test conducted in saturated porous formation: Comparison of gravel-backfilled and cement-grouted borehole heat exchangers. Renewable Energy *96*, 891–903.

Choi, J.C., Lee, S.R., and Lee, D.S. (2011). Numerical simulation of vertical ground heat exchangers: Intermittent operation in unsaturated soil conditions. Computers and Geotechnics *38*, 949–958.

Choi, J.C., Park, J., and Lee, S.R. (2013). Numerical evaluation of the effects of groundwater flow on borehole heat exchanger arrays. Renewable Energy *52*, 230–240.

Choi, W., Ooka, R., and Nam, Y. (2018). Impact of long-term operation of ground-source heat pump on subsurface thermal state in urban areas. Sustainable Cities and Society *38*, 429–439.

Choudhury, B. (1997). Global pattern of potential evaporation calculated from the Penman-Monteith equation using satellite and assimilated data. Remote Sensing of Environment *61*, 64–81.

Churchill, S.W. (1977a). Friction Factor Equations Spans All Fluid-Flow Regimes. Chemical Engineering Journal *84*, 91–92.

Churchill, S.W. (1977b). Comprehensive Correlating Equations for Heat, Mass and Momentum Transfer in Fully Developed Flow in Smooth Tubes. Ind. Eng. Chem. Fund. *16*, 109–116.

Cimmino, M. (2015). The effects of borehole thermal resistances and fluid flow rate on the g-functions of geothermal bore fields. International Journal of Heat and Mass Transfer *91*, 1119–1127.

Cimmino, M. (2018). Fast calculation of the g-functions of geothermal borehole fields using similarities in the evaluation of the finite line source solution. Journal of Building Performance Simulation *11*, 655–668.

Cimmino, M., and Bernier, M. (2014). A semi-analytical method to generate g-functions for geothermal bore fields. International Journal of Heat and Mass Transfer *70*, 641–650.

Claesson, J., and Eskilson, P. (1988). Conductive heat extraction to a deep borehole: Thermal analyses and dimensioning rules. Energy *13*, 509–527.

Claesson, J., and Javed, S. (2011). An Analytical Method to Calculate Borehole Fluid Temperatures for Time-scales from Minutes to Decades. ASHRAE Transactions 11.

Ćojbašić, Ž., and Brkić, D. (2013). Very accurate explicit approximations for calculation of the Colebrook friction factor. International Journal of Mechanical Sciences *67*, 10–13.

Cole, R. (1976). The longwave radiation incident upon the external surface of buildings. Build. Serv. Eng. *44*, 195–206.

Congedo, P.M., Colangelo, G., and Starace, G. (2012). CFD simulations of horizontal ground heat exchangers: A comparison among different configurations. Applied Thermal Engineering *33–34*, 24–32.

Côté, J., and Konrad, J.-M. (2005). A generalized thermal conductivity model for soils and construction materials. Can. Geotech. J. *42*, 443–458.

Cui, Y., and Zhu, J. (2017). 3D transient heat transfer numerical analysis of multiple energy piles. Energy and Buildings *134*, 129–142.

Cui, Y.-J., and Zornberg, J.G. (2008). Water Balance and Evapotranspiration Monitoring in Geotechnical and Geoenvironmental Engineering. Geotechnical and Geological Engineering *26*, 783–798.

Cui, P., Yang, H., and Fang, Z. (2008). Numerical analysis and experimental validation of heat transfer in ground heat exchangers in alternative operation modes. Energy and Buildings 7.

Cui, W., Gawecka, K.A., Potts, D.M., Taborda, D.M.G., and Zdravković, L. (2016). Numerical analysis of coupled thermo-hydraulic problems in geotechnical engineering. Geomechanics for Energy and the Environment *6*, 22–34.

Cui, Y., Zhu, J., and Meng, F. (2018). Techno-economic evaluation of multiple energy piles for a ground-coupled heat pump system. Energy Conversion and Management *178*, 200–216.

Cui, Y.J., Gao, Y.B., and Ferber, V. (2010). Simulating the water content and temperature changes in an experimental embankment using meteorological data. Engineering Geology *114*, 456–471.

Cuny, M., Lin, J., Siroux, M., and Fond, C. (2015). Simplification of Boundary Conditions of the Modeling of Shallow Geothermal Systems. In French Thermal Congress, (La Rochelle (France)), p.

Daguenet, M. (1985). Les Séchoirs solaires: théorie et pratique (Unesco).

Desmedt, J., Van Bael, J., Hoes, H., and Robeyn, N. (2012). Experimental performance of borehole heat exchangers and grouting materials for ground source heat pumps: Experimental performance of borehole heat exchangers. Int. J. Energy Res. *36*, 1238–1246.

Dietrich, O., Fahle, M., and Seyfarth, M. (2016). Behavior of water balance components at sites with shallow groundwater tables: Possibilities and limitations of their simulation using different ways to control weighable groundwater lysimeters. Agricultural Water Management *163*, 75–89.

Eck, B. (1973). Technische Stromungslehre (New York: Springer).

EGEC (2019). Geothermal Market Report 2018 (European Geothermal Energy Council).

Eidesgaard, Ó.R., Schovsbo, N.H., Boldreel, L.O., and Ólavsdóttir, J. (2019). Shallow geothermal energy system in fractured basalt: A case study from Kollafjørður, Faroe Islands, NE-Atlantic Ocean. Geothermics *82*, 296–314.

Eklöf, C., and Gehlin, S. (1996). TED-a Mobile Equipment for Thermal Response Tests. M.S. Thesis. Lulea University of Technology.

Emmi, G., Zarrella, A., De Carli, M., and Galgaro, A. (2015). An analysis of solar assisted ground source heat pumps in cold climates. Energy Conversion and Management *106*, 660–675.

Erol, S., and François, B. (2014). Efficiency of various grouting materials for borehole heat exchangers. Applied Thermal Engineering *70*, 788–799.

Erol, S., and François, B. (2018). Multilayer analytical model for vertical ground heat exchanger with groundwater flow. Geothermics *71*, 294–305.

ES (2017a). ES inaugure la mise en production industrielle du site g eothermique de Soultz-sous-Forets, pionnier mondial de la geothermie profonde.

ES (2017b). Centrale de geothermie profonde d'Illkirch-Graffenstaden.

Esen, H., Inalli, M., Sengur, A., and Esen, M. (2008). Forecasting of a ground-coupled heat pump performance using neural networks with statistical data weighting pre-processing. International Journal of Thermal Sciences *47*, 431–441.

Eskilson, P. (1987). Thermal Analysis of Heat Extraction Boreholes. 222.

Evett, S.R., Prueger, J.H., and Tolk, J.A. (2011). Water and Energy Balances in the Soil–Plant–Atmosphere Continuum (Boca Raton, Florida, USA: CRC Press).

Fannou, J.-L., Rousseau, C., Lamarche, L., and Stanislaw, K. (2014). Experimental analysis of a direct expansion geothermal heat pump in heating mode. Energy and Buildings *75*, 290–300.

Farouki, O.T. (1981). Thermal Properties of Soils (US Army Corps of Engineers, Cold Regions Research and Engineering Laboratory, Hanover).

Fine, J.P., Nguyen, H.V., Friedman, J., Leong, W.H., and Dworkin, S.B. (2018). A simplified ground thermal response model for analyzing solar-assisted ground source heat pump systems. Energy Conversion and Management *165*, 276–290.

Florides, G., and Kalogirou, S. (2007). Ground heat exchangers—A review of systems, models and applications. Renewable Energy *32*, 2461–2478.

Florides, G., and Kalogirou, S. (2008). First in situ determination of the thermal performance of a U-pipe borehole heat exchanger, in Cyprus. Applied Thermal Engineering *28*, 157–163.

Florides, G.A., Christodoulides, P., and Pouloupatis, P. (2013). Single and double U-tube ground heat exchangers in multiple-layer substrates. Applied Energy *102*, 364–373.

Fossa, M. (2011). The temperature penalty approach to the design of borehole heat exchangers for heat pump applications. Energy and Buildings *43*, 1473–1479.

Fredlund, D.G., and Xing, A. (1994). Equations for the soil-water characteristic curve. Canadian Geotechnical Journal *31*, 521–532.

Fredlund, D.G., Rahardjo, H., and Fredlund, M.D. (2012). Unsaturated Soil Mechanics in Engineering Practice (John Wiley & Sons).

Fu, B.P. (1981). On the calculation of the evaporation from land surface. Sci. Atmos. Sin *5*, 23–31.

Fujii, H., Okubo, H., Nishi, K., Itoi, R., Ohyama, K., and Shibata, K. (2009). An improved thermal response test for U-tube ground heat exchanger based on optical fiber thermometers. Geothermics *38*, 399–406.

Fujii, H., Okubo, H., Cho, N., and Ohyama, K. (2010). Field Tests of Horizontal Ground Heat Exchangers. (Bali, Indonesia), p. 6.

Fujii, H., Nishi, K., Komaniwa, Y., and Chou, N. (2012). Numerical modeling of slinky-coil horizontal ground heat exchangers. Geothermics *41*, 55–62.

Gan, G. (2013). Dynamic thermal modelling of horizontal ground-source heat pumps. International Journal of Low-Carbon Technologies *8*, 95–105.

Gan, G. (2014). Dynamic interactions between the ground heat exchanger and environments in earth–air tunnel ventilation of buildings. Energy and Buildings *85*, 12–22.

Gan, G. (2018). Dynamic thermal performance of horizontal ground source heat pumps – The impact of coupled heat and moisture transfer. Energy *152*, 877–887.

Gang, W., and Wang, J. (2013). Predictive ANN models of ground heat exchanger for the control of hybrid ground source heat pump systems. Applied Energy *112*, 1146–1153.

Gang, W., Wang, J., and Wang, S. (2014). Performance analysis of hybrid ground source heat pump systems based on ANN predictive control. Applied Energy *136*, 1138–1144.

Gao, Y., Fan, R., Li, H., Liu, R., Lin, X., Guo, H., and Gao, Y. (2016). Thermal performance improvement of a horizontal ground-coupled heat exchanger by rainwater harvest. Energy and Buildings *110*, 302–313.

Garbrecht, J., Ogden, F.L., DeBarry, P.A., and Maidment, D.R. (2001). GIS and Distributed Watershed Models. I: Data Coverages and Sources. Journal of Hydrologic Engineering *6*, 506–514.

Garcia Gonzalez, R., Verhoef, A., Vidale, P.L., Main, B., Gan, G., and Wu, Y. (2012). Interactions between the physical soil environment and a horizontal ground coupled heat pump, for a domestic site in the UK. Renewable Energy *44*, 141–153.

Gardner, W.R. (1958a). Some Steady-State Solutions of the Unsaturated Moisture Flow Equation with Application to Evaporation from a Water Table. Soil Science *85*, 228–232.

Gardner, W.R. (1958b). Mathematics of Isothermal Water Conduction I•ll Unsaturated Soil. In Proceedings of the 40 International Symposuim on Physio-Chemical Phenomenon in Soils Highway Research Board, (Washington DC), pp. 78–87.

Gehlin, S., and Nordell, B. (2003). Determining undistrubed ground temperature for thermal response test. ASHRAE Transactions *109*, 151–156.

Genter, A., Guillou-Frottier, L., Feybesse, J.-L., Nicol, N., Dezayes, C., and Schwartz, S. (2003). Typology of potential Hot Fractured Rock resources in Europe. Geothermics *32*, 701–710.

Genter, A., Baujard, C., Cuenot, N., Dezayes, C., Kohl, T., Sanjuan, B., Scheiber, J., Schill, E., Schmittbuhl, J., and Vidal, J. Geology, Geophysics and Geochemistry in the Upper Rhine Graben: the frame for geothermal energy use. 6.

Gentry, G.E. (2007). Simulation and Validation of Hybrid Ground Source and WaterLoop Heat Pump Systems. Oklahoma State University.

van Genuchten, M.Th. (1980). A Closed-form Equation for Predicting the Hydraulic Conductivity of Unsaturated Soils1. Soil Science Society of America Journal *44*, 892.

Gérard, A., Genter, A., Kohl, T., Lutz, P., Rose, P., and Rummel, F. (2006). The deep EGS (Enhanced Geothermal System) project at Soultz-sous-Forêts (Alsace, France). Geothermics *35*, 473–483.

Gerrits, A.M.J., Savenije, H.H.G., Veling, E.J.M., and Pfister, L. (2009). Analytical derivation of the Budyko curve based on rainfall characteristics and a simple evaporation model: BUDYKO CURVE. Water Resour. Res. *45*.

Ghanbarian-Alavijeh, B., Liaghat, A., Huang, G.-H., and Van Genuchten, M.Th. (2010). Estimation of the van Genuchten Soil Water Retention Properties from Soil Textural Data. Pedosphere *20*, 456–465.

Ghuman, B.S., and Lal, R. (1985). Thermal conductivity, thermal diffusivity, and thermal capacity of some Nigerian soils. Soil Science *139*, 74–80.

Glen Dimplex Deutschland GmbH (2016). Heat Pump SI30TERþ, Equipment Data.

Gnielinski, V. (1976). New equations for heat and mass transfer in turbulent pipe and channel flow. International Chemical Engineering *16*, 359–368.

Go, G.-H., Lee, S.-R., Yoon, S., and Kim, M.-J. (2016). Optimum design of horizontal ground-coupled heat pump systems using spiral-coil-loop heat exchangers. Applied Energy *162*, 330–345.

Godefroy, V. (2014). Élaboration et validation d'une suite volutive de modèles d'échangeurs géothermiques verticaux. M.A.Sc thesis. École Polytechnique de Montréal.

Ground Source Heat Pump Association (2012). Thermal Pile Design, Installation & Materials Standards (UK).

Gu, Y. (1995). Effects of backfill on the performance of a vertical U-tube ground-coupled heat pump. Texas A&M University.

Guber, A.K., and Pachepsky, Y.A. (2010). Multimodeling with Pedotransfer Functions. Documentation and User Manual for PTF Calculator (CalcPTF) Version 2.0. 25.

Haaland, S.E. (1983). Simple and Explicit Formulas for the Skin Friction in Turbulent Pipe Flow. ASME J. Fluids Eng. *105*, 89–90.

Habibi, M., and Hakkaki-Fard, A. (2018). Evaluation and improvement of the thermal performance of different types of horizontal ground heat exchangers based on techno-economic analysis. Energy Conversion and Management *171*, 1177–1192.

Haigh, S.K. (2012). Thermal conductivity of sands. Géotechnique *62*, 617–625.

Halldin, S., and Lindroth, A. (1992). Errors in net radiometry: comparison and evaluation of six radiometer designs. Journal of Atmospheric and Oceanic Technology *9*, 762–783.

Han, C., Ellett, K.M., Naylor, S., and Yu, X. (Bill) (2017). Influence of local geological data on the performance of horizontal ground-coupled heat pump system integrated with building thermal loads. Renewable Energy *113*, 1046–1055.

Hartley, J.G., and Black, W.Z. (1981). Transient Simultaneous Heat and Mass Transfer in Moist, Unsaturated Soils. J. Heat Transfer *103*, 376.

He, M., Rees, S.J., and Shao, L. (2009). APPLICATIONS OF A DYNAMIC THREE-DIMENSIONAL NUMERICAL MODEL FOR BOREHOLE HEAT EXCHANGERS. In Proceedings of Effstock, (Stockholm International Fairs, Stockholm, Sweden), p. 9.

He, M., Rees, S., and Shao, L. (2011). Simulation of a domestic ground source heat pump system using a three-dimensional numerical borehole heat exchanger model. Journal of Building Performance Simulation *4*, 141–155.

Hein, P., Kolditz, O., Görke, U.-J., Bucher, A., and Shao, H. (2016). A numerical study on the sustainability and efficiency of borehole heat exchanger coupled ground source heat pump systems. Applied Thermal Engineering *100*, 421–433.

Hemmati, S., Gatmiri, B., Cui, Y.-J., and Vincent, M. (2012). Thermo-hydro-mechanical modelling of soil settlements induced by soil-vegetation-atmosphere interactions. Engineering Geology *139–140*, 1–16.

Hermanns, M., and Ibáñez, S. (2019). On the ill-posedness of the g-function model for the thermal response of geothermal heat exchangers. International Journal of Thermal Sciences *138*, 285–292.

Hern, S.A. (2004). Design of an Experimental Facility for Hybrid Ground Source Heat Pump Systems. Oklahoma State University.

Heusinkveld, B.G., Jacobs, A.F.G., Holtslag, A.A.M., and Berkowicz, S.M. (2004). Surface energy balance closure in an arid region: role of soil heat flux. Agricultural and Forest Meteorology *122*, 21–37.

Hooijkaas, G.R., Genter, A., and Dezayes, C. (2006). Deep-seated geology of the granite intrusions at the Soultz EGS site based on data from 5km-deep boreholes. Geothermics *35*, 484–506.

Incropera, F.P., Dewitt, D.P., Bergman, T.L., and Lavine, A.S. (2007). Fundamentals of Heat and Mass Transfer (Hoboken, New Jersey: John Wiley & Sons).

Ingersoll, L.R., Plass, H.J., and Wis, M. (1948). Theory of the ground pipe source for the heat pump. Heating, Piping & Air Conditioning *20*, 119–123.

International Energy Agency (IEA) (2018). Global Energy and CO2 Status Report 2018. Energy Demand 29.

Irmak, S., Mutiibwa, D., and Payero, J.O. (2010). Net Radiation Dynamics: Performance of 20 Daily Net Radiation Models as Related to Model Structure and Intricacy in Two Climates. Transactions of the ASABE *53*, 1059–1076.

Jackson, R.D., Reginato, R.J., and Kimball, B.A. (1974). Diurnal soil-water evaporation: Comparison of measured and calculated soil-water fluxes. Soil Science Society of America Proceddings *38*.

Javadi, H., Mousavi Ajarostaghi, S.S., Rosen, M.A., and Pourfallah, M. (2019). Performance of ground heat exchangers: A comprehensive review of recent advances. Energy *178*, 207–233.

Javed, S., and Fahlén, P. (2010). Development and Planned Operation of a Ground Source Heat Pump Test Facility. IEA Heat Pump Newsletter *28*, 32–35.

Jensen, M., Burman, R., and Allen, R. (1990). Evapotranspiration and irrigation water requirements (New York).

Jensen-Page, L., Narsilio, G.A., Bidarmaghz, A., and Johnston, I.W. (2018). Investigation of the effect of seasonal variation in ground temperature on thermal response tests. Renewable Energy *125*, 609–619.

Jeon, J.-S., Lee, S.-R., Kim, M.-J., and Yoon, S. (2018a). Suggestion of a Scale Factor to Design Spiral-Coil-Type Horizontal Ground Heat Exchangers. Energies *11*, 2736.

Jeon, J.-S., Lee, S.-R., and Kim, M.-J. (2018b). A modified mathematical model for spiral coil-type horizontal ground heat exchangers. Energy *152*, 732–743.

Johansen, O. (1975). Thermal Conductivity of Soils. 322.

Johnsson, J., and Adl-Zarrabi, B. (2019). Modelling and evaluation of groundwater filled boreholes subjected to natural convection. Applied Energy *253*, 113555.

Kahraman, A., and Çelebi, A. (2009). Investigation of the Performance of a Heat Pump Using Waste Water as a Heat Source. Energies *2*, 697–713.

Kerme, E.D., and Fung, A.S. (2020). Heat transfer simulation, analysis and performance study of single U-tube borehole heat exchanger. Renewable Energy *145*, 1430–1448.

Kersten, M.S. (1949). THERMAL PROPERTIES OF SOILS. 233.

Kim, M.-J., Lee, S.-R., Yoon, S., and Go, G.-H. (2016). Thermal performance evaluation and parametric study of a horizontal ground heat exchanger. Geothermics *60*, 134–143.

Kim, M.-J., Lee, S.-R., Yoon, S., and Jeon, J.-S. (2018). Evaluation of geometric factors influencing thermal performance of horizontal spiral-coil ground heat exchangers. Applied Thermal Engineering *144*, 788–796.

Knapp, H.V., Durgunoglu, A., and Ortel, T.W. (1991). A review of rainfall-runoff modeling for stormwater management (Illinois District).

Kondo, J., Saigusa, N., and Sato, T. (1990). A parameterization of evaporation from bare soil surfaces. Journal of Applied Meteorology *29*, 385–389.

Kupiec, K., Larwa, B., and Gwadera, M. (2015). Heat transfer in horizontal ground heat exchangers. Applied Thermal Engineering *75*, 270–276.

Kurevija, T., Macenić, M., and Borović, S. (2017). Impact of grout thermal conductivity on the long-term efficiency of the ground-source heat pump system. Sustainable Cities and Society *31*, 1–11.

Kustas, W.P., and Daughtry, C.S.T. (1990). Estimation of the soil heat flux/net radiation ratio from spectral data. Agricultural and Forest Meteorology *49*, 205–223.

Lamarche, L. (2017). g-function generation using a piecewise-linear profile applied to ground heat exchangers. International Journal of Heat and Mass Transfer *115*, 354–360.

Lamarche, L. (2019). Horizontal ground heat exchangers modelling. Applied Thermal Engineering *155*, 534–545.

Lamarche, L., and Beauchamp, B. (2007). A new contribution to the finite line-source model for geothermal boreholes. Energy and Buildings *39*, 188–198.

Larwa, B., Teper, M., Grzywacz, R., and Kupiec, K. (2019). Study of a slinky-coil ground heat exchanger – Comparison of experimental and analytical solution. International Journal of Heat and Mass Transfer *142*, 118438.

Lee, C., Lee, K., Choi, H., and Choi, H.-P. (2010). Characteristics of thermally-enhanced bentonite grouts for geothermal heat exchanger in South Korea. Sci. China Ser. E-Technol. Sci. *53*, 123–128.

Lee, C., Park, M., Min, S., Kang, S.-H., Sohn, B., and Choi, H. (2011). Comparison of effective thermal conductivity in closed-loop vertical ground heat exchangers. Applied Thermal Engineering *31*, 3669–3676.

Lee, C., You, J., and Park, H. (2018). In-situ response test of various borehole depths and heat injection rates at standing column well geothermal heat exchanger systems. Energy and Buildings *172*, 201–208.

Leij, F.J., Alves, W.J., an Genuchten, M.Th., and Williams, J.R. (1996). Unsaturated Soil Hydraulic Database, UNSODA 1.0 User's Manual. (USEPA, Ada, OK).

Leong, E.C., and Rahardjo, H. (1997). Review of Soil-Water Characteristic Curve Equations. Journal of Geotechnical and Geoenvironmental Engineering *123*, 1106–1117.

Li, M., and Lai, A.C.K. (2015). Review of analytical models for heat transfer by vertical ground heat exchangers (GHEs): A perspective of time and space scales. Applied Energy *151*, 178–191.

Li, C., Mao, J., Zhang, H., Xing, Z., Li, Y., and Zhou, J. (2017a). Numerical simulation of horizontal spiral-coil ground source heat pump system: Sensitivity analysis and operation characteristics. Applied Thermal Engineering *110*, 424–435.

Li, H., Nagano, K., and Lai, Y. (2012). Heat transfer of a horizontal spiral heat exchanger under groundwater advection. International Journal of Heat and Mass Transfer *55*, 6819–6831.

Li, J., Li, Z., Guo, M., Li, P., and Cheng, S. (2017b). Effects of urban grass coverage on rainfall-induced runoff in Xi'an loess region in China. Water Science and Engineering *10*, 320–325.

Li, W., Li, X., Du, R., Wang, Y., and Tu, J. (2019). Experimental investigations of the heat load effect on heat transfer of ground heat exchangers in a layered subsurface. Geothermics *77*, 75–82.

Lin, J., Nowamooz, H., Braymand, S., Wolff, P., and Fond, C. (2018). Impact of soil moisture on the long-term energy performance of an earth-air heat exchanger system. Renewable Energy.

Liu, S., Lu, L., Mao, D., and Jia, L. (2007). Evaluating parameterizations of aerodynamic resistance to heat transfer using field measurements. Hydrol. Earth Syst. Sci. *11*, 769–783.

Liu, Z., Xu, W., Qian, C., Chen, X., and Jin, G. (2015). Investigation on the feasibility and performance of ground source heat pump (GSHP) in three cities in cold climate zone, China. Renewable Energy *84*, 89–96.

Liu, Z., Xu, W., Zhai, X., Qian, C., and Chen, X. (2017). Feasibility and performance study of the hybrid ground-source heat pump system for one office building in Chinese heating dominated areas. Renewable Energy *101*, 1131–1140.

Lu, S., Ren, T., Gong, Y., and Horton, R. (2007). An Improved Model for Predicting Soil Thermal Conductivity from Water Content at Room Temperature. Soil Science Society of America Journal *71*, 8.

Lund, J.W., and Boyd, T.L. (2016). Direct utilization of geothermal energy 2015 worldwide review. Geothermics *60*, 66–93.

Luo, J., Rohn, J., Bayer, M., and Priess, A. (2013). Thermal performance and economic evaluation of double U-tube borehole heat exchanger with three different borehole diameters. Energy and Buildings *67*, 217–224.

Luo, J., Rohn, J., Bayer, M., Priess, A., and Xiang, W. (2014). Analysis on performance of borehole heat exchanger in a layered subsurface. Applied Energy *123*, 55–65.

Luo, J., Rohn, J., Xiang, W., Bertermann, D., and Blum, P. (2016). A review of ground investigations for ground source heat pump (GSHP) systems. Energy and Buildings *117*, 160–175.

Luo, J., Luo, Z., Xie, J., Xia, D., Huang, W., Shao, H., Xiang, W., and Rohn, J. (2018a). Investigation of shallow geothermal potentials for different types of ground source heat pump systems (GSHP) of Wuhan city in China. Renewable Energy *118*, 230–244.

Luo, J., Tuo, J., Huang, W., Zhu, Y., Jiao, Y., Xiang, W., and Rohn, J. (2018b). Influence of groundwater levels on effective thermal conductivity of the ground and heat transfer rate of borehole heat exchangers. Applied Thermal Engineering *128*, 508–516.

Man, Y., Yang, H., Diao, N., Liu, J., and Fang, Z. (2010). A new model and analytical solutions for borehole and pile ground heat exchangers. International Journal of Heat and Mass Transfer *53*, 2593–2601.

Marcotte, D., and Pasquier, P. (2008). On the estimation of thermal resistance in borehole thermal conductivity test. Renewable Energy *33*, 2407–2415.

McKee, C.R., and Bumb, A.C. (1987). Flow-Testing Coalbed Methane Production Wells in the Presence of Water and Gas. SPE Formation Evaluation *2*, 599–608.

McMahon, T.A., Peel, M.C., Lowe, L., Srikanthan, R., and McVicar, T.R. (2013). Estimating actual, potential, reference crop and pan evaporation using standard meteorological data: a pragmatic synthesis. Hydrology and Earth System Sciences *17*, 1331–1363.

Mei, V.C. (1986). Theoretical heat pump ground coil analysis with variable ground farfield boundary conditions. AIChE J. *32*, 1211–1215.

Mensah, K., Jang, Y.-S., and Choi, J.M. (2017). Assessment of design strategies in a ground source heat pump system. Energy and Buildings *138*, 301–308.

Mikhaylova, O., Johnston, I.W., and Narsilio, G.A. (2016). Uncertainties in the design of ground heat exchangers. Environmental Geotechnics *3*, 253–264.

Moeck, I.S. (2014). Catalog of geothermal play types based on geologic controls. Renewable and Sustainable Energy Reviews *37*, 867–882.

Mogensen, P. (1983). Fluid to duct wall heat transfer in duct system heat storage. In Proceedings of the International Conference on Surface Heat Storage in Theory and Practice, (Stockholm), pp. 652–657.

Molina-Giraldo, N., Blum, P., Zhu, K., Bayer, P., and Fang, Z. (2011). A moving finite line source model to simulate borehole heat exchangers with groundwater advection. International Journal of Thermal Sciences *50*, 2506–2513.

Monteith, J. (1965). Evaporation and environment. Symposia of the Society for Experimental Biology *19*, 205–234.

Monzó, P., Mogensen, P., Acuña, J., Ruiz-Calvo, F., and Montagud, C. (2015). A novel numerical approach for imposing a temperature boundary condition at the borehole wall in borehole fields. Geothermics *56*, 35–44.

Moody, L.F. (1944). Friction Factors for Pipe Flow. Transactions of the ASME *66*, 671–681.

Mualem, Y. (1976). A new model for predicting the hydraulic conductivity of unsaturated porous media. Water Resour. Res. *12*, 513–522.

Muñoz-Castelblanco, J.A., Pereira, J.M., Delage, P., and Cui, Y.J. (2012). The water retention properties of a natural unsaturated loess from northern France. Géotechnique *62*, 95–106.

Naicker, S.S., and Rees, S.J. (2020). Long-term high frequency monitoring of a large borehole heat exchanger array. Renewable Energy *145*, 1528–1542.

Naldi, C., and Zanchini, E. (2018). Effects of the total borehole length and of the heat pump inverter on the performance of a ground-coupled heat pump system. Applied Thermal Engineering *128*, 306–319.

Naylor, S., Ellett, K.M., and Gustin, A.R. (2015). Spatiotemporal variability of ground thermal properties in glacial sediments and implications for horizontal ground heat exchanger design. Renewable Energy *81*, 21–30.

Nguyen, V.T., Heindl, H., Pereira, J.M., Tang, A.M., and Frost, J.D. (2017). Water retention and thermal conductivity of a natural unsaturated loess. Géotechnique Letters *7*, 286–291.

Nian, Y.-L., and Cheng, W.-L. (2018). Analytical g-function for vertical geothermal boreholes with effect of borehole heat capacity. Applied Thermal Engineering *140*, 733–744.

Nikoosokhan, S., Nowamooz, H., and Chazallon, C. (2016). Effect of dry density, soil texture and time-spatial variable water content on the soil thermal conductivity. Geomechanics and Geoengineering *11*, 149–158.

Nordell, B. (2011). Thermal Response Test (TRT) State-of-the art 2011: IEA ECES ANNEX 21 (Luleå tekniska universitet).

Nowamooz, H., Nikoosokhan, S., Lin, J., and Chazallon, C. (2015). Finite difference modeling of heat distribution in multilayer soils with time-spatial hydrothermal properties. Renewable Energy *76*, 7–15.

Oke, T.R. (1987). Boundary layer climates (Methuen & Co. Ltd).

Ol'dekop, E.M. (1911). On evaporation from the surface of river basins. Transactions on Meteorological Observations *4*, 200.

Olivella, S., and Gens, A. (2000). Vapour Transport in Low Permeability Unsaturated Soils with Capillary Effects. Transport in Porous Media *40*, 219–241.

Omer, A.M. (2018). Some Aspects of Soil Thermal Properties. 42.

Ortega-Farias, S., Antonioletti, R., and Olioso, A. (2000). Net radiation model evaluation at an hourly time step for mediterranean conditions. Agronomie *20*, 157–164.

Pachepsky, Y., and Park, Y. (2015). Saturated Hydraulic Conductivity of US Soils Grouped According to Textural Class and Bulk Density. Soil Science Society of America Journal *79*, 1094.

Park, Sk., Lee, S.-R., Park, H., Yoon, S., and Chung, J. (2013). Characteristics of an analytical solution for a spiral coil type ground heat exchanger. Computers and Geotechnics *49*, 18–24.

Penman, H.L. (1948). Natural Evaporation from Open Water, Bare Soil and Grass. Proceedings of the Royal Society A: Mathematical, Physical and Engineering Sciences *193*, 120–145.

Pike, J.G. (1964). The estimation of annual run-off from meteorological data in a tropical climate. Journal of Hydrology *2*, 116–123.

Ponce, V.M., and Hawkins, R.H. (1996). Runoff Curve Number: Has It Reached Maturity? Journal of Hydrologic Engineering *1*, 11–19.

Potter, N.J., and Zhang, L. (2009). Interannual variability of catchment water balance in Australia. Journal of Hydrology *369*, 120–129.

Pouloupatis, P.D., Florides, G., and Tassou, S. (2011). Measurements of ground temperatures in Cyprus for ground thermal applications. Renewable Energy *36*, 804–814.

Priestley, B. (1972). On the Assessment of Surface Heat Flux and Evaporation Using Large-Scale Parameters. Mon. Weather Rev *100*, 81–92.

Pu, L., Xu, L., Qi, D., and Li, Y. (2018). Structure optimization for horizontal ground heat exchanger. Applied Thermal Engineering *136*, 131–140.

Radioti, G., Cerfontaine, B., Charlier, R., and Nguyen, F. (2018). Experimental and numerical investigation of a long-duration Thermal Response Test: Borehole Heat Exchanger behaviour and thermal plume in the heterogeneous rock mass. Geothermics *71*, 245–258.

Rahimi, A., Rahardjo, H., and Leong, E.-C. (2015). Effects of soil–water characteristic curve and relative permeability equations on estimation of unsaturated permeability function. Soils and Foundations *55*, 1400–1411.

Rajeev, P., Chan, D., and Kodikara, J. (2012). Ground–atmosphere interaction modelling for long-term prediction of soil moisture and temperature. Can. Geotech. J. *49*, 1059–1073.

Rammal, D., Mroueh, H., and Burlon, S. (2018). Impact of thermal solicitations on the design of energy piles. Renewable and Sustainable Energy Reviews *92*, 111–120.

Raymond, J., Therrien, R., Gosselin, L., and Lefebvre, R. (2011a). Numerical analysis of thermal response tests with a groundwater flow and heat transfer model. Renewable Energy *36*, 315–324.

Raymond, J., Therrien, R., Gosselin, L., and Lefebvre, R. (2011b). A Review of Thermal Response Test Analysis Using Pumping Test Concepts. Ground Water *49*, 932–945.

Raymond, J., Malo, M., Tanguay, D., Grasby, S., and Bakhteya, F. (2015). Direct Utilization of Geothermal Energy from Coast to Coast: a Review of Current Applications and Research in Canada. 10.

Raymond, J., Lamarche, L., and Malo, M. (2016). Extending thermal response test assessments with inverse numerical modeling of temperature profiles measured in ground heat exchangers. Renewable Energy *99*, 614–621.

Rees, S.W., Adjali, M.H., Zhou, Z., Davies, M., and Thomas, H.R. (2000). Ground heat transfer effects on the thermal performance of earth-contact structures. Renewable and Sustainable Energy Reviews 53.

Richards, L.A. (1931). CAPILLARY CONDUCTION OF LIQUIDS THROUGH POROUS MEDIUMS. Physics *1*, 318–333.

Rivera, J.A., Blum, P., and Bayer, P. (2015). Ground energy balance for borehole heat exchangers: Vertical fluxes, groundwater and storage. Renewable Energy *83*, 1341–1351.

Rose, C. (1968). Water transport in soil with a daily temperature wave. I. Theory and experiment. Australian Journal of Soil Research *6*, 31–44.

Ruiz-Calvo, F., Cervera-Vázquez, J., Montagud, C., and Corberán, J.M. (2016). Reference data sets for validating and analyzing GSHP systems based on an eleven-year operation period. Geothermics *64*, 538–550.

Saito, H., Šimůnek, J., and Mohanty, B.P. (2006). Numerical Analysis of Coupled Water, Vapor, and Heat Transport in the Vadose Zone. Vadose Zone Journal *5*, 784.

Saito, H., Saito, T., Kohgo, Y., Hamamoto, S., Moldrup, P., and Komatsu, T. (2014a). Effect of reducing the test period on estimating effective thermal conductivity from Kelvin's line source function in thermal response test: a numerical study. J Jpn Soc Soil Phys *128*, 11–20.

Saito, T., Hamamoto, S., Ei Mon, E., Takemura, T., Saito, H., Komatsu, T., and Moldrup, P. (2014b). Thermal properties of boring core samples from the Kanto area, Japan: Development of predictive models for thermal conductivity and diffusivity. Soils and Foundations *54*, 116–125.

Saito, T., Hamamoto, S., Ueki, T., Ohkubo, S., Moldrup, P., Kawamoto, K., and Komatsu, T. (2016). Temperature change affected groundwater quality in a confined marine aquifer during long-term heating and cooling. Water Research *94*, 120–127.

Sakashita H., and Kumada T. (1998). Heat Transfer Model for Predicting Thermal Conductivity of Highly Compacted Bentonite. Journal of the Atomic Energy Society of Japan / Atomic Energy Society of Japan *40*, 235–240.

Salim Shirazi, A., and Bernier, M. (2014). A small-scale experimental apparatus to study heat transfer in the vicinity of geothermal boreholes. HVAC&R Research *20*, 819–827.

Salimshirazi, A. (2012). TRANSIENT HEAT TRANSFER IN VERTICAL GROUND HEAT EXCHANGERS. UNIVERSITÉ DE MONTRÉAL.

Samson, M., Dallaire, J., and Gosselin, L. (2018). Influence of groundwater flow on cost minimization of ground coupled heat pump systems. Geothermics *73*, 100–110.

Sangi, R., and Müller, D. (2018). Dynamic modelling and simulation of a slinky-coil horizontal ground heat exchanger using Modelica. Journal of Building Engineering *16*, 159–168.

Sanner, B. (2017). Ground Source Heat Pumps-history, development, current status, and future prospects. In 12th IEA Heat Pump Conference, (Giessen (Germany)), p.

Sanner, B., Karytsas, C., Mendrinos, D., and Rybach, L. (2003). Current status of ground source heat pumps and underground thermal energy storage in Europe. Geothermics *32*, 579–588.

Schill, E., Genter, A., Cuenot, N., and Kohl, T. (2017). Hydraulic performance history at the Soultz EGS reservoirs from stimulation and long-term circulation tests. Geothermics *70*, 110–124.

Schreiber, P. (1904). Uber die Beziehungen zwischen dem Niederschlag und der Wasserfuhrung der Fluβe in Mitteleuropa. Z. Meteorol. 441–452.

Selamat, S., Miyara, A., and Kariya, K. (2015). Analysis of Short Time Period of Operation of Horizontal Ground Heat Exchangers. Resources *4*, 507–523.

Selamat, S., Miyara, A., and Kariya, K. (2016). Numerical study of horizontal ground heat exchangers for design optimization. Renewable Energy *95*, 561–573.

Self, S.J., Reddy, B.V., and Rosen, M.A. (2013). Geothermal heat pump systems: Status review and comparison with other heating options. Applied Energy *101*, 341–348.

Serageldin, A.A., Sakata, Y., Katsura, T., and Nagano, K. (2018). Thermo-hydraulic performance of the U-tube borehole heat exchanger with a novel oval cross-section: Numerical approach. Energy Conversion and Management *177*, 406–415.

Serghides, T.K. (1984). Estimate friction factor accurately. Chem Eng *91*, 63–64.

Shao, H., Hein, P., Sachse, A., and Kolditz, O. (2016). Geoenergy Modeling II: Shallow Geothermal Systems (Cham: Springer International Publishing).

Shirazi, A.S., and Bernier, M. (2013). Thermal capacity effects in borehole ground heat exchangers. Energy and Buildings *67*, 352–364.

Shortall, R., Davidsdottir, B., and Axelsson, G. (2015). Geothermal energy for sustainable development: A review of sustainability impacts and assessment frameworks. Renewable and Sustainable Energy Reviews *44*, 391–406.

Shrestha, G., Uchida, Y., Yoshioka, M., Fujii, H., and Ioka, S. (2015). Assessment of development potential of ground-coupled heat pump system in Tsugaru Plain, Japan. Renewable Energy *76*, 249–257.

Singh, R.M., Sani, A.K., and Amis, T. (2019). An overview of ground-source heat pump technology. In Managing Global Warming, (Elsevier), pp. 455–485.

Smith, D.C., Elmore, A.C., and Thompson, J. (2018). The effect of seasonal groundwater saturation on the effectiveness of large scale borehole heat exchangers in a karstic aquifer. Geothermics *75*, 164–170.

Soldo, V., Borović, S., Lepoša, L., and Boban, L. (2016). Comparison of different methods for ground thermal properties determination in a clastic sedimentary environment. Geothermics *61*, 1–11.

Spitler, J.D., and Gehlin, S. (2019). Measured Performance of a Mixed-Use Commercial-Building Ground Source Heat Pump System in Sweden. Energies *12*, 2020.

Spitler, J.D., and Gehlin, S.E.A. (2015). Thermal response testing for ground source heat pump systems—An historical review. Renewable and Sustainable Energy Reviews *50*, 1125–1137.

Spitler, J.D., Bernier, M., Kummert, M., Cui, P., and Liu, X. (2009). Preliminary intermodel comparison of ground heat exchanger simulation models. (Stockholm), p. 8.

Spitler, J.D., Javed, S., and Ramstad, R.K. (2016). Natural convection in groundwater-filled boreholes used as ground heat exchangers. Applied Energy *164*, 352–365.

Standards Australia (1996). Residential Slabs and Footings, Australian Standard AS2870.

Sterpi, D. (2020). Insights into the Behaviour of Energy Piles Under Different Head Constraints and Thermal Loads. In Geotechnical Research for Land Protection and Development, F. Calvetti, F. Cotecchia, A. Galli, and C. Jommi, eds. (Cham: Springer International Publishing), pp. 763–772.

Suryatriyastuti, M.E., Mroueh, H., and Burlon, S. (2012). Understanding the temperature-induced mechanical behaviour of energy pile foundations. Renewable and Sustainable Energy Reviews *16*, 3344–3354.

Swamee, P.K., and Jain, A.K. (1976). Explicit equation for pipe flow problems. J Hydr Div ASCE *102*, 657–664.

Swinbank, W.C. (1963). Long-wave radiation from clear skies. Q.J Royal Met. Soc. *89*, 339–348.

Synergy (2018). Geological Survey/TRT/Design.

Tang, A.-M., Cui, Y.-J., and Le, T.-T. (2008). A study on the thermal conductivity of compacted bentonites. Applied Clay Science *41*, 181–189.

Tedela, N.H. (2009). RAINFALL-RUNOFF RELATIONSHIPS FOR SMALL, MOUNTAINOUS, FORESTED WATERSHEDS IN THE EASTERN UNITED STATES. The University of Georgia.

Tsagarakis, K.P., Efthymiou, L., Michopoulos, A., Mavragani, A., Anđelković, A.S., Antolini, F., Bacic, M., Bajare, D., Baralis, M., Bogusz, W., et al. (2018). A review of the legal framework in shallow geothermal energy in selected European countries: Need for guidelines. Renewable Energy S0960148118311911.

Tsutsumi, A., Jinno, K., and Berndtsson, R. (2004). Surface and subsurface water balance estimation by the groundwater recharge model and a 3-D two-phase flow model. Hydrological Sciences-Journal-Des Sciences Hydrologiques *49*, 22.

Tuller, M., and Or, D. (2005). WATER RETENTION AND CHARACTERISTIC CURVE. In Encyclopedia of Soils in the Environment, (Elsevier), pp. 278–289.

Turc, L. (1954). Le Bilan d'eau des sols : relations entre les précipitations, l'évaporation et l'écoulement. Annales Agronomiques *5*, 491–569.

Vereecken, H. (1995). Estimating the unsaturated hydraulic conductivity from theoretical models using simple soil properties. Geoderma *65*, 81–92.

Vidal, J., Genter, A., Schmittbuhl, J., Whitechurch, H., Baujard, C., and Dalmais, E. (2015). Evolution of concepts for the geothermal projects in the Upper Rhine Graben. 5.

de Vries, D.A. (1963). Thermal properties of soil. Physics of Plant Environment 210–235.

Wang, S., and Wang, H. (2018). Extending the Rational Method for assessing and developing sustainable urban drainage systems. Water Research *144*, 112–125.

Wang, D., Lu, L., and Cui, P. (2016a). A new analytical solution for horizontal geothermal heat exchangers with vertical spiral coils. International Journal of Heat and Mass Transfer *100*, 111–120.

Wang, Z., Wang, F., Ma, Z., Wang, X., and Wu, X. (2016b). Research of heat and moisture transfer influence on the characteristics of the ground heat pump exchangers in unsaturated soil. Energy and Buildings *130*, 140–149.

Weiss, A. (1982). An Experimental Study of Net Radiation, Its Components and Prediction1. Agronomy Journal *74*, 871.

Westcot, D.W., and Wierenga, P.J. (1974). Transfer of Heat by Conduction and Vapor Movement in a Closed Soil System. Soil Science Society of America *38*, 9–14.

van Wijk, W.R. (1963). Physics of plant environment (Amsterdam: North Holland Publishing Company).

Wood, D.J. (1968). An Explicit friction factor relationship. Civil Eng. 60–61.

Wright, J., and Jensen, M. (1972). Peak water requirements of crops in Southern Idaho. Journal of Irrigation and Drainage Engineering *96*, 193–201.

Wu, Y., Gan, G., Verhoef, A., Vidale, P.L., and Gonzalez, R.G. (2010). Experimental measurement and numerical simulation of horizontal-coupled slinky ground source heat exchangers. Applied Thermal Engineering *30*, 2574–2583.

Wu, Z., You, S., Zhang, H., Fan, M., Zheng, W., Wang, Y., and Zhang, Y. (2019). Mathematical Modeling and Performance Analysis of Seawater Heat Exchanger in Closed-Loop Seawater-Source Heat Pump System. J. Energy Eng. *145*, 04019012.

Xia, L. (2017). Performance evaluation and optimisation of stand-alone ground source heat pumps and hybrid ground source heat pumps with integrated solar photovoltaic thermal collectors. University of Wollongong.

Xiong, Z., Fisher, D.E., and Spitler, J.D. (2015). Development and validation of a Slinky^{TM} ground heat exchanger model. Applied Energy *141*, 57–69.

Yang, Y., and Li, M. (2014). Short-time performance of composite-medium line-source model for predicting responses of ground heat exchangers with single U-shaped tube. International Journal of Thermal Sciences *82*, 130–137.

Yang, H., Cui, P., and Fang, Z. (2010). Vertical-borehole ground-coupled heat pumps: A review of models and systems. Applied Energy *87*, 16–27.

Yavuzturk, C., and Spitler, J.D. (2001). Field Validation of a Short Time Step Model for Vertical Ground-Loop Heat Exchangers. ASHRAE Transactions *107*, 10.

Yoon, S., Lee, S.-R., and Go, G.-H. (2015a). Evaluation of thermal efficiency in different types of horizontal ground heat exchangers. Energy and Buildings *105*, 100–105.

Yoon, S., Lee, S.-R., and Go, G.-H. (2015b). Evaluation of thermal efficiency in different types of horizontal ground heat exchangers. Energy and Buildings *105*, 100–105.

You, T., Wang, B., Wu, W., Shi, W., and Li, X. (2015). Performance analysis of hybrid ground-coupled heat pump system with multi-functions. Energy Conversion and Management *92*, 47–59.

Yuan, Y., Cao, X., Sun, L., Lei, B., and Yu, N. (2012). Ground source heat pump system: A review of simulation in China. Renewable and Sustainable Energy Reviews *16*, 6814–6822.

Yuan, Y., Cao, X., Wang, J., and Sun, L. (2016). Thermal interaction of multiple ground heat exchangers under different intermittent ratio and separation distance. Applied Thermal Engineering *108*, 277–286.

Zanchini, E., and Lazzari, S. (2013). Temperature distribution in a field of long Borehole Heat Exchangers (BHEs) subjected to a monthly averaged heat flux. Energy *59*, 570–580.

Zeng, H.Y., Diao, N.R., and Fang, Z.H. (2002). A finite line-source model for boreholes in geothermal heat exchangers. Heat Trans. Asian Res. *31*, 558–567.

Zhai, Q., and Rahardjo, H. (2015). Estimation of permeability function from the soil–water characteristic curve. Engineering Geology *199*, 148–156.

Zhang, F., and Fredlund, D.G. (2015). Examination of the estimation of relative permeability for unsaturated soils. Can. Geotech. J. *52*, 2077–2087.

Zhang, C., Song, W., Sun, S., and Peng, D. (2015a). Parameter estimation of in-situ thermal response test with unstable heat rate. Energy *88*, 497–505.

Zhang, L., Dawes, W.R., and Walker, G.R. (2001). Response of mean annual evapotranspiration to vegetation changes at catchment scale. Water Resour. Res. *37*, 701–708.

Zhang, L., Hickel, K., Dawes, W.R., Chiew, F.H.S., Western, A.W., and Briggs, P.R. (2004). A rational function approach for estimating mean annual evapotranspiration: ESTIMATING MEAN ANNUAL EVAPOTRANSPIRATION. Water Resour. Res. *40*.

Zhang, L., Zhao, L., Yang, L., and Hu Songtao (2015b). Analyses on soil temperature responses to intermittent heat rejection from BHEs in soils with groundwater advection. Energy and Buildings *107*, 355–365.

Zhang, L., Huang, G., Zhang, Q., and Wang, J. (2018). An hourly simulation method for the energy performance of an office building served by a ground-coupled heat pump system. Renewable Energy *126*, 495–508.

Zhang, X., Zhang, T., Jiang, Y., and Li, B. (2019). Improvement on an analytical finite line source model considering complex initial and boundary conditions: Part 1, model development and validation. Energy and Buildings *198*, 1–10.

Zhao, J., Li, Y., and Wang, J. (2016). A Review on Heat Transfer Enhancement of Borehole Heat Exchanger. Energy Procedia *104*, 413–418.

Zhou, Y., Zhao, L., and Wang, S. (2017). Determination and analysis of parameters for an in-situ thermal response test. Energy and Buildings *149*, 151–159.

Zigrang, D.J., and Sylvester, N.D. (1982). Explicit approximations to the Colebrook's friction factor. AIChE J *28*, 514–515.

ETUDE NUMERIQUE SUR LES ECHANGEURS DE CHALEUR SOUTERRAINS INSTALLES DANS LES SOLS

Doctorant : Fu-Jiao TANG

Directeur de Thèse : Hossein NOWAMOOZ

Laboratoire : Laboratoire des sciences de l'ingénieur, de l'informatique et de l'imagerie (ICube, UMR 7357, CNRS), INSA de Strasbourg, 67084, Strasbourg Cedex, France

Résumé étendu

Les énergies renouvelables continuent de gagner en importance du fait que les sources d'énergies traditionnelles ne sont pas illimitées à long terme, surtout à une époque où la demande énergétique augmente. De plus, des risques environnementaux tels que la pollution de l'air, l'acidification régionale et le changement climatique (Shortall et al., 2015) apparaissent progressivement en consommant des combustibles fossiles. La construction et l'exploitation des bâtiments représentent 36 % de la consommation finale d'énergie mondiale et 39 % des émissions de dioxyde de carbone (CO_2) données de 2017. Ainsi, la domine du bâtiment représente la plus grande part de l'énergie et des émissions (International Energy Agency (IEA), 2018). Par conséquent, l'utilisation de l'énergie pour les bâtiments joue un rôle

dominant dans la transition vers une énergie propre ces dernières années (Sterpi, 2020). Sangi et Müller (2018) rapportent que l'Union Européenne (UE) s'est fixé comme objectif de réduire ses émissions de CO_2 de 20 % d'ici 2020 par rapport à 2007 et que les énergies renouvelables sont essentielles pour atteindre cet objectif.

L'énergie géothermique constitue l'une des nombreuses sources d'énergie renouvelable. Et au cours de ces dernières années, qui a forcément attiré l'attention. D'une manière générale, la géothermie est identifiée par trois catégories: la géothermie profonde à haute température (supérieure à 150 ºC) pour la production d'électricité; la géothermie intermédiaire (moins de 150 ºC) pour l'utilisation directe; le réservoir basse température (moins de 32 ºC) pour les pompes à chaleur géothermiques (GSHPs) (Omer, 2018). Pour la production d'électricité et l'utilisation directe de l'énergie géothermique, il existe des restrictions sur la profondeur des puits et les conditions géologiques locales contrairement aux systèmes de GSHP. En effet, ces derniers comportent moins de restrictions puisque la température du sol fluctue de façon négligeable lorsque la profondeur atteint 10 m sous la surface terrestre, où il fait frais en été et chaud en hiver. Depuis la préhistoire, on profite de la température constante sous la surface de la terre pour stocker de la nourriture ou pour y vivre (Sanner, 2017). L'énergie géothermique peu profonde est également accessible de jour comme de nuit, sans interruption. L'Environmental Protection Agency (EPA) des États-Unis a déterminé que les systèmes de pompes à chaleur couplées au sol (GCHP) constituent l'option de chauffage et de climatisation la plus écoénergétique et écologique (Atam and Helsen, 2016).

Objectifs de la thèse

La présente enquête vise principalement quatre objectifs :

1. Application du transfert hydrothermique dans le modèle de simulation numérique pour échangeur de chaleur de forage (BHE) et échangeur de chaleur horizontal (HGHE). Le modèle serait également utilisé pour analyser le transfert hydrothermal dans des milieux poreux entourant l'échangeur de chaleur souterrain pendant une période d'un an.

2. Exploration de différents facteurs influençant la performance d'un BHE peu profond installé dans des sols insaturés. Dans de nombreuses études, le transfert hydrothermique dans des milieux poreux autour des échangeurs de chaleur souterrains est négligé. Le milieu poreux est traditionnellement censé être homogène dans ces œuvres. Cette simulation numérique est plus proche de l'état in situ, ce qui lui permet d'être plus précise que les modèles prenant en

compte les milieux environnants homogènes autour des échangeurs de chaleur souterrains. De plus, quinze facteurs conventionnels vont être étudiés dans ce travail, ce qui rend ce travail plus complet. Cette étude peut aider les ingénieurs à choisir les paramètres appropriés concernant les différents facteurs à l'étape de conception d'un BHE peu profond.

3. Fournir une approche pour estimer la conductivité thermique effective du sol autour du BHE en effectuant numériquement les tests de réponse thermique (TRTs). Les TRT coûtent très cher, ce qui n'est pas abordable pour les petits et moyens projets. Par conséquent, il est intéressant de fournir une approche analytique pour estimer la conductivité thermique efficace du sol à l'étape de la conception de ces projets.

4. Estimer de la différence de performance d'une HGHE entre la prise en compte de la condition limite de Dirichlet souvent utilisée et de la condition limite de Neumann à la surface du sol. Par convention, les bilans énergétiques de la surface terrestre ne sont pas pris en compte dans la simulation numérique de l'HGHE. Avec l'approche traditionnelle de Dirichlet, on l'étude elle influence la performance de l'HGHE.

Performance à long terme d'un BHE peu profond sur un champ géothermique en Alsace

Un champ multicouche situé à Illkirch (région Alsace, France) a été étudié pour sa capacité de stockage d'énergie géothermique peu profonde. Pour poursuivre les différents aspects qui influencent la performance des BHE peu profonds, COMSOL a été utilisé pour les simulations numériques par méthode des éléments finis. La conduite et le fluide porteur ont été considérés comme un domaine 1D, tandis que le coulis et les sols environnants comme un milieu 3D.

Les premiers profils hydrothermaux locaux ont été obtenus après avoir atteint un stade d'équilibre. Le profil d'aspiration et de température dans cette phase d'équilibre est présenté à la Fig. 1. Le profil d'aspiration initial (Fig. 1) indique que la nappe phréatique se trouve à une profondeur de 7,63 m. Pour une profondeur inférieure à 7,63 m, le sol est donc censé être saturé. La figure 1-b montre que le gradient de température en dessous de 30 m est de 0,1 $K.m^{-1}$, ce qui correspond à la condition limite inférieure imposée.

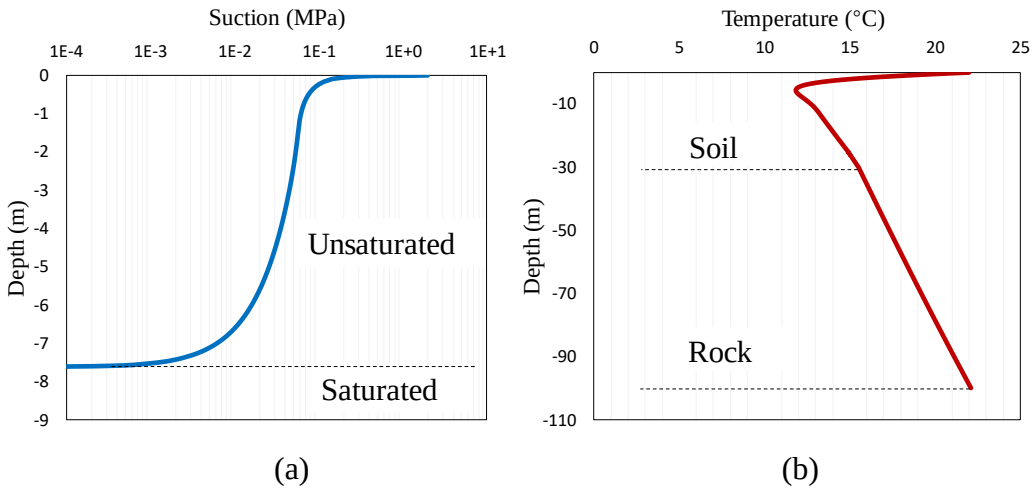

Fig. 1. Profils hydrothermaux initiaux : a) aspiration initiale (MPa) et b) température initiale (°C)

Deux scénarios différents ont été étudiés ici: une température d'entrée constante et une charge thermique saisonnière variable (Bidarmaghz et al., 2016; Shao et al., 2016). Dans les deux scénarios, le BHE peu profond a consommé la même quantité d'énergie sur une période d'un an. La température d'entrée constante (5 °C) et la charge thermique saisonnière (variant entre 8,82 et 26,45 W.m^{-1}) sont indiquées à la Fig. 2.

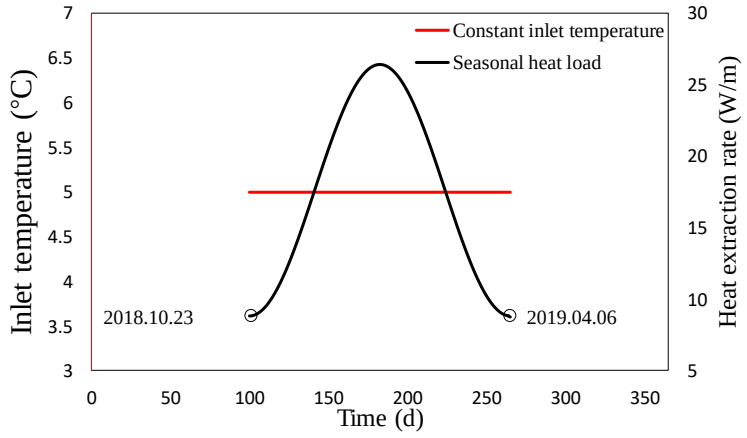

Fig. 2. Température d'entrée imposée (°C) et taux d'extraction de chaleur variable (W.m^{-1}) pendant la période de travail d'un BHE peu profond

Fig. 3 illustre la variation du coefficient de performance (COP) et de l'énergie totale extraite (TEE) de la pompe à chaleur du BHE peu profond sur un an pour les deux scénarios. Pour TEE, les deux scénarios prescrits extraient la même quantité d'énergie sur une année, ce qui

indique que le BHE peu profond est capable d'exploiter 17,63 W d'énergie pour 1 mètre. Le TEE pour le scénario de température d'entrée constante augmente presque linéairement pendant la période de travail du BHE peu profond, tandis qu'il varie de façon non linéaire pour le scénario de charge thermique saisonnière.

Le COP de la pompe à chaleur pour le scénario de température d'entrée constante, restant presque stable pendant les jours ouvrables, se situe entre 4,8 et 4,9. Alors que le COP pour le scénario de charge thermique saisonnière, qui dépend fortement de sa charge thermique, se situe entre 4,3 et 5,7.

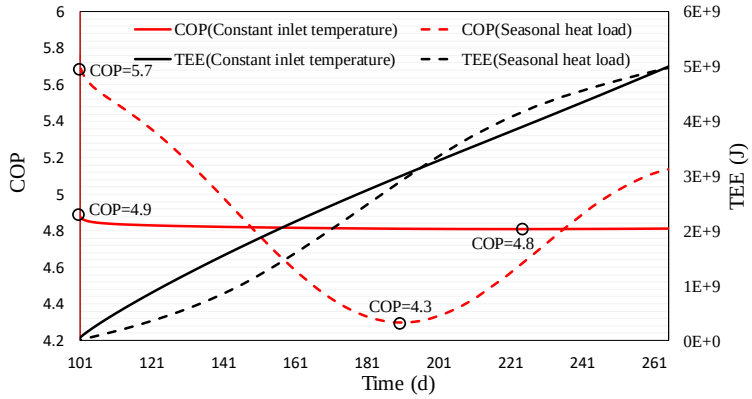

Fig. 3. Pompe à chaleur COP et TEE pendant la période de travail du BHE peu profond pour les deux scénarios prescrits

Afin d'évaluer la performance du BHE peu profond sur une période plus longue, une autre analyse numérique considérant un fonctionnement sur 5 ans du même BHE peu profond a été effectuée pour le scénario de température d'entrée constante. La figure 4 montre l'énergie extraite par année, tandis que l'écart énergétique le plus important existe entre la première et la deuxième année (5,44 %). A partir de la troisième année, la différence devient moins significative. Dans notre cas, une période de 4 ans est nécessaire pour atteindre ce stade d'équilibre.

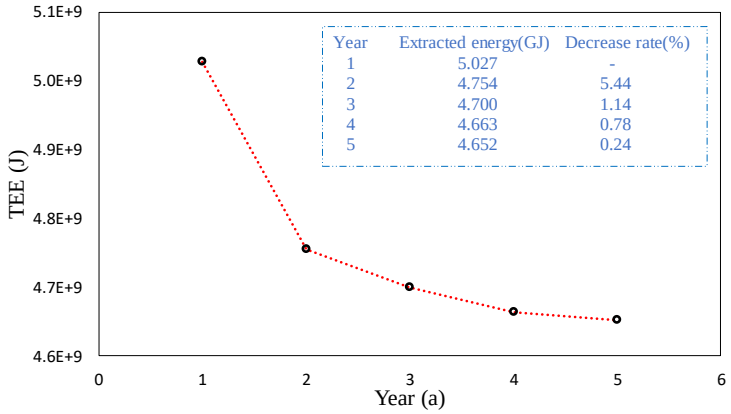

Fig. 4. Energie extraite par an sur une période de 5 ans

Facteurs influant sur la performance de le BHE peu profond

Dans ce chapitre, les facteurs affectant la performance d'un BHE avec un tube en U de 20 m sont étudiés, sensibles aux variations hydrothermales saisonnières en raison de sa faible profondeur. Un modèle de simulation numérique 3D par éléments finis a été utilisé pour estimer le COP annuel moyen des pompes à chaleur de deux modèles de référence typiques : le premier a été installé dans le sable et l'autre dans l'argile. Finalement, les variations du COP moyen annuel de la pompe à chaleur ont été étudiées pour le BHE peu profond installé dans les deux sols sous l'influence de 15 facteurs, tels que les conditions météorologiques, les conditions hydrauliques, la solution multi-pipe, etc.

En général, 54 cas ont été étudiés pour chaque sol. Le Tableau 1 résume les 15 facteurs, y compris les différents paramètres étudiés. Les paramètres de référence (sont également présentés au Tableau 1.

Tableau 1. Résumé des facteurs étudiés avec leurs valeurs correspondantes

No.	*Facteur*	*Paramètre (unité)*	*Paramètre de référence*
1	Conditions météorologiques	Climat froid, doux et chaud (-)	Climat doux
2	Condition hydraulique	Champ ouvert, herbe et forestier (-)	Champ d'herbe
3	Écoulement de l'eau souterraine	0, 1E-7, 2E-7, 3E-7 ($m.s^{-1}$)	0
4	Conductivité thermique du coulis	0.8, 1.4, 2.0, 2.5, 3.2 ($W.m^{-1}.K^{-1}$)	2.5
5	Capacité calorifique volumétrique du coulis	1.2,1.6,2.0,2.4, 3.5 ($MJ.m^{-3}.K^{-1}$)	2.0
6	Diamètre du coulis	0.10, 0.14, 018, 0.22 (m)	0.14

7	Écartement des tiges	0.03, 0.04, 0.05, 0.06, 0.09, 0.11 (m)	0.05
8	Solution multi-pipe	Simple, double (parallèle et croix), triple (parallèle et croix) (-)	Simple
9	Diamètre intérieur du tube	0.018, 0.022, 0.026, 0.030 (m)	0.022
10	Epaisseur du tube	0.001, 0.0015, 0.0020, 0.0025 (m)	0.0015
11	Conductivité thermique de la tuyauterie	0.25, 0.5, 2, 6, 11, 16 ($W.m^{-1}.K^{-1}$)	0.5
12	Matériau fluide porteur	Prop.glycol (25%), prop.glycol (33%), ethanol (24%), $CaCl_2$ (20%) (-)	Ethanol (24%)
13	Vitesse du fluide porteur	0.1, 0.2, 0.3, 0.4, 0.5, 0.6, 0.7, 0.8 ($m.s^{-1}$)	0.5
14	Mode charge thermique	Charge thermique saisonnière, charge thermique stable (-)	Charge thermique saisonnière
15	Niveau de charge thermique	0-36, 5-41, 10-46, 15-51, 20-56 ($W.m^{-1}$)	10-46

Fig. 5 présente statistiquement l'influence des 15 facteurs sur le COP annuel moyen de la pompe à chaleur pour le BHE peu profond installé dans le sable et l'argile par rapport aux modèles de référence. Les points suivants ont été observés :

- Les conditions météorologiques ont l'impact le plus important (41,6 % dans le sable et 45,3 % dans l'argile) sur la performance du BHE peu profond ;
- La conductivité thermique du coulis (27,2 % dans le sable, 30,1 % dans l'argile) et le niveau de charge thermique (29,4 % dans le sable, 36,4 % dans l'argile) ont également un impact élevé sur la performance du BHE peu profond ;
- La solution multitubulaire, la vitesse du fluide porteur et le niveau de charge thermique influencent le COP annuel moyen dans les deux sols entre 12,2% et 16,2% ;
- L'état hydraulique, le débit d'eau souterraine, la capacité calorifique volumétrique du coulis, le diamètre du coulis, l'espacement des tiges, le diamètre intérieur du tuyau, l'épaisseur du tuyau, la conductivité thermique du tuyau, le matériau du fluide porteur et le mode de charge thermique ont un impact moindre sur le COP moyen annuel de la pompe à chaleur (entre 0,0 et 11,6%).

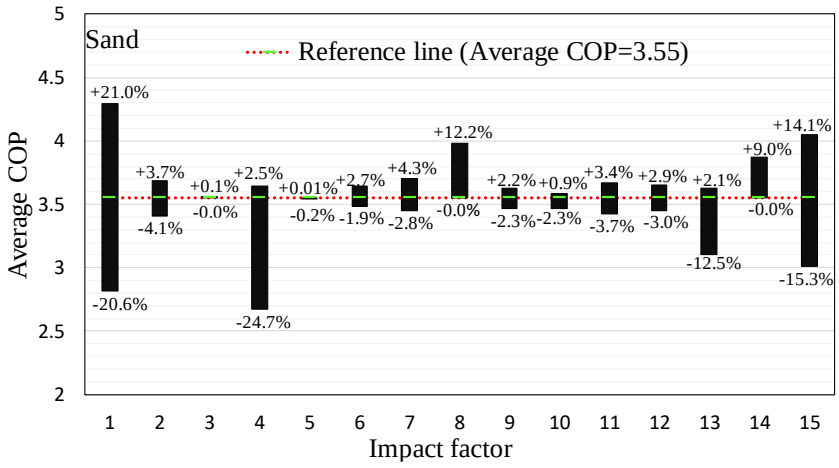

1-Meteorological condition 2-Hydraulic condition 3-Underground water 4-Grout thermal conductivity 5-Grout volumetric heat capacity 6-Grout diameter 7-Shank spacing 8-Multi-pipe solution 9-Pipe inner diameter 10-Pipe thickness 11-Pipe thermal conductivity 12-Carrying fluid material 13-Carrying fluid velocity 14-Heat load mode 15-Heat load level

(a)

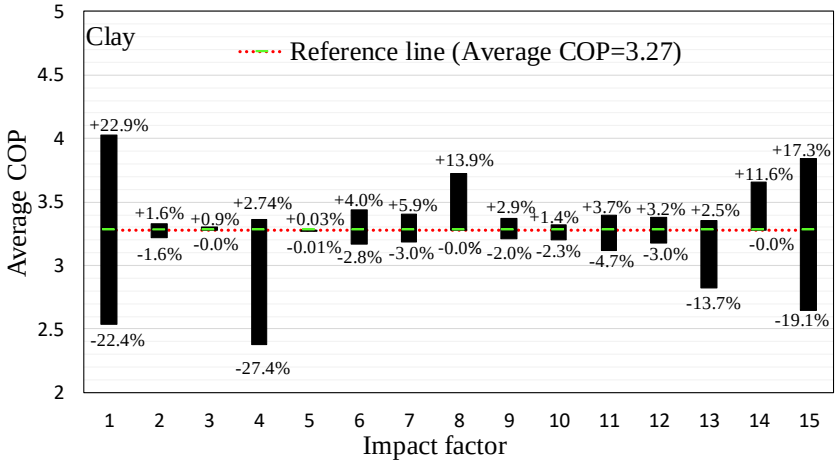

1-Meteorological condition 2-Hydraulic condition 3-Underground water 4-Grout thermal conductivity 5-Grout volumetric heat capacity 6-Grout diameter 7-Shank spacing 8-Multi-pipe solution 9-Pipe inner diameter 10-Pipe thickness 11-Pipe thermal conductivity 12-Carrying fluid material 13-Carrying fluid velocity 14-Heat load mode 15-Heat load level

(b)

Fig. 5. Influence statistique de chaque facteur sur le COP annuel moyen de la pompe à chaleur par rapport aux modèles de référence pour le BHE peu profond installé dans deux sols : a) sable et b) argile

Analyse sensible de la conductivité thermique effective du TRT dans le sol

Dans ce contexte, COMSOL a été adopté pour simuler la TRT pendant les jours les plus chauds d'une année en été et pendant les jours les plus froids d'une année en hiver. Les sols

étudiés sont constitués de zones insaturées et saturées, où les propriétés thermiques dans la zone saturée sont constantes et les propriétés thermiques du sol dans la zone insaturée sont déterminées par le profil hydraulique du sol. En raison de la courte durée d'essai du TRT, la température à la surface du sol et le profil hydraulique du sol environnant ont été considérés comme constants pendant la simulation.

En analysant les différents cas dans les simulations numériques, une nouvelle approche analytique a également été proposée pour l'estimation de la conductivité thermique effective du sol dans les applications BHE.

Dans la pratique, un BHE est traditionnellement entouré de sols insaturés et saturés, et la profondeur de la zone insaturée varie en fonction du niveau de l'eau. Les propriétés thermiques du sol varient avec le temps et l'espace, en particulier dans la zone non saturée. Pour mieux étudier l'influence de cette zone insaturée sur la conductivité thermique effective du sol, un rapport λ est introduit :

$$\lambda = \frac{z_u}{z_{U-pipe}} \tag{1}$$

Où z_u est la profondeur de la zone insaturée/niveau d'eau (m), $z_{U\text{-}pipe}$ désigne la longueur de conduite en U (m). Dans l'enquête, le rapport de λ se situe entre 0 et 1, ce qui indique que la zone insaturée ne dépasse pas la longueur de l'U-pipe.

Afin d'avoir une enquête plus complète, 10 scénarios ont été envisagés en modifiant soit la longueur de la conduite en U, soit le niveau de l'eau. Dans ce travail, la longueur de la conduite en U est comprise entre 11,5 et 34,03 m, le niveau d'eau entre 8,45 et 15 m et le rapport λ entre 0,34 et 1. Le Tableau 2 résume ces scénarios avec leurs rapports correspondants λ.

Tableau 2. Résumé des 10 scénarios pour 6 longueurs de conduites en U et 3 niveaux d'eau

Scénario	*Longueur du tube en U $z_{U\text{-}pipe}$ (m)*	*Niveau d'eau z_u (m)*	*$\lambda = z_u/z_{U\text{-}pipe}$*
S1	15	8.45	0.56
S2		11.5	0.77
S3		15.0	1
S4	20.42	11.5	0.56
S5	11.5		1
S6	25	8.45	0.34
S7		11.5	0.46
S8		15.0	0.6
S9	34.03	11.5	0.34
S10	19.17		0.6

Afin de mieux analyser les résultats du TRT et d'explorer l'effet du rapport λ et de la longueur de la conduite en U sur les résultats, les essais ont été divisés en deux groupes, tel que présenté au Tableau 3.

Tableau 3. Deux groupes proposés pour une analyse plus complète des TRTs

Group	*Scénario*	*Nappe phréatique (m)*	*Longueur du tube en U (m)*
1	S1, S2, S3, S6, S7, S8	Variable	15 & 25 (Constant)
2	S2, S4, S5, S7, S9, S10	11.5 (Constante)	Variable

La Fig. 6 montre la variation de la conductivité thermique effective de l'argile, du limon sableux et du sable avec le rapport λ et la longueur de l'U-pipe en été et en hiver pour les deux groupes. Les résultats du deuxième groupe sont présentés avec le rapport λ et la longueur de conduite en U.

La figure montre que les conductivités thermiques effectives du sol obtenu en hiver sont supérieures à celles obtenues en été (3,8 % à 14,0 % pour l'argile, 5,8 % à 24,3 % pour le loam sableux et 5,2 % à 17,9 % pour le sable) et que la différence la plus importante existe pour le tuyau en U le plus court. Le phénomène est dû à un transfert de chaleur favorable pendant la période d'injection de chaleur en hiver.

La figure montre également que la conductivité thermique effective du sol varie linéairement avec le rapport λ (Fig. 6 a-f) et qu'elle varie en outre sous forme polynomiale (2ème degré) avec la longueur du tube en U (Fig. 6 g-i).

Généralement, l'argile a la plus faible conductivité thermique effective parmi les 3 sols. Le sable et le limon sableux ont une plus grande variation des conductivités thermiques effectives que l'argile. De plus, le limon sableux a une conductivité thermique plus efficace que le sable dans les tuyaux en U peu profonds. Le phénomène peut être expliqué par la figure 6.5-a, où le limon sableux a une conductivité thermique plus élevée dans sa zone non saturée. Toutefois, l'avantage diminuerait avec l'augmentation de la longueur de la conduite en U, puisque le sable a une conductivité thermique plus élevée dans la zone saturée.

Dans le groupe 1 avec un niveau d'eau variable, la diminution de la conductivité thermique effective du sol avec le rapport λ est observée pour tous les sols (Fig. 6 a-c). Dans le groupe 2

avec une longueur de conduite en U variable, la même tendance est observée pour l'argile et le limon sableux en été tandis qu'une augmentation de leur conductivité thermique effective se produit en hiver (Fig. 6-d & e). La figure 6-f montre que la conductivité thermique effective du sable dans le sol diminue avec le rapport λ en été et en hiver.

De plus, la différence entre la conductivité thermique effective en été et en hiver diminue avec l'augmentation de la longueur de la conduite en U, et le taux de diminution est stabilisé pour les longueurs supérieures à 30 m (Fig. 6 g-i). Cela signifie que le temps d'essai affecte moins les résultats du TRT et que les tuyaux en U sont plus longs.

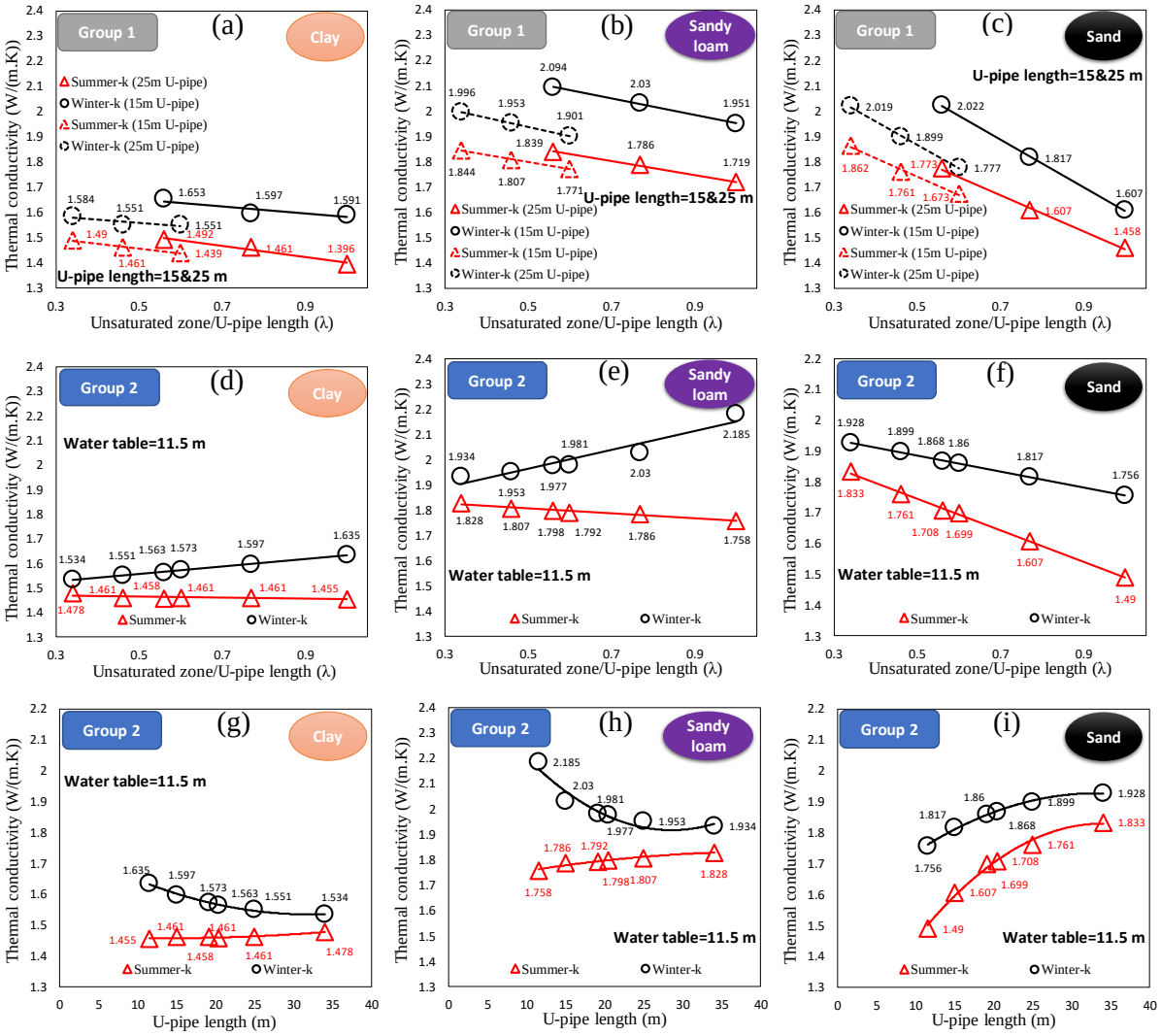

Fig. 6. Variation effective de la conductivité thermique du sol des 3 sols en été et en hiver pour le groupe 1 avec le rapport λ (a à c) et pour le groupe 2 avec le rapport λ (d à f) et la longueur en U (g à i)

Selon les résultats de la dernière section, la solution suivante est proposée pour prédire la conductivité thermique effective du sol:

$$k_{eff} = \begin{cases} a + b \cdot \lambda + c \cdot \chi^2 + d \cdot \chi & (\chi < 1) \\ e + b \cdot \lambda & (\chi \geq 1) \end{cases} \quad (2)$$

Où a ($W.m^{-1}.K^{-1}$), b ($W.m^{-1}.K^{-1}$), c ($W.m^{-1}.K^{-1}$), d ($W.m^{-1}.K^{-1}$) et e ($W.m^{-1}.K^{-1}$) sont des paramètres constants. χ est un autre facteur sans dimension, défini comme suit:

$$\chi = \frac{z_{U-pipe}}{L_{\max}} \quad (3)$$

Températures de sortie d'un HGHE avec l'interaction atmosphère-sol

L'objectif principal de cette étude est de construire un cadre de simulation numérique robuste pour évaluer la performance de l'HGHE sur le terrain en tenant compte du bilan énergétique et hydrique à la surface du sol.

Cette étude vise également à visualiser comment l'HGHE influence la température à la surface du sol et le flux de chaleur à travers la surface du sol, rarement étudié jusqu'à présent. De plus, l'étude a comparé les résultats de la simulation numérique dans deux conditions limites de surface différentes (avec/sans prise en compte de l'interaction atmosphère-sol), ce qui permet d'identifier la fiabilité de la méthode traditionnelle en définissant la température variable dans le temps comme limite de surface terrestre.

Les résultats de la simulation ont montré que le fonctionnement de l'HGHE affectait la température à la surface du sol et, par conséquent, son flux de chaleur souterraine. Pour visualiser cet effet, la fluctuation du flux de chaleur est présentée le long de la sonde de la ligne de surface. Le flux de chaleur du sol reste inchangé pendant les 99 premiers jours. Lorsque l'HGHE commence à fonctionner, le flux de chaleur du sol dans la zone affectée par l'HGHE est plus élevé que dans la zone non affectée en raison de l'extraction de chaleur pendant la saison de chauffage. Plus précisément, les flux de chaleur du sol dans la zone touchée par l'HGHE sont de 2,7, 9,2, 8,5 et 2,7 W.m-2 plus élevés que dans la zone non touchée les jours 130, 182,5, 200 et 260, respectivement.

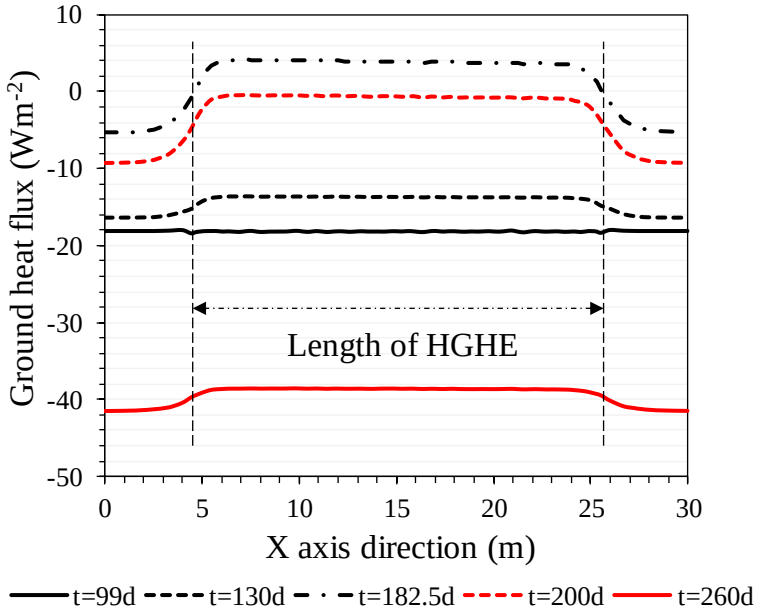

Fig. 7. Fluctuation du flux de chaleur du sol détectée par la sonde de ligne horizontale 1 à la surface du sol

La Fig. 8 compare les températures moyennes annuelles de sortie des fluides des conditions aux limites de la surface terrestre avec et sans l'influence de l'interaction atmosphère-sol. En général, une installation profonde améliore la température de sortie du fluide. Lorsque la profondeur d'installation passe de 0,5 à 2 m, les températures moyennes annuelles de sortie de fluide augmentent respectivement de 61,11% et 27,56% pour les scénarios avec et sans prise en compte de l'interaction atmosphère-sol. L'augmentation de la profondeur d'installation de 0,5 à 1 m n'a qu'un effet insignifiant sur les températures moyennes annuelles de sortie de fluide dans les deux scénarios.

De plus, les résultats confirment l'influence significative de l'interaction atmosphère-sol dans les simulations HGHE. Les températures moyennes annuelles de sortie de fluide sont fortement surestimées lorsque l'interaction est absente des calculs, surtout si l'HGHE est installé près de la surface du sol. La surestimation causée par la non prise en compte de l'interaction atmosphère-sol diminue avec l'augmentation de la profondeur d'installation. En général, la surestimation diminue de 47,99% à 17,16% lorsque la profondeur d'installation augmente de 0,5 à 2 m.

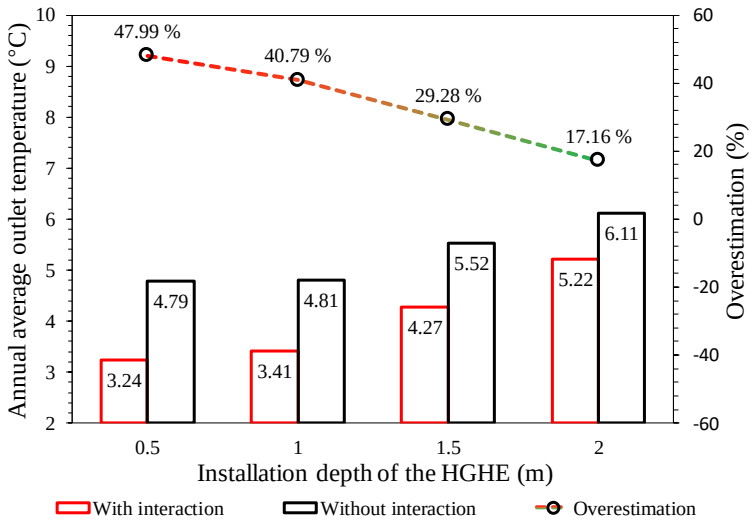

Fig. 8. Comparaison entre les températures moyennes annuelles de sortie des fluides avec et sans l'interaction atmosphère-sol

Conclusions et perspectives

Cette thèse présente un modèle de transfert hydrothermique dans le sol entourant les échangeurs de chaleur souterrains, étudie les facteurs influençant la performance d'un échangeur de chaleur souterrain peu profond, effectue une analyse sensible des TRT et estime la différence de performance d'une HGHE avec et sans l'interaction atmosphère-sol.

Dans un premier temps, un cadre de simulation numérique validé prenant en compte le transfert hydrothermal a été construit pour estimer la performance du BHE peu profond installé dans un champ géothermique de la région Alsace (France).

Deuxièmement, quinze facteurs influençant la performance d'un BHE peu profond ont été étudiés en considérant le transfert hydrothermal dans le sol. Les paramètres de chaque facteur ont été choisis avec une fourchette rationnelle.

Troisièmement, une approche analytique a été proposée après avoir effectué une analyse sensible sur les TRT en tenant compte des différentes durées d'essai, des conditions sur le terrain et des longueurs de conduite en U. La solution analytique peut aider à estimer la conductivité thermique efficace du sol dans le cas de projets avec investissements limités.

Ensuite, l'étude compare l'influence de l'utilisation des conditions limites de Dirichlet (sans l'interaction atmosphère-sol) et de Neumann (avec l'interaction atmosphère-sol) sur la surface terrestre de l'HGHE.

En perspective, un certain nombre de points reste à traiter :

- Conditions météorologiques précises sur le terrain et propriétés thermiques du sol dans la modélisation numérique.
- Comparer les performances in situ et numériques simulées à long terme de l'échangeur de chaleur souterrain.
- D'autres études sur le comportement mécanique du sol entourant les échangeurs de chaleur souterrains.
- Aspects économiques des systèmes GSHP.
- Systèmes hybrides GSHP.

Bibliographies

Atam, E., and Helsen, L. (2016). Ground-coupled heat pumps: Part 1 – Literature review and research challenges in modeling and optimal control. Renewable and Sustainable Energy Reviews *54*, 1653–1667.

Bidarmaghz, A., Narsilio, G.A., Johnston, I.W., and Colls, S. (2016). The importance of surface air temperature fluctuations on long-term performance of vertical ground heat exchangers. Geomechanics for Energy and the Environment *6*, 35–44.

International Energy Agency (IEA) (2016). TOWARDS LOW-GHG AND RESILIENT BUILDINGS.

Omer, A.M. (2018). Some Aspects of Soil Thermal Properties. 42.

Sangi, R., and Müller, D. (2018). Dynamic modelling and simulation of a slinky-coil horizontal ground heat exchanger using Modelica. Journal of Building Engineering *16*, 159–168.

Sanner, B. (2017). Ground Source Heat Pumps-history, development, current status, and future prospects. In 12th IEA Heat Pump Conference, (Giessen (Germany)), p.

Shao, H., Hein, P., Sachse, A., and Kolditz, O. (2016). Geoenergy Modeling II: Shallow Geothermal Systems (Cham: Springer International Publishing).

Shortall, R., Davidsdottir, B., and Axelsson, G. (2015). Geothermal energy for sustainable development: A review of sustainability impacts and assessment frameworks. Renewable and Sustainable Energy Reviews *44*, 391–406.

Sterpi, D. (2020). Insights into the Behaviour of Energy Piles Under Different Head Constraints and Thermal Loads. In Geotechnical Research for Land Protection and Development, F. Calvetti, F. Cotecchia, A. Galli, and C. Jommi, eds. (Cham: Springer International Publishing), pp. 763–772.

Université de Strasbourg

汤伏蛟

基于数值模拟方法对安装于土体中的地埋管换热器的研究

摘要

作为一种可再生能源，浅层地热能对实现人类可持续发展的目标有着重要的战略作用。土壤耦合热泵便能有效地利用浅层地热能。作为土壤耦合式地缘热泵系统的一个重要组成部分，地埋管换热器对其能量效率有着直接的影响。浅层地埋管换热器由于埋深浅的特性而常被安装于土体中，而土的水热特性在竖直剖面上具有较大的非均质性。本论文主要研究和分析安装于土中体竖直和水平地埋管换热器的性能。本论文主要进行的研究有：

第一，在有限元数值模拟中加上引入水-土运移模型并对安装于法国阿尔萨斯地区的浅层地埋管换热器进行研究。本章节主要研究土体季节性的水-热波动以及预测安装于多层土中的浅层竖直地埋管换热器的性能。研究结果显示土体中的水-热分布受制于各层土的土壤特性。接下来，基于本数值模拟模型对安装于相同场地的浅层地埋管换热器进行了两种场景的研究：恒定进口温度和季节性热荷载。模拟结果表明热泵效率在恒定进口温度场景下基本保持稳定，但是在季节性热荷载场景下有较大的波动。除此之外，本章节还预估了地埋管换热器在恒定进口温度下 5 年期内的性能。研究表明地埋管换热器在此场景下年采热量逐渐减少，而第四年后这种减少可以忽略不计。

第二，确定影响安装在土体中的浅层地埋管换热器性能的因素。结果发现安装在沙土中的换热器在大多数研究场景中比粘土中的性能好约 8%。结果发现气象条件（地埋管换热器周围温度），灌浆导热系数和热荷载对年平均热泵性能的影响超过 27.2%。多管模式和管内载液流速影对热泵性能的影响范围在 12.2%和 16.2%之间。此外，水力条件，地下水，灌浆体积热容，灌浆直径，管间距，管道内径，管道厚度，管道导热系数，载液材料和热负荷模式对热泵性能的影响介于 0 和 11.6%之间。

第三，对安装在土体中的地埋管换热器的热响应测试进行敏感性分析。本研究目的是寻找一种通过考虑测试季节，土体特性和 U 型管长度来估算有效导热系数的替代方法。为了达到这个目标，本章节采用数值模拟方法在一年中最热和最冷的季节对安装于粘土，砂质壤土和沙土中的地埋管进行了热响应测试，该测试包含不同 U 型管长度和不同地下水位。分析结果表明冬季的有效土壤热导率要高于夏季，而这种差异对超过 30m 的 U 型管不再明显。有效土壤热导率随新定义的 λ（地下水位与 U 型管长度与之比）线性变化，它也以多项式形式（2 次方）随 U 形管长度而变化。最后，本章节提出了一种估算土壤的有效导热系数的数学分析方法。

第四，识别使用 Neumann 和 Dirichlet 作为地表边界条件模拟水平地埋管换热器性能的差异。本章节提出并验证了考虑大气-土-水平地埋管换热器相互作用的数值模拟模型应用框架。然后在地热供暖条件下研究了安装在多层土中的水平螺旋式地埋管换热器的出口温度。研究结果显示水平地埋管换热器在运行期间会对地表温度和地表热通量有明显的影响。安装深度从 0.5m 增加到 2m 也会提高载液流出温度。但是这种效应在安装深度从 0.5m 到 1m 时是不明显的。分析结果显示不考虑大气-土壤相互作用会高估年平均载液流出温度，而当安装深度从 0.5m 增加到 2m 时，这种高估程度会从 47.99%降低到 17.16%。

关键词

浅层地热能; 地埋管换热器; 土体; 数值模拟; 水-热变化; 性能; 热响应试验。

Université de Strasbourg

Fu-Jiao TANG

Investigation numérique sur l'échangeur de chaleur installé dans des sols peu profonds

Résumé

La géothermie peu profonde est une énergie renouvelable qui peut aider l'humanité à atteindre les objectifs du développement durable. La thermopompe couplée au sol est traditionnellement utilisée pour bénéficier de cette énergie. En tant qu'élément principal d'un système de pompe à chaleur géothermique, le rendement d'un échangeur de chaleur souterrain peut influer directement l'efficacité énergétique d'un système de pompe à chaleur géothermique. Les échangeurs de chaleur souterrains peu profonds sont normalement installés dans les sols, qui présentent une grande hétérogénéité des propriétés hydrothermales le long des profils de sol. L'objectif principal de ce projet est d'identifier le comportement des échangeurs de chaleur souterrains dans les sols. Les échangeurs de chaleur souterrains inclus dans ce projet sont l'échangeur de chaleur de puits de forage et l'échangeur de chaleur géothermique horizontal. En résumé, les enquêtes suivantes ont été menées dans le cadre de ce projet :

La première consiste à introduire le transfert hydrothermique dans la modélisation numérique des échangeurs géothermiques installés sur un site en Alsace (France). Dans cette partie, les fluctuations hydrothermales saisonnières et la performance de l'échangeur de chaleur de forage peu profond du site avec un système de sol multicouche ont été prédites. Les résultats ont montré que les profils hydrothermiques du sol dépendaient fortement des propriétés du sol dans différentes couches. Par la suite, le modèle a été utilisé pour estimer la performance d'un échangeur de chaleur de forage peu profond installé au même endroit sur une année en considérant deux scénarios différents : une température d'entrée constante et une charge thermique saisonnière. On a constaté que le coefficient de performance dans le scénario de température d'entrée constante reste presque stable pendant la période de service. Cependant, le coefficient de performance de la thermopompe dépend fortement de la charge thermique et montre plus de variance dans le scénario de charge thermique saisonnière. Le rendement de l'échangeur de chaleur peu profond du puits de forage a été estimé pour une période de cinq ans en supposant la température d'entrée constante. On a constaté que l'énergie annuelle totale extraite diminue chaque année, mais cette diminution est devenue négligeable après la quatrième année.

La seconde enquête consiste à identifier les facteurs qui influencent la performance d'un échangeur de chaleur de forage peu profond installé dans les sols. Il a été constaté que l'échangeur de chaleur de forage peu profond installé dans le sable est plus performant que celui de l'argile de 8%. La même différence de performance entre le sable et l'argile a été observée dans la plupart des scénarios étudiés. Le rendement annuel moyen des thermopompes a présenté une variation de plus de 27,2 % selon les conditions météorologiques, la conductivité thermique du coulis et le niveau de charge thermique. La solution multitubulaire et la vitesse du fluide caloporteur ont également influencé le rendement de la thermopompe, variant entre 12,2 et 16,2 %. D'autres facteurs tels que l'état hydraulique, le débit d'eau souterraine, la capacité calorifique volumétrique du coulis, le diamètre du coulis, l'espacement des tiges, le diamètre intérieur du tuyau, l'épaisseur du tuyau, la conductivité thermique du tuyau, le matériau du fluide porteur et le mode de charge thermique ont eu un impact moindre sur le coefficient de performance de la thermopompe, variant entre 0 et 11,6%.

La troisième étude concerne l'analyse de sensibilité des essais de réponse thermique pour les échangeurs de chaleur de forage installés dans les sols. Cette étude a été menée pour trouver une approche alternative à l'estimation de la conductivité thermique effective sur le terrain en tenant compte de différents moments d'essai, conditions de terrain et longueurs de conduite en U. Pour atteindre cet objectif, les essais de

réponse thermique ont été effectués numériquement dans de l'argile, du limon sableux et du sable pendant les jours les plus chauds d l'année en été et les jours les plus froids de l'année en hiver avec différentes longueurs de tuyaux en U et différents niveaux d'eau souterraine. Les résultats ont montré que la conductivité thermique effective du sol était plus élevée en hiver qu'en été, tandis que cette différence devenait moins significative pour les conduites en U de plus de 30 m. La conductivité thermique effective du sol variait linéairement avec un nouveau rapport défini λ (la profondeur du niveau d'eau divisée par la longueur des conduites en U). Elle variait également en fonction de la longueur de la conduite en U sous forme polynomiale (second degré). Enfin, une approche analytique est proposée pour estimer la conductivité thermique effective du sol.

La dernière étude traite l'identification de la différence de performance d'un modèle de simulation numérique avec les limites de Neumann et de Dirichlet à la surface du sol pour un échangeur horizontal de chaleur souterraine. Dans le cadre de cette étude, un cadre numérique tenant compte de l'interaction entre l'atmosphère, le sol et l'échangeur de chaleur géothermique horizontal a été proposé et validé. Les températures de sortie d'un échangeur horizontal de chaleur de type slinky-type installé dans un sol multicouche ont ensuite été étudiées dans le cadre du scénario de chauffage. Les résultats ont montré que le fonctionnement de l'échangeur de chaleur géothermique horizontal affectait évidemment la température à la surface du sol et le flux de chaleur souterraine. L'augmentation de la profondeur de montage de 0,5 à 2 m a augmenté la température de sortie. Cependant, cette augmentation était négligeable lorsque la profondeur d'installation passait de 0,5 à 1 m. On a également constaté que la non prise en compte de l'interaction atmosphère-sol surestimait la température annuelle de sortie du fluide dans le scénario de chauffage, et cette surestimation a diminué de 47,99 % à 17,16 % lorsque la profondeur d'installation passait de 0,5 à 2 m.

Mots-clés

Géothermie peu profonde; Échangeur de chaleur souterrain; Sol; Modélisation numérique; Fluctuation hydrothermale; Performance; Essai de réponse thermique.

Fu-Jiao TANG

Numerical investigation on the ground heat exchanger installed in shallow depth soils

Abstract

Shallow geothermal energy is a renewable energy that can help humanity to achieve the goal of sustainable development. Ground-Coupled Heat Pump system is traditionally used to benefit this energy. As a main element the system, ground heat exchanger performance can directly influence its energy efficiency. The shallow ground heat exchangers are normally installed in soils, which show high heterogeneity of hydrothermal properties along the soil profile. The main objective of this project is identifying how ground heat exchanger behaves in the soil. The ground heat exchangers included in this project are Borehole Heat Exchanger and Horizontal Ground Heat Exchanger. In summary, the following investigations have been conducted:

The first is introducing hydrothermal transfer in the numerical modeling of ground heat exchangers installed at a site in Alsace region (France). In this part, seasonal hydrothermal fluctuations and shallow Borehole Heat Exchanger performance of the site with a multi-layered soil system were predicted. The results showed that the soil hydrothermal profiles depended highly on the soil properties in different layers. Subsequently, the model was used to explore the performance of a shallow Borehole Heat Exchanger installed at the same place over a year considering two different scenarios: constant inlet temperature and seasonal heat load. It was found that the Coefficient of Performance in constant inlet temperature scenario remained almost stable during the service period. While heat pump Coefficient of Performance depended strongly on the heat load and shows more variance in the seasonal heat load scenario. The performance of the shallow Borehole Heat Exchanger was estimated for a 5-year period considering the constant inlet temperature scenario. It was found that the yearly Total Extracted Energy decreases annually, while this reduction became negligible after the fourth year.

The second is identifying the factors influencing the performance of a shallow Borehole Heat Exchanger installed in soils. It was found that the shallow Borehole Heat Exchanger installed in sand has a better performance of 8% than in clay. The same performance difference between sand and clay was observed in most of the investigated scenarios. The annual average heat pump performance presented a variation more than 27.2% with the meteorological condition, the grout thermal conductivity and the heat load level. The multi-pipe solution and the carrying fluid velocity also influenced the heat pump performance, ranging between 12.2 and 16.2%. Other factors such as the hydraulic condition, the groundwater flow, the grout volumetric heat capacity, the grout diameter, the shank spacing, the pipe inner diameter, the pipe thickness, the pipe thermal conductivity, the carrying fluid material and the heat load mode had less impact on the heat pump Coefficient of Performance, varying between 0 and 11.6%.

The third is conducting sensitive analysis of Thermal Response Tests for Borehole Heat Exchanger installed in soils. This investigation was conducted to find an alternative approach to estimating the field effective thermal conductivity by considering various testing times, field conditions and U-pipe lengths. To reach this objective, the Thermal Response Tests were conducted numerically in clay, sandy loam and sand during the hottest day(s) of a year in summer and the coldest day(s) of a year in winter with various U-pipe lengths and groundwater levels. The results showed that there was a higher effective soil thermal conductivity in winter than in summer while this difference became less significant for the U-pipes longer than 30 m. The effective soil thermal conductivity varied linearly with a newly defined λ ratio (the water level depth divided by the U-pipe length). It also varied with the U-pipe length in a polynomial form (2nd degree). Finally, an analytical approach is proposed to estimate the effective soil thermal conductivity.

The fourth is identifying the performance difference of a numerical simulation model with Neumann and Dirichlet boundaries on the ground surface for a Horizontal Ground Heat Exchanger. In this investigation, a numerical framework considering the atmosphere-soil-Horizontal Ground Heat Exchanger interaction was proposed and validated. The outlet temperatures of a slinky-type Horizontal Ground Heat Exchanger installed in a multi-layered soil field were then investigated under the heating scenario. The results showed that the operation of the Horizontal Ground Heat Exchanger affected obviously the ground surface temperature and the ground heat flux. The increase of the installation depth from 0.5 to 2 m increased the outlet temperatures. However, this increase was insignificant when the installation depth increased from 0.5 to 1 m. It was further identified that the non-consideration of the atmosphere-soil interaction overestimated the annual fluid outlet temperature in the heating scenario, and this overestimation decreased from 47.99% to 17.16% as the installation depth increased from 0.5 to 2 m.

Keywords

Shallow geothermal energy; Ground heat exchanger; Soil; Numerical modeling; Hydrothermal fluctuation; Performance; Thermal Response Test.